

AFIT/DS/ENG/02-03



ELECTROMAGNETIC SCATTERING FROM A GAP IN A MAGNETO-DIELECTRIC
COATING ON AN INFINITE GROUND PLANE

DISSERTATION
George Robert Simpson

AFIT/DS/ENG/02-03

DEPARTMENT OF THE AIR FORCE
AIR UNIVERSITY

AIR FORCE INSTITUTE OF TECHNOLOGY

Wright-Patterson Air Force Base, Ohio

APPROVED FOR PUBLIC RELEASE; DISTRIBUTION UNLIMITED

Report Documentation Page		
Report Date 8 Oct 02	Report Type Final	Dates Covered (from... to) Dec 97 - Sep 02
Title and Subtitle Electromagnetic Scattering From a Gap in a Magneto-Dielectric Coating on an Infinite Ground Plane	Contract Number	
	Grant Number	
	Program Element Number	
Author(s) George R. Simpson	Project Number	
	Task Number	
	Work Unit Number	
Performing Organization Name(s) and Address(es) Air Force Institute of Technology Graduate School of Engineering and Management (AFIT/EN) 2950 P Street, Bldg 640 WPAFB OH 45433-7765	Performing Organization Report Number AFIT/DS/ENG/02-03	
Sponsoring/Monitoring Agency Name(s) and Address(es) AFRL/SNS ATTN: Dr. Kueichien C. Hill 2519 K Street, Bldg 254 WPAFB OH 45433-7602	Sponsor/Monitor's Acronym(s)	
	Sponsor/Monitor's Report Number(s)	
Distribution/Availability Statement Approved for public release, distribution unlimited		
Supplementary Notes		
Abstract <p>The electromagnetic scattering from a gap in a magneto-dielectric coating on an infinite ground plane is analyzed. In this context, the gap forms a break only in the magneto-dielectric slab coating while the ground plane is continuous and unbroken. Volume equivalence is used to convert the gap region to one containing unknown volumetric equivalent electric and magnetic currents. The equivalent problem then is one of these currents radiating in the presence of an unbroken grounded magneto-dielectric slab. A Greens function for this geometry is developed consisting of two terms: a direct coupling term and correction term to account for the multiple reflected wave series resulting from the grounded-slab geometry. This bounce correction term is formulated using periodic array theory and is derived using the Array Scanning Method. A set of coupled integral equations based on these equivalent currents is then solved via the Method of Moments using pulse basis and delta testing functions. The model can represent a gap that is of a general 2D shape (the gap is assumed to be infinite in its translational direction) and can be filled with an inhomogeneous material possessing isotropic magnetic and dielectric constitutive properties different from those of the slab coating. Scattering from the gap is evaluated for plane wave illumination that is either TM or TE with respect to the gap.</p>		
Subject Terms Electromagnetic scattering, hybrid Greens function/Method of Moments, Array Scanning Method		
Report Classification unclassified	Classification of this page unclassified	

Classification of Abstract unclassified	Limitation of Abstract UU
Number of Pages 191	

The views expressed in this dissertation are those of the author and do not reflect the official policy or position of the Department of Defense or the United States Government.

AFIT/DS/ENG/02-03

Electromagnetic Scattering from a Gap in a Magneto-Dielectric Coating on an Infinite
Ground Plane

DISSERTATION

Presented to the Faculty of the School of Engineering and Management
of the Air Force Institute of Technology

Air University

In Partial Fulfillment of the
Requirements for the Degree of
Doctor of Philosophy

George Robert Simpson, B.S.E.E., M.S.E.E.

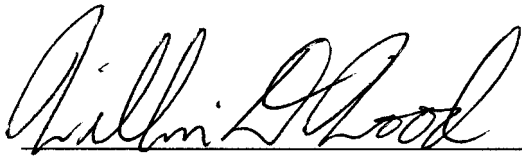
December 2002

Approved for public release; distribution unlimited

Electromagnetic Scattering from a Gap in a
Magneto-Dielectric Coating on an Infinite Ground Plane

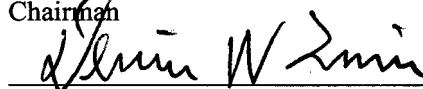
George Robert Simpson, B.S.E.E., M.S.E.E.

Approved:



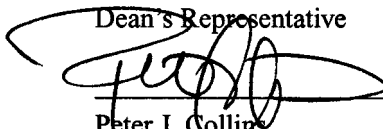
William D. Wood
Chairman

28 Oct 02
Date




Dennis W. Quinn
Dean's Representative

28 OCT 02
Date



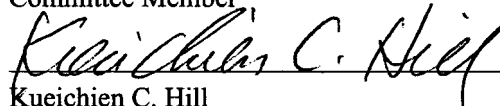
Peter J. Collins
Committee Member

21 OCT 02
Date



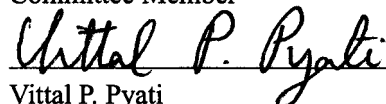
William P. Baker
Committee Member

28 Oct 02
Date




Kueichien C. Hill
Committee Member

28 Oct 02
Date



Vittal P. Pyati
Committee Member

29 Oct 02
Date



Robert A. Calico, Jr
Dean

Acknowledgments

I would like to express my appreciation to my faculty advisors, Pete Collins and Bill Wood, for their guidance and support throughout this effort. I also want to acknowledge and thank my committee for their collective efforts to keep me on track over the years. I thank also various friends and colleagues who have continually supported and encouraged me along the way.

I want to express my appreciation for my organization, the Air Force Research Laboratory Signature Technology Office, for the sponsorship and latitude granted me for the entire duration of this research effort. I thank my directors; Marv Spector, Art Duke, and Robert Williams, for their patience and continued support during my time at AFIT. I thank all my supervisors; Joe Faison, Bob Knapp, Mike Cox, Brian Kent, and Garry Grider, for their unwavering support during this long period of $\frac{1}{2}$ -time employment. And I especially thank my coworkers in the Measurement and Predictions Division, past and present, for their patience, support, and encouragement all the while.

I thank the Air Force Research Laboratory for their support, through the Long Term/Full Time and Work/Study programs, which enabled me to begin this endeavor. I especially want to acknowledge and thank the Dayton Area Graduate Studies Institute (DAGSI) for their financial support of my dissertation research, which enabled me to complete the effort.

Finally, I want to express my most sincere appreciation to my wife, whose unfailing love and devotion has been matched only by her patience and understanding; and to my children; who in their own way have motivated, supported, and encouraged me throughout this experience. Had it not been for the support of my family I would not have completed (nor even begun) this work. I am most of all dedicated to each of you.

George Robert Simpson

Table of Contents

	Page
Acknowledgments	iii
List of Figures	viii
Abstract	xiii
 I. Introduction	 1-1
1.1 Background and Problem Statement	1-1
1.2 Proposed Solution	1-2
1.3 Related Work	1-3
1.3.1 Gaps in Ground Planes	1-4
1.3.2 Gaps in Material Coated Ground Planes	1-5
1.3.3 Hybrid Moment Method / Green's Function Techniques	1-7
1.4 Overview of Solution Approach	1-9
1.4.1 Solution Approach Summary	1-9
1.5 Dissertation Summary	1-15
 II. Theoretical Development	 2-1
2.1 Scalar Green's Function for the Coated Conducting Plane	2-1
2.2 Dyadic Green's Function for the Coated Conducting Plane	2-7
2.3 Expressions Applied to TM Polarization Case	2-9
2.3.1 Form of the Dyadic Green's Function for TM Polarization	2-9
2.3.2 The T-factor for TM Polarization	2-11
2.3.3 Complete Expressions for TM Polarization	2-19
2.4 Expressions for the TE Polarization Case	2-23
2.4.1 Dyadic Green's Function	2-23
2.4.2 T-factor for TE Polarization	2-23

	Page
2.4.3 Complete Expressions for TE Polarization	2-27
2.5 The External Green's Function	2-28
2.6 Incident Fields	2-32
III. Numerical Implementation	3-1
3.1 Bounce Correction Term Integrands	3-1
3.1.1 The Canonical ASM Integrand Function	3-2
3.1.2 Integrand Functions for Dyadic Green's Function Components	3-7
3.1.3 Summary	3-14
3.2 Moment Method Solution	3-14
3.2.1 TM Polarization	3-15
3.2.2 TE Polarization	3-18
3.3 Evaluation of Moment Method Expressions	3-19
3.3.1 Evaluation of Self Terms	3-19
3.3.2 Adjacent Terms	3-23
3.3.3 Distant terms	3-24
3.3.4 Summary	3-25
3.4 Evaluation of Incident Fields	3-25
3.5 Far Zone Scattering and 2-D Echo Width	3-25
IV. Results	4-1
4.1 The Ram2d Numerical Test Body	4-2
4.2 Gap in Pure Dielectric Slab Coating, TM Polarization	4-4
4.3 Gap in Magneto-dielectric Material and Comparison to Measurements, TM Polarization	4-14
4.4 Gap in Magneto-dielectric Material and Comparison to Measurements, TE Polarization	4-19
4.5 Convergence of the Hybrid Code	4-25
4.6 Summary of Results	4-29

	Page
V. Summary	5-1
5.1 Conclusion	5-1
5.2 Recommendations for Further Development	5-2
Appendix A. Spatial Domain to Spectral Domain Transformation via the Poisson Sum Formula	A-1
Appendix B. The Array Scanning Method	B-1
Appendix C. Additional Plots of the ASM Integrand	C-1
C.1 Additional Integrand Functions for Dyadic Green's Function Components	C-1
C.2 Integrand Functions for the Case of Self Coupling	C-7
C.3 Green's Function Integrands for Cases With Vertical Separation of Source and Receiver	C-13
C.4 Green's Function Integrands for Cases With Horizontal Separation of Source and Receiver	C-16
C.5 Appendix C Summary	C-19
Appendix D. Echo Width Measurements and the AFRL Compact Range	D-1
Appendix E. Measurement of Material Properties	E-1
Appendix F. A Synopsis of the Skinner Theory and Code	F-1
F.1 Introduction	F-1
F.2 Integral Equation and Moment Method Solution	F-2
F.3 Internal Green's Function	F-5
F.4 Far Zone Scattered Fields	F-8
F.5 Skinner's <i>gaptm</i> Computer Code	F-9
F.6 Comparison of Skinner Theory to Dissertation	F-10
Bibliography	BIB-1

	Page
Vita	VITA-1

List of Figures

Figure		Page
1.1.	Typical gaps in aircraft skin or skin coating	1-2
1.2.	Representative gap geometries found in the literature	1-4
1.3.	General gap geometry of Moore and Ling, [10]	1-6
1.4.	Geometry of Cylinder and Strip from Newman [3]	1-8
1.5.	Two-dimensional gap geometry	1-9
1.6.	2-D space filled with material having $\epsilon = \epsilon_r, \mu = \mu_r$	1-10
1.7.	Equivalence extraction of gap region having $\epsilon = \epsilon_g, \mu = \mu_g$	1-11
1.8.	Discretization of gap region for Moment Method solution showing domain of the equivalent currents.	1-14
2.1.	Four fundamental bounce modes within the slab	2-2
2.2.	Infinite array of line sources within the slab	2-3
2.3.	Reflection Coefficient for Lossless Material, TM pol	2-13
2.4.	Reflection Coefficient for Lossy Material, TM pol	2-14
2.5.	Complex Behavior of r_{y0} and r_{y1} Factors	2-15
2.6.	Reflection Coefficient for Lossless Magneto-Dielectric Material, TM pol	2-16
2.7.	Reflection Coefficient for Lossy Magneto-Dielectric Material, TM pol	2-17
2.8.	2-18
2.9.	Reflection Coefficient for Lossless Dielectric, TE pol	2-24
2.10.	Reflection Coefficient for Lossy Dielectric, TE pol	2-25
2.11.	Reflection Coefficient for Lossless Magneto-Dielectric, TE pol	2-26
2.12.	Reflection Coefficient for Lossy Magneto-Dielectric, TE pol	2-27
2.13.	2-28
2.14.	Coupling paths for the external Green's function	2-29
3.1.	Representative Gap Geometry	3-2

Figure		Page
3.2.	Canonical Green's Function Integrand	3-3
3.3.	Canonical Green's Function Integrand, Lossy Material	3-5
3.4.	Canonical Green's Function Integrand, TE Polarization	3-6
3.5.	Canonical Green's Function Integrand for Lossy Material	3-7
3.6.	Green's Function Integrand for G_{xx} Component, TM Polarization	3-8
3.7.	Green's Function Integrand for G_{xy} Component, TE Polarization	3-9
3.8.	Green's Function Integrand for G_{xz} Component, TM Polarization	3-10
3.9.	Green's Function Integrand for G_{yy} Component, TE Polarization	3-11
3.10.	Green's Function Integrand for G_{yy} Component, TM Polarization	3-12
3.11.	Green's Function Integrand for G_{zy} Component, TE Polarization	3-13
3.12.	Circle Extraction Technique	3-20
3.13.	Circle Extraction Technique Error Estimate	3-23
3.14.	Field Point Locations for External Green's Function	3-27
3.15.	Field Point 5 Inches Above Source Point	3-28
3.16.	Field Point 10 Inches Above Source Point	3-29
3.17.	Field Point 20 Inches Above Source Point	3-30
3.18.	Geometry definitions for stationary phase evaluation	3-31
4.1.	Ram2d Numerical Test Body	4-3
4.2.	Comparison for rectangular gap in lossless dielectric, 8 GHz	4-5
4.3.	Comparison for rectangular gap in lossless dielectric, 12 GHz	4-6
4.4.	Comparison for rectangular gap in lossless (denser) dielectric, 12 GHz	4-7
4.5.	Comparison for wide rectangular gap in lossless dielectric, 12 GHz	4-8
4.6.	Comparison for rectangular gap in lossy dielectric, 12 GHz	4-9
4.7.	Comparison for treated rectangular gap in lossy dielectric, 12 GHz	4-10
4.8.	Comparison for non-rectangular gap in lossy dielectric, 12 GHz	4-12
4.9.	Gap Geometry for Results Plotted in Figure 4.8	4-12
4.10.	Comparison for non-symmetric gap in lossy dielectric, 12 GHz	4-13

Figure		Page
4.11.	Gap Geometry for Results Plotted in Figure 4.10	4-13
4.12.	Comparison for air filled gap in lossy magneto-dielectric, 8 GHz, TM pol .	4-15
4.13.	Comparison for air filled gap in lossy magneto-dielectric, 10 GHz, TM pol	4-16
4.14.	Comparison for air filled gap in lossy magneto-dielectric, 12 GHz, TM pol	4-17
4.15.	Comparison for treated gap in lossy magneto-dielectric, 8 GHz, TM pol . .	4-18
4.16.	Comparison for treated gap in lossy magneto-dielectric, 10 GHz, TM pol .	4-19
4.17.	Comparison for treated gap in lossy magneto-dielectric, 12 GHz, TM pol .	4-20
4.18.	Comparison for 60 mil air filled gap in lossy magneto-dielectric, TM pol .	4-21
4.19.	Comparison for 60 mil treated gap in lossy magneto-dielectric, TM pol . .	4-22
4.20.	Comparison for TE polarization	4-23
4.21.	Comparison for air filled gap in lossy magneto-dielectric, 8 GHz, TE pol .	4-24
4.22.	Comparison for air filled gap in lossy magneto-dielectric, 10 GHz, TE pol	4-25
4.23.	Comparison for air filled gap in lossy magneto-dielectric, 12 GHz, TE pol	4-26
4.24.	Comparison for treated gap in lossy magneto-dielectric, 8 GHz, TE pol . .	4-27
4.25.	Comparison for treated gap in lossy magneto-dielectric, 10 GHz, TE pol .	4-28
4.26.	Comparison for treated gap in lossy magneto-dielectric, 12 GHz, TE pol .	4-29
4.27.	Comparison for 60 mil air filled gap, TE pol	4-31
4.28.	Comparison for 60 mil treated gap, TE pol	4-31
4.29.	Convergence Progress for TM pol case	4-32
4.30.	Expanded y-axis scale	4-32
4.31.	Convergence Progress for TE pol case	4-33
4.32.	Expanded y-axis scale	4-33
C.1.	G_{xx} Integrand Function for Lossy Material Case, TE Polarization	C-2
C.2.	G_{xy} Integrand Function for Lossy Material Case, TE Polarization	C-3
C.3.	G_{xz} Integrand Function for Lossy Material Case, TE Polarization	C-4
C.4.	G_{yy} Integrand Function for Lossy Material Case, TE Polarization	C-5
C.5.	G_{zy} Integrand Function for Lossy Material Case, TE Polarization	C-6

Figure		Page
C.6.	G_{xx} Integrand Function for Self Coupling Case, TE Polarization	C-7
C.7.	G_{xy} Integrand Function for Self Coupling Case, TM Polarization	C-8
C.8.	G_{xz} Integrand Function for Self Coupling Case, TM Polarization	C-9
C.9.	G_{yy} Integrand Function for Self Coupling Case, TE Polarization	C-10
C.10.	G_{zy} Integrand Function for Self Coupling Case, TE Polarization	C-11
C.11.	G_{zz} Integrand Function for Lossy Material Case, TM Polarization	C-12
C.12.	G_{xx} Integrand Function Vertical Separation Case, TE Polarization	C-13
C.13.	G_{xy} Integrand Function for Vertical Separation Case, TE Polarization . . .	C-14
C.14.	G_{xz} Integrand Function for Vertical Separation Case, TE Polarization . . .	C-15
C.15.	G_{yy} Integrand Function for Horizontal Separation Case, TE Polarization .	C-16
C.16.	G_{zy} Integrand Function for Horizontal Separation Case, TE Polarization .	C-17
C.17.	G_{zz} Integrand Function for Horizontal Separation Case, TE Polarization .	C-18
D.1.	Side View Drawing of the AFRL Compact Range	D-1
D.2.	Top Down View of the Boat Test Fixture	D-2
D.3.	Tip View of the Boat Test Fixture	D-3
D.4.	Photo of the Boat Test Fixture During Test	D-4
D.5.	Photo of Gap Detail on Boat Test Fixture	D-5
D.6.	60 mil Gap on Boat Test Fixture	D-6
E.1.	Photo of the GTRI Focused Arch Apparatus	E-1
E.2.	Cross Section Drawing of the GTRI Focused Arch System	E-2
E.3.	Slab coating material permittivity.	E-3
E.4.	Slab coating material permeability	E-4
E.5.	Gap filler material permittivity	E-5
E.6.	Gap filler material permeability	E-5
E.7.	Comparison for air filled gap scatter	E-6
E.8.	Comparison for treated gap scatter	E-7

Figure		Page
F.1.	Rectangular Gap in a Dielectric Coated Ground Plane	F-1
F.2.	Infinite Array of Radiating Current Filaments	F-6

Abstract

The electromagnetic scattering from a gap in a magneto-dielectric coating on an infinite ground plane is analyzed. In this context, the gap forms a break only in the magneto-dielectric slab coating while the ground plane is continuous and unbroken. The volume equivalence theorem is used to convert the gap region to one containing unknown volumetric equivalent electric and magnetic currents. The equivalent problem then is one of equivalent currents radiating in the presence of an unbroken grounded magneto-dielectric slab. A Green's function for this geometry is developed which consists of two terms: a direct coupling term and correction term to account for the multiple reflected wave series resulting from the grounded-slab geometry. This bounce correction term is formulated using periodic array theory and is derived using the Array Scanning Method (ASM). A set of coupled integral equations based on these equivalent currents is then solved via the Method of Moments (MoM) using pulse basis and delta testing functions.

The model can represent a gap that is of a general two-dimensional (2D) shape (the gap is assumed to be infinite in its translational direction) and can be filled with an inhomogeneous material possessing isotropic magnetic and dielectric constitutive properties different from those of the slab coating. The properties of both the gap filler and the slab coating materials can be complex in representation of lossy materials. The scattering from the gap is evaluated for plane wave illumination that is either transverse magnetic (TM) or transverse electric (TE) with respect to the axis of the gap.

This hybrid Green's Function/MoM technique is validated using a general-purpose MoM reference code and measured data obtained on a Radar Cross Section (RCS) measurement range. The results show that the hybrid method is accurate and more time efficient than methods relying on existing general-purpose reference codes. The result is a technique in which the 2-D RCS of a gap, and potential gap filler treatment materials, can be analyzed in a rapid and efficient manner.

Electromagnetic Scattering from a Gap in a Magneto-Dielectric Coating on an Infinite Ground Plane

I. Introduction

1.1 Background and Problem Statement

Designers and manufacturers of aerospace vehicles have been concerned with the presence and effects of gaps or breaks in the surfaces of aerodynamic vehicles for many years. More recently, engineers designing aerospace vehicles with controlled (and perhaps reduced) radar signatures have become concerned with the effects of gaps on the scattering of radar energy from a vehicle's surface. Of particular interest, is the effect on a vehicle's radar cross section (RCS) due to a gap or break in an electromagnetic material coating on the surface of a vehicle.

Gaps in an aircraft's skin or in electromagnetic material coatings can be required for a number of reasons. Aerodynamic control surfaces and canopy/fuselage seams are but two examples of situations creating a gap or break in the vehicle's skin or in any coating on the surface of the vehicle in the vicinity of these features. Such situations are notionally depicted in Figure 1.1. Other examples can be avionics or other equipment access panels, ordnance bay doors, landing gear cover doors, and fuel nozzle covers. Modern aircraft, even those designed and constructed for reduced signature levels, can possess numerous breaks and gaps in the aircraft's skin which can greatly complicate signature analysis and control efforts.

Improved gap analysis techniques are required for rapid numerical prototyping of potential gap treatment techniques. Presently available general-purpose (fully three dimensional) computational electromagnetic (CEM) codes, which are capable of computing the effects of these gaps, require large amounts of technician time for grid generation and can require significant amounts of expensive computer time. This is especially true if the finer details of a gap or break are to be modelled. Most general-purpose CEM codes that can accommodate large targets are designed to compute the scattering from an entire test fixture or body, not from an isolated surface feature. In order to study the effects of a surface feature, such as a gap in a material coated region, two runs

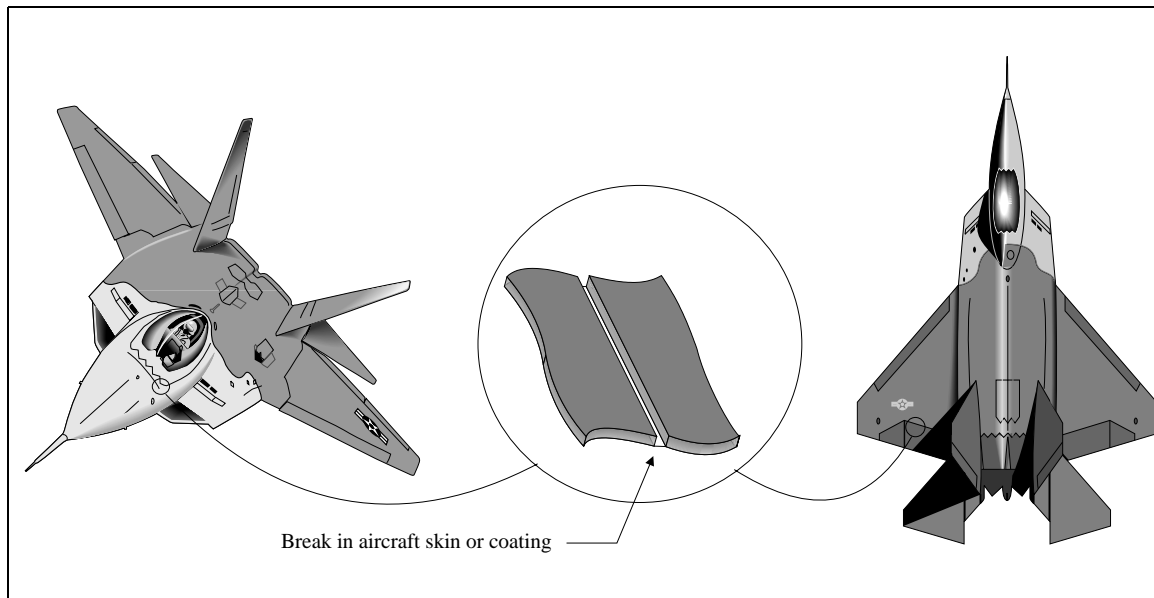


Figure 1.1 Typical gaps in aircraft skin or skin coating

would be necessary with the CEM code, one with the gap present and a second without the gap. The results from the two runs would then have to be coherently subtracted to isolate the scattering from the gap itself. In many instances, it may not be necessary to model a gap with a general-purpose CEM code if a suitable, accurate, and inexpensive tool is available. Thus, the objective of this research is to develop and validate a new approach to determine the electromagnetic scattering from gaps in a material coatings and to more efficiently evaluate potential gap treatment solutions.

1.2 Proposed Solution

A new approach of analyzing the electromagnetic scattering caused by gaps in coated ground planes is proposed based on the concept of a hybrid Green's function. The hybrid Green's function combines a 'free space' coupling term with a 'bounce' coupling correction term. The free space component is the familiar free space Green's function radiating in a material medium having the same constitutive properties as those of the grounded material coating of interest. The bounce correction term is derived from a multiple reflected wave series, similar to an example in Collin [1: Section 2.9], and takes into account the geometry of the grounded material coating. This hybrid Green's function is used in an integral equation formulation which is then solved approximately by the method of moments (MoM) in a manner similar to cases demonstrated by Newman [2, 3]. For

the purpose of studying specifically the scattering created by the presence of a gap in a material coated ground plane, it is anticipated that a special-purpose code based on this hybrid Green's function approach will provide results more rapidly than presently available CEM codes.

In order to prove this concept this project will consider the scattering from a gap in the coating of a material coated ground plane. Since the impact of this gap on the far zone scattered field (or RCS) is the primary observable of interest, we make the initial presumption that the required information can be obtained from the decomposition of the scattered fields into transverse electric (TE) and transverse magnetic (TM) components. This means a full three dimensional analysis is not required and we can take advantage of the simplifications of analyzing two-dimensional gap geometries. Since most materials of interest are not simple dielectrics but exhibit loss and magnetic permeability, the materials to be analyzed will be lossy magneto-dielectrics. Although anisotropic and ferrite materials are often encountered in reduced observables applications, they are seldom, if ever, employed in or near situations such as those suggested in Figure 1.1. Consequently, we will examine only homogeneous, isotropic materials in which the relative magnetic permeability can be represented as a scalar (such as in the carbonyl iron type materials, [36: Section 8.6]). Analytical models for the TM and TE scattering cases are derived using the hybrid Green's functions and the material constitutive properties of interest. Based on these analytical results, computer codes are developed for each polarization case. These codes are validated against existing two-dimensional CEM code predictions and, where applicable, against measured reference data.

1.3 Related Work

The engineering and scientific literature contains numerous examples of attempts to model the electromagnetic scattering from various types of surface features. Works related to the scattering from gaps or cracks in surfaces are not numerous but can be classified into essentially two categories: gaps or troughs in perfectly electric conducting (PEC) ground planes and gaps, breaks, or discontinuities in materials grounded by PEC ground planes. The distinction between these two categories is shown in Figure 1.2.

More frequently found in the literature are examples of electromagnetic scattering problems analyzed using the hybrid Green's function technique. The remainder of this section will address

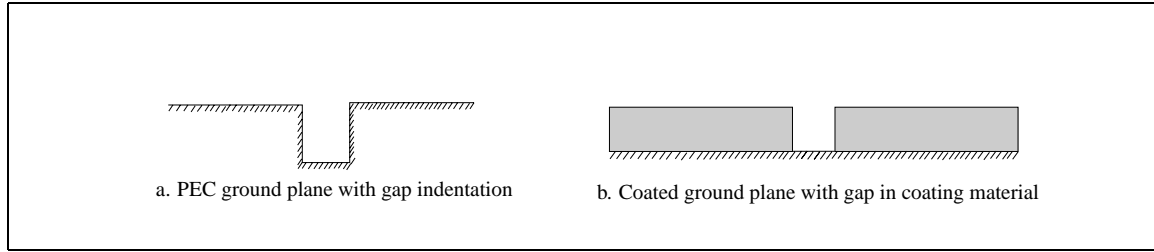


Figure 1.2 Representative gap geometries found in the literature

these areas, summarize the available references, and comment on their applicability to the research problem posed here.

1.3.1 Gaps in Ground Planes. Researchers studying the electromagnetic scattering from gaps or indentations in perfectly conducting ground planes form the bulk of the literature in this area. In the mid-1980's, the Wright Research and Development Center Signature Technology Directorate commissioned a research study effort that came to be known as the “Surface Waves and Gaps” (SWAG) study [4]. SWAG examined the scattering from two and three dimensional surface features that included gaps, impedance discontinuities, metal-dielectric joins, and surface discontinuities (e.g., steps). While SWAG looked at a number of interesting scenarios in the general surface feature problem, the scattering from a gap in a material coated ground plane was not one of them. Interestingly, SWAG also used in some analytical formulations, a hybrid Green's function to take into account the presence of an infinite ground plane. This Green's function with a “reflection” or “image” correction term is probably the simplest and most familiar case of a hybrid Green's function, having the form

$$G = G_{fs} + G_{image}$$

where G_{fs} is the free space component and G_{image} is the bounce or “image” correction term. The presence of the infinite ground plane is represented by the “images” of the various sources existent in the problem, and is incorporated into the analysis via the Green's function [18: Section 12.8].

Other works published in the engineering literature include various solutions of an aperture surface integral equation, where the fields in the gap area (or the cavity behind the gap aperture) are modelled using either surface integral equations or finite element techniques [5, 6, 7, 8]. As in the SWAG study, these papers also use the reflection or image Green's function in the moment

method or boundary element portion of the formulation to take into account the presence of the infinite ground plane. This suggests that the term “ground plane Green’s function” is appropriate for describing work in which such a reflection or image corrected Green’s function term is used to incorporate the infinite ground plane geometry.

An interesting departure from the other works discussed so far is the work of Bindiganavale and Volakis [9] where an impedance boundary condition (IBC) approximation is used to simulate the presence of the gap and any materials filling the cavity behind the gap. They then use a ground plane Green’s function in a surface integral equation formulation to analyze the scattering from the gap. For narrow gaps (gaps of aperture width $k_o w \ll 1$, where w is the width of the gap and k_o is the free space propagation constant), the equivalent currents in the aperture are approximated to simplify and expedite the computations. They validate their analysis with comparisons to Moore and Ling [10] and Aberle [11] by extending the IBC approximation to the conducting ground plane in order to simulate material coated ground planes.

1.3.2 Gaps in Material Coated Ground Planes. The works of Moore and Ling [10] and Aberle [11] cited above represent examples in the literature of attempts to study and analyze gaps in material coated ground planes such as in the geometry shown in Figure 2b. The work in [10] is interesting in that a two-dimensional gap geometry similar to that proposed for study in this effort was accomplished using a boundary integral equation (moment method) formulation with semi-infinite (physical) and sub-domain basis functions. The semi-infinite basis functions were used to represent the surface wave and physical optics fields along the boundary of the dielectric coatings on each side of (but some distance away from) the gap while the sub-domain basis functions were used to represent the fields in the vicinity of the gap. This approach could provide an analyst with the flexibility of modelling a gap in a material coating in which the thickness of the coatings on either side of the gap is different. This could easily occur in a number of situations for an aircraft structure and such a tool could be very useful.

However, Moore and Ling do not pursue this aspect of the work in [10]. Instead, they intend to devise a technique whereby they can extract a numerical diffraction coefficient for the gap. This numerical diffraction coefficient could then be used in high frequency codes (e.g., a code based on the Uniform Theory of Diffraction) to approximate the presence of gaps in large (but finite)

scattering structures. Furthermore, the formulation used by Moore and Ling does not readily lend itself to the design engineer's task of finding a treatment solution for such a gap. The boundary integral formulation breaks the geometry of the problem into three homogeneous regions: one in each of the two semi-infinite dielectric regions and one in the combined gap and half space above the coating as shown in Figure 1.3. The gap is assumed to be free space with constitutive properties

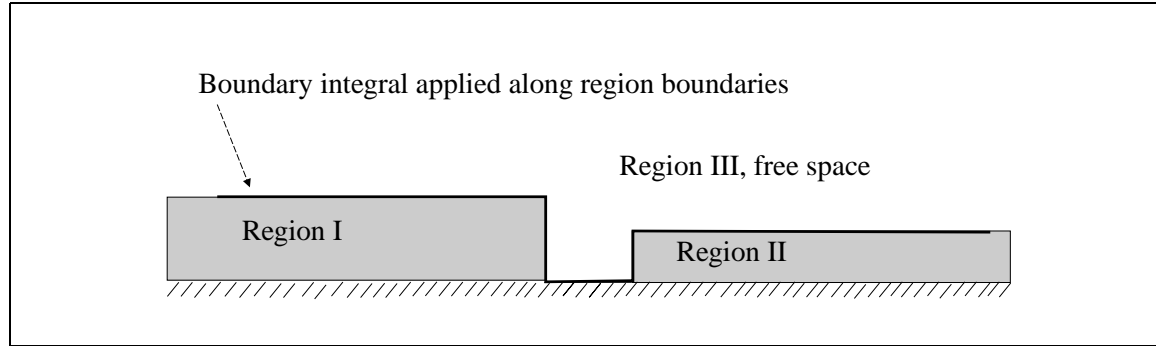


Figure 1.3 General gap geometry of Moore and Ling, [10]

μ_0, ϵ_0 as shown in Figure 2 of [10]. Thus, the technique of [10] would not be suitable for such gap filler treatment design or study purposes.

Moore and Ling also empirically investigated the TE-polarized scattering from a gap in a dielectric coated conducting plate with two French researchers [12]. The goal of this work was to investigate techniques for extracting target characteristics for target identification purposes. Consequently, this paper describes only the experimental setup and the Fourier transform techniques employed to extract scattering center information from the small target tested. Broadband measurements and signal processing techniques (data windowing and wavelet transform) form the bulk of the technical discussion content of this particular paper.

Aberle [11] uses a hybrid finite element (FE) technique to analyze a two-dimensional cavity-backed slot configuration in which the ground plane may also have a material coating. The gap problem becomes a special case of this geometry if the cavity is the same width as the slot. The hybrid FE method, in which the cavity portion is represented by discretized partial differential equations and the aperture/boundary region is represented by a boundary integral equation, is an excellent technique to use for this problem. This approach is rapidly coming into widespread use for large multi-region problems. The motivation for Aberle's research is to address antenna radia-

tion and scattering problems for complex structures containing cavity-backed slots and embedded striplines. For very complex structures, Aberle's approach would be the most highly recommended. However, as Aberle notes for a homogeneously filled cavity, a moment method (all integral equation) approach could be more efficient. We believe this to be the case also, and we expect that by using an integral equation formulation far fewer unknowns (resulting in a much smaller, though dense, matrix) will be required to analyze the gap region and should allow for more expeditious run times.

1.3.3 Hybrid Moment Method / Green's Function Techniques. Numerous papers and texts can be found that discuss at some length the technique referred to as a hybrid Green's function technique. Newman may actually have coined the term "hybrid MM/Green's function technique" and has been prolific in this area applying the technique to several problems in demonstration of its utility [2, 3, 4]. Simply stated, the hybrid MM/Green's function technique replaces the free space Green's function in a moment method application with a Green's function developed for a "canonical" scattering object. As stated earlier, the reflection or image Green's function developed for analyzing objects on or near a perfectly conducting ground plane is an example of a hybrid Green's function for the ground plane. This ground plane Green's function has been used by many workers to analyze various problems [4, 5, 6, 7, 8] as well as many others not specifically cited here.

The hybrid MM/Green's function technique is dependent; however, on the availability of either a closed form or readily calculable Green's function expression for the scattering object in a scattering problem. Usually this is the larger or largest scattering object in the scattering problem as demonstrated by the ground plane Green's function examples. In [2, 13], Newman demonstrates the technique by replacing a half plane by an appropriate Green's function in the moment method procedure. In this manner, the scattered fields from the cylinders are determined "in the presence of the half plane." This avoids the need to determine currents on the half plane, as would be necessary in a standard moment method application. Obviously, for a problem geometry that includes an infinite structure, the standard moment method procedure cannot be applied since the resulting impedance matrix would be of doubly infinite dimension.

In [3], Newman calculates the scattering from a curved PEC strip in the presence of a PEC circular cylinder with a hybrid MM/Green's function. This geometry is shown in Figure 1.4.

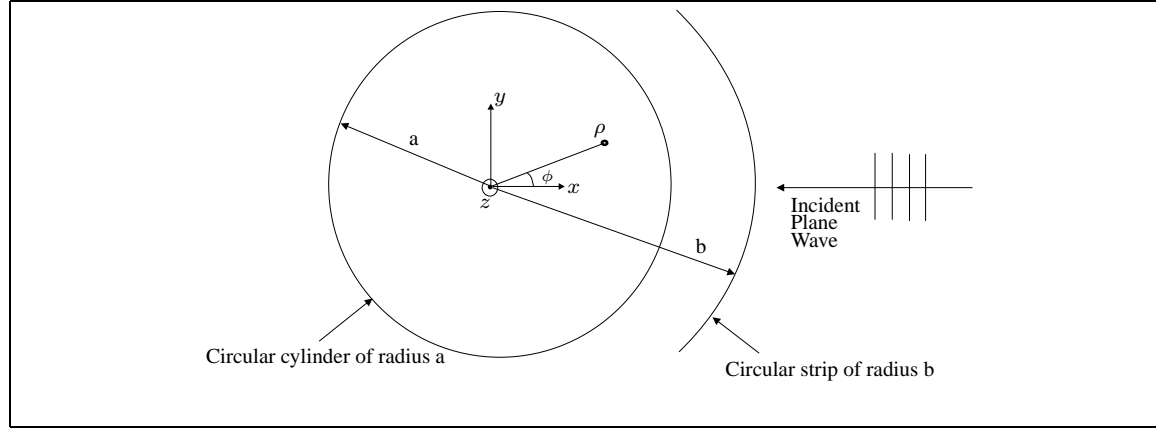


Figure 1.4 Geometry of Cylinder and Strip from Newman [3]

By incorporating the exact eigenfunction cylinder Green's function into the integral equation for the unknown currents on the curved strip, the currents on the strip are calculated “in the presence of the circular cylinder.” Thus, the need to solve for the unknown currents on the cylinder itself is avoided. As an example, in a standard moment method application using free space Green's functions, if there are N_1 unknowns on the strip and N_2 unknowns on the cylinder, the resulting impedance matrix would be of dimension $(N_1 + N_2) \times (N_1 + N_2)$. In the hybrid MM/Green's function technique, the unknowns on the cylinder are accounted for by the cylinder Green's function such that the resulting impedance matrix is of dimension $N_1 \times N_1$. For a large cylinder, the benefit of using this technique is readily apparent, especially since the matrix solve time can dominate run time in a moment method computation. The penalty one pays for this advantage is that the impedance matrix elements are now computed with the more complicated cylinder Green's function instead of the comparatively simple free space Green's function. One thus trades increased matrix fill time for decreased matrix solve time. Usually this trade is advantageous to the potential users of such a special purpose electromagnetic scattering code.

A final example of a hybrid Green's function approach is the work of Michalski, Nevels, and Zheng [14]. These authors analyze a two dimensional arbitrary strip in the presence of a circular cylinder. The motivation for their work is to study the relative merits of a Lorentz gauge versus a Coulomb gauge formulation for TE polarization. To accomplish this, they decompose the

Green's function into solenoidal and lamellar (non-solenoidal) components formulated under the different gauge conditions and examine the resulting matrix elements for the types of singularities that ensue. This paper is chiefly of interest because it demonstrates that there are numerous ways of not only decomposing a Green's function for a particular problem but also showing that Green's functions may assume different functional forms depending on the underlying assumptions and electromagnetic formulations.

1.4 Overview of Solution Approach

To illustrate the proposed hybrid MM/Green's function technique to be used in this dissertation, consider the two-dimensional problem geometry shown in Figure 1.5. In this figure we define our coordinate system such that the origin is located at the lower left corner of the gap region with the $x - z$ plane being that of the infinite PEC ground plane.

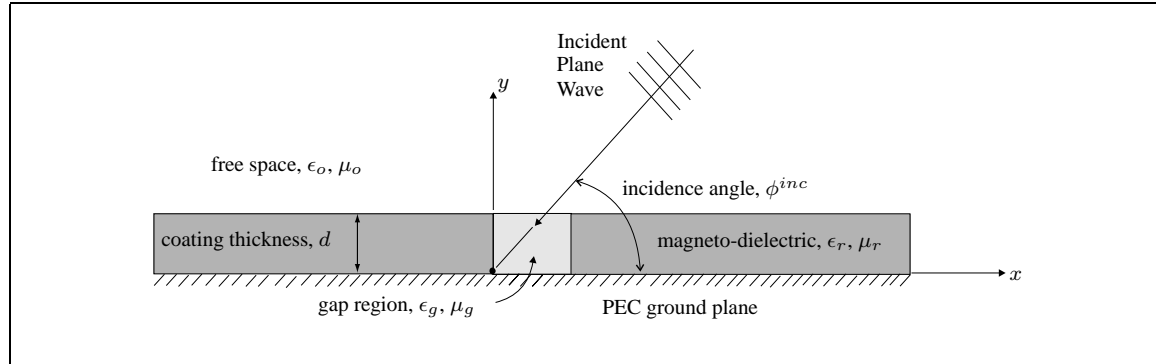


Figure 1.5 Two-dimensional gap geometry

1.4.1 Solution Approach Summary. The mathematical method to be used in this dissertation is that of finding integral equations which, when solved approximately through use of the method of moments, yield the volumetric equivalent electric and magnetic currents in the region of the gap. With the equivalent currents found, the two dimensional radar cross section (or echo width) can be calculated.

The development of the hybrid MM/Green's function method to calculate the echo width of the gap in the material coating is based upon the following physical reasoning. First, consider all two-dimensional space to be filled with a material having the same constitutive properties as those

of the coating material in Figure 1.5, possessing constitutive properties ϵ_r, μ_r . This is notionally depicted in Figure 1.6.

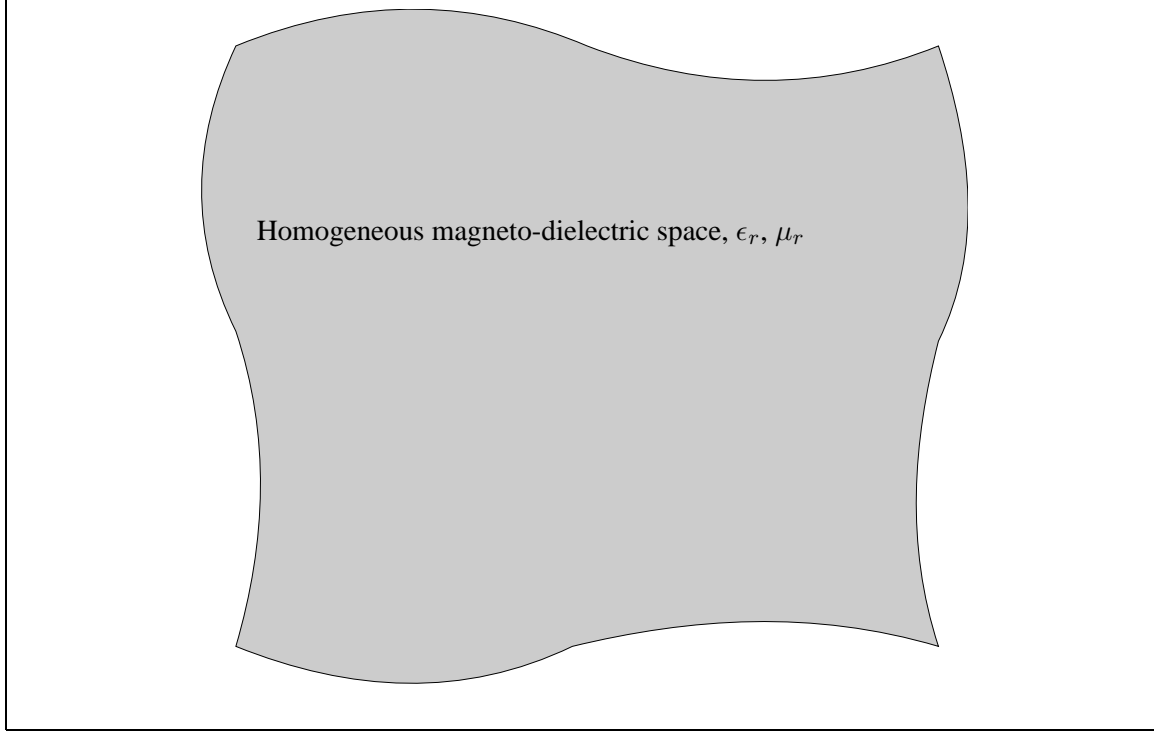


Figure 1.6 2-D space filled with material having $\epsilon = \epsilon_r, \mu = \mu_r$

The gap region is then extracted from this space using the volume equivalence principle [15: Section 7.7] by defining equivalent volume electric and magnetic currents that occupy the space corresponding to the gap region. These equivalent currents will have the form

$$\bar{J} = j\omega(\epsilon_g - \epsilon_r)\bar{E}_T, \text{ and } \bar{M} = j\omega(\mu_g - \mu_r)\bar{H}_T \quad (1.1)$$

where \bar{J} , and \bar{M} are the equivalent electric and magnetic volume equivalent currents and \bar{E}_T, \bar{H}_T are the total electric and magnetic fields in the region of the gap. These volume equivalent currents radiate fields \bar{E}^J, \bar{H}^J due to equivalent current \bar{J} and \bar{E}^M, \bar{H}^M due to equivalent current \bar{M} . The total fields \bar{E}_T, \bar{H}_T are composed of these fields radiated by the equivalent currents and the incident fields \bar{E}^i, \bar{H}^i in the presence of the coated ground plane geometry. In the gap region, we may now have a material possessing constitutive properties ϵ_g, μ_g representing a gap filler material. This situation is depicted in Figure 1.7. An empty gap (or air gap) would be represented by setting

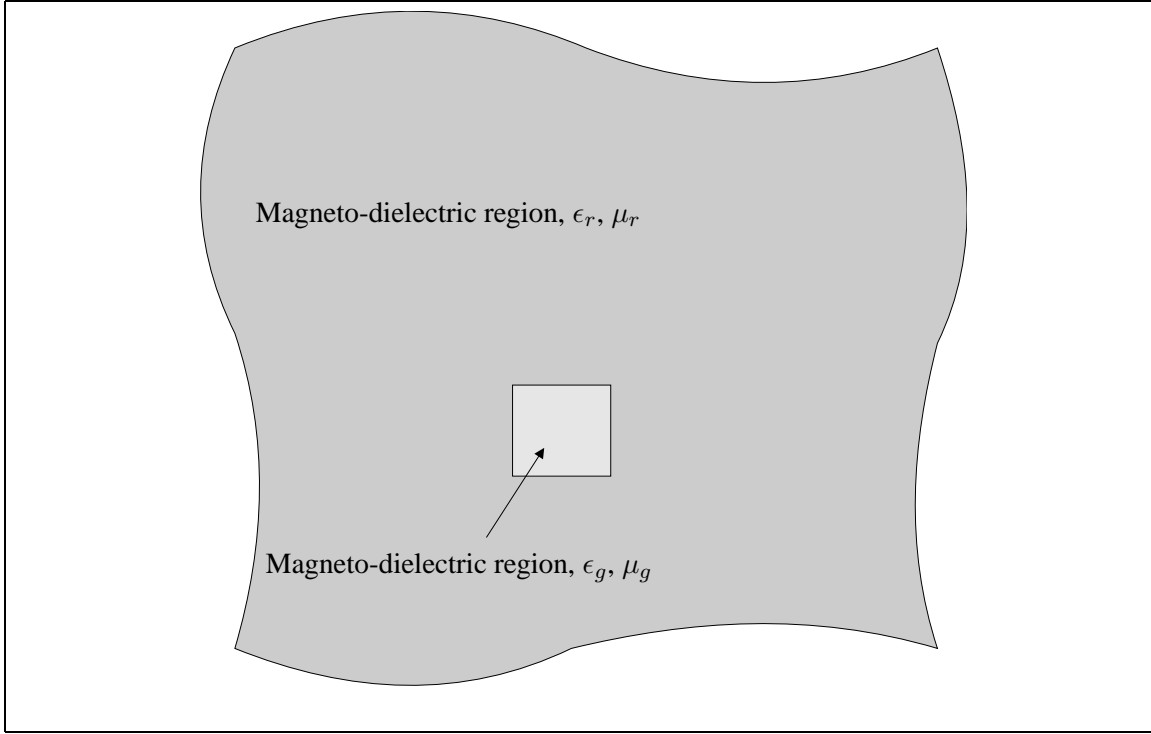


Figure 1.7 Equivalence extraction of gap region having $\epsilon = \epsilon_g, \mu = \mu_g$

the gap region's constitutive properties to be $\epsilon_g = \epsilon_o$ and $\mu_g = \mu_o$.

Using this equivalence representation, expressions for the total fields can be written as

$$\bar{E}_T = \begin{cases} \bar{E}^i + \bar{E}^J + \bar{E}^M & \text{all space, including the gap} \\ \frac{\bar{J}}{j\omega(\epsilon_g - \epsilon_r)} & \text{in the gap} \end{cases} \quad (1.2)$$

$$\bar{H}_T = \begin{cases} \bar{H}^i + \bar{H}^J + \bar{H}^M & \text{all space, including the gap} \\ \frac{\bar{M}}{j\omega(\mu_g - \mu_r)} & \text{in the gap} \end{cases} \quad (1.3)$$

These are coupled integral equations for the volume equivalent currents \bar{J} and \bar{M} since the fields \bar{E}^J, \bar{H}^J and \bar{E}^M, \bar{H}^M can be written as integrals over the gap region of \bar{J} or \bar{M} respectively, weighted by the appropriate Green's function. These expressions are derived by many authors such as [1, 2, 16]. In dyadic notation, and for the geometry of the present problem, they become

$$\bar{E}^J = -j\omega\mu_r \iint_{V_{gap}} \bar{\bar{G}}_e \cdot \bar{J} dV_{gap} \quad (1.4)$$

$$\bar{H}^J = \iint_{V_{gap}} \bar{\bar{G}}_m \cdot \bar{J} dV_{gap} \quad (1.5)$$

$$\bar{H}^M = -j\omega\epsilon_r \iint_{V_{gap}} \bar{\bar{G}}_e \cdot \bar{M} dV_{gap} \quad (1.6)$$

$$\bar{E}^M = - \iint_{V_{gap}} \bar{\bar{G}}_m \cdot \bar{M} dV_{gap} \quad (1.7)$$

Here, $\bar{\bar{G}}_e$ and $\bar{\bar{G}}_m$ are, respectively, the electric and magnetic dyadic Green's functions for the coated ground plane.

The electric and magnetic dyadic Green's functions, as defined by [1] and [16], are related to the scalar Green's function G by the relations

$$\bar{\bar{G}}_e = \left(\bar{\bar{I}} + \frac{\nabla\nabla}{k^2} \right) G \quad (1.8)$$

$$\bar{\bar{G}}_m = \bar{\bar{I}} \times \nabla G \quad (1.9)$$

where $\bar{\bar{I}}$ is the idem-factor or identity dyadic and k is the propagation constant of the magneto-dielectric coating material. The development of this scalar Green's function G for the problem geometry in this dissertation is the subject of the next chapter. At this point, we say only that through the Green's function, the problem space is altered to its final form as shown in Figure 1.5, placing a magneto-dielectric - air interface at the top of the gap region and a perfectly conducting ground plane at the bottom.

Once the form of this hybrid scalar Green's function G is determined, the solution to the problem proceeds in a straightforward manner. We will closely follow the Newman's approach in [2, 13]. For the TM excitation case the incident electric field is polarized in the \hat{z} direction only. Thus, all \bar{J} equivalent currents are \hat{z} polarized while the \bar{M} equivalent currents are \hat{x} and \hat{y} polarized. The vector equations (1.2) and (1.3) then reduce to the following coupled scalar equations valid in the region of the gap:

$$H_x^i = -H_x^{M_x} - H_x^{M_y} - H_x^{J_z} + \frac{M_x}{j\omega(\mu_g - \mu_r)} \quad (1.10)$$

$$H_y^i = -H_y^{M_x} - H_y^{M_y} - H_y^{J_z} + \frac{M_y}{j\omega(\mu_g - \mu_r)} \quad (1.11)$$

$$E_z^i = -E_z^{M_x} - E_z^{M_y} - E_z^{J_z} + \frac{J_z}{j\omega(\epsilon_g - \epsilon_r)} \quad (1.12)$$

In equations (1.10) – (1.12), the superscripts indicate the source of the field components and the subscripts indicate the orientation of the field component. For example, $E_z^{M_y}$ is the \hat{z} oriented electric field resulting from the \hat{y} oriented magnetic volume equivalent current. The left hand sides are simply the indicated components of the incident field.

For the TE excitation case, we have the dual to that above in which the incident magnetic field is \hat{z} polarized. This produces \bar{M} equivalent currents which are purely \hat{z} polarized and \bar{J} equivalent currents which are \hat{x} and \hat{y} polarized. For this case, the vector equations (1.2) and (1.3) become the following coupled scalar equations valid in the region of the gap:

$$E_x^i = -E_x^{J_x} - E_x^{J_y} - E_x^{M_z} + \frac{J_x}{j\omega(\epsilon_g - \epsilon_r)} \quad (1.13)$$

$$E_y^i = -E_y^{J_x} - E_y^{J_y} - E_y^{M_z} + \frac{J_y}{j\omega(\epsilon_g - \epsilon_r)} \quad (1.14)$$

$$H_z^i = -H_z^{J_x} - H_z^{J_y} - H_z^{M_z} + \frac{M_z}{j\omega(\mu_g - \mu_r)} \quad (1.15)$$

A pulse basis and point matching moment method solution is proposed for these sets of equations for both the TM and TE polarization cases. We can solve these equations using a piecewise-linear cellular discretization of the gap region. For proof of concept purposes we shall restrict the gap region cross section to trapezoidal shapes such that the gap region can be gridded from within the computer program and an external grid generation software package will not be needed. The gap region is then segmented into the smaller trapezoidal cells as shown in Figure 1.8.

The moment method solution then proceeds by expanding the unknown volume equivalent currents in a series of known ‘pulse’ basis functions weighted by unknown expansion coefficients. The pulse basis in each cell is defined by the boundaries of the cell and the expansion coefficients are defined at the centroid of the cell. We then have for these currents

$$\bar{J} = \hat{z}J_z = \hat{z} \sum_{n=1}^N c_n P_n^J \quad (1.16)$$

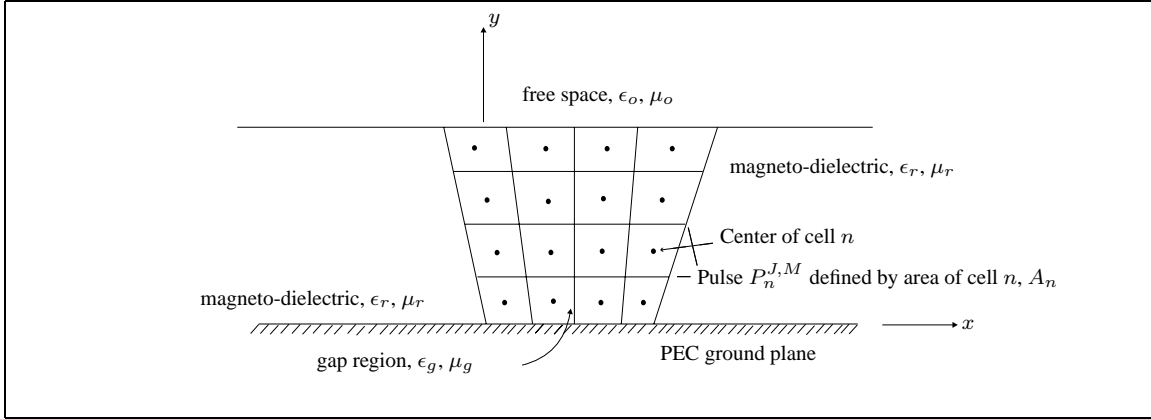


Figure 1.8 Discretization of gap region for Moment Method solution showing domain of the equivalent currents.

and

$$\bar{M} = \hat{x}M_x + \hat{y}M_y = \hat{x} \sum_{n=1}^N d_{xn} P_n^M + \hat{y} \sum_{n=1}^N d_{yn} P_n^M \quad (1.17)$$

where $P_n^{J,M}$ are the pulse basis functions and c_n , $d_{(x,y)n}$ are the unknown coefficients for each cell R_n . At this point, it becomes apparent that for each of the N cells comprising the gap region, there can be N , $2N$, or $3N$ unknowns in our moment method matrix equation, depending on the properties of the magneto-dielectric slab coating. If we define A_n as the area of each gap cell R_n , the pulse expansion functions can be defined as

$$P_n^J = \begin{cases} 1/A_n & \text{within gap cell } R_n \\ 0 & \text{otherwise} \end{cases} \quad (1.18)$$

for the electric volume equivalent currents, and

$$P_n^M = \begin{cases} 1/A_n & \text{within gap cell } R_n \\ 0 & \text{otherwise} \end{cases} \quad (1.19)$$

for the magnetic volume equivalent currents, where the superscript J or M designates the pulse function as representing either the electric or magnetic equivalent current, respectively.

For the TE polarization case the resultant impedance matrix is derived from equations (1.13) – (1.15), the development of which is dual to that for the TM polarization case. Again, for a general magneto-dielectric slab coating material, a $3N \times 3N$ system results from segmentation of the gap

region into N cells. For this case, we would have the currents expanded as

$$\bar{M} = \hat{z}M_z = \hat{z} \sum_{n=1}^N d_n P_n^M \quad (1.20)$$

and

$$\bar{J} = \hat{x}J_x + \hat{y}J_y = \hat{x} \sum_{n=1}^N c_{xn} P_n^J + \hat{y} \sum_{n=1}^N c_{yn} P_n^J \quad (1.21)$$

The definitions of the variables in these expressions are identical to those in equations (1.16) and (1.17). Other than this change in the polarization orientation of the unknown currents, the TE problem is identical in procedure to the TM case. With the notable exception of the fact that we will be retaining the PEC ground plane, instead of having a perfect magnetic conducting ground plane for TE polarization, the TE problem is the electromagnetic dual of the TM problem, [15: Chapter 7]. Thus, no further development of the TE case is needed at this point.

1.5 Dissertation Summary

The remaining chapters in this dissertation take the general procedure outlined above and apply it to the problem depicted in Figure 1.5. Chapter 2 begins by deriving the form of the scalar and dyadic Green's functions for the grounded magneto-dielectric slab problem. Next, the chapter formulates the complex impedance matrix for the TM and TE polarization cases. The chapter continues with a discussion of how the excitation vector entries are computed and how the solution vector entries are used to compute the far-field radiation pattern for the scattering from the gap. Chapter 3 presents the numerical implementation of the theory presented in Chapter 2 beginning with an examination of a critical aspect of the hybrid Green's function developed for this problem. Chapter 4 examines the validity of the approach taken in this dissertation by comparing results to those from reference computer codes and RCS range scattering measurements. Finally, Chapter 5 summarizes the dissertation and suggests areas for further research and improvement of the techniques developed here.

II. Theoretical Development

2.1 Scalar Green's Function for the Coated Conducting Plane

For a multiple-region problem such as that depicted in Figure 1.5, the Green's function is dependent upon the spatial location of the 'source' and 'receiver' position vectors. To determine the unknown volume equivalent currents, a Green's function formulated for fields radiated and observed entirely within the material slab region (actually, both source and receiver in the 'gap' region) must be used. We call this an 'internal' Green's function valid only in the region $0 \leq y \leq d$. An 'external' Green's function must be used for the region $y > d$. The external Green's function is formulated for a source located inside the gap region and a receiver located in the exterior, free space region. This Green's function must be used to calculate the echo width of the gap, once the equivalent currents have been determined via the internal Green's function.

The internal Green's function is composed of two distinct components: a 'direct' coupling term and a 'bounce' correction term. In our case, the direct coupling term is related to the mutual impedance between the source and receiver due to the direct path, line of sight coupling between these elements in an infinite magneto-dielectric medium. The bounce correction term provides an additive correction to the direct coupling term that is required by the presence of the coated conducting plane geometry with the infinite ground plane below the magneto-dielectric medium and material/free space (air) interface above. The bounce correction term thus provides the amount of correction needed to properly adjust the amplitude and phase of the coupling between the source and receiver in the presence of this slab-coated conducting ground plane geometry.

The direct coupling term for the internal Green's function is given by the familiar two-dimensional Green's function term found in many sources such as [15, 17, 18]¹,

$$G_{dc} = -\frac{j}{4} H_o^{(2)}(k|\bar{\rho} - \bar{\rho}'|) \quad (2.1)$$

where k is the complex propagation constant of the magneto-dielectric medium, $\bar{\rho}$ and $\bar{\rho}'$ are the position vectors of the receiver and source locations, respectively, and $H_o^{(2)}(\cdot)$ is the zeroth order Hankel function of the second kind. The argument of the Hankel function, $k|\bar{\rho} - \bar{\rho}'|$, takes on

¹In this dissertation we use the $e^{j\omega t}$ time convention. The factor $e^{j\omega t}$ is assumed and suppressed throughout.

the value $k\sqrt{(x-x')^2 + (y-y')^2}$, where (x, y) and (x', y') are the receiver and source locations respectively. For the TM polarization case, we can interpret this as an electric line source radiating in the infinite magneto-dielectric medium. For the TE polarization case, it is interpreted as a magnetic line source. We note that since the medium in which this term is defined is in general lossy, k is in general complex and the subroutines used in the computer codes must be able to compute the Hankel function for complex-valued arguments.

The slab-coated conducting ground plane geometry provides two reflection surfaces: the conducting ground plane and the material/free space interface. These give rise to the multiple reflected wave series nature of the bounce correction term as will be shown now for the internal Green's function G_{int} . Figure 2.1 depicts the four fundamental bounce path contributions to the multiple reflected wave series. The source and receiver modes for the four cases shown are taken

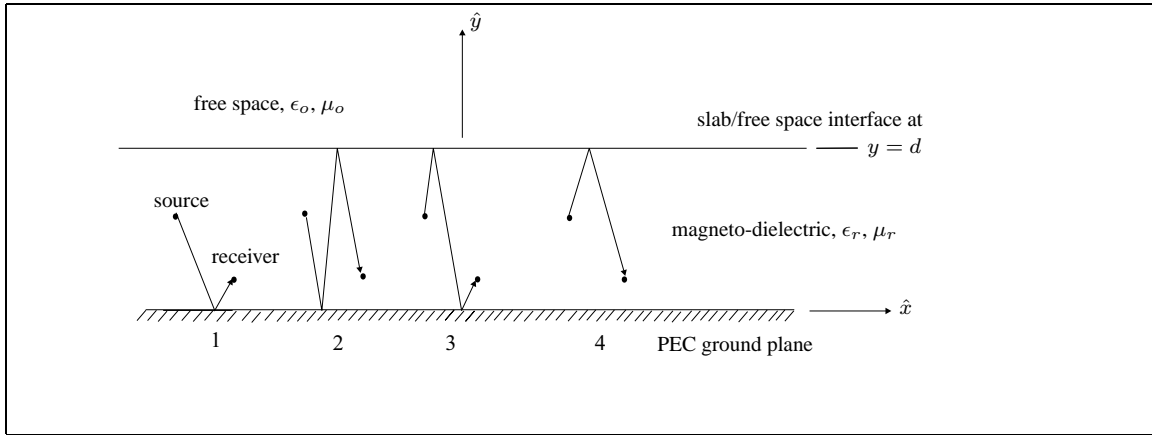


Figure 2.1 Four fundamental bounce modes within the slab

to be located within the gap region shown in Figure 1.8. The source is interpreted to be a two-dimensional line source element radiating within the region of the gap and the receiver is a line element located at the point within the gap region at which the field is sampled. Higher order bounce paths are composed of sums of multiples of these four basic paths resulting in an infinite geometric series of these four basic paths representing all possible bounce path contributions [15: Section 5.5], [19: Section 5.6]. We will use this approach to construct a mathematical expression for the bounce correction term of the slab-coated conducting ground plane Green's function. More will be said later about this geometric series representation of the multiple bounce terms.

Recall the line source located within the material region shown in Figure 1.5. Now, instead of a single line source, consider an infinite periodic array of \hat{z} -directed line sources with inter-element spacing D_x as shown in Figure 2.2. We use this periodic array of line source elements to

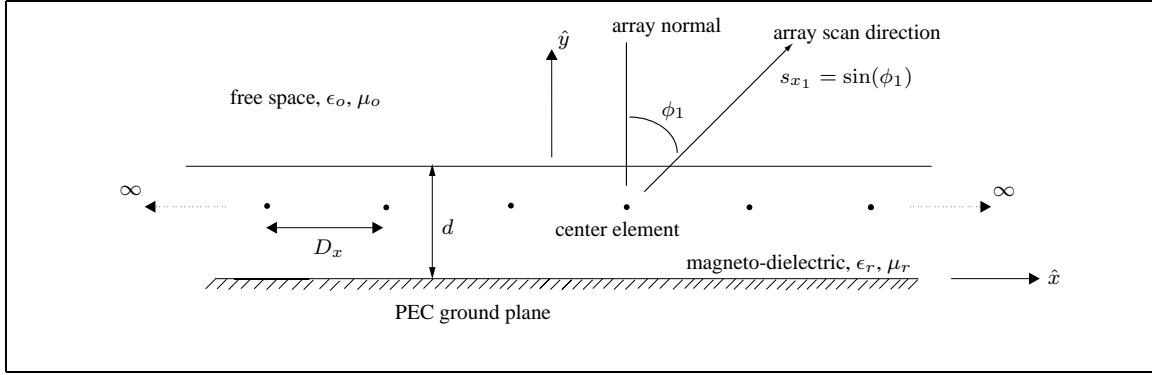


Figure 2.2 Infinite array of line sources within the slab

construct the bounce correction terms of the internal Green's function through a technique called the 'Array Scanning Method' (ASM) [21]. The ASM was originally developed at The Ohio State University for treating certain classes of problems using periodic array theory. A chief advantage of this technique is that it allows one to analyze half-space problems using a method alternative to Sommerfeld integral techniques. The basic difference is that the plane wave expansion in the ASM is performed in a discrete mode fashion rather than by a continuous variable approach as in the traditional Sommerfeld formulation (see [28: Chapter 5]). The ASM results in an infinite sum of plane wave expansion terms, each containing a definite integral over the 'scan' variable, rather than a single infinite integral expression. Using the Poisson sum formula, the infinite series within the ASM integral can be transformed into an exponentially convergent sum requiring that only a few terms be evaluated to achieve convergence. The Poisson sum formula transformation of the spatial domain expression into the spectral domain is summarized in Appendix A and the ASM development of the spectral domain integrals is summarized in Appendix B.

The currents on the line source elements in the array of Figure 2.2 are identical in amplitude but vary in phase according to a direction cosine phase steering parameter s_{x_1} . The radiation from an infinite array in a homogeneous magneto-dielectric medium may be expressed as the spatial

sum

$$G_{array, homo} = -\frac{j}{4} \sum_{m=-\infty}^{\infty} H_o^{(2)} \left(k \sqrt{(mD_x - (x - x'))^2 + (y - y')^2} \right) e^{jkmD_x s_{x_1}} \quad (2.2)$$

Equation (2.2) represents an infinite sum of line sources, each represented by an expression analogous to Equation (2.1), but with the additional spatial separation along the x coordinate and the corresponding phase progression. Through the Poisson sum formula [19, 20], this spatial sum can be converted into a spectral sum expressed as

$$G_{array, homo} = -\frac{j}{2kD_x} \sum_{n=-\infty}^{\infty} \frac{e^{-jk(\bar{\rho}-\bar{\rho}') \cdot \hat{r}_{1\pm}}}{r_{y_1}} \quad (2.3)$$

where contained in the exponential term is the representation for the plane wave modes that comprise the spectral expansion. We discuss next the meaning of the various spectral domain variables. Additional details of the spatial domain, Equation (2.2), to spectral domain, Equation (2.3), transformation are presented in Appendix A.

Introducing variables and notation unique to Munk's approach to periodic array theory [19, 22, 23], in expression (2.3), we have

$$\hat{r}_{1\pm} = \hat{x}r_{x_1} \pm \hat{y}r_{y_1} \quad (2.4)$$

which is the spectral domain plane wave propagation-direction unit vector in media '1' (the slab coating material). The factors

$$r_{x_1} = \frac{Re(k)}{k} \left(s_{x_1} + \frac{n\lambda_1}{D_x} \right) \quad (2.5)$$

and

$$r_{y_1} = \sqrt{1 - r_{x_1}^2} \quad (2.6)$$

are, respectively, the x and y components of this unit vector. In Equation (2.5), n is the spectral domain plane wave mode number. The factor $\frac{Re(k)}{k}$ in Equation (2.5) arises from the fact that we anticipate dealing with lossy materials. Written this way, r_{x_1} remains purely real if the media in our problem are lossless. An alternate but equivalent form for r_{x_1} , also applicable to the case of lossy media, can be found in [21]. As was mentioned earlier, s_{x_1} is a direction cosine phase

steering parameter and is related as shown to the \hat{x} -directed spectral domain propagation direction term r_{x_1} .

The \hat{y} -directed spectral domain propagation direction term, r_{y_1} , is chosen to normalize the propagation direction unit vector $\hat{r}_{1\pm}$, and the choice of sign for $\pm\hat{y}r_{y_1}$ is made depending upon which side of the array the field point is located. This choice depends solely on the relative locations of the source and field points and then only determined by the \hat{y} -directed spatial variables (y, y') . When employed in the context of multiple planar arrays and dielectric layers, [19], the $\pm\hat{y}r_{y_1}$ takes on values $-\hat{y}r_{y_1}$ if the field point is in the $-\hat{y}$ direction relative to the source location of interest, and $+\hat{y}r_{y_1}$ if the field point is in the $+\hat{y}$ direction relative to the source location. In our problem geometry, we have a PEC ground plane in the $-\hat{y}$ direction for all ASM arrays that may be generated in the slab material region. This ground plane will reflect all $-\hat{y}$ -directed plane wave modes resulting in a net $+\hat{y}$ direction of propagation for the entire set of plane wave mode terms arising from Equation (2.3). This enables us to simplify the y component of the exponential in (2.3) by noting that $\pm(y - y')r_{y_1} = |y - y'|r_{y_1}$. This functional dependence can be likened to that of a one-dimensional scalar Green's function for a Helmholtz operator which satisfies radiation conditions at $\pm\infty$ of its spatial variable [24].

Equation (2.3) is an infinite spectral sum of plane wave modes that is fully equivalent to the spatial sum expression in Equation (2.2). As higher order modes are evaluated (as $|n|$ increases in Equation (2.5), r_{y_1} is seen to become imaginary when $|r_{x_1}| > 1$. When this occurs, we choose the root of r_{y_1} that is in keeping with the radiation condition, i.e., $r_{y_1} = -j\sqrt{r_{x_1}^2 - 1}$. For cases where k is complex, r_{x_1} is complex for all values of n . When this occurs, r_{y_1} is also complex for all values of n , and we choose the roots of r_{y_1} such that the imaginary parts are negative. In either case, as $|n|$ increases, the negative imaginary part of r_{y_1} increases, resulting in exponential decay in (2.3). With this exponential decay, only a few terms (values of n) in (2.3) need to be evaluated beyond the central ($n = 0$) term before convergence of the summation is achieved.

Using methods developed by Munk [19], the radiation of an array within a stratified medium can be written as the radiation of the array in a homogeneous region weighted by a 'T-factor.' It is this T-factor that accounts for the slab coated conducting ground plane geometry by incorporating the bounce path terms from Figure 2.1 into the infinite series expression in Equation (2.3). Thus,

the Green's function for the array in a homogeneous medium is expressed simply as

$$G_{array, slab} = G_{array, homo} \cdot T \quad (2.7)$$

For the coated conducting ground plane geometry, the T-factor for the internal Green's function case is

$$T = \frac{\Gamma_{10}e^{-j2kdr_{y1}} \left(e^{jk(y+y')r_{y1}} + 2\Gamma_{12} \cos[k(y-y')r_{y1}] \right) + \Gamma_{12}e^{-jk(y+y')r_{y1}}}{1 - \Gamma_{12}\Gamma_{10}e^{-j2kdr_{y1}}} \quad (2.8)$$

where Γ_{10} is the Fresnel reflection coefficient at the material/free space interface for a wave incident from the slab coating material side and Γ_{12} is the reflection coefficient at the conducting ground plane. The T-factor is seen to contain four propagation path terms in its numerator and the geometric series factor in its denominator. The four propagation path terms correspond to the four fundamental bounce paths indicated in Figure 2.2 which are readily identified. Bounce mode '1' corresponds to the first exponential term, the paths '2' and '3' are combined into the cosine term, and path '4' corresponds to the $\Gamma_{12}e^{-jk(y+y')r_{y1}}$. We will later modify this expression for the T-factor since the reflection coefficients are slightly different for the TM and TE polarization cases. Finally, we note the T-factor has a functional dependence only on the spatial variables y and y' and is independent of the spatial variable x . It is also dependent on the spectral plane wave mode number n and scan angle parameter s_{x1} through the r_{y1} factor.

An overview of the ASM is given in Appendix B and the reader is referred there for details regarding the development of the method. Using the resulting ASM integral expression developed in Appendix B, we choose an interelement spacing for our 2-D line source array of $D_x = \lambda_1/2$, (where λ_1 is the electromagnetic wavelength in the slab coating material) as this choice minimizes the number of propagating plane wave modes² and leads to limits of integration in the ASM integral that correspond to "scanning the array" from -90° to $+90^\circ$. This choice also influences the spectral domain propagation direction factors r_{x1} and r_{y1} since now we see that Equation (2.5) becomes $r_{x1} = \frac{Re(k)}{k}(s_{x1} + 2n)$. The ASM expression for the bounce correction term of the internal Green's

²Propagating modes beyond the central ($n = 0$) mode term, are referred to as grating lobes and are familiar in the context of array antennas. They are undesirable in this application since their presence slows convergence of the plane wave expansion summations.

function becomes

$$G_{bounce} = \frac{1}{2} \int_{-1}^1 G_{array, slab} ds_{x_1} \quad (2.9)$$

or, upon inserting (2.3) into (2.6), and noting that $D_x = \pi/Re(k)$.

$$G_{bounce} = -\frac{jRe(k)}{4\pi k} \int_{-1}^1 \sum_{n=-\infty}^{\infty} \frac{e^{-jk(\bar{\rho}-\bar{\rho}') \cdot \hat{r}_{1\pm}}}{r_{y_1}} T ds_{x_1} \quad (2.10)$$

This term is then added to the direct coupling term in Equation (2.1) to become the scalar Green's function for the slab-coated ground plane geometry of Figure 1.5. We will refer to it as our 'canonical' Green's function term since, as we shall see in the next section, it is used to generate additional Green's function component terms for problems involving transverse equivalent current sources. Finally, we point out here that the integration variable in the ASM bounce correction term, s_{x_1} , is purely real. That the integration of the ASM integral is forced to occur along the real axis of the scan angle variable of integration is an important distinction between the ASM approach and traditional methods employing a Sommerfeld integral.

2.2 Dyadic Green's Function for the Coated Conducting Plane

We next apply Equations (1.8) and (1.9) to the sum of Equations (2.1) and (2.10) in order to arrive at the expressions for the various Green's function terms needed to compute the scattering from a gap in a general magneto-dielectric coating. Repeating these equations here for convenience, we have

$$\bar{\bar{G}}_e = \left(\bar{\bar{I}} + \frac{\nabla \nabla}{k^2} \right) G \quad (2.11)$$

$$\bar{\bar{G}}_m = \bar{\bar{I}} \times \nabla G \quad (2.12)$$

where G is our canonical Green's function, the sum of the scalar direct coupling and bounce correction Green's function terms

$$G = -\frac{j}{4} H_o^{(2)}(k|\bar{\rho} - \bar{\rho}'|) - \frac{jRe(k)}{4\pi k} \int_{-1}^1 \sum_{n=-\infty}^{\infty} \frac{e^{-jk(\bar{\rho}-\bar{\rho}') \cdot \hat{r}_{1\pm}}}{r_{y_1}} T ds_{x_1} \quad (2.13)$$

There are several ways one may choose to explicitly represent dyadic Green's functions. In this dissertation, we choose to display them as matrices for the purpose of clarity. As such, each

block or entry of the matrix will represent the Green's function of a particular field orientation (at an observation or field point) resulting from a particular source orientation. In this matrix format the Equations (2.11) and (2.12), when expanded, become

$$\overline{\overline{G}}_e = \begin{bmatrix} 1 + \frac{1}{k^2} \frac{\partial^2}{\partial x^2} & \frac{1}{k^2} \frac{\partial^2}{\partial x \partial y} & \frac{1}{k^2} \frac{\partial^2}{\partial x \partial z} \\ \frac{1}{k^2} \frac{\partial^2}{\partial y \partial x} & 1 + \frac{1}{k^2} \frac{\partial^2}{\partial y^2} & \frac{1}{k^2} \frac{\partial^2}{\partial y \partial z} \\ \frac{1}{k^2} \frac{\partial^2}{\partial z \partial x} & \frac{1}{k^2} \frac{\partial^2}{\partial z \partial y} & 1 + \frac{1}{k^2} \frac{\partial^2}{\partial z^2} \end{bmatrix} G \quad (2.14)$$

$$\overline{\overline{G}}_m = \begin{bmatrix} 0 & -\frac{\partial}{\partial z} & \frac{\partial}{\partial y} \\ \frac{\partial}{\partial z} & 0 & -\frac{\partial}{\partial x} \\ -\frac{\partial}{\partial y} & \frac{\partial}{\partial x} & 0 \end{bmatrix} G \quad (2.15)$$

Since in this dissertation we are restricting ourselves to working in two-dimensional space (essentially the $x-y$ plane) we can simplify these dyadic expressions by noting that all geometric structures and fields are invariant along the \hat{z} -direction. Thus any term containing a $\partial/\partial z$ term is zero. The two matrix expressions can then be simplified and combined to provide the general Green's function matrix expression³

$$\overline{\overline{G}} = \begin{bmatrix} 1 + \frac{1}{k^2} \frac{\partial^2}{\partial x^2} & \frac{1}{k^2} \frac{\partial^2}{\partial x \partial y} & \frac{\partial}{\partial y} \\ \frac{1}{k^2} \frac{\partial^2}{\partial y \partial x} & 1 + \frac{1}{k^2} \frac{\partial^2}{\partial y^2} & -\frac{\partial}{\partial x} \\ -\frac{\partial}{\partial y} & \frac{\partial}{\partial x} & 1 \end{bmatrix} G \quad (2.16)$$

The differential operator matrix expression now 'operates' on the canonical Green's function to produce the terms in the impedance matrix. We represent this step by the following form of the matrix expression.

$$\overline{\overline{G}} = \begin{bmatrix} G_{xx} & G_{xy} & G_{xz} \\ G_{yx} & G_{yy} & G_{yz} \\ G_{zx} & G_{zy} & G_{zz} \end{bmatrix} \quad (2.17)$$

³We can do this here because we have restricted ourselves to the 2-D case. In the general 3-D case, or if we were considering the 2-D oblique incidence case, we would not be able to combine the electric and magnetic dyadic Green's Functions matrices in this manner.

We can now explicitly identify each term in the matrix as,

$$\begin{aligned} G_{xx} &= G + \frac{1}{k^2} \frac{\partial^2 G}{\partial x^2} & G_{xy} &= \frac{1}{k^2} \frac{\partial^2 G}{\partial x \partial y} & G_{xz} &= \frac{\partial G}{\partial y} \\ G_{yx} &= \frac{1}{k^2} \frac{\partial^2 G}{\partial y \partial x} & G_{yy} &= G + \frac{1}{k^2} \frac{\partial^2 G}{\partial y^2} & G_{yz} &= -\frac{\partial G}{\partial x} \\ G_{zx} &= -\frac{\partial G}{\partial y} & G_{zy} &= \frac{\partial G}{\partial x} & G_{zz} &= G \end{aligned}$$

At this point, we look forward a bit and note that each term in this matrix of Green's function expressions will become, in general, a submatrix block of the overall impedance matrix. In our development, we will have occasion to refer to specific blocks of the matrix to facilitate discussions specific to each block. In keeping with conventional notation, we designate block 1 as that corresponding to G_{xx} , block 2 corresponding to G_{xy} , block 3 corresponding to G_{xz} , and so forth. As mentioned above, each block of the Green's function matrix represents the Green's function relating a certain field orientation due to a specific source orientation. The notation used in Equation (2.17) will become clear as we apply it in the following sections to the specific cases of TM and TE polarization.

2.3 Expressions Applied to TM Polarization Case

2.3.1 Form of the Dyadic Green's Function for TM Polarization. Recall from Equations (1.4) - (1.7) that the electric and magnetic field quantities are related to the various equivalent current sources by

$$\bar{E}^J = -j\omega\mu_r \iint_{V_{gap}} \bar{\bar{G}}_e \cdot \bar{J} dV_{gap} \quad (2.18)$$

$$\bar{H}^J = \iint_{V_{gap}} \bar{\bar{G}}_m \cdot \bar{J} dV_{gap} \quad (2.19)$$

$$\bar{H}^M = -j\omega\epsilon_r \iint_{V_{gap}} \bar{\bar{G}}_e \cdot \bar{M} dV_{gap} \quad (2.20)$$

$$\bar{E}^M = - \iint_{V_{gap}} \bar{\bar{G}}_m \cdot \bar{M} dV_{gap} \quad (2.21)$$

If we consider now the case of TM polarization illumination of the gap structure, we apply these expressions and cast both the resultant field quantities and equivalent current sources in a matrix

format as follows,

$$\begin{bmatrix} H_x \\ H_y \\ E_z \end{bmatrix} = \begin{bmatrix} j\omega\epsilon_r \langle G_{xx}, M_x \rangle & j\omega\epsilon_r \langle G_{xy}, M_y \rangle & - \langle G_{xz}, J_z \rangle \\ j\omega\epsilon_r \langle G_{yx}, M_x \rangle & j\omega\epsilon_r \langle G_{yy}, M_y \rangle & - \langle G_{yz}, J_z \rangle \\ \langle G_{zx}, M_x \rangle & \langle G_{zy}, M_y \rangle & j\omega\mu_r \langle G_{zz}, J_z \rangle \end{bmatrix} \quad (2.22)$$

where the inner product symbology,

$$\langle f, g \rangle = \iint_{V_{gap}} f(x, y)g(x, y)dV$$

is used to represent the integrations shown in Equations (2.18) - (2.21). Note that these are not the total fields required to solve our problem, rather, these are the fields arising specifically from the equivalent current sources. Referring back to Equations (1.2) and (1.3), we need to add the incident fields along with the fields directly proportional to the equivalent currents, which occur only in the gap region. Following Newman's lead [2], we define an impedance matrix of the form

$$V = [Z + \Delta Z] \cdot I \quad (2.23)$$

and thus we see that the matrix in Equation (2.22) is the matrix product $Z \cdot I$. The matrix ΔZ arises from the equivalent source terms and modifies only those blocks of Z corresponding to like-directed equivalent source terms. In other words, the matrix product $\Delta Z \cdot I$ can be expressed as

$$\Delta Z \cdot I = \begin{bmatrix} \frac{M_x}{j\omega(\mu_g - \mu_r)} & 0 & 0 \\ 0 & \frac{M_y}{j\omega(\mu_g - \mu_r)} & 0 \\ 0 & 0 & \frac{J_z}{j\omega(\epsilon_g - \epsilon_r)} \end{bmatrix} \quad (2.24)$$

The vector V represents the incident field voltage values within the gap region and I represents the current vector

$$V = \begin{bmatrix} H_x^i \\ H_y^i \\ E_z^i \end{bmatrix}, \text{ and } I = \begin{bmatrix} M_x \\ M_y \\ J_z \end{bmatrix}$$

These equations hold only for values of the spatial variables (x, y) located in the gap region of our problem geometry.

2.3.2 The T-factor for TM Polarization. The T-factor, Equation (2.8), was given earlier in a general form. We now take polarization into account as the T-factor expression will vary slightly between the TM and TE polarization cases. The difference arises from the fact that the reflection coefficient expressions embedded in the T-factor have different forms for TM and TE polarization as is well known [15: Chapter 5]. The methods developed by Munk [19, 22, 23] extend the traditional definitions of the Fresnel reflection and transmission coefficients to enable one to incorporate complex evanescent modes into these coefficients at planar material interfaces. This ability to incorporate Fresnel coefficients in a plane wave spectrum solution approach is a distinct advantage of the spectral domain method. The definitions used by Munk result in spectral domain reflection and transmission coefficients (for TM polarization) of the form

$$\Gamma_{10} = \frac{\eta_o r_{y_1} - \eta_1 r_{y_o}}{\eta_o r_{y_1} + \eta_1 r_{y_o}} \quad (2.25)$$

and

$$\tau_{10} = \frac{2\eta_o r_{y_1}}{\eta_o r_{y_1} + \eta_1 r_{y_o}} \quad (2.26)$$

where η_1 is the impedance of the magneto-dielectric medium, η_o is the impedance of the air (or free space) medium above the slab material region, and τ_{10} is the spectral domain Fresnel transmission coefficient for the slab coating material/free space interface (incident from the slab material side) at $y = d$ in Figure 2.1. From Fresnel theory, τ_{10} is defined as $\tau_{10} = 1 + \Gamma_{10}$ [15, 19]. The propagation factor r_{y_1} is again the \hat{y} -component of the propagation direction vector in the magneto-dielectric medium. The factor r_{y_o} is the \hat{y} -component of the propagation direction vector in the free space medium, $y > d$. It will be seen throughout this report that by using these definitions and notation, we extend the applicability of the Fresnel reflection and transmission coefficients to accommodate evanescent (non-propagating) plane wave modes.

The array scanning parameter s_{x_1} , seen earlier in Equations (2.2) and (2.3), was used to set the x -component of the spectral domain plane wave mode propagation direction vector through $r_{x_1} = \frac{Re(k_1)}{k_1}(s_{x_1} + 2n)$. A similar quantity, r_{x_o} , is now required for the free space medium above the slab. Recall from the development of the Fresnel reflection coefficient [15: pages 186-187] that the enforcement of boundary conditions leads to a familiar relation known as Snell's law of

refraction. In our notation, we state Snell's law of refraction as

$$k_1 r_{x_1} = k_o r_{x_o} \quad (2.27)$$

thereby defining r_{x_o} in terms of r_{x_1} . We note also that this expression, with the product $k_1 r_{x_1}$, remains purely real even for complex k_1 .

We can now define r_{y_o} in a similar fashion to that of r_{y_1} :

$$r_{y_o} = \begin{cases} \sqrt{1 - r_{x_o}^2} & , r_{x_o}^2 \leq 1 \\ -j\sqrt{r_{x_o}^2 - 1} & , r_{x_o}^2 > 1 \end{cases} \quad (2.28)$$

choosing the $-j$ root for imaginary r_{y_o} in keeping with the physical requirements of the radiation condition. We note that given the relation in Equation (2.27), r_{y_o} will be either purely real or purely imaginary regardless of the properties of the slab coating material.

It is instructive to examine the functional form of the reflection coefficient using these spectral domain parameters. For the internal Green's function we are interested in the reflection of the plane wave spectrum on the slab coating material/free space interface at $y = d$, with the waves originating from the slab material side. To be representative of a case of practical interest, we choose slab material parameters of $\epsilon_r = 3.25$, $\mu_r = 1.0$ (a pure, lossless dielectric). The resulting spectral domain reflection coefficient is plotted in Figure 2.3. The horizontal axis is shown as s_x which, for the purpose of illustration, is a combination of the scan parameter s_{x_1} and the ASM mode number n , i.e., $s_x = s_{x_1} + 2n$. We do this because the combination of the two essentially form a continuous variable which, in the case of a lossless medium such as in this example, is identical to the spectral domain variable r_{x_1} . For cases where the slab medium is lossy, this s_x parameter remains purely real, differing from r_{x_1} by the factor $Re(k)/k$.

In the figure, Γ_{10} is symmetric about $s_x = 0$ and, for the material property values used in this case, decays to $\Gamma_{10} = 0$ beyond $|s_x| > 3$. We see that Γ_{10} exhibits the critical angle phenomena in the region $-1 < s_x < 1$ which corresponds to the region where $n = 0$.⁴ The critical angle is the angle at which a plane wave, traversing the interface from a denser media '1' into a less dense

⁴We refer to this range of the variable s_x as the central region.

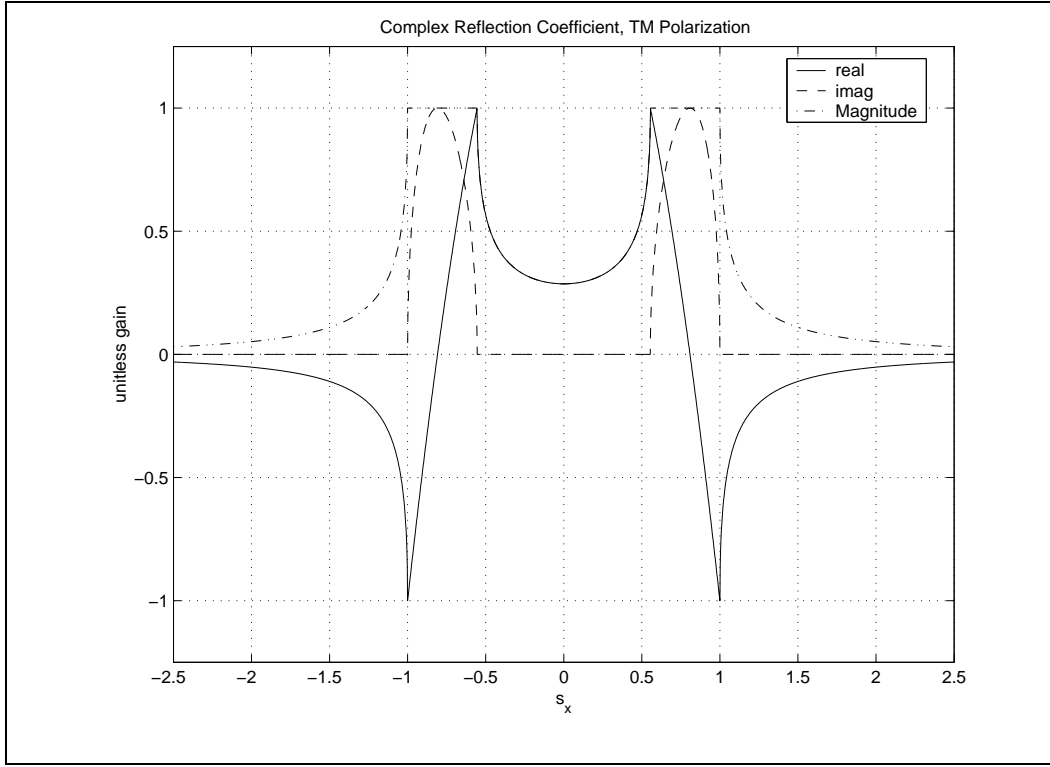


Figure 2.3 Spectral Domain Fresnel Reflection Coefficient Γ_{10} for slab coating material $\epsilon_r = 3.25$, $\mu_r = 1$.

media '0' (i.e., $\sqrt{\mu_1 \epsilon_1} > \sqrt{\mu_0 \epsilon_0}$) experiences total internal reflection at the interface between the two media [15: Section 5.3.4]. From traditional Fresnel theory, we expect the critical angle to occur at $s_c = s_x = \pm Re(\sqrt{\epsilon_0 \mu_0 / \epsilon_1 \mu_1}) \simeq \pm 0.5547$, in agreement with what is seen in Figure 2.3. We have also plotted the magnitude of the reflection coefficient and note that it takes on the value $|\Gamma_{10}| = 1$ in the region of total internal reflection, $|s_c| \leq |s_x| \leq 1$.

In this region where $|\Gamma_{10}| = 1$, the factor r_{y0} has become purely imaginary (the second line in Equation (2.28)), abruptly changing from real to imaginary precisely at the critical angle. This implies that waves are attenuated in the \hat{y} direction in the free space region $y > d$ for $|s_x| > |s_c|$. This is the classic description of total internal reflection and for the existence of a surface wave in the free space region, bound to the interface [15: Section 5.3.4]. The factor r_{y1} for these values of s_x where $|\Gamma_{10}| = 1$ remains purely real (for lossless slab coating materials) which implies that, inside the slab coating, we still have a propagating plane wave. It is only when we reach the value

$|s_x| = 1$ that r_{y1} also abruptly changes from a purely real value to purely imaginary, at which point we encounter another singularity.

What happens to the spectral domain Fresnel reflection coefficient if loss is added to the slab coating material? Such a case is plotted in Figure 2.4 where we have added a dielectric loss component to the slab coating material. The singularities previously observed at the points $|s_x| = 1$

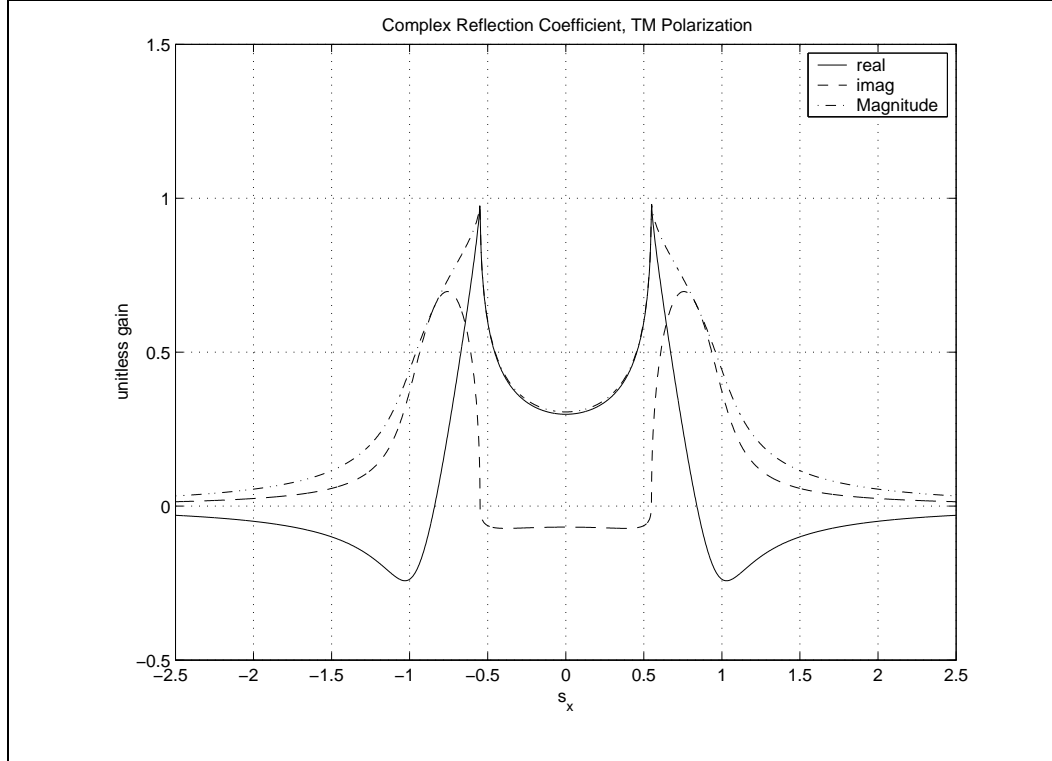


Figure 2.4 Spectral Domain Fresnel Reflection Coefficient Γ_{10} for slab coating material $\epsilon_r = 3.25 - j1$, $\mu_r = 1$.

have been removed from the real s_x axis since, for lossy materials, the factor r_{y1} is complex for all values of s_x (except at $s_x = 0$ where $r_{y1} = 1$). We also notice that the decay to $\Gamma_{10} = 0$ becomes slightly less rapid, also due to the fact that r_{y1} is not purely imaginary, retaining a small real component. The magnitude of the reflection coefficient in this case is $|\Gamma_{10}| < 1$ for all values of s_x .

In order to help visualize some of these changes that occur in the reflection coefficients due to the factors r_{y1} and r_{y0} as s_x varies, we plot these factors in Figure 2.5 using the same lossy material property values used for the reflection coefficient plotted in Figure 2.4. We see that r_{y0}

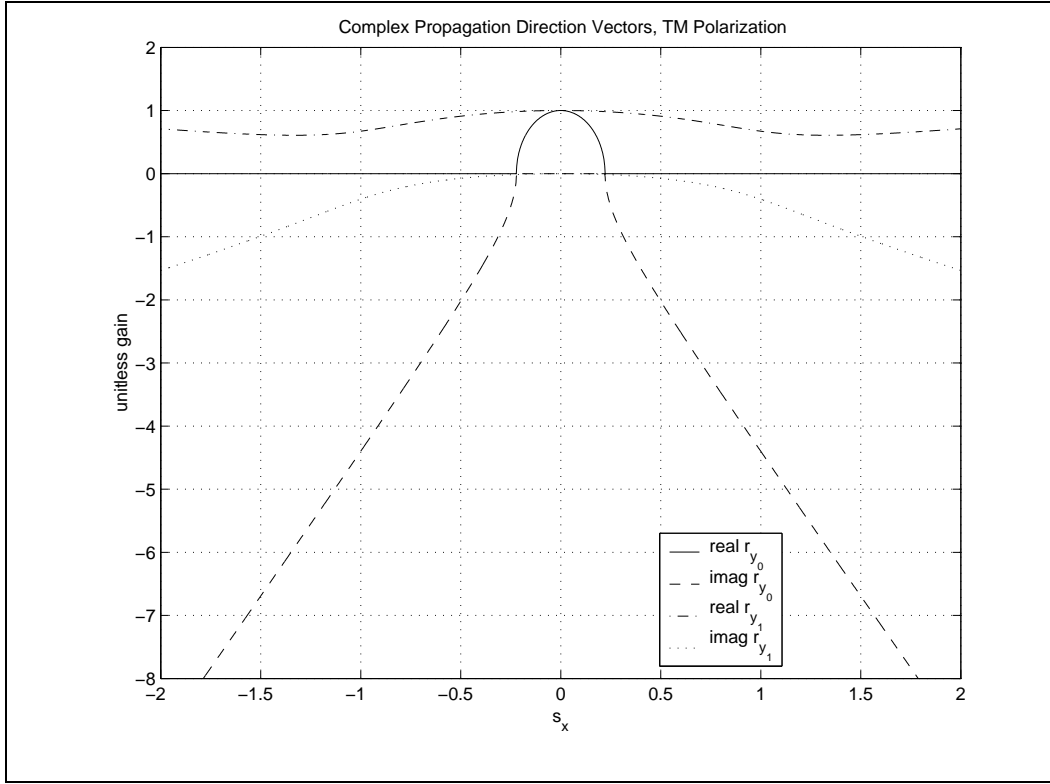


Figure 2.5 Complex behavior of the r_{y0} and r_{y1} factors for case with slab coating material properties $\epsilon_r = 3.25 - j1$, $\mu_r = 1$.

is real only in the range $-s_c \leq s_x \leq s_c$ and negative imaginary elsewhere. r_{y1} is complex (with a negative imaginary part) for all s_x except at $s_x = 0$ where $r_{y1} = 1$. If the slab coating material in this case was lossless, the factor r_{y0} would remain unchanged. The factor r_{y1} , however, would take on an appearance somewhat similar to r_{y0} : the real part of r_{y1} would be nonzero only in the central region going to zero at $s_x = \pm 1$; the imaginary part of r_{y1} would be zero out to $s_x = \pm 1$, and for $|s_x| > 1$, would become increasingly negative imaginary for increasing $|s_x|$. For lossless materials, it is these abrupt changes in r_{y1} and r_{y0} that impart the singular behavior to the reflection coefficients at the critical angles and at $s_x = \pm 1$. For lossy materials, only the r_{y0} factor produces the singular behavior at the critical angles in the reflection coefficient.

Next we ask if instead of a lossless dielectric material, what will be the functional form of Γ_{10} for a lossless magneto-dielectric slab coating material? The result is similar. As shown in Figure 2.6, we see pronounced inward movement of the critical angle and a correspondingly larger region where $|\Gamma_{10}| = 1$. We also note that the reflection coefficient for this case no longer decays

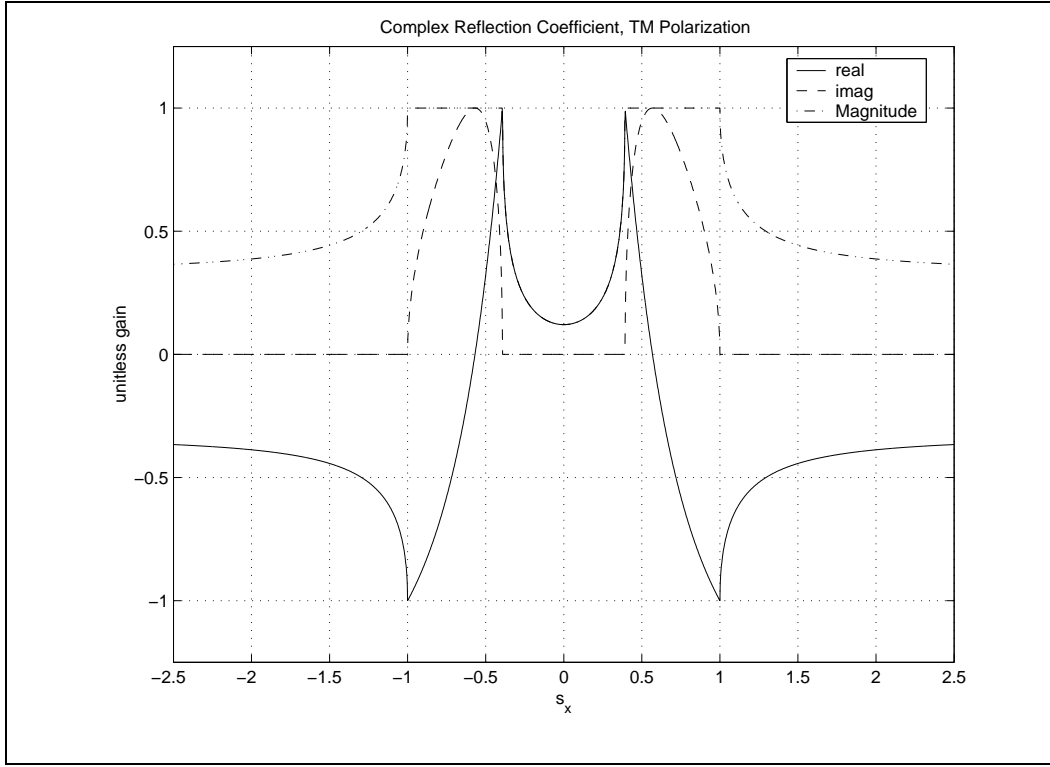


Figure 2.6 Spectral Domain Fresnel Reflection Coefficient Γ_{10} for slab coating material $\epsilon_r = 3.25$, $\mu_r = 2$.

to zero beyond the central region but, instead, to a value $|\Gamma_{10}| < 1$, due solely to the presence of the increased magnetic permeability in the slab coating material. The singularities present in the case of the lossless dielectric material are present here also and are the result of the same processes.

Adding a magnetic loss component (as well as dielectric loss) to the slab material results in additional smoothing of the former singularities at $s_x = \pm 1$ and an appreciable imaginary component for all higher order plane wave modes, i.e., for all $|s_x| > 1$. This case is shown in Figure 2.7. Interestingly, we note that this case also exhibits a region where $|\Gamma_{10}| > 1$. The question naturally arises as to how it is that $|\Gamma_{10}|$ can exceed unity in this (or in any) case. It must first be remembered that Equation (2.25) is a spectral domain quantity and the fields associated with the reflection coefficient in this region (where $|\Gamma_{10}| > 1$) are associated with a single plane wave mode and do not constitute the ‘total’ fields on either side of the interface. So to have $|\Gamma_{10}|$ slightly > 1 in this small region does not necessarily imply a violation of conservation of energy. To verify that this combination of geometry and material properties do not produce $|\Gamma| > 1$, it is a

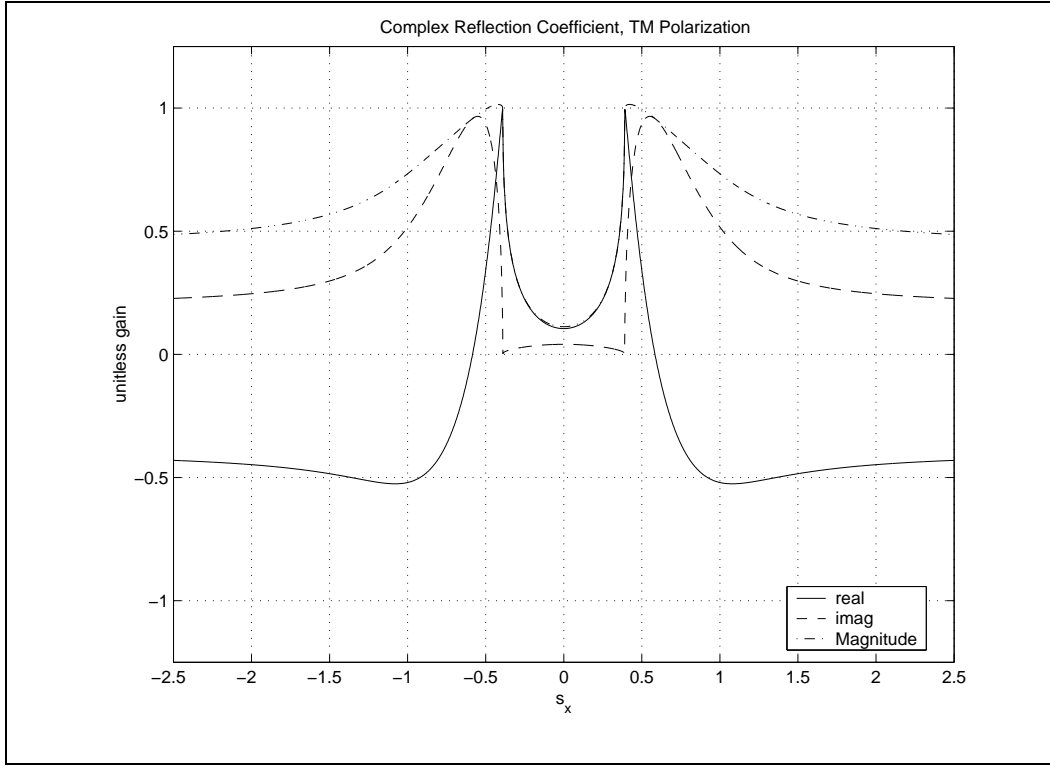


Figure 2.7 Spectral Domain Fresnel Reflection Coefficient Γ_{10} for slab coating material $\epsilon_r = 3.25 - j1$, $\mu_r = 2 - j1$.

simple matter to check the spatial domain form of the reflection coefficient, [15: Equation 5-17a]. This evaluation found that $|\Gamma_{10}|$ in fact does not exceed unity.

The essential point in this sequence is that Γ_{10} is a well-behaved function, with the exception of the singular points occurring at the critical angles, $|s_x| = s_c$, and at the points $|s_x| = 1$ for lossless materials, for values of slab coating material constitutive properties of practical interest.

Returning now to our discussion of the T-factor, the other reflection coefficient in the T-factor, Γ_{12} , is the reflection coefficient of a perfectly electric conducting (PEC) ground plane and has the value -1 for all plane wave modes. We thus see that the T-factor for the TM polarized case takes the form

$$T = \frac{\Gamma e^{-j2kdr_{y1}} \left(e^{jk(y+y')r_{y1}} - 2 \cos[k(y-y')r_{y1}] \right) - e^{-jk(y+y')r_{y1}}}{1 + \Gamma e^{-j2kdr_{y1}}} \quad (2.29)$$

where we have dropped the now-unnecessary subscripts on Γ_{10} .

In order for the geometric series representation of the T-factor established in Equation (2.29) to be valid, it is required that $|\Gamma e^{-j2kdr_{y1}}| < 1$ (strictly less than 1). However, the Fresnel reflection coefficient and the exponential term are only guaranteed to have magnitudes ≤ 1 in cases where the slab coating material is lossless. As we saw in the plots of the reflection coefficient, there are values of s_x for which $|\Gamma| > 1$ when the slab coating material is lossy. But it's the product, $\Gamma e^{-j2kdr_{y1}}$, that is of interest regarding the validity of the geometric series form. In Figure 2.8, we plot this product (using the same scale and material properties) for the case where we saw $|\Gamma| > 1$ in Figure 2.7. The exponential term acquires a strong damping component precisely in the region

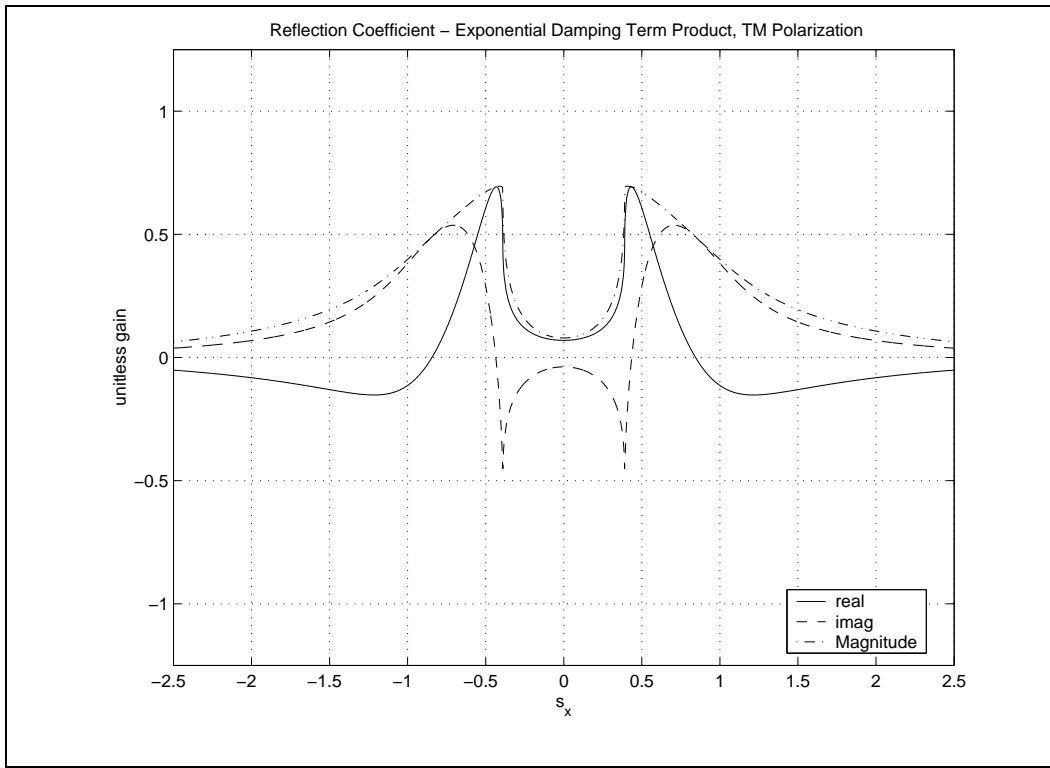


Figure 2.8 Product $\Gamma e^{-j2kdr_{y1}}$ for slab coating material $\epsilon_r = 3.25 - j1$, $\mu_r = 2 - j1$.

where $|\Gamma| > 1$. Furthermore, we see that the product decays to zero for higher order modes. Thus we conclude that the geometric series form of the T-factor is a valid representation of the multiple reflected wave series occurring within the slab coating material.

From Equation (2.16), we see that we will eventually need to use not only the T-factor in its form (2.29), but also derivatives of the T-factor in various blocks of the Green's function matrix. We noted earlier that the T-factor is dependent only on the spatial variables y and y' so that any

terms containing $\frac{\partial T(y, y')}{\partial x} = 0$. Straightforward differentiation of the T-factor yields,

$$\frac{\partial T(y, y')}{\partial y} = jkr_{y1} \frac{\Gamma e^{-j2kdr_{y1}} \left(e^{jk(y+y')r_{y1}} - 2j \sin[k(y-y')r_{y1}] \right) + e^{-jk(y+y')r_{y1}}}{1 + \Gamma e^{-j2kdr_{y1}}} \quad (2.30)$$

and

$$\frac{\partial^2 T(y, y')}{\partial y^2} = -(kr_{y1})^2 \frac{\Gamma e^{-j2kdr_{y1}} \left(e^{jk(y+y')r_{y1}} - 2 \cos[k(y-y')r_{y1}] \right) - e^{-jk(y+y')r_{y1}}}{1 + \Gamma e^{-j2kdr_{y1}}} \quad (2.31)$$

It is convenient to designate the right hand side of Equation (2.30) as $jk r_{y1} T^*$ where

$$T^* = \frac{\Gamma e^{-j2kdr_{y1}} \left(e^{jk(y+y')r_{y1}} - 2j \sin[k(y-y')r_{y1}] \right) + e^{-jk(y+y')r_{y1}}}{1 + \Gamma e^{-j2kdr_{y1}}}$$

and (2.31) as $-(kr_{y1})^2 T$, where T is the original T-factor. We now introduce a new T-factor, T^r , called the ‘reduced T-factor’ which is obtained by subtracting the original T-factor from T^* .

$$T^r = T^* - T = \frac{2e^{-jk(y+y')r_{y1}} \left[1 + \Gamma e^{-j2k(d-y')r_{y1}} \right]}{1 + \Gamma e^{-j2kdr_{y1}}} \quad (2.32)$$

We will use T^r in the next section to determine the complete Green’s function expression for the TM polarization case.

2.3.3 Complete Expressions for TM Polarization. We now combine the expressions that have been developed thus far for the TM polarization case in preparation of their numerical implementation in Chapter 3. In order to accomplish this we must first fully expand the expressions in (2.16), carrying out all indicated differentiations. As noted by the form of Equation (2.13), the canonical Green’s function for our problem is a combination of a direct term and a bounce correction term. Fortunately, we can differentiate these terms separately and display them independently.

Looking first at the direct coupling term, we merely state the results of the various differentiations of Equation (2.1) as these are straightforward.

$$\frac{\partial G_{dc}}{\partial x} = \frac{jk}{4} H_1^{(2)}(kR) \frac{(x-x')}{R} \quad (2.33)$$

$$\frac{\partial G_{dc}}{\partial y} = \frac{jk}{4} H_1^{(2)}(kR) \frac{(y-y')}{R} \quad (2.34)$$

$$\frac{\partial^2 G_{dc}}{\partial x^2} = \frac{jk^2}{4} \left[H_o^{(2)}(kR) \left(\frac{(x-x')^2}{R^2} \right) + \frac{H_1^{(2)}(kR)}{kR} \left(1 - 2 \frac{(x-x')^2}{R^2} \right) \right] \quad (2.35)$$

$$\frac{\partial^2 G_{dc}}{\partial y^2} = \frac{jk^2}{4} \left[H_o^{(2)}(kR) \left(\frac{(y-y')^2}{R^2} \right) + \frac{H_1^{(2)}(kR)}{kR} \left(1 - 2 \frac{(y-y')^2}{R^2} \right) \right] \quad (2.36)$$

$$\frac{\partial^2 G_{dc}}{\partial x \partial y} = \frac{\partial^2 G_{dc}}{\partial y \partial x} = -\frac{jk^2}{4} \frac{(x-x')}{R} \frac{(y-y')}{R} \left(2 \frac{H_1^{(2)}(kR)}{kR} - H_o^{(2)}(kR) \right) \quad (2.37)$$

where $R = \sqrt{(x-x')^2 + (y-y')^2}$. Thus, including block 9 of the Green's function matrix (which is just G_{dc}), there are six unique terms in the matrix. The three diagonal terms are unique and the upper off-diagonal terms are either equivalent or the negative of their corresponding lower off-diagonal terms.

Turning to the bounce correction term, we recall that the scalar component was expressed in Equation (2.10) and that the explicit y, y' dependence of the T-factor was not shown. Additionally, the argument of the exponential can be written,

$$-jk(\bar{\rho} - \bar{\rho}') \cdot \hat{r}_{1,\pm} = -jk[(x-x')r_{x_1} + |y-y'|r_{y_1}]$$

We utilize the chain rule to perform the differentiations on this component of the Green's function to get,

$$\frac{\partial G_{bounce}}{\partial x} = -\frac{Re(k)}{4\pi} \int_{-1}^1 \sum_{n=-\infty}^{\infty} T \frac{r_{x_1}}{r_{y_1}} e^{-jk[(x-x')r_{x_1} + |y-y'|r_{y_1}]} ds_{x_1} \quad (2.38)$$

$$\frac{\partial G_{bounce}}{\partial y} = \frac{Re(k)}{4\pi} \int_{-1}^1 \sum_{n=-\infty}^{\infty} T^r e^{-jk[(x-x')r_{x_1} + |y-y'|r_{y_1}]} ds_{x_1} \quad (2.39)$$

$$\frac{\partial^2 G_{bounce}}{\partial x^2} = \frac{jkRe(k)}{4\pi} \int_{-1}^1 \sum_{n=-\infty}^{\infty} \frac{Tr_{x_1}^2}{r_{y_1}} e^{-jk[(x-x')r_{x_1} + |y-y'|r_{y_1}]} ds_{x_1} \quad (2.40)$$

$$\frac{\partial^2 G_{bounce}}{\partial y^2} = -\frac{jkRe(k)}{4\pi} \int_{-1}^1 \sum_{n=-\infty}^{\infty} 2r_{y_1} T^r e^{-jk[(x-x')r_{x_1} + |y-y'|r_{y_1}]} ds_{x_1} \quad (2.41)$$

$$\frac{\partial^2 G_{bounce}}{\partial x \partial y} = -\frac{jkRe(k)}{4\pi} \int_{-1}^1 \sum_{n=-\infty}^{\infty} T^r r_{x_1} e^{-jk[(x-x')r_{x_1} + |y-y'|r_{y_1}]} ds_{x_1} \quad (2.42)$$

Now we proceed with combining the expressions given above into the complete expressions for the Green's function matrix entries. These become (in some cases omitting several algebraic steps),

$$\begin{aligned}
G_{xx} &= G + \frac{1}{k^2} \frac{\partial^2 G}{\partial x^2} = G_{dc} + G_{bounce} + \frac{1}{k^2} \frac{\partial^2}{\partial x^2} (G_{dc} + G_{bounce}) \\
&= -\frac{j}{4} \left[H_o^{(2)}(kR) \left(1 - \frac{(x-x')^2}{R^2} \right) - \frac{H_1^{(2)}(kR)}{kR} \left(1 - 2 \frac{(x-x')^2}{R^2} \right) \right] \\
&\quad + \frac{jRe(k)}{4\pi k} \int_{-1}^1 \sum_{n=-\infty}^{\infty} T r_{y1} e^{-jk[(x-x')r_{x1} + |y-y'|r_{y1}]} ds_{x1}
\end{aligned} \tag{2.43}$$

$$\begin{aligned}
G_{xy} &= \frac{1}{k^2} \frac{\partial^2 G}{\partial x \partial y} = \frac{1}{k^2} \frac{\partial^2}{\partial x \partial y} (G_{dc} + G_{bounce}) \\
&= -\frac{j}{4} \frac{(x-x')}{R} \frac{(y-y')}{R} \left(2 \frac{H_1^{(2)}(kR)}{kR} - H_o^{(2)}(kR) \right) \\
&\quad - \frac{jRe(k)}{4\pi k} \int_{-1}^1 \sum_{n=-\infty}^{\infty} T^r r_{x1} e^{-jk[(x-x')r_{x1} + |y-y'|r_{y1}]} ds_{x1}
\end{aligned} \tag{2.44}$$

$$\begin{aligned}
G_{xz} &= \frac{\partial G}{\partial y} = \frac{\partial}{\partial y} (G_{dc} + G_{bounce}) \\
&= \frac{jk}{4} H_1^{(2)}(kR) \frac{(y-y')}{R} \\
&\quad + \frac{Re(k)}{4\pi} \int_{-1}^1 \sum_{n=-\infty}^{\infty} T^r e^{-jk[(x-x')r_{x1} + |y-y'|r_{y1}]} ds_{x1}
\end{aligned} \tag{2.45}$$

$$\begin{aligned}
G_{yx} &= \frac{1}{k^2} \frac{\partial^2 G}{\partial y \partial x} = \frac{1}{k^2} \frac{\partial^2}{\partial y \partial x} (G_{dc} + G_{bounce}) \\
&= -\frac{j}{4} \frac{(x-x')}{R} \frac{(y-y')}{R} \left(2 \frac{H_1^{(2)}(kR)}{kR} - H_o^{(2)}(kR) \right) \\
&\quad - \frac{jRe(k)}{4\pi k} \int_{-1}^1 \sum_{n=-\infty}^{\infty} T^r r_{x1} e^{-jk[(x-x')r_{x1} + |y-y'|r_{y1}]} ds_{x1}
\end{aligned} \tag{2.46}$$

$$\begin{aligned}
G_{yy} &= G + \frac{1}{k^2} \frac{\partial^2 G}{\partial y^2} = G_{dc} + G_{bounce} + \frac{1}{k^2} \frac{\partial^2}{\partial y^2} (G_{dc} + G_{bounce}) \\
&= -\frac{j}{4} \left[H_o^{(2)}(kR) \left(1 - \frac{(y-y')^2}{R^2} \right) - \frac{H_1^{(2)}(kR)}{kR} \left(1 - 2 \frac{(y-y')^2}{R^2} \right) \right] \\
&\quad - \frac{jRe(k)}{4\pi k} \int_{-1}^1 \sum_{n=-\infty}^{\infty} \left[\frac{T}{r_{y1}} + 2r_{y1} T^r \right] e^{-jk[(x-x')r_{x1} + |y-y'|r_{y1}]} ds_{x1} \quad (2.47)
\end{aligned}$$

$$\begin{aligned}
G_{yz} &= -\frac{\partial G}{\partial x} = -\frac{\partial}{\partial x} (G_{dc} + G_{bounce}) \\
&= -\frac{jk}{4} H_1^{(2)}(kR) \frac{(x-x')}{R} \\
&\quad + \frac{Re(k)}{4\pi} \int_{-1}^1 \sum_{n=-\infty}^{\infty} T \frac{r_{x1}}{r_{y1}} e^{-jk[(x-x')r_{x1} + |y-y'|r_{y1}]} ds_{x1} \quad (2.48)
\end{aligned}$$

$$\begin{aligned}
G_{zx} &= -\frac{\partial G}{\partial y} = -\frac{\partial}{\partial y} (G_{dc} + G_{bounce}) \\
&= -\frac{jk}{4} H_1^{(2)}(kR) \frac{(y-y')}{R} \\
&\quad - \frac{Re(k)}{4\pi} \int_{-1}^1 \sum_{n=-\infty}^{\infty} T^r e^{-jk[(x-x')r_{x1} + |y-y'|r_{y1}]} ds_{x1} \quad (2.49)
\end{aligned}$$

$$\begin{aligned}
G_{zy} &= \frac{\partial G}{\partial x} = \frac{\partial}{\partial x} (G_{dc} + G_{bounce}) \\
&= \frac{jk}{4} H_1^{(2)}(kR) \frac{(x-x')}{R} \\
&\quad - \frac{Re(k)}{4\pi} \int_{-1}^1 \sum_{n=-\infty}^{\infty} T \frac{r_{x1}}{r_{y1}} e^{-jk[(x-x')r_{x1} + |y-y'|r_{y1}]} ds_{x1} \quad (2.50)
\end{aligned}$$

$$\begin{aligned}
G_{zz} &= G = G_{dc} + G_{bounce} \\
&= -\frac{j}{4} H_o^{(2)}(kR) - \frac{jRe(k)}{4\pi k} \int_{-1}^1 \sum_{n=-\infty}^{\infty} \frac{T}{r_{y1}} e^{-jk[(x-x')r_{x1} + |y-y'|r_{y1}]} ds_{x1} \quad (2.51)
\end{aligned}$$

These equations are then used to fill the matrix blocks of Equation (2.19).

2.4 Expressions for the TE Polarization Case

2.4.1 Dyadic Green's Function. The equations for the case of TE polarization are dual to those for TM polarization, with the notable exception that we still have a PEC ground plane which will require different Fresnel reflection coefficients in the T-factor. Whereas Equations (2.14) – (2.17) are general in nature and apply to both TE and TM polarizations; the orientation of the incident fields and, consequently, the equivalent current sources located within the gap region, will assume different orientations for the two cases. Hence, the equations analogous to (2.18) – (2.21) for TE polarization are

$$\begin{bmatrix} E_x \\ E_y \\ H_z \end{bmatrix} = \begin{bmatrix} j\omega\mu_r \langle G_{xx}, J_x \rangle & j\omega\mu_r \langle G_{xy}, J_y \rangle & \langle G_{xz}, M_z \rangle \\ j\omega\mu_r \langle G_{yx}, J_x \rangle & j\omega\mu_r \langle G_{yy}, J_y \rangle & \langle G_{yz}, M_z \rangle \\ -\langle G_{zx}, J_x \rangle & -\langle G_{zy}, J_y \rangle & j\omega\epsilon_r \langle G_{zz}, M_z \rangle \end{bmatrix} \quad (2.52)$$

The ‘impedance’ matrix for the TE polarization case will again have the form $Z + \Delta Z$. For this case, the ΔZI matrix becomes

$$\Delta ZI = \begin{bmatrix} \frac{J_x}{j\omega(\epsilon_g - \epsilon_r)} & 0 & 0 \\ 0 & \frac{J_y}{j\omega(\epsilon_g - \epsilon_r)} & 0 \\ 0 & 0 & \frac{M_z}{j\omega(\mu_g - \mu_r)} \end{bmatrix} \quad (2.53)$$

The V and I vectors for this case become

$$V = \begin{bmatrix} E_x^i \\ E_y^i \\ H_z^i \end{bmatrix}, \text{ and } I = \begin{bmatrix} J_x \\ J_y \\ M_z \end{bmatrix}$$

2.4.2 T-factor for TE Polarization. The T-factor expression (2.8) will now be applied to the TE polarization case where we use the appropriate Fresnel reflection coefficients for a PEC ground plane. For the TM polarization case, all variables and expressions were derived referring to the electric field since the incident field was of the form $\vec{E}^i = \hat{z}E_z$. For the TE case, we will be

referring all variables and expressions to the magnetic field and assuming an incident field of the form $\bar{H}^i = \hat{z}H_z$. Under these conditions, the appropriate spectral domain Fresnel reflection and transmission coefficients at the slab material/free space interface are

$$\Gamma_{10} = \frac{\eta_1 r_{y1} - \eta_o r_{yo}}{\eta_1 r_{y1} + \eta_o r_{yo}} \quad (2.54)$$

and

$$\tau_{10} = \frac{2\eta_1 r_{y1}}{\eta_1 r_{y1} + \eta_o r_{yo}} \quad (2.55)$$

where we note that the form of each is slightly different from the forms in Equations (2.25) and (2.26) resulting from the rearrangement of the constituent factors appropriate for TE polarization [15: Section 5.3].

Plots of the reflection coefficients for TE polarization, using the same material properties used for the corresponding TM reflection coefficient sequence plotted in Figures 2.3 - 2.4 and 2.6 - 2.7, are shown in Figures 2.9 - 2.12.

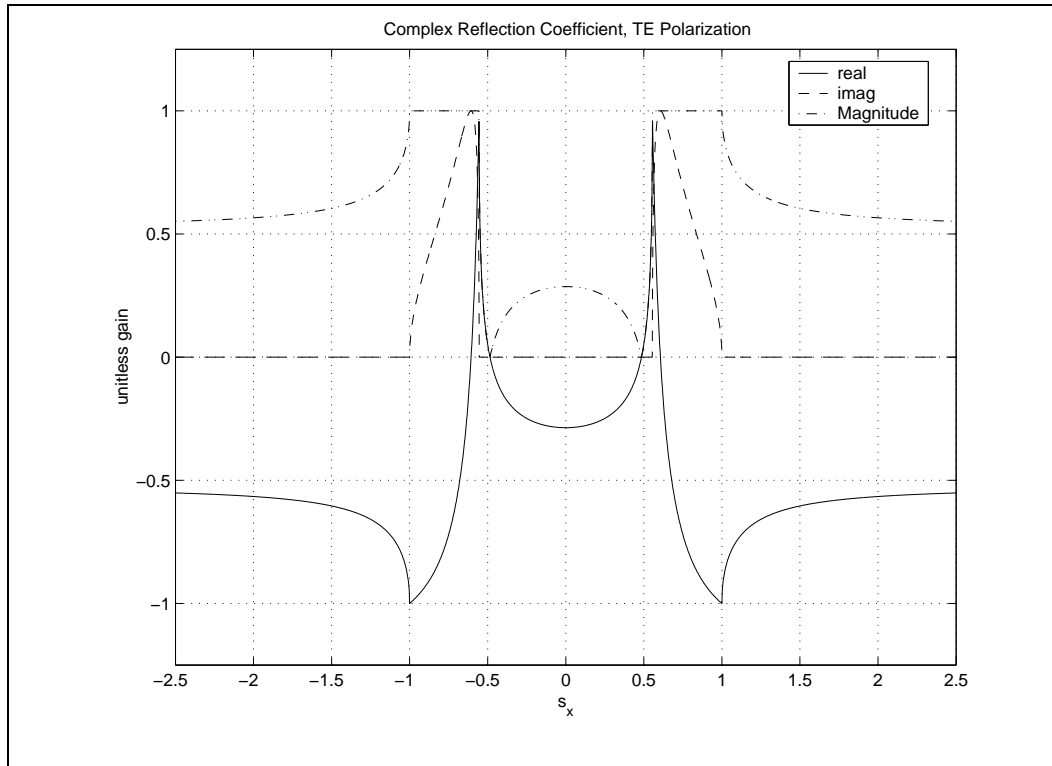


Figure 2.9 Spectral Domain Fresnel Reflection Coefficient for slab coating material $\epsilon_r = 3.25$, $\mu_r = 1$.

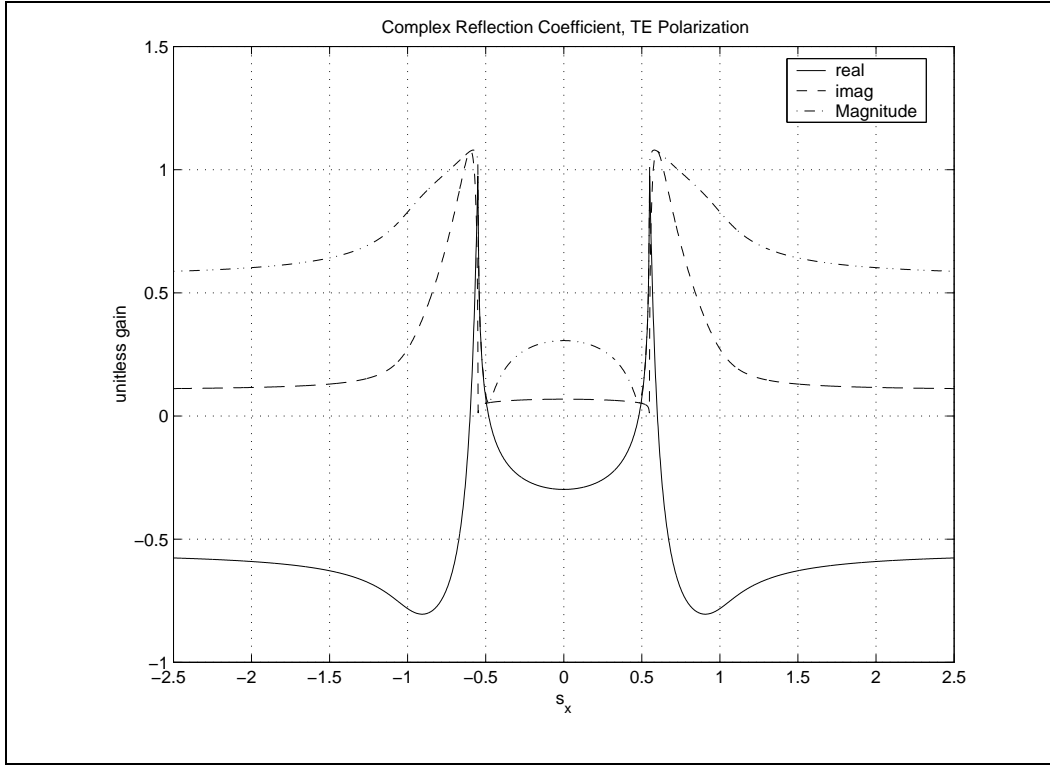


Figure 2.10 Spectral Domain Fresnel Reflection Coefficient for slab coating material $\epsilon_r = 3.25 - j1$, $\mu_r = 1$.

As was the case for the TM reflection coefficient, the TE result is symmetric about $s_x = 0$, but now decays to a value $\Gamma = -0.5$ for higher order plane wave modes. Statements made earlier about changes in the TM reflection coefficient resulting from changes in the slab coating material properties apply also to the TE reflection coefficient. In keeping with the ‘dual’ nature of the TE polarization case relative to TM, we see in Figure 2.10 that for some values of s_x in the central plane wave mode region that $|\Gamma| > 1$ in the case of a lossy dielectric slab coating material. We emphasize here again that this does not imply a violation of conservation of energy, and make the same arguments presented in discussion of Figure 2.7. For the lossy magneto-dielectric case plotted in Figure 2.12, $|\Gamma| < 1$ for all values of s_x .

Returning now to our evaluation of the T-factor for TE polarization, the reflection coefficient at the PEC ground plane, referred to the H-field, is $\Gamma_{12} = +1$. Thus, the T-factor for this case takes the form

$$T = \frac{\Gamma e^{-j2kdr_{y1}} \left(e^{jk(y+y')r_{y1}} + 2 \cos[k(y-y')r_{y1}] \right) + e^{-jk(y+y')r_{y1}}}{1 - \Gamma e^{-j2kdr_{y1}}} \quad (2.56)$$

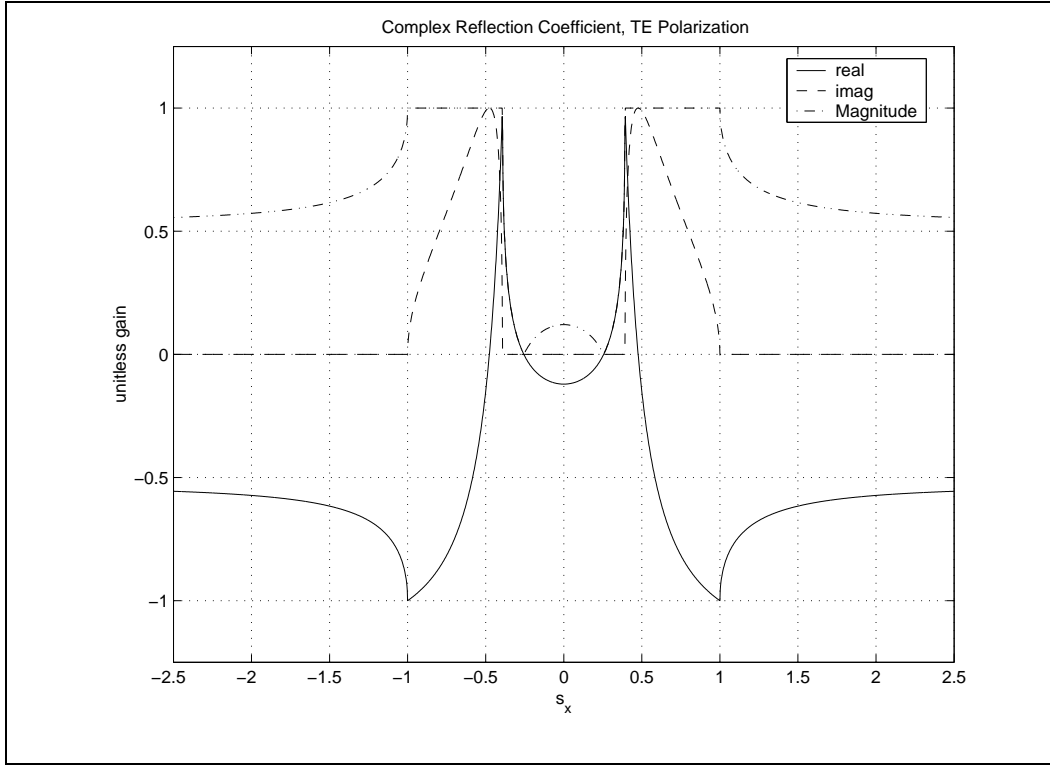


Figure 2.11 Spectral Domain Fresnel Reflection Coefficient for slab coating material $\epsilon_r = 3.25$, $\mu_r = 2$.

Here, we again ask about the validity of the geometric series form of Equation (2.56) as we did before in the TM polarization case. The same comments made earlier for the TM polarization case apply here as well. We want to examine the case where $|\Gamma| > 1$ in Figure 2.10 when we plot in Figure 2.13 the product $\Gamma e^{-j2kdr_{y1}}$, using the same scale and material parameters. We see again that the exponential term contributes a damping component precisely in the region where $|\Gamma| > 1$ such that the product $\Gamma e^{-j2kdr_{y1}} < 1$ for all values of s_x . Thus we see that the geometric series form of the T-factor is a valid representation for the infinite multiple reflected waves that ‘rattle’ back and forth inside the slab coating between the interface and the ground plane.

We will also need a T^* and T^r for the TE-polarization case. In this instance they have forms similar to those of the TM polarization case, the differences arising through the different reflection coefficients for TE polarization.

$$T^* = \frac{\Gamma e^{-j2kdr_{y1}} \left(e^{jk(y+y')r_{y1}} + 2j \sin[k(y-y')r_{y1}] \right) - e^{-jk(y+y')r_{y1}}}{1 - \Gamma e^{-j2kdr_{y1}}} \quad (2.57)$$

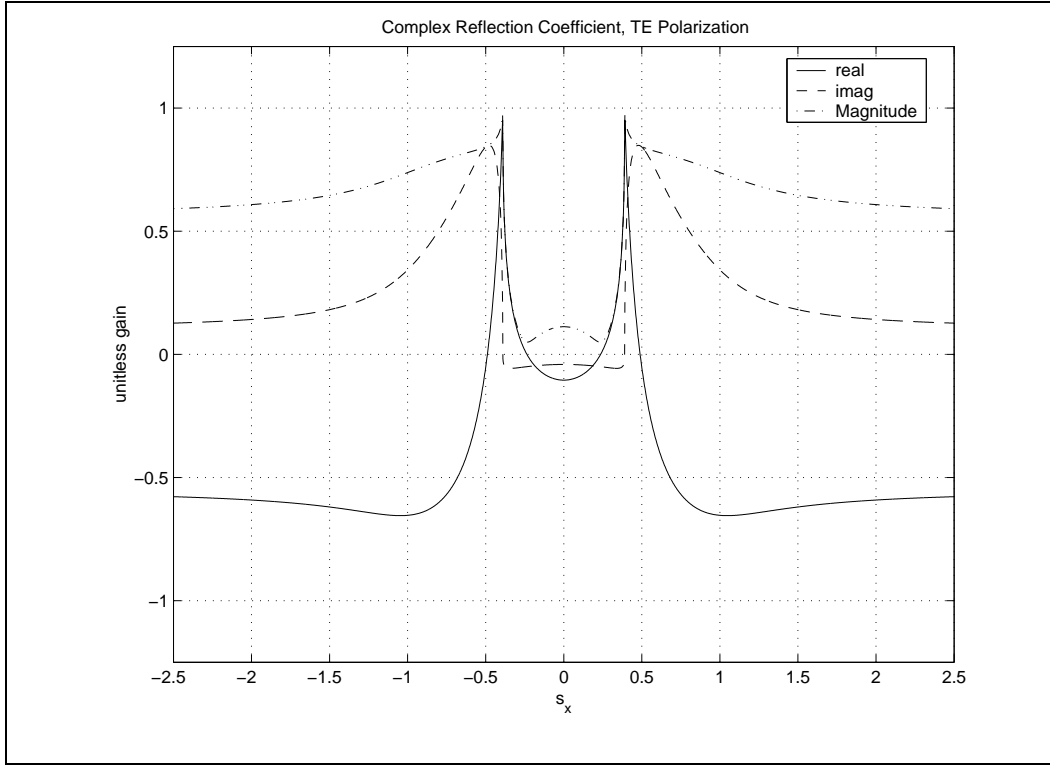


Figure 2.12 Spectral Domain Fresnel Reflection Coefficient for slab coating material $\epsilon_r = 3.25 - j1$, $\mu_r = 2 - j1$.

and

$$T^r = T^* - T = \frac{-2e^{-jk(y+y')r_{y1}} \left[1 + \Gamma e^{-j2k(d-y')r_{y1}} \right]}{1 - \Gamma e^{-j2kdr_{y1}}} \quad (2.58)$$

2.4.3 Complete Expressions for TE Polarization. We now combine our expressions for TE polarization as we did for TM. The direct component of the Green's function is the same in this case as it was for TM so Equations (2.33) – (2.37) are still applicable. The same is also true for the bounce correction terms in the general sense that the form of Equations (2.38) – (2.42) still apply, but we use the T-factors for TE polarization. Thus, the matrix entries, Equations (2.43) – (2.51), apply also to the TE case as long as these modifications are taken into account.

This essentially completes the development of the internal Green's function expressions for our problem. We turn now to the development of the external Green's function which will be needed to compute the scattered fields radiated by the equivalent gap currents.

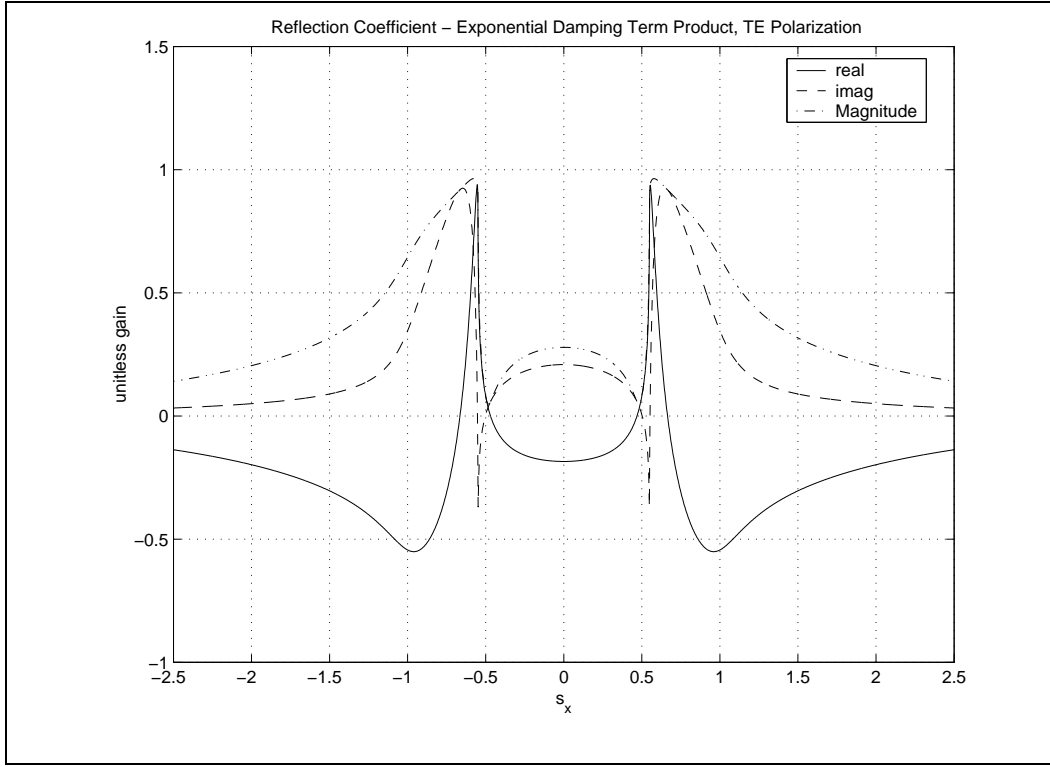


Figure 2.13 Product $\Gamma e^{-j2kdr_{y1}}$ for slab coating material $\epsilon_r = 3.25 - j1$, $\mu_r = 1$.

2.5 The External Green's Function

The expressions developed thus far are valid only within the region of the gap in the magneto-dielectric slab medium. In order to evaluate fields exterior to the gap region, another (and different) Green's function is needed to account for the geometry of the problem as shown in Figure 1.5. This Green's function, called the external Green's function, is valid for observation points external to the gap region, in the region $y > d$. We will need this Green's function in order to compute the fields scattered by the gap (e.g., the echo width of the gap.)

To construct the external Green's function, we will again employ the methods of Munk [19] to arrive at an expression that couples a transmitting line source element located within the gap region to a receiving line source element in the exterior region. Pictorially, this situation is shown in Figure 2.14, where it is seen that there is no direct coupling path since the transmitter and receiver elements are separated by an interface.

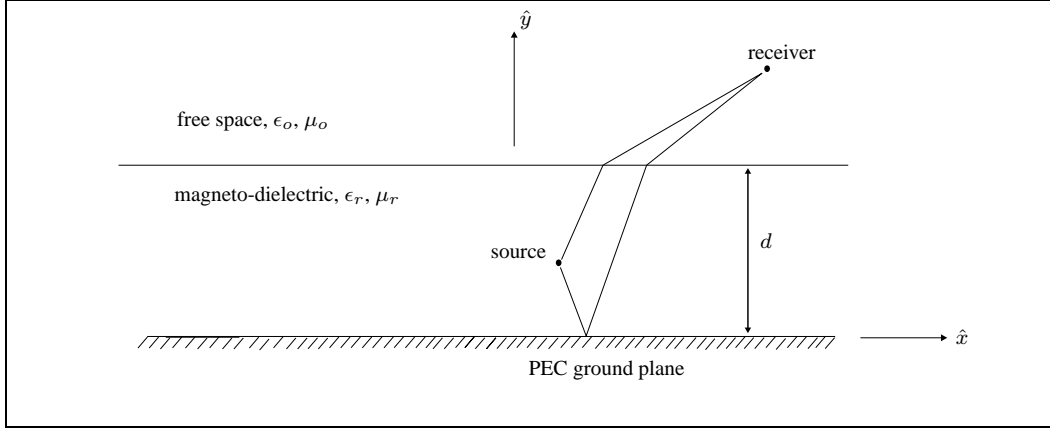


Figure 2.14 Coupling paths for the external Green's function

Seeking an expression analogous to Equation (2.10), we develop the external Green's function starting with an expression from Munk [19: Equation (5.33)]⁵ for coupling in a stratified media scenario in which the source and field points are located in different media. In the notation used in this dissertation, and after application of the ASM, this Green's function expression is

$$G^{ext} = -\frac{jRe(k_1)}{4\pi k_1} \int_{-1}^1 \sum_{n=-\infty}^{\infty} \frac{e^{-jk_1(\hat{y}d - \hat{\rho}') \cdot \hat{r}_1}}{r_{y1}} T^{ext} e^{-jk_o(\hat{\rho} - \hat{y}d) \cdot \hat{r}_o} ds_{x1} \quad (2.59)$$

where [19: Equation (5.34)]

$$T^{ext} = \tau_{10} \frac{\left[1 + \Gamma_{12}e^{-j2k_1y'r_{y1}}\right] \left[1 + \Gamma_{\infty}e^{-j2k_o(d-y)r_{y_o}}\right]}{1 - \Gamma_{12}\Gamma_{10}e^{-j2k_1dr_{y1}}}$$

Equation (2.59) is derived in the same manner as was the internal Green's function for the bounce correction component, Equation (2.10), but has a different T-factor to account for the fact that the source, (x', y') , and receiver, (x, y) , locations are now in different regions separated by an interface. Γ_{∞} is a reflection coefficient 'on the other side' of the receiver (from the origin). In our two-media problem this exterior region is free space and there is no reflection from the domain boundary at $y = \infty$ so $\Gamma_{\infty} = 0$. Other variables in this equation have been defined previously.

⁵The equation in this citation is developed for the induced voltage on an element in a doubly-infinite array in a general stratified medium. We can use this same model for the external Green's function for our one-dimensional array via suitable replacement of constants and a single summation over our 2-D plane wave mode set.

Thus, the external T-factor becomes,

$$T^{ext} = \tau_{10} \frac{[1 + \Gamma_{12} e^{-j2k_1 y' r_{y1}}]}{1 - \Gamma_{12} \Gamma_{10} e^{-j2k_1 d r_{y1}}} \quad (2.60)$$

We again place the ASM array in Equation (2.59) within the magneto-dielectric slab medium since that is where the volumetric equivalent currents exist. This will be to our advantage in this case because it will allow us to limit the extent of our spectral scan (in s_{x1}). With reference to Figure 2.14, when the equivalent currents radiate from within the slab to the exterior free space region $y > d$, the rays are refracting from a more dense into a less dense medium. In order to scan in the free space region from $\pm 90^\circ$ we need only scan out to the critical angle inside the slab ($\pm s_c$), the critical angle being that angle at which the plane waves in the denser slab medium become totally internally reflected). The relationship between the range of scan angles (and, in the ASM bounce correction integral, the range of integration) in one medium to that in another is determined by Snell's Law, Equation (2.27). Application of this principle here enables us to avoid having to deal with the singularities that may arise in the integrals when the factor r_{y1} vanishes (and changes from being purely real to purely imaginary), which always occurs at $|s_x| = 1$, beyond the critical angles.

At the same time, since we are ultimately interested in the propagation of the scattered fields into the free space region, we want to change the variable of integration from s_{x1} to s_{xo} . We again use Snell's Law relationship to change the variable of integration and the scan angle (limits of integration) noted above. We employ these modifications to rewrite Equation (2.59) as,

$$G^{ext} = -\frac{jk_o}{4\pi k_1} \int_{-1}^1 \sum_{n=-\infty}^{\infty} \frac{e^{-jk_1[(d-y')r_{y1} - x' r_{x1}]} T^{ext} e^{-jk_o[(y-d)r_{yo} + x r_{xo}]} ds_{xo}}{r_{y1}} \quad (2.61)$$

where the real-valued factor k_o replaces $Re(k_1)$ as a result of the application of Snell's Law.

We now can specialize Equation (2.61) for the two polarization cases. For the TM-polarization case, we have as before $\Gamma_{12} = -1$, $\Gamma_{10} = \Gamma$ (Equation (2.25)) and τ_{10} ($= \tau_{TM}$) is Equation (2.26). For TE polarization, $\Gamma_{12} = 1$ (referred to the H -field), and Γ_{10} , τ_{10} ($= \tau_{TE}$) are Equations (2.54) and (2.55) respectively. Making these substitutions in Equation (2.60), we have for the external

T-factors,

$$T_{TM}^{ext} = \tau_{TM} \frac{[1 - e^{-j2k_1 y' r_{y1}}]}{1 + \Gamma e^{-j2k_1 d r_{y1}}} \quad (2.62)$$

and

$$T_{TE}^{ext} = \tau_{TE} \frac{[1 + e^{-j2k_1 y' r_{y1}}]}{1 - \Gamma e^{-j2k_1 d r_{y1}}} \quad (2.63)$$

With these T-factors substituted into Equation (2.61) for each appropriate polarization, we can then describe the scattered fields radiated into the free space region once we know the volume equivalent currents determined by the internal Green's function.

In our 2-D problem geometry, we can define the scattering width (or 2-D RCS) of the gap using the expressions [15: pg 577]

$$\sigma_{2-D} = \lim_{\rho \rightarrow \infty} 2\pi\rho \frac{|\bar{E}^s|^2}{|\bar{E}^i|^2} = \lim_{\rho \rightarrow \infty} 2\pi\rho \frac{|\bar{H}^s|^2}{|\bar{H}^i|^2}$$

where \bar{E}^s , \bar{E}^i , \bar{H}^s , and \bar{H}^i are scattered electric field, incident electric field, scattered magnetic field, and incident magnetic field. For TM polarization, the electric field is \hat{z} polarized throughout while for TE polarization, the magnetic field is. This enables us to write separately,

$$\sigma_{TM} = \lim_{\rho \rightarrow \infty} 2\pi\rho \frac{|E_z^s|^2}{|E_z^i|^2} \quad (2.64)$$

$$\sigma_{TE} = \lim_{\rho \rightarrow \infty} 2\pi\rho \frac{|H_z^s|^2}{|H_z^i|^2} \quad (2.65)$$

We note from Equations (2.64) and (2.65) that only \hat{z} -directed scattered fields are required to compute the echo width of the gaps. We see by inspection of Equations (2.22) and (2.52) that for cases where \hat{x} and \hat{y} directed equivalent currents are part of the solution, we will need external Green's function components G_{zx}^{ext} and G_{zy}^{ext} to radiate these equivalent currents into the free space region. We then identify Equation (2.61) as our 'canonical' external Green's function, G_{zz}^{ext} , and note that from Equations (2.16) and (2.17) that

$$G_{zx}^{ext} = -\frac{\partial G_{zz}^{ext}}{\partial y'}, \quad G_{zy}^{ext} = \frac{\partial G_{zz}^{ext}}{\partial x'}$$

Carrying out the indicated differentiations gives,

$$G_{zx}^{ext} = -\frac{k_o}{4\pi} \int_{-1}^1 \sum_{n=-\infty}^{\infty} \frac{e^{-jk_1[(d-y')r_{y1}-x'r_{x1}]} }{r_{y1}} T_r^{ext} e^{-jk_o[(y-d)r_{y0}+xr_{x0}]} ds_{x_o} \quad (2.66)$$

$$G_{zy}^{ext} = \frac{k_o}{4\pi} \int_{-1}^1 \sum_{n=-\infty}^{\infty} \frac{r_{x1}}{r_{y1}} e^{-jk_1[(d-y')r_{y1}-x'r_{x1}]} T_r^{ext} e^{-jk_o[(y-d)r_{y0}+xr_{x0}]} ds_{x_o} \quad (2.67)$$

where we define

$$T_r^{ext} = \tau_{TM} \frac{1 + e^{-j2k_1 y' r_{y1}}}{1 + \Gamma e^{-j2k_1 d r_{y1}}} \quad (2.68)$$

for TM polarization and

$$T_r^{ext} = \tau_{TE} \frac{1 - e^{-j2k_1 y' r_{y1}}}{1 - \Gamma e^{-j2k_1 d r_{y1}}} \quad (2.69)$$

for TE polarization as the ‘reduced’ external T-factors which result from the process of differentiating the integrand in Equation (2.61) with respect to y' . The differentiation of Equation (2.61) with respect to x' simply produces the r_{x1} factor in the numerator of Equation (2.67).

2.6 Incident Fields

For the TM polarization case, the electric field is purely \hat{z} -directed. The field incident upon the gap from the free space region ($y > d$) can be expressed as

$$E_z^{inc}(x, y, \phi^{inc}) = e^{jk_o x \sin \phi^{inc}} e^{jk_o y \cos \phi^{inc}} \quad (2.70)$$

To find the incident field values within the gap region ($0 < y < d$), we must use a more generalized expression to account for the presence of the magneto-dielectric slab coated ground plane geometry. This generalized incident field is,

$$E_z^{ginc}(x, y, \phi^{inc}) = e^{jk_o x \sin \phi^{inc}} e^{jk_o d \cos \phi^{inc}} \tau_{01} \left[\frac{e^{-jk_1(d-y) \cos \phi_1} (1 - e^{-j2k_1 y \cos \phi_1})}{1 + \Gamma e^{-j2k_1 d \cos \phi_1}} \right] \quad (2.71)$$

where we have used the more familiar form of Snell’s law of refraction

$$k_1 \sin \phi_1 = k_o \sin \phi^{inc}$$

to obtain the refracted angle ϕ_1 within the slab medium. We recognize that k_1 can become complex for a lossy magneto-dielectric slab medium. In this event, the angle of refraction ϕ_1 will also become complex in a manner such that the product $k_1 \sin \phi_1$ remains purely real and the equality holds.

In Equation (2.71), τ_{01} is the Fresnel transmission coefficient from the free space region into the slab medium and Γ is the reflection coefficient from the slab medium onto the slab-free space interface. These expressions are

$$\tau_{01} = \frac{2\eta_1 \cos \phi^{inc}}{\eta_o \cos \phi_1 + \eta_1 \cos \phi^{inc}} \quad (2.72)$$

and

$$\Gamma = \frac{\eta_o \cos \phi_1 - \eta_1 \cos \phi^{inc}}{\eta_o \cos \phi_1 + \eta_1 \cos \phi^{inc}} \quad (2.73)$$

In working with the incident fields, there is no need to resort to the spectral domain expressions for these parameters. This is because the incident field is a uniform plane wave and there are no higher order plane wave expansion modes associated with it.

For the case of a general homogeneous magneto-dielectric slab medium, we will require the magnetic fields induced within the gap region. These are obtained through straightforward application of Faraday's Law,

$$\bar{H} = -\frac{1}{j\omega\mu_1} \nabla \times \bar{E} \quad (2.74)$$

which becomes for our application,

$$\bar{H}^{ginc} = -\frac{1}{j\omega\mu_1} \left(\hat{x} \frac{\partial}{\partial y} E_z^{ginc} - \hat{y} \frac{\partial}{\partial x} E_z^{ginc} \right) \quad (2.75)$$

Proceeding first for the y -component as indicated, we have

$$\begin{aligned} H_y^{ginc} &= \frac{1}{j\omega\mu_1} \frac{\partial}{\partial x} E_z^{ginc} \\ &= \frac{k_o \sin \phi^{inc}}{\omega\mu_1} e^{jk_o x \sin \phi^{inc}} e^{jk_o d \cos \phi^{inc}} \tau_{01} \left[\frac{e^{-jk_1(d-y) \cos \phi_1} (1 - e^{-j2k_1 y \cos \phi_1})}{1 + \Gamma e^{-j2k_1 d \cos \phi_1}} \right] \\ &= \frac{k_o \sin \phi^{inc}}{\omega\mu_1} E_z^{ginc} \end{aligned}$$

Applying Snell's law to the last equality and noting that $\frac{k_1}{\omega\mu_1} = \frac{1}{\eta_1}$ allows us to write,

$$H_y^{ginc} = \frac{\sin \phi_1}{\eta_1} E_z^{ginc} \quad (2.76)$$

For the x -component, we have

$$\begin{aligned} H_x^{ginc} &= -\frac{1}{j\omega\mu_1} \frac{\partial}{\partial y} E_z^{ginc} \\ &= -\frac{k_1 \cos \phi_1}{\omega\mu_1} e^{-jk_o x \sin \phi^{inc}} e^{jk_o d \cos \phi^{inc}} \tau_{01} \left[\frac{e^{-jk_1(d-y) \cos \phi_1} (1 + e^{-j2k_1 y \cos \phi_1})}{1 + \Gamma e^{-j2k_1 d \cos \phi_1}} \right] \end{aligned}$$

For later convenience (since the bracketed term is now slightly different), we define a new parameter,

$$H_{inc} = e^{jk_o x \sin \phi^{inc}} e^{jk_o d \cos \phi^{inc}} \tau_{01} \left[\frac{e^{-jk_1(d-y) \cos \phi_1} (1 + e^{-j2k_1 y \cos \phi_1})}{1 + \Gamma e^{-j2k_1 d \cos \phi_1}} \right] \quad (2.77)$$

so that we can write for the x -component of the magnetic field,

$$H_x^{ginc} = -\frac{\cos \phi_1}{\eta_1} H_{inc} \quad (2.78)$$

For TE polarization we have equations dual to those for the TM case, save for the form of the reflection and transmission coefficients. For the incident field we have,

$$H_z^{inc}(x, y, \phi^{inc}) = e^{jk_o x \sin \phi^{inc}} e^{jk_o y \cos \phi^{inc}} \quad (2.79)$$

and for the generalized incident field,

$$H_z^{ginc}(x, y, \phi^{inc}) = e^{jk_o x \sin \phi^{inc}} e^{jk_o d \cos \phi^{inc}} \tau_{01} \left[\frac{e^{-jk_1(d-y) \cos \phi_1} (1 + e^{-j2k_1 y \cos \phi_1})}{1 - \Gamma e^{-j2k_1 d \cos \phi_1}} \right] \quad (2.80)$$

where Γ and τ_{01} are now the appropriate TE polarization quantities referred to the magnetic field.

For this case, these are

$$\tau_{01} = \frac{2\eta_o \cos \phi^{inc}}{\eta_o \cos \phi^{inc} + \eta_1 \cos \phi_1} \quad (2.81)$$

and

$$\Gamma = \frac{\eta_1 \cos \phi_1 - \eta_o \cos \phi^{inc}}{\eta_1 \cos \phi_1 + \eta_o \cos \phi^{inc}} \quad (2.82)$$

We again require the corresponding electric field expressions to accommodate a magneto-dielectric slab medium. These are derived from Ampere's Law,

$$\bar{E} = \frac{1}{j\omega\epsilon_1} \nabla \times \bar{H}$$

and are dual to the expressions given above for the TM polarization case. Stating these results we have,

$$E_y^{ginc} = -\eta_1 \sin \phi_1 H_z^{ginc} \quad (2.83)$$

and

$$E_x^{ginc} = \eta_1 \cos \phi_1 E_{inc} \quad (2.84)$$

where we have used Snell's law again, substituted $\eta_1 = k_1/\omega\epsilon_1$, and where E_{inc} , analogous to H_{inc} , is,

$$E_{inc} = e^{jk_o x \sin \phi^{inc}} e^{jk_o d \cos \phi^{inc}} \tau_{01} \left[\frac{e^{-jk_1(d-y) \cos \phi_1} (1 - e^{-j2k_1 y \cos \phi_1})}{1 - \Gamma e^{-j2k_1 d \cos \phi_1}} \right] \quad (2.85)$$

III. Numerical Implementation

The solution technique to be used in this dissertation was briefly outlined in Chapter 1 where the coupled integral equations arising from the problem geometry were described. In Chapter 2, we developed the Green's functions for the magneto-dielectric slab coated ground plane geometry, one for coupling between source and receiver when both are located within the gap region (the internal Green's function) and one for coupling between a source located within the gap region and a receiver located in the free space region (the external Green's function). In this chapter, we outline the discretization of the integral equations and describe how they are solved with these complicated Green's functions utilizing standard numerical analysis techniques. To this end, we begin by looking at the bounce correction terms of the various Green's function components. As seen in the preceding development, these integral expressions play a critical role in the solution and the need to evaluate them will impact our choice of solution approach for the larger moment method problem.

3.1 Bounce Correction Term Integrands

For accurate numerical implementation of the complete expressions developed for the internal Green's functions in Section (2.3.3) (Equations (2.43) - (2.51)), it is crucial to understand the behavior of these expressions for cases of practical interest. We are concerned at this point with the ASM-derived bounce correction terms since the direct coupling terms are various combinations of Hankel functions which are both well understood and easily computed using algorithms available in the open literature. We will need, however, to look at how the 'self' coupling terms are computed as this will involve dealing with the singularity in the Hankel functions as the arguments tend toward zero. This will be accomplished in a later section.

The ASM-derived bounce correction terms are integrals that must be evaluated to determine the bounce correction contribution to the Green's function. Looking at Equations (2.43) - (2.51), it is apparent that numerical integration is required to evaluate these terms. In this section, we will look at representative examples of these integrand functions. Our goal is to gain an understanding as to what type of numerical integration routines will be required and to be aware of any potential difficulties.

3.1.1 The Canonical ASM Integrand Function. We begin by looking at the behavior of the integral term in Equation (2.51), the canonical Green's function term, which, through Equations (2.11) and (2.12), produces the nine blocks of the dyadic (or matrix) Green's function in Equation (2.17). In particular, we are interested in looking at the ASM-derived portion of Equation (2.51), the bounce correction term of the scalar Green's function. Repeating for convenience this component of Equation (2.51), we have,

$$G_{bounce, zz} = -\frac{jRe(k_1)}{4\pi k_1} \int_{-1}^1 \sum_{n=-\infty}^{\infty} \frac{T}{r_{y1}} e^{-jk_1[(x-x')r_{x1} + |y-y'|r_{y1}]} ds_{x1} \quad (3.1)$$

It is important that we understand the numerical complexities Equation (3.1) will add to our efforts of constructing a Moment Method solution to our problem. The bounce correction integral expressions must be evaluated for each Green's function component in the impedance matrix. For the purpose of illustration we will look at how the various integrand functions behave for both TM and TE polarization for representative slab coating material properties for source and receiver locations corresponding to a representative gap geometry. We make this distinction because the integrand functions are independent of the existence of any gap. We merely choose values of $(x, y), (x', y')$ that will be consistent with the representative gap geometry shown in Figure 3.1.

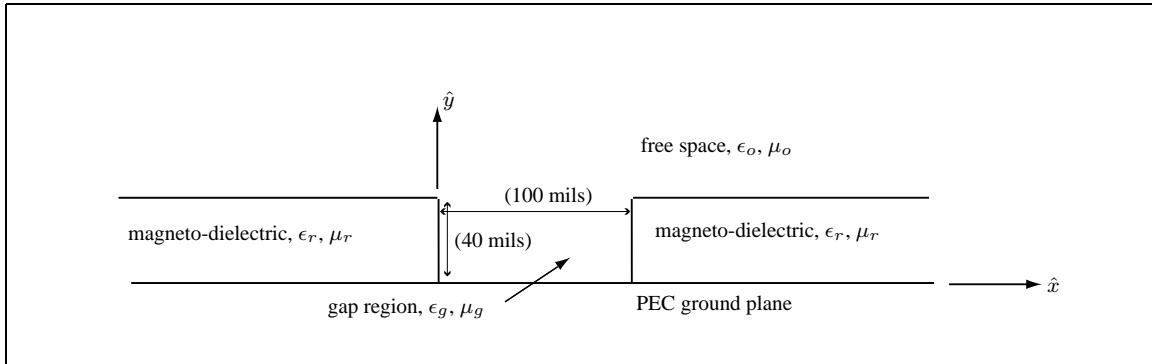


Figure 3.1 Representative Gap Geometry for examination of Green's Function Integrands

For the examples displayed in this section, we choose a hypothetical gap of rectangular shape, 100 mils wide, in a magneto-dielectric slab 40 mils thick with $\epsilon_r = 3.25$ and with either a lossless permeability of $\mu_r = 2.0$ or a lossy permeability of $\mu_r = 2.0 - j1.0$. For all cases shown here we choose a frequency of 11.8 GHz which corresponds to a free space wavelength

of 1 inch. We point out that the integrand function in Equation (3.1) will greatly vary depending on choices of x , x' , y , y' , ϵ_r , and μ_r , and we select only a representative set to display here. Additional integrand function plots are shown in Appendix C to provide additional information and insight into the behavior of these ASM-derived integrand expressions for different choices of source-receiver locations and/or representative material properties.

The maximum physical separation between a source and field element in the gap geometry shown in Figure 3.1 would occur if they were located in opposite corners of the gap region, say the source point (x', y') at $(0, 0)$, and the field point (x, y) at $(100, 40)$ (all geometric dimensions in mils). The integrand of Equation (3.1) for this case is plotted in Figure 3.2.

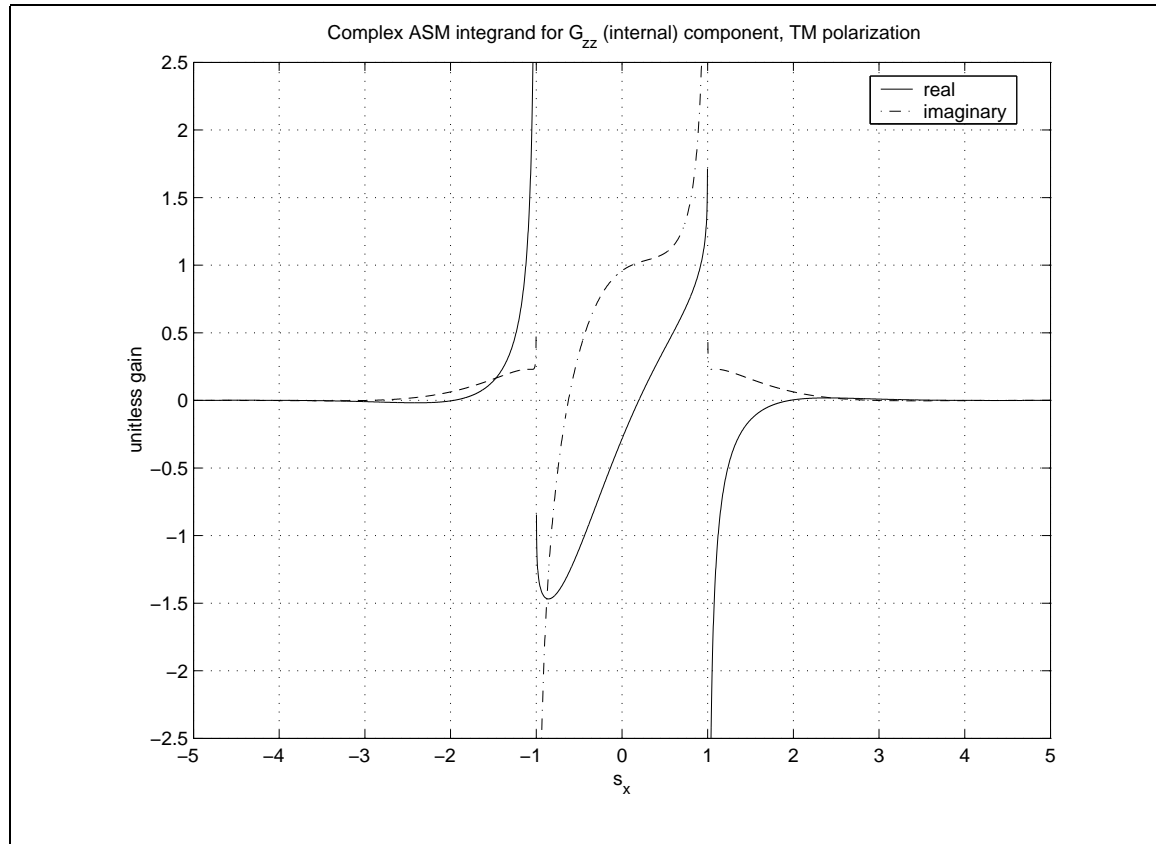


Figure 3.2 Source point at $(x', y') = (0, 0)$, field point at $(x, y) = (100, 40)$. Slab coating material thickness = 40, $\epsilon_r = 3.25$, $\mu_r = 2.0$.

Taking an approach similar to that in Chapter 2 when looking at the functional form of the reflection coefficients, we combine the scan parameter s_{x_1} and the ASM mode parameter n into a single variable, s_x (i.e., $s_x = (s_{x_1} + 2n)$). This s_x has the same relation as before to r_{x_1} in that

they are equivalent for the case of a lossless slab coating medium but differ by the factor $Re(k)/k$ when the slab material is lossy. We note that s_x ranges in Figure 3.2 from -5 to $+5$. This range is somewhat arbitrary and is chosen to demonstrate the decay of the function outside the ‘central region’ (the region $-1 \leq s_x \leq 1$) of the integrand function. This central region corresponds to the region where the plane wave mode parameter $n = 0$ and the scan angle parameter $s_{x_1} = s_x$. The range (or region) $-3 \leq s_x \leq -1$ corresponds to $n = -1$ and the region $1 \leq s_x \leq 3$ corresponds to $n = +1$ (s_{x_1} in both cases varies $-1 \leq s_{x_1} \leq 1$) and so on. In this manner, we see that s_x behaves as a continuous real variable.

It appears in Figure 3.2 that the most important features of the integrand occur in the central region and just immediately beyond it. The integrand has singularities at the upper and lower bounds of the central region, $s_x = \pm 1$. This is caused by the factor r_{y_1} becoming zero at precisely these points. Also at that point, r_{y_1} abruptly changes from a purely real-valued function to purely imaginary. This is a feature unique to the case of lossless slab coating materials. Beyond the central region, $|s_x| > 1$, the function decays very rapidly and there are no singularities.

We observe symmetry in the integrand function in Figure 3.2 in that the real part of the integrand is odd symmetric about $s_x = 0$ outside the central region while the imaginary part displays even symmetry. The function is not symmetric in the central region.

What happens to the integrand function when we add the loss component to the permeability of the slab coating material? With source and field points in the same location as in Figure 3.2, the ASM integrand for this case is shown in Figure 3.3. Figure 3.3 is plotted to the same scale used for Figure 3.2 to highlight the effects of lossy material parameters on the integrand function.

We immediately notice that the loss component of the permeability has caused the shape of the integrand function to be altered, removing the singularities in the function at $s_x = \pm 1$.¹ For cases where the slab coating material is lossy, the factor r_{y_1} is complex with a negative imaginary part for all values of s_x and there is no abrupt change in r_{y_1} going from pure real to pure imaginary. Finally, we notice the function outside the central region is not symmetric and decays at different rates on either side of the central region for increasing $|s_x|$.

¹The singularities have moved off the real s_x axis

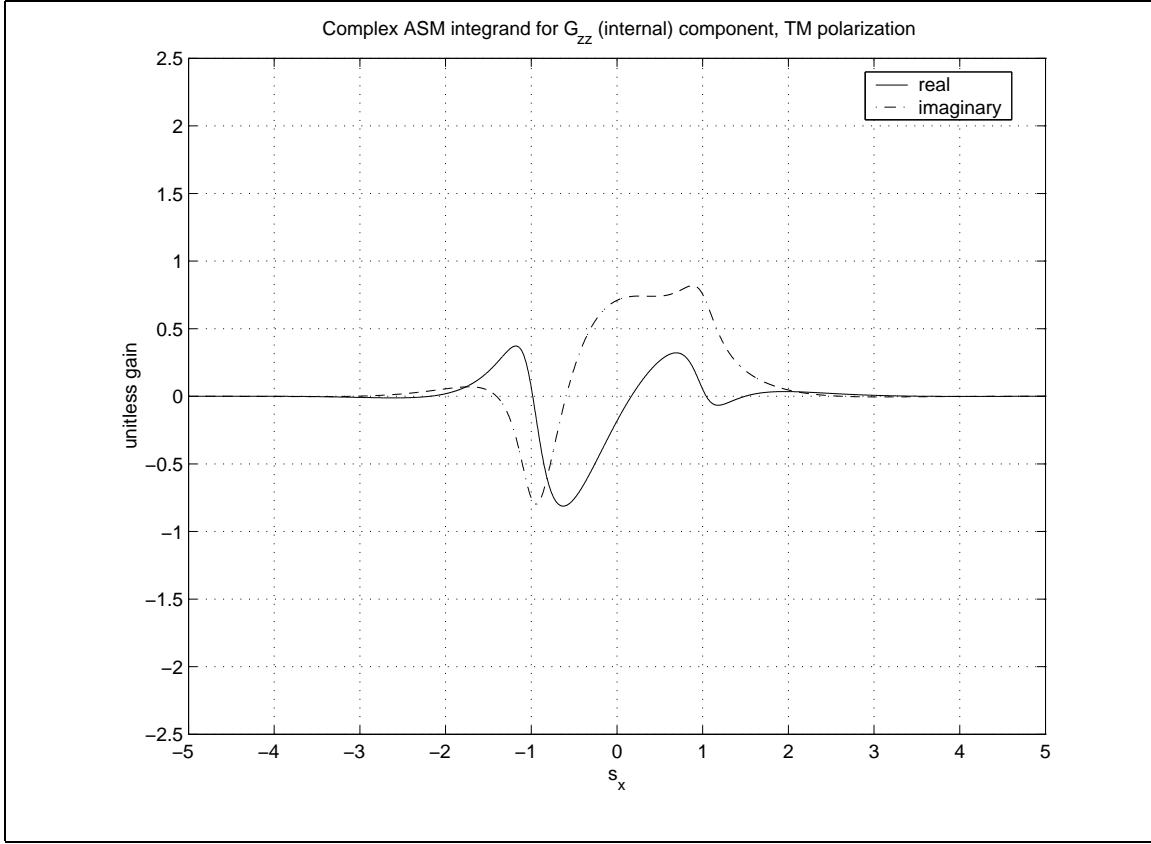


Figure 3.3 Source point at $(x', y') = (0, 0)$, field point at $(x, y) = (100, 40)$. Slab coating material thickness = 40, $\epsilon_r = 3.25$, $\mu_r = 2 - j1$.

Looking now at the behavior of the G_{zz} integrand function for TE polarization, we plot the function for the case of a lossless magneto-dielectric slab coating material having $\epsilon_r = 3.25$ and $\mu_r = 2$. This case is plotted in Figure 3.4. The first impression is that this integrand function is much more complicated than that seen in the lossless material case for TM polarization. Strong singularities are present at $|s_x| = 1$ and at the critical angles (having values $s_c = \pm 0.3922$ for these material property values). The singularities at $|s_x| = 1$ are again caused by the r_{y1} going to zero at those points. The singularities at the critical angles arise from the factor r_{y0} vanishing (and abruptly changing from purely real to purely imaginary) at those points, in the reflection coefficient for TE polarization in Equation (2.54).

For the lossy material case ($\mu_r = 2 - j1$), Figure 3.5, we again see strong singularities at the critical angles but the singularities at $|s_x| = 1$ are removed from the real s_x axis since the factor r_{y1} for this case is complex. The singularities at the critical angles remain, however, because the factor

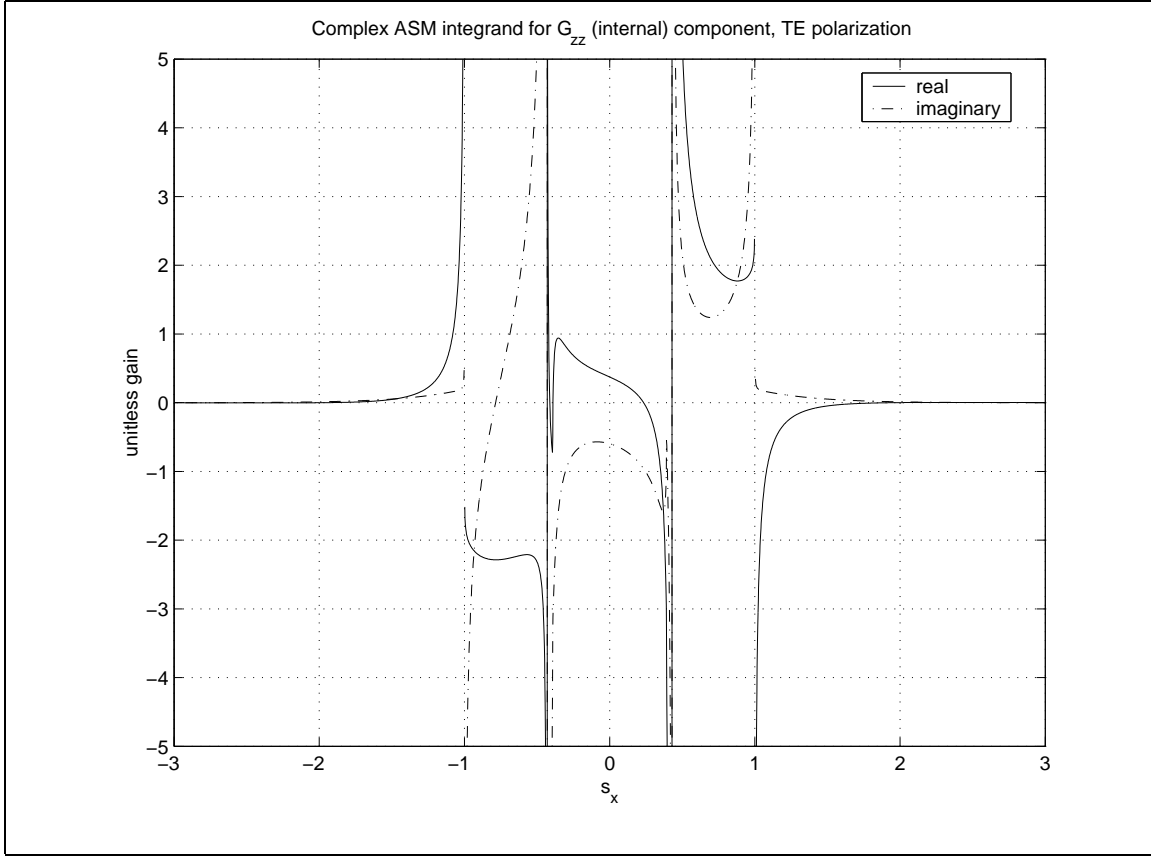


Figure 3.4 Source point at $(x', y') = (0, 0)$, field point at $(x, y) = (100, 40)$. Slab coating material thickness = 40, $\epsilon_r = 3.25$, $\mu_r = 2.0$.

r_{y_o} still vanishes and exhibits the abrupt change from real to imaginary at the critical angles. As was seen in Figure (2.4), r_{y_o} is either pure real or pure imaginary, abruptly changing at the location of the critical angles, and is independent of any loss components in the slab coating material. As was discussed in Chapter 2, the reflection coefficient and T-factors for TE polarization are more sensitive to this change in r_{y_o} .

In summarizing this section, it is readily apparent that numerical integration of these integrand functions will be difficult. For the cases presented here, there is in general no symmetry in the integrand functions that could be exploited to accelerate the numerical integration process. For the lossless materials, integration along the real s_x axis will require the avoidance of strong singularities, especially in the case of TE polarization.

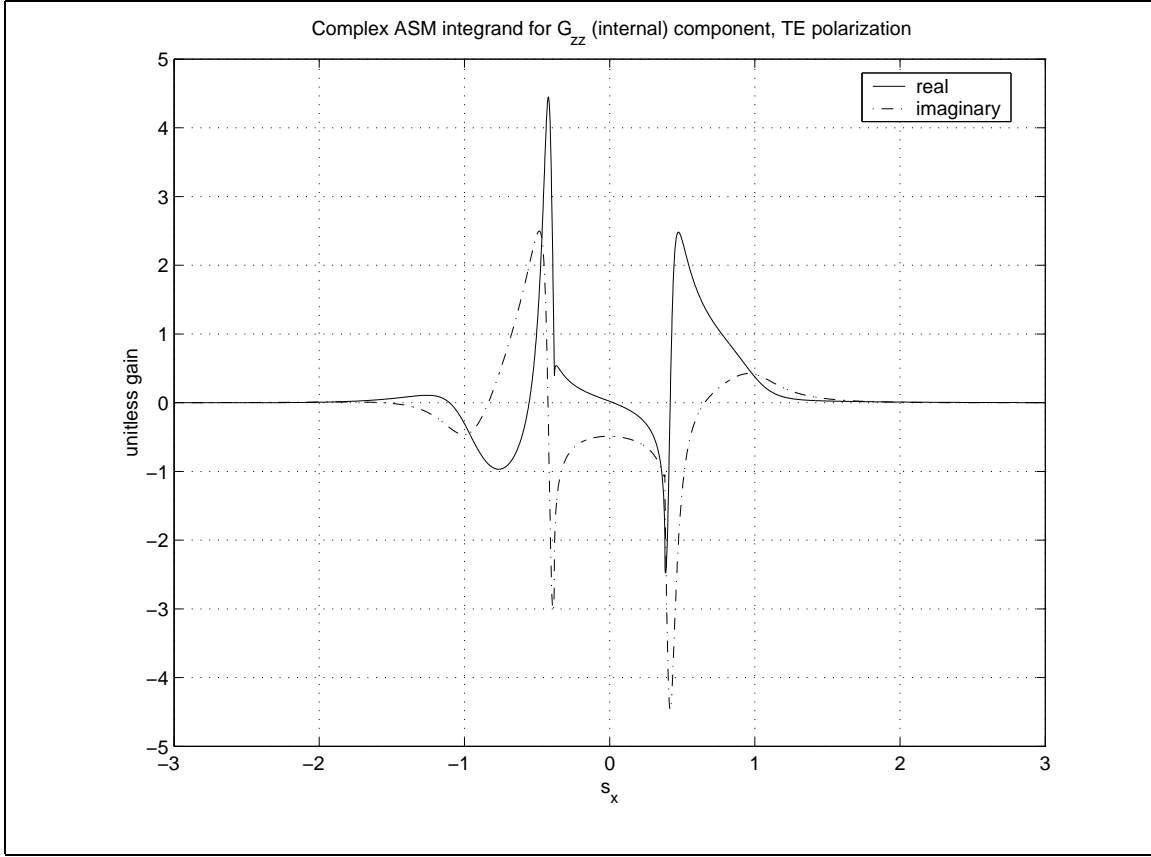


Figure 3.5 Source point at $(x', y') = (0, 0)$, field point at $(x, y) = (100, 40)$. Slab coating material thickness = 40, $\epsilon_r = 3.25$, $\mu_r = 2 - j1$.

3.1.2 Integrands Functions for Dyadic Green's Function Components. So far, we have briefly examined only integrand functions occurring in the canonical Green's function term G_{zz} , Equation (3.1). We look now at other integrand functions arising in the matrix representation of the dyadic Green's function expression of Equation (2.17). The final form of the bounce correction component expressions were identified in Equations (2.43) - (2.50) for G_{xx} , G_{xy} , G_{xz} , G_{yy} , and G_{yz} .

We will use the same lossless material property values used in the previous section for the canonical Green's function term, noting that the lossless material property cases present the greatest challenge for numerical integration. Also, recall that we need look at only the five additional integrand functions specified above since $G_{xy} = G_{yx}$, $G_{zx} = -G_{xz}$, and $G_{zy} = -G_{yz}$, for both polarization cases.

Again choosing the frequency to be 11.8 GHz, plots for several examples of these component integrand functions are shown in Figures 3.6 through 3.11. Additional integrand function plots for

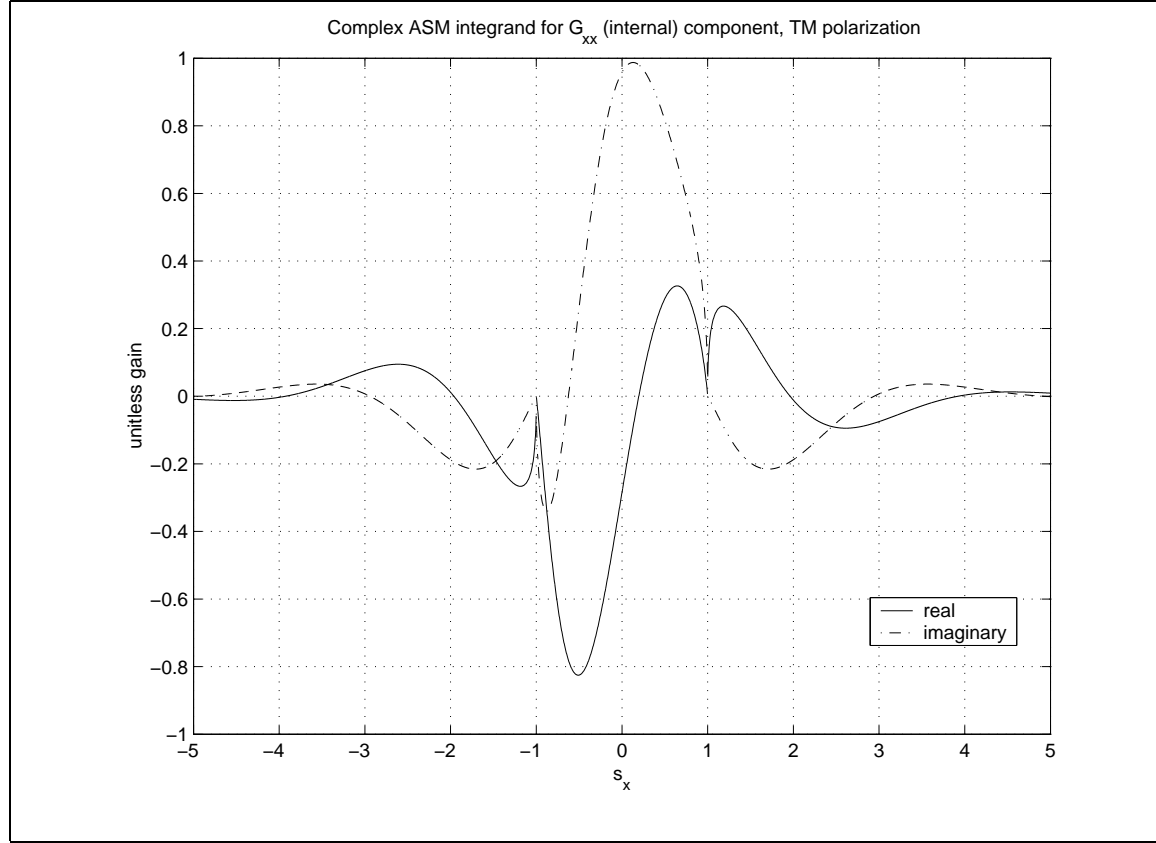


Figure 3.6 Source point at $(x', y') = (0, 0)$, field point at $(x, y) = (100, 40)$. Slab coating material thickness = 40, $\epsilon_r = 3.25$, $\mu_r = 2.0$.

these Green's function components are included in Appendix C.

In Figure 3.6, the integrand function for the G_{xx} bounce correction term for TM polarization is plotted. From Equation (2.43), the expression for this term is

$$G_{bounce, xx} = \frac{jRe(k_1)}{4\pi k_1} \int_{-1}^1 \sum_{n=-\infty}^{\infty} Tr_{y_1} e^{-jk_1[(x-x')r_{x1} + |y-y'|r_{y1}]} ds_{x1}$$

We see in the figure that singularities occur at $|s_x| = 1$ due to the factor r_{y1} vanishing at precisely these points. As in the case of G_{zz} for lossless material, the real part of the integrand function exhibits odd symmetry outside the central region while the imaginary part exhibits even symmetry, but no symmetry is observed in the central region. Comparing Figure 3.6 to Figure 3.2, an interest-

ing and important difference between the G_{xx} and G_{zz} integrand function behavior is the slower rate of decay of the G_{xx} integrand function for increasing $|s_x|$. Whereas integration of G_{zz} in the region $5 \leq |s_x| \leq 3$ would yield a result of approximately zero, such is obviously not the case for G_{xx} , and higher order plane wave modes (modes $|n| > 1$) make a non-trivial contribution to the value of the integral.

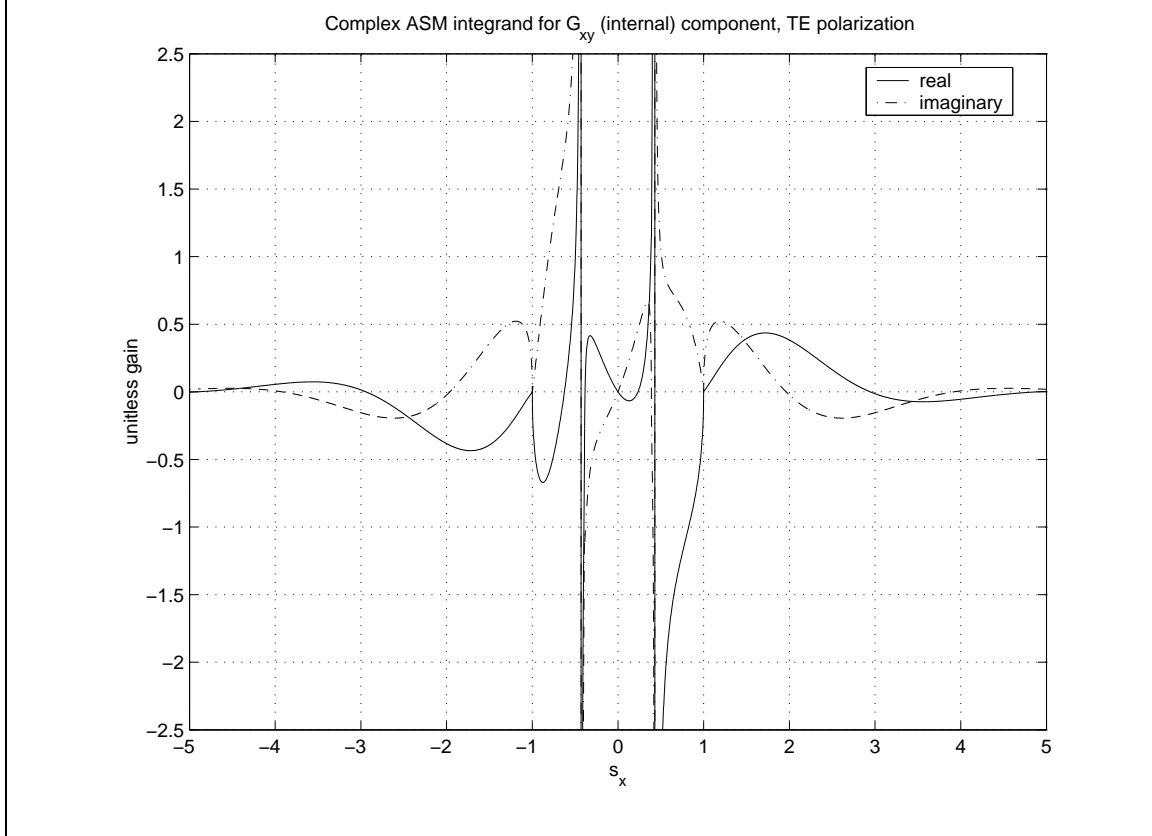


Figure 3.7 Source point at $(x', y') = (0, 0)$, field point at $(x, y) = (100, 40)$. Slab coating material thickness = 40, $\epsilon_r = 3.25$, $\mu_r = 2.0$.

In Figure 3.7 is shown the bounce correction integrand function for G_{xy} for TE polarization. This expression, given earlier as part of Equation (2.44), is

$$G_{bounce, xy} = -\frac{jRe(k_1)}{4\pi k_1} \int_{-1}^1 \sum_{n=-\infty}^{\infty} T^r r_{x1} e^{-jk_1[(x-x')r_{x1} + |y-y'|r_{y1}]} ds_{x1}$$

For the TE polarization, lossless material case, we again observe strong singularities at the critical angles. Singularities are also observed at $|s_x| = 1$ and a slow rate of decay of the function outside

the central region implies that additional plane wave modes will have to be included in the integral for the most accurate results.

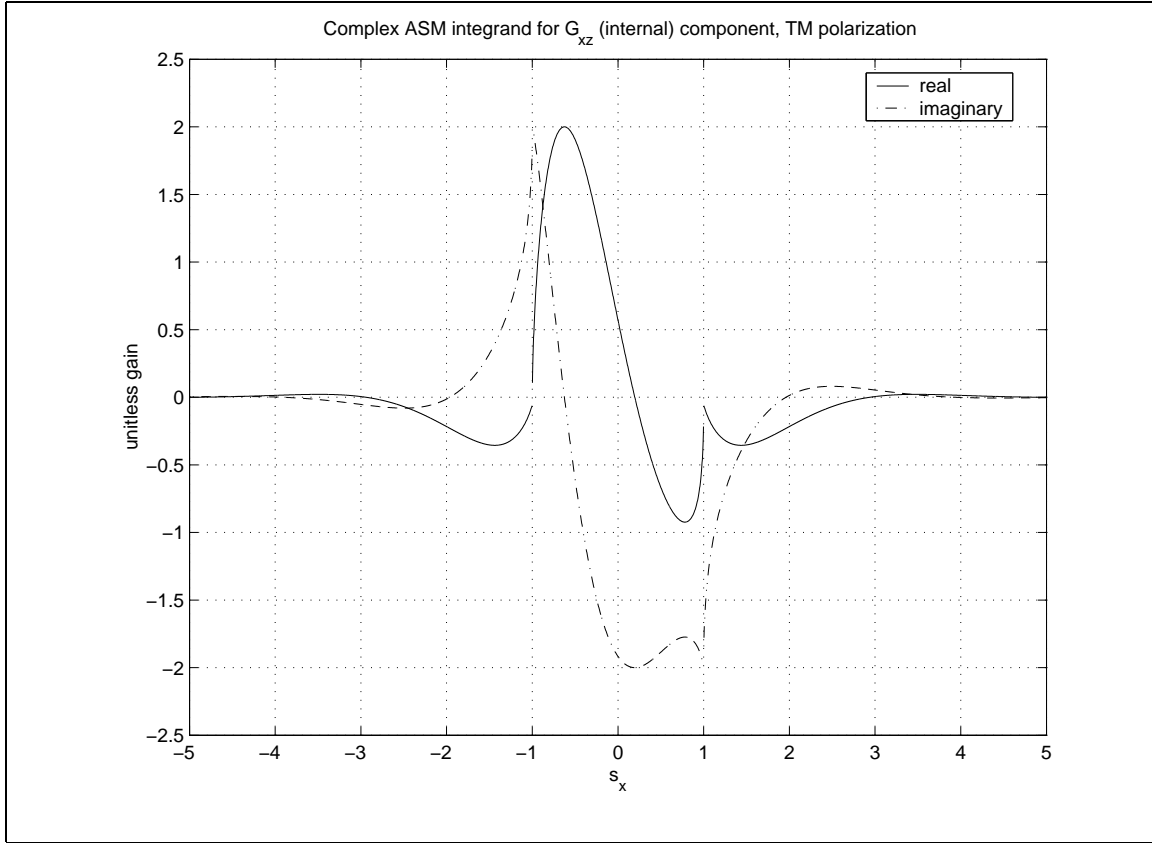


Figure 3.8 Source point at $(x', y') = (0, 0)$, field point at $(x, y) = (100, 40)$. Slab coating material thickness = 40, $\epsilon_r = 3.25$, $\mu_r = 2.0$.

Figure 3.8 is a plot of the integrand function for the G_{xz} Green's function term. This expression, from Equation (2.45), is

$$G_{bounce, xz} = \frac{Re(k_1)}{4\pi} \int_{-1}^1 \sum_{n=-\infty}^{\infty} T^r e^{-jk_1[(x-x')r_{x1} + |y-y'|r_{y1}]} ds_{x1}$$

Again for this case, singularities at $|s_x| = 1$ are observed. Interestingly, this plot exhibits even symmetry for the real part of the integrand function outside the central region and odd symmetry for the imaginary part.

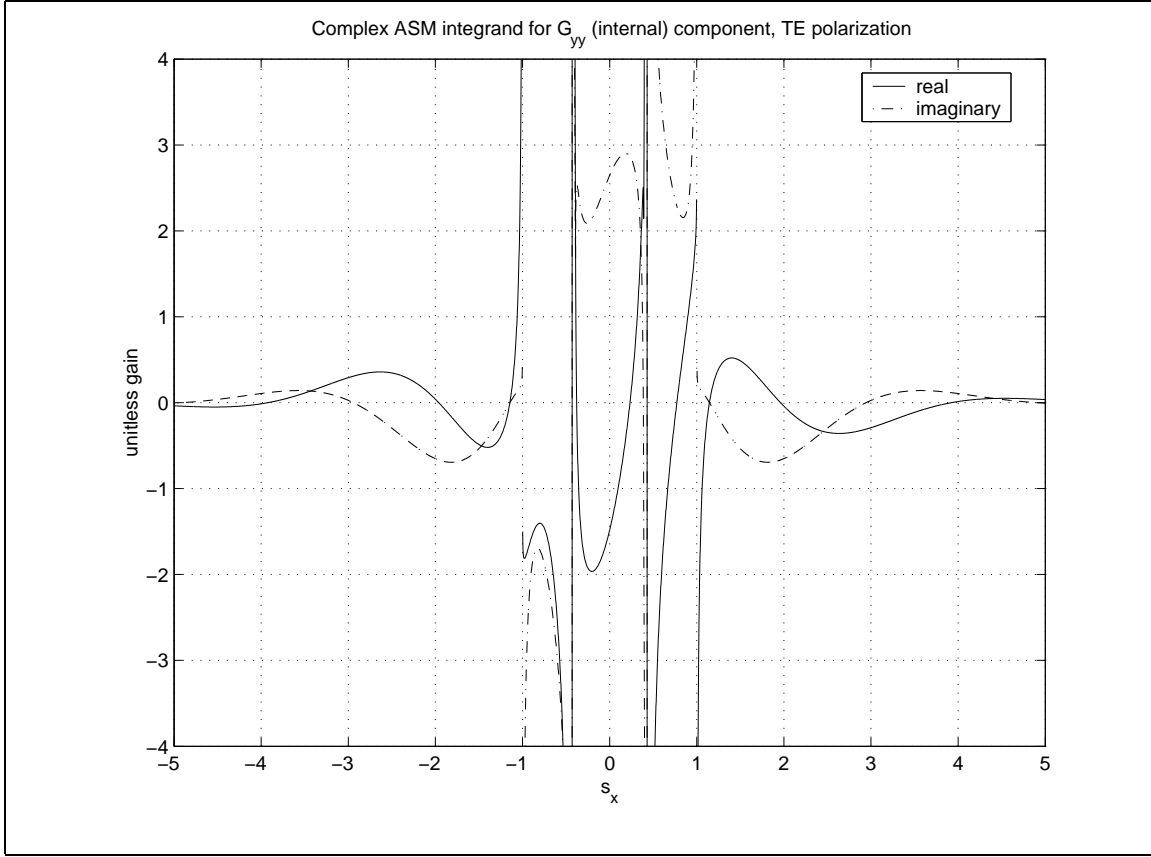


Figure 3.9 Source point at $(x', y') = (0, 0)$, field point at $(x, y) = (100, 40)$. Slab coating material thickness = 40, $\epsilon_r = 3.25$, $\mu_r = 2.0$.

In Figure 3.9, the integrand function for the G_{yy} bounce correction term for TE polarization is plotted. From Equation (2.47), this rather complicated expression is

$$G_{bounce, yy} = -\frac{jRe(k_1)}{4\pi k_1} \int_{-1}^1 \sum_{n=-\infty}^{\infty} \left[\frac{T}{r_{y1}} + 2r_{y1}T^r \right] e^{-jk_1[(x-x')r_{x1} + |y-y'|r_{y1}]} ds_{x1}$$

Strong singularities are observed at the critical angles and at $|s_x| = 1$. Even symmetry in the imaginary part of the function and odd symmetry in the real part is seen outside the central region, as well as a slow decay in the function again implying that higher order plane wave modes contribute to the integral.

The austere appearance of the G_{yy} integrand function for TE polarization in Figure 3.9 may perhaps raise one's curiosity about the nature of the G_{yy} integrand function for TM polarization. How does a change in polarization affect the behavior of this integrand function when all other

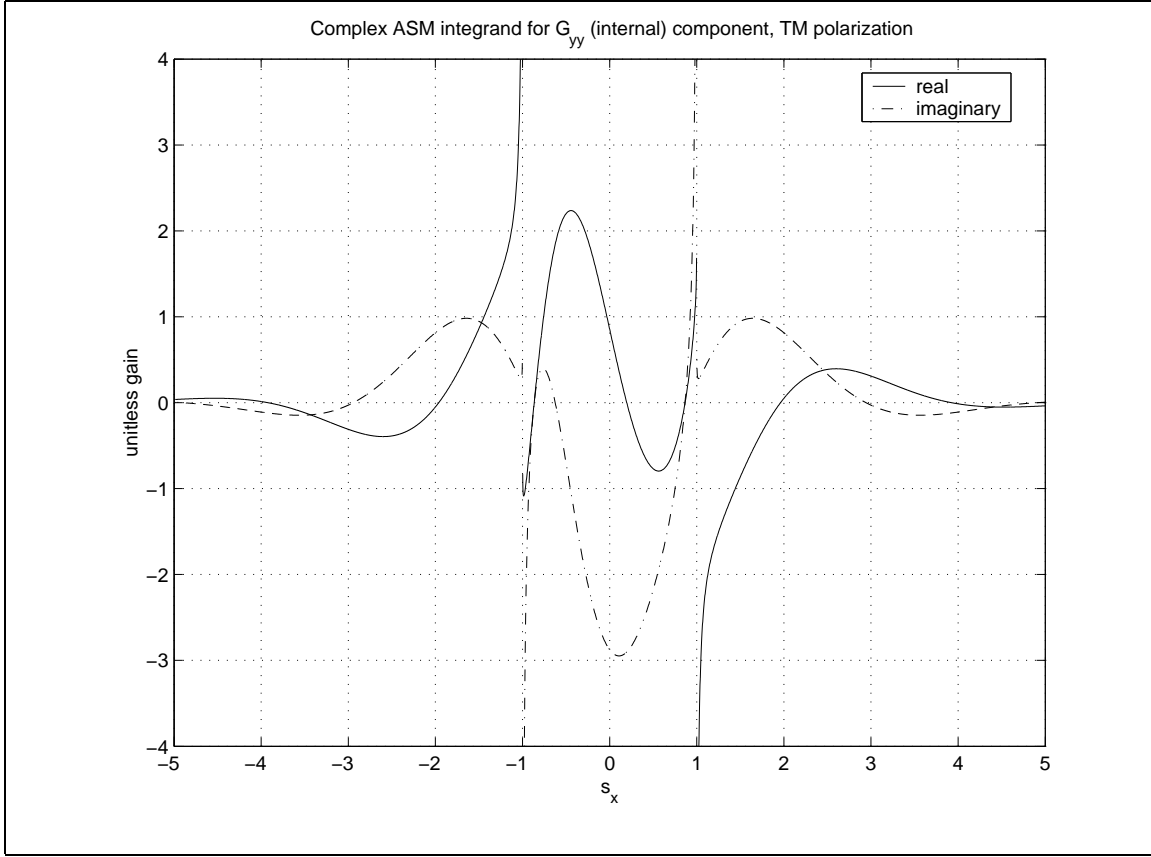


Figure 3.10 Source point at $(x', y') = (0, 0)$, field point at $(x, y) = (100, 40)$. Slab coating material thickness = 40, $\epsilon_r = 3.25$, $\mu_r = 2.0$.

parameters remain the same? In Figure 3.10 is a plot (using the same scale) of the G_{yy} term for TM polarization. We see the singularities at $|s_x| = 1$ are still present but the singularities at the critical angles are not. The symmetry characteristics and decay rates of the functions are similar. Judging from appearances, however, numerical integration of the function for TM polarization should be somewhat less difficult.

The final case we examine here is for the G_{zy} integrand function. For TE polarization, this function is plotted in Figure 3.11. The expression was given in Equation (2.50), and is

$$G_{bounce, zy} = -\frac{Re(k_1)}{4\pi} \int_{-1}^1 \sum_{n=-\infty}^{\infty} T \frac{r_{x1}}{r_{y1}} e^{-jk_1[(x-x')r_{x1} + |y-y'|r_{y1}]} ds_{x1}$$

Again, strong singularities are in evidence at the critical angles and at $|s_x| = 1$. For this function, the real part displays even symmetry outside the central region while the imaginary part displays

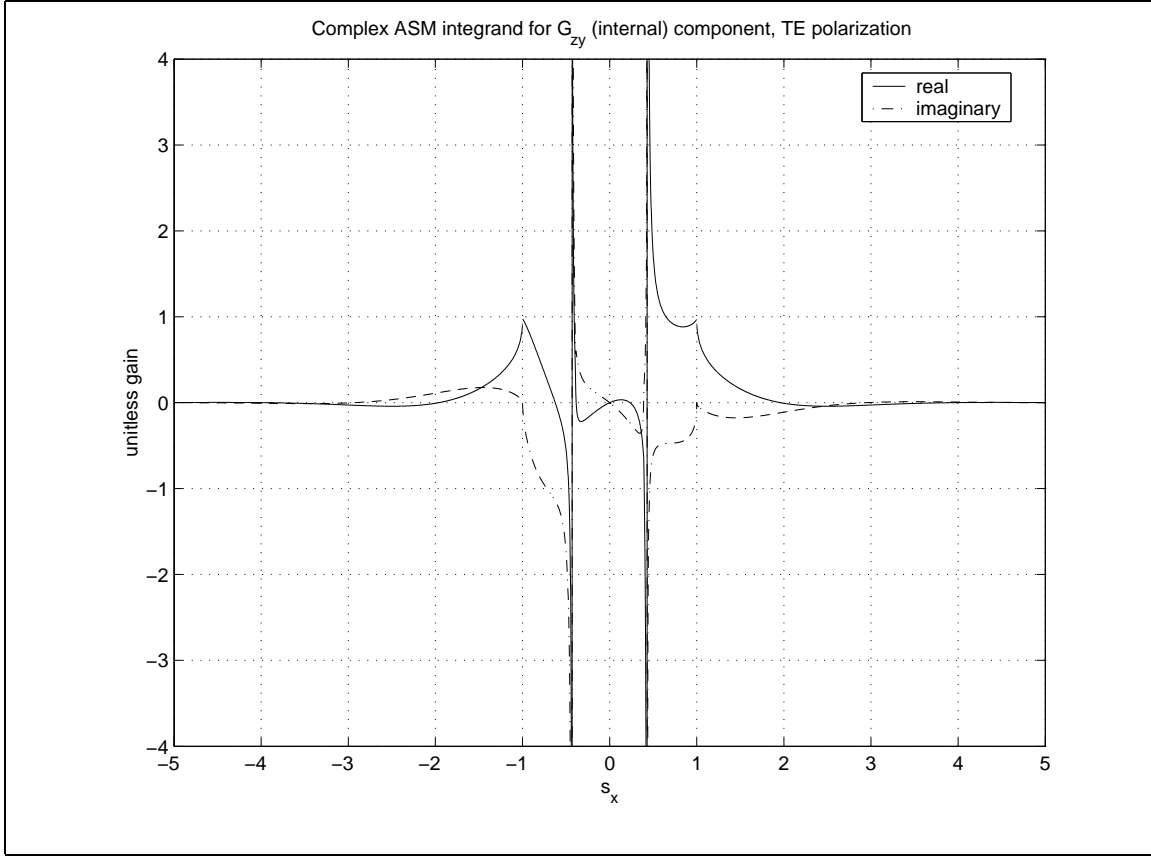


Figure 3.11 Source point at $(x', y') = (0, 0)$, field point at $(x, y) = (100, 40)$. Slab coating material thickness = 40, $\epsilon_r = 3.25$, $\mu_r = 2.0$.

odd symmetry. Also outside the central region, the function decays almost as rapidly as the G_{zz} function as seen in Figure 3.4.

From the figures shown in this section, we see a number of similarities in the behavior of these various Green's function integrands compared to the canonical term. Numerical integration of these terms must accommodate the singularities seen at the critical angles and at $|s_x| = 1$ in cases of lossless slab coating material. We also see that some of these integrands decay at different rates outside the central region, sometimes much more slowly than in the case of the G_{zz} Green's function. The rate of decay of these integrand functions directly impacts the number of ASM modes which must be included in the integration to obtain an accurate result. To be most efficient, we wish to integrate over as few modes as necessary.

3.1.3 Summary. In summary, the numerical integration of the ASM-derived Green's function bounce correction terms must be performed very carefully for lossless slab coating material cases. For lossy material cases, the TM polarization integrand functions are not as difficult but the TE polarization integrand functions still present singularities at the critical angles. In order to keep the number of function evaluations to a minimum, and to efficiently handle the wide variety of function shapes—ranging from the singular lossless material cases to the smooth, continuous lossy material cases—the integration algorithm should be adaptive. It is also desirable that the integration routine provide a means to evaluate the integrals to within some error tolerance value.

To this end, a recursive adaptive Simpson's rule algorithm available in version 6 of the Matlab® commercial software package is used to evaluate these integrand functions. This routine, though not a true open end formula, checks for infinities located at the end points of the integration range and adjusts the end points if an infinity is found. The integrand functions are subdivided, with breaks occurring at $s_x = \pm s_c$ and $s_x = \pm 1$, and fed sequentially to the integration algorithm resulting in multiple calls to the subroutine for each integral expression evaluated. In essence, we are employing the algorithm referred to as Method I in Section 6.2 of Isaacson and Keller, [39], then breaking the range of integration at points where a singularity can be expected to occur, as in Section 6.1 of [39].

3.2 Moment Method Solution

We have seen now that the ASM-derived bounce correction terms of the internal Green's function expressions will be difficult to numerically integrate. Since a recursive adaptive algorithm may require several iterations to converge to a solution, it is desirable to minimize the number of times these integrals need be evaluated. In the Method of Moments, the pulse basis expansion - delta function testing approach, also known as point matching, will require the minimum number of function evaluations. This statement is based on the fact that the pulse basis expansion function becomes a constant unknown coefficient in each moment method cell. And with the delta function testing, we utilize the sifting property of the delta function to greatly simplify the evaluation of the resulting integrals.

In Section 1.4.1 a brief overview of the solution procedure was presented culminating in Equations (1.16) through (1.21), which expanded the unknown equivalent volume currents into

pulse basis functions and unknown expansion coefficients. We pick up the Moment Method solution from that point, presenting the details of the solution procedure for both TM and TE polarization cases.

3.2.1 TM Polarization. Beginning with the TM polarization case, we substitute the pulse basis equivalent currents into the coupling matrix of Equation (2.22) and the ΔZ matrix of Equation (2.24). This produces the set of coupled equations,

$$\begin{aligned} H_x^i = & j\omega\epsilon_r \iint_{V_{gap}} G_{xx} \sum_{n=1}^N d_{xn} P_n^M dV_{gap} + j\omega\epsilon_r \iint_{V_{gap}} G_{xy} \sum_{n=1}^N d_{yn} P_n^M dV_{gap} \\ & - \iint_{V_{gap}} G_{xz} \sum_{n=1}^N c_n P_n^J dV_{gap} + \frac{\sum_{n=1}^N d_{xn} P_n^M}{j\omega(\mu_g - \mu_r)} \end{aligned} \quad (3.2)$$

$$\begin{aligned} H_y^i = & j\omega\epsilon_r \iint_{V_{gap}} G_{yx} \sum_{n=1}^N d_{xn} P_n^M dV_{gap} + j\omega\epsilon_r \iint_{V_{gap}} G_{yy} \sum_{n=1}^N d_{yn} P_n^M dV_{gap} \\ & - \iint_{V_{gap}} G_{yz} \sum_{n=1}^N c_n P_n^J dV_{gap} + \frac{\sum_{n=1}^N d_{yn} P_n^M}{j\omega(\mu_g - \mu_r)} \end{aligned} \quad (3.3)$$

$$\begin{aligned} E_z^i = & \iint_{V_{gap}} G_{zx} \sum_{n=1}^N d_{xn} P_n^M dV_{gap} + \iint_{V_{gap}} G_{zy} \sum_{n=1}^N d_{yn} P_n^M dV_{gap} \\ & + j\omega\mu_r \iint_{V_{gap}} G_{zz} \sum_{n=1}^N c_n P_n^J dV_{gap} + \frac{\sum_{n=1}^N c_n P_n^J}{j\omega(\epsilon_g - \epsilon_r)} \end{aligned} \quad (3.4)$$

in which the d_{xn} , d_{yn} and c_n are the unknown expansion coefficients to be determined.

We want to be more specific at this point in defining some of our symbols and notation. While the Green's function terms are each a combination of a spatial domain term (the direct, free space Hankel function components) and the spectral domain term (the ASM-derived bounce correction components), the spatial dependence of each has always been the variables $(x, y; x', y')$. The integration variables denoted by the differential term, dV_{gap} , are the source (primed) coordinate variables, i.e., $dV_{gap} = dx' dy'$, where the range of integration is constrained to the gap region geometry. We also recall the definition of the terms P_n^J and P_n^M , given in Equations (1.18) and (1.19), as that of being the inverse of the subcell area, A_n , which will be a constant in each integral. We can now exchange the order of summation and integration in Equations (3.2) – (3.4) and rewrite them in a simplified manner by extracting the various constants that have been introduced.

Further simplification (or at least, a more compact notation) is achieved by introducing an operator notation to represent the common integration operations. To this end, we define

$$L_{\alpha\beta}(P_n^{J,M}) = \frac{1}{A_n} \iint_{\text{cell}_n} G_{\alpha\beta}(x, y; x', y') dx' dy' \quad (3.5)$$

and now rewrite Equations (3.2) - (3.4) as

$$H_x^i = \sum_{n=1}^N \left[j\omega\epsilon_r d_{xn} L_{xx}(P_n^M) + j\omega\epsilon_r d_{yn} L_{xy}(P_n^M) - c_n L_{xz}(P_n^J) + \frac{d_{xn} P_n^M}{j\omega(\mu_g - \mu_r)} \right] \quad (3.6)$$

$$H_y^i = \sum_{n=1}^N \left[j\omega\epsilon_r d_{xn} L_{yx}(P_n^M) + j\omega\epsilon_r d_{yn} L_{yy}(P_n^M) - c_n L_{yz}(P_n^J) + \frac{d_{yn} P_n^M}{j\omega(\mu_g - \mu_r)} \right] \quad (3.7)$$

$$E_z^i = \sum_{n=1}^N \left[d_{xn} L_{zx}(P_n^M) + d_{yn} L_{zy}(P_n^M) + j\omega\mu_r c_n L_{zz}(P_n^J) + \frac{c_n P_n^J}{j\omega(\epsilon_g - \epsilon_r)} \right] \quad (3.8)$$

The next step in the moment method procedure is to introduce a testing function which is used to form an inner product with the pulse basis expansion set shown in Equations (3.6) - (3.8). For our inner product we will use the symmetric product,

$$\langle f, g \rangle = \iiint_V f \cdot g dV$$

[26] where $dV = dx dy$. Calling our testing function θ_m (where $m = 1, 2, 3, \dots N$) we write,

$$\begin{aligned} \langle H_x^i, \theta_m \rangle &= \sum_{n=1}^N \left[j\omega\epsilon_r d_{xn} \langle L_{xx}(P_n^M), \theta_m \rangle + j\omega\epsilon_r d_{yn} \langle L_{xy}(P_n^M), \theta_m \rangle \right. \\ &\quad \left. - c_n \langle L_{xz}(P_n^J), \theta_m \rangle + \frac{d_{xn}}{j\omega(\mu_g - \mu_r)} \langle P_n^M, \theta_m \rangle \right] \end{aligned} \quad (3.9)$$

$$\begin{aligned} \langle H_y^i, \theta_m \rangle &= \sum_{n=1}^N \left[j\omega\epsilon_r d_{xn} \langle L_{yx}(P_n^M), \theta_m \rangle + j\omega\epsilon_r d_{yn} \langle L_{yy}(P_n^M), \theta_m \rangle \right. \\ &\quad \left. - c_n \langle L_{yz}(P_n^J), \theta_m \rangle + \frac{d_{yn}}{j\omega(\mu_g - \mu_r)} \langle P_n^M, \theta_m \rangle \right] \end{aligned} \quad (3.10)$$

$$\langle E_z^i, \theta_m \rangle = \sum_{n=1}^N \left[d_{xn} \langle L_{zx}(P_n^M), \theta_m \rangle + d_{yn} \langle L_{zy}(P_n^M), \theta_m \rangle \right]$$

$$\left. + j\omega\mu_r c_n < L_{zz}(P_n^J), \theta_m > + \frac{c_n}{j\omega(\epsilon_g - \epsilon_r)} < P_n^J, \theta_m > \right] \quad (3.11)$$

For our problem we will choose the testing functions to be delta functions located at the center of each volumetric subcell of the discretized gap region (recall Figure 1.8). With this testing function, defined as $\theta_m = \delta(x - x_m)\delta(y - y_m)$ and where (x_m, y_m) are the locations of the centers of the volumetric subcells, we can employ the sifting property of the delta function to greatly simplify our set of equations. On the left hand side, where each incident field component carries an implicit (x, y) functional dependence, each term is now evaluated at each of the N centers comprising the gap region, e.g., $< E_z^i, \theta_m > = E_z^i(x_m, y_m)$. On the right hand side, the operator terms become

$$< L_{\alpha\beta}(P_n^{J,M}), \theta_m > = \frac{1}{A_n} \iint_{\text{cell } n} G_{\alpha\beta}(x_m, y_m; x', y') dx' dy' \quad (3.12)$$

where, in this instance, (x', y') are the coordinates associated with volumetric source cell n . We will discuss later how this equation is solved for various cases depending on how close the field (x, y) and source (x', y') points are to one another. Finally, the ΔZ matrix terms, after substituting, for example, $P_n^J = 1/A_n$ become,

$$\frac{c_n < 1, \theta_m >}{j\omega A_n(\epsilon_g - \epsilon_r)} = \frac{c_n \delta_{mn}}{j\omega A_n(\epsilon_g - \epsilon_r)}$$

where δ_{mn} is the Kronecker delta,

$$\delta_{mn} = \begin{cases} 1, & m = n \\ 0, & m \neq n \end{cases}$$

This implies that the ΔZ matrix terms only occur on the diagonal of the ΔZ matrix and therefore, only modify the self impedance terms of the G_{xx} , G_{yy} , and G_{zz} blocks of the full impedance matrix.

3.2.2 *TE Polarization.* This is the dual of the TM Polarization case. We can write equations analogous to Equations (3.2) - (3.4),

$$E_x^i = j\omega\mu_r \iint_{V_{gap}} G_{xx} \sum_{n=1}^N d_{xn} P_n^J dV_{gap} + j\omega\mu_r \iint_{V_{gap}} G_{xy} \sum_{n=1}^N d_{yn} P_n^J dV_{gap} + \iint_{V_{gap}} G_{xz} \sum_{n=1}^N c_n P_n^M dV_{gap} + \frac{\sum_{n=1}^N d_{xn} P_n^J}{j\omega(\epsilon_g - \epsilon_r)} \quad (3.13)$$

$$E_y^i = j\omega\mu_r \iint_{V_{gap}} G_{yx} \sum_{n=1}^N d_{xn} P_n^J dV_{gap} + j\omega\mu_r \iint_{V_{gap}} G_{yy} \sum_{n=1}^N d_{yn} P_n^J dV_{gap} + \iint_{V_{gap}} G_{yz} \sum_{n=1}^N c_n P_n^M dV_{gap} + \frac{\sum_{n=1}^N d_{yn} P_n^J}{j\omega(\epsilon_g - \epsilon_r)} \quad (3.14)$$

$$H_z^i = - \iint_{V_{gap}} G_{zx} \sum_{n=1}^N d_{xn} P_n^J dV_{gap} - \iint_{V_{gap}} G_{zy} \sum_{n=1}^N d_{yn} P_n^J dV_{gap} + j\omega\epsilon_r \iint_{V_{gap}} G_{zz} \sum_{n=1}^N c_n P_n^M dV_{gap} + \frac{\sum_{n=1}^N c_n P_n^M}{j\omega(\mu_g - \mu_r)} \quad (3.15)$$

and use the definition in Equation (3.5) to write

$$E_x^i = \sum_{n=1}^N \left[j\omega\mu_r d_{xn} L_{xx}(P_n^J) + j\omega\mu_r d_{yn} L_{xy}(P_n^J) + c_n L_{xz}(P_n^M) + \frac{d_{xn} P_n^J}{j\omega(\epsilon_g - \epsilon_r)} \right] \quad (3.16)$$

$$E_y^i = \sum_{n=1}^N \left[j\omega\mu_r d_{xn} L_{yx}(P_n^J) + j\omega\mu_r d_{yn} L_{yy}(P_n^J) + c_n L_{yz}(P_n^M) + \frac{d_{yn} P_n^J}{j\omega(\epsilon_g - \epsilon_r)} \right] \quad (3.17)$$

$$H_z^i = \sum_{n=1}^N \left[-d_{xn} L_{zx}(P_n^J) - d_{yn} L_{zy}(P_n^J) + j\omega\epsilon_r c_n L_{zz}(P_n^M) + \frac{c_n P_n^M}{j\omega(\mu_g - \mu_r)} \right] \quad (3.18)$$

analogous to Equations (3.6) - (3.8). Using the same inner product and testing function definitions used for TM polarization, applying the moment method procedure we can write

$$\begin{aligned} \langle E_x^i, \theta_m \rangle &= \sum_{n=1}^N \left[j\omega\mu_r d_{xn} \langle L_{xx}(P_n^J), \theta_m \rangle + j\omega\mu_r d_{yn} \langle L_{xy}(P_n^J), \theta_m \rangle \right. \\ &\quad \left. + c_n \langle L_{xz}(P_n^M), \theta_m \rangle + \frac{d_{xn} \delta_{mn}}{j\omega A_n(\epsilon_g - \epsilon_r)} \right] \end{aligned} \quad (3.19)$$

$$\langle E_y^i, \theta_m \rangle = \sum_{n=1}^N \left[j\omega\mu_r d_{xn} \langle L_{yx}(P_n^J), \theta_m \rangle + j\omega\mu_r d_{yn} \langle L_{yy}(P_n^J), \theta_m \rangle \right]$$

$$+ c_n < L_{yz}(P_n^M), \theta_m > + \frac{d_{yn}\delta_{mn}}{j\omega A_n(\epsilon_g - \epsilon_r)} \Big] \quad (3.20)$$

$$\begin{aligned} < H_z^i, \theta_m > = \sum_{n=1}^N \left[-d_{xn} < L_{zx}(P_n^J), \theta_m > -d_{yn} < L_{zy}(P_n^J), \theta_m > \right. \\ & \quad \left. + j\omega\epsilon_r c_n < L_{zz}(P_n^M), \theta_m > + \frac{c_n\delta_{mn}}{j\omega A_n(\mu_g - \mu_r)} \right] \end{aligned} \quad (3.21)$$

analogous to Equations (3.9) - (3.11).

3.3 Evaluation of Moment Method Expressions

Successful computation with the expressions developed in the previous section for either polarization is dependent on accurate evaluation of the various operator terms represented by Equation (3.12). As is typical in most moment method implementations, we will perform this evaluation somewhat differently depending on the relative location of the source and receiver cells. We will look at three categories: distant terms, where the receiver is separated from the source cell by more than one cell width; adjacent terms where the receiver is located in a cell adjoining the source cell; and self terms, where the source and receiver are collocated inside a cell. Of the three categories, the most crucial to achieving highest computational accuracy is the self term. It is also the most difficult to evaluate due to singularities that arise in the direct coupling terms as spatial distances between source and receiver locations vanish. While we saw previously in this chapter that singularities occur in the ASM-derived bounce correction terms, these singularities were associated with spectral domain factors. While these spectral domain singularities were most pronounced for self term cases, no singularities occur in the bounce correction terms as a result of collocation of source and receiver in a self term.

3.3.1 Evaluation of Self Terms. The self terms of each of the operator expressions given earlier are integrals over the subcell area of the hybrid Green's function expressions developed in Chapter 2. These hybrid Green's functions are composed of the direct coupling component terms and bounce correction term derived from the ASM technique. We note from the bounce correction term expressions given in Chapter 2, and from the various plots of the ASM integrand functions presented earlier in this chapter, that the bounce correction terms do not suffer from any

singularities as a result of the coalescing of the source and receiver locations. These expressions remain finite even when the source and receiver points are collocated. The singularities observed in these integrand functions were the result of the spectral domain nature of these expressions. What remains now is to look at the direct coupling components in which we expect to encounter singularities as a result of the coalescence of source and receiver locations as these components were all seen to be various combinations of Hankel functions.

As was mentioned before, there exist open source literature routines for computing these Hankel functions, even with complex argument. We are speaking of the well known Amos sub-routines, developed at the Sandia National Laboratory a number of years ago [25]. This Bessel function computation package has been incorporated into Matlab® version 6. Thus, we need expend no effort in developing a routine of our own for computing the needed Hankel functions for this application. However, we will need to look at what is required to evaluate the self terms for the various Hankel functions contained in the Green's function expression components.

We will employ the circle extraction technique [30] to evaluate the self terms of the direct coupling expressions. The basic concept of the approach is depicted in Figure 3.12. To begin, we

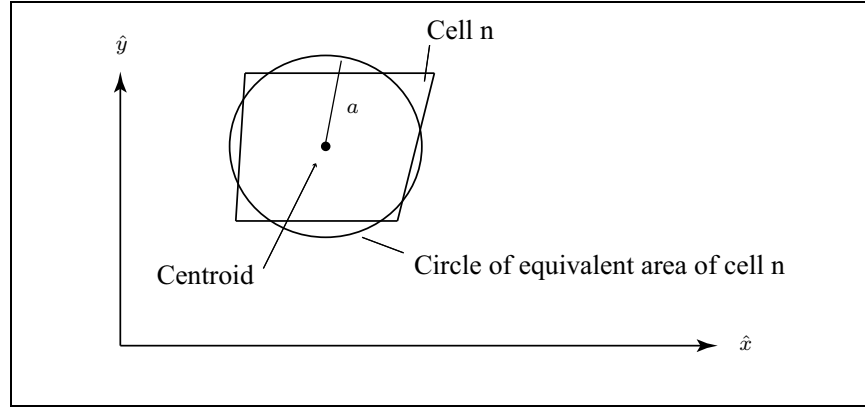


Figure 3.12 Circle Extraction Technique Computes the Self Term by Replacing the Moment Method Cell with a Circle of the Same Area

recast the direct coupling terms in Equations (2.43) - (2.51) into a cylindrical coordinate system with origin at the center of an arbitrary moment method cell such that $\rho' = 0$ (there is no loss in generality in doing this),

$$G_{xx,dc} = \frac{1}{4j} \left[H_o^{(2)}(k\rho) \sin^2(\phi) - \frac{H_1^{(2)}(k\rho)}{k\rho} \cos(2\phi) \right] \quad (3.22)$$

$$G_{xy,dc} = \frac{1}{4j} \cos(\phi) \sin(\phi) \left(2 \frac{H_1^{(2)}(k\rho)}{k\rho} - H_o^{(2)}(k\rho) \right) \quad (3.23)$$

$$G_{xz,dc} = -\frac{k}{4j} H_1^{(2)}(k\rho) \sin(\phi) \quad (3.24)$$

$$G_{yx,dc} = \frac{1}{4j} \cos(\phi) \sin(\phi) \left(2 \frac{H_1^{(2)}(k\rho)}{k\rho} - H_o^{(2)}(k\rho) \right) \quad (3.25)$$

$$G_{yy,dc} = \frac{1}{4j} \left[H_o^{(2)}(k\rho) \cos^2(\phi) - \frac{H_1^{(2)}(k\rho)}{k\rho} \cos(2\phi) \right] \quad (3.26)$$

$$G_{yz,dc} = \frac{k}{4j} H_1^{(2)}(k\rho) \cos(\phi) \quad (3.27)$$

$$G_{zx,dc} = \frac{k}{4j} H_1^{(2)}(k\rho) \sin(\phi) \quad (3.28)$$

$$G_{zy,dc} = -\frac{k}{4j} H_1^{(2)}(k\rho) \cos(\phi) \quad (3.29)$$

$$G_{zz,dc} = \frac{1}{4j} H_o^{(2)}(k\rho) \quad (3.30)$$

and apply the circle extraction technique to each. Starting with the simplest, G_{zz} , we have that

$$\frac{1}{4j} \int_0^{2\pi} \int_0^a H_o^{(2)}(k\rho) \rho d\rho d\phi = \frac{a\pi}{2jk} H_1^{(2)}(ka) - \frac{1}{k^2}$$

where a is the effective radius of our moment method cells obtained from $a = \sqrt{A_n/\pi}$, and A_n is the area of moment method cell n .

Looking next at the similar terms for G_{yz} , G_{zy} , G_{zx} and G_{xz} , we have

$$\pm \frac{1}{4j} \int_0^{2\pi} \int_0^a k\rho \begin{Bmatrix} \cos(\phi) \\ \sin(\phi) \end{Bmatrix} H_1^{(2)}(k\rho) d\rho d\phi = \pm \frac{1}{4j} \int_0^a k\rho H_1^{(2)}(k\rho) \begin{Bmatrix} \sin(\phi) \\ -\cos(\phi) \end{Bmatrix} \Big|_0^{2\pi} d\rho = 0$$

and find that the self terms for G_{yz} , G_{zy} , G_{zx} and G_{xz} are zero.

Next, employing the identity $2 \cos(\phi) \sin(\phi) = \sin(2\phi)$, we have for G_{xy} and G_{yx} ,

$$\begin{aligned} \frac{1}{8j} \int_0^{2\pi} \int_0^a \sin(2\phi) \left[2 \frac{H_1^{(2)}(k\rho)}{k} - \rho H_o^{(2)}(k\rho) \right] d\rho d\phi = \\ \frac{1}{8j} \int_0^a \left[2 \frac{H_1^{(2)}(k\rho)}{k} - \rho H_o^{(2)}(k\rho) \right] \left[-\frac{1}{2} \cos(2\phi) \right] \Big|_0^{2\pi} d\rho = 0 \end{aligned}$$

and see that these two self terms also vanish.

Finally, for G_{xx} and G_{yy} we have

$$\begin{aligned} \frac{1}{4j} \int_0^{2\pi} \int_0^a \left[H_o^{(2)}(k\rho) \cos^2(\phi) - \frac{H_1^{(2)}(k\rho)}{k\rho} \cos(2\phi) \right] \rho d\rho d\phi = \\ \frac{1}{4j} \int_0^a \left[\pi H_o^{(2)}(k\rho) - \frac{H_1^{(2)}(k\rho)}{k\rho} \left[\frac{1}{2} \sin(2\phi) \right] \Big|_0^{2\pi} \right] \rho d\rho \end{aligned}$$

We recognize that the second term in the integrand on the right hand side vanishes. That which remains is

$$\frac{\pi}{4j} \int_0^a \rho H_o^{(2)}(k\rho) d\rho = \frac{\pi^2 a}{2jk} H_1^{(2)}(ka) - \frac{\pi}{k^2}$$

and thus we see that the only non-zero direct coupling self terms are those obtained from G_{xx} , G_{yy} and G_{zz} .

In Figure 3.12, the circle extraction technique is depicted as it might be applied to a cell of irregular shape. A cell shaped like this could arise from a gap region that is non-rectangular in shape. Since the circle extraction technique is an approximation employed to represent the value of the integral of the Hankel function expressions over a square cell, it is natural to ask how the approximation degrades as the shape of the cell departs from a square. To address this issue, an algorithm was devised that compares the physical region of a rectangular cell to the region of it's equivalent circle, and computes the 2D integral of the Hankel function expression in the areas remaining after subtracting the circle region from the rectangular cell region. This algorithm was applied to a series of rectangular cells of aspect ratios² ranging from 1 (a square) to 2 and the result is plotted in Figure 3.13 for two different slab coating materials each at a different frequency. For a square cell, the circle approximation should be fairly good, and the value of the integral over the circular cell is used as the 'truth' value in calculating these percentage differences. While neither line increases monotonically, the trend is both obvious and consistent for the two slab materials modelled. The plot suggests that it is desirable to keep our moment method cells as nearly square as possible. For gaps that are non-rectangular in shape, the gap region gridding algorithm will produce

²where the aspect ratio is defined as the width of the cell (x dimension) divided by it's height (y dimension)

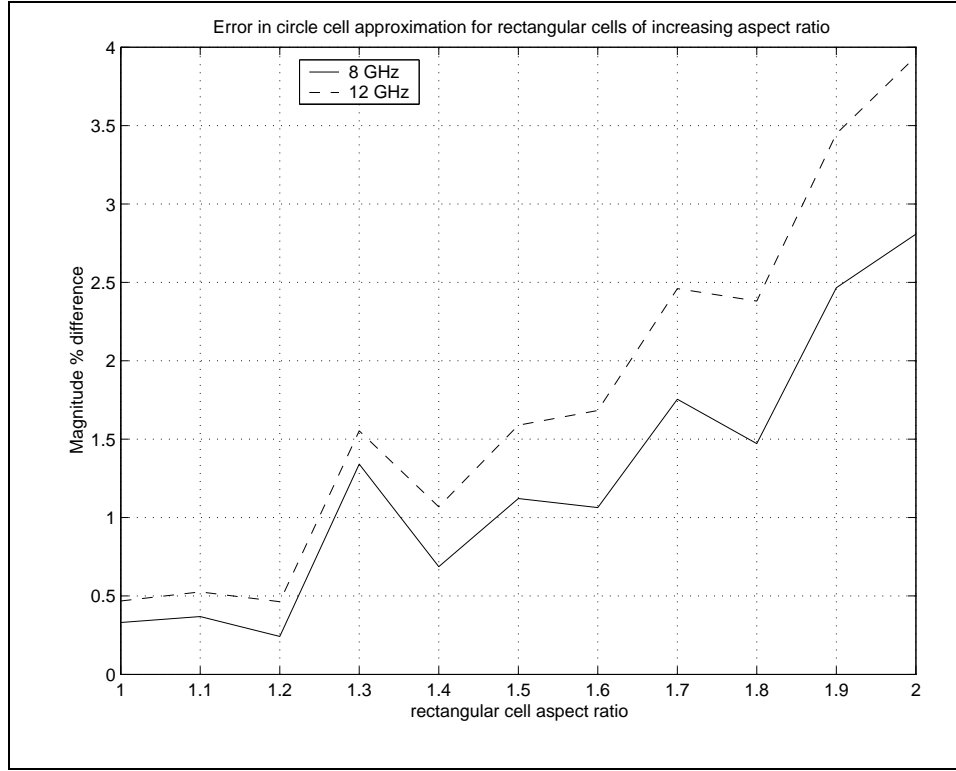


Figure 3.13 Slab coating material properties are $\epsilon_r = 3.25$, $\mu_r = 1.0$ at 8 GHz; and $\epsilon_r = 10.6$, $\mu_r = 1.3 - j1.3$ at 12 GHz. Both curves for TM polarization.

cells that are non-rectangular, and we expect that as the aspect ratio of these non-rectangular cells increases, a similar degradation in the approximation as that shown in Figure 3.13 will occur.

3.3.2 Adjacent Terms. In this implementation, we define adjacent terms as those which occur between moment method cells that share a common cell side. If we approximate our moment method cells as square, we can apply from Section 25.4.62 of [31] a formula for two dimensional numerical integration. Desiring to evaluate Equation (3.22) at as few points as possible within each adjacent cell, we choose the formula for four points per cell. Each evaluation then has a weight of $\frac{1}{4}$ and the inner product expressions (3.9) - (3.11) are evaluated, using our notation, at field points $(x, y) = \pm \frac{1}{2} \sqrt{\frac{1}{3}} (\Delta x, \Delta y)$, measured from the center of the cell, where $(\Delta x, \Delta y)$ are the average width and height of each moment method cell, and (x', y') the center of the source cell. This is seen to be very nearly a simple averaging of the inner product expressions evaluated at nearly the centers of the four quadrants of the cell. For this Gauss-Legendre two dimensional integration

formula, the integral evaluation points occur at $\sim \pm 0.29(\Delta x, \Delta y)$. The remainder associated with this integration formula is given [31] for a square cell to be on the order of $\frac{A_n^2}{16}$.

Alternative approaches that could be used to evaluate the adjacent terms are two dimensional Trapezoidal or Simpson rules. In either case, these alternative approaches would likely result in an increased number of function evaluations.

3.3.3 Distant terms. Distant terms are applicable to moment method cells that are more than one cell width apart (that is to say, the centers of these cells are more than a cell width apart). For these cases, the inner product expressions are approximated as if the Green's function is constant over the field cell [15: pg 689]. Equation (3.12) for this case is then simply evaluated as,

$$\langle L_{\alpha\beta}(P_n^{J,M}), \theta_m \rangle = G_{\alpha\beta}(x_m, y_m; x_n, y_n) \quad (3.31)$$

where (x_m, y_m) is the center of the field cell m , and (x_n, y_n) is the center of the source cell n . This amounts to a function evaluation, part of that function being the ASM-derived bounce correction term.

The definition of an adjacent cell can be easily expanded to include cells that share a common vertex (or corner). This suggests a simple numerical experiment that can give us an indication of the error induced by using the simple distant term approximation in Equation (3.31). When the definition of adjacent cells is expanded, the coupling between cells that share a common vertex is computed using the four point integration algorithm described in the previous section instead of the simpler approximation given here.

When this numerical experiment was carried out, a slight increase in coupling between these newly defined adjacent cells was observed (in the experiment we assumed a slab coating material having properties $\epsilon_r = 10.6$, $\mu_r = 1.3 - j1.3$, at a frequency of 12 GHz, with square cells 10 mils per side). The increase in coupling magnitude was observed to be about 1.5%. However, when the matrix was solved and the scattering from the gap computed, no difference was observed and the comparative data were graphically equivalent. What was discernable, however, was that the calculations were slowed by 20% using the expanded definition of adjacent cells. Thus we conclude that there is no need to define adjacent cells as those sharing common vertices in the gap

region discretization, and the definition of distant cells given in Equation (3.31) yields sufficient accuracy.

3.3.4 Summary. In summarizing this section, we see that the quadrature techniques employed call for the gap region to be discretized into square cells. For cases where this is not possible, the gap region should be discretized so that the cells are as close to square as possible. Alternative evaluation techniques are available that may produce more accurate representations for a wider variety of cell shapes. However, these alternative techniques are likely to require many additional function evaluations. In an effort to keep the number of function evaluations to a minimum, we employ the approximations described here with the knowledge that more accurate techniques are available, and could be implemented, but at the cost of lengthier computation time. Since our primary purpose here is to verify the theory developed in Chapter 2, we employ the approximations described above.

3.4 Evaluation of Incident Fields

From Equations (3.9) - (3.11) for TM polarization and Equations (3.18) - (3.20) for TE polarization, we can readily evaluate the incident field expressions obtained in Section 2.6. Recalling the definition of our symmetric product, we express the left side of Equation (3.9) as

$$\langle H_x^i(x, y), \theta_m \rangle = \iint_{V_{gap}} H_x^i(x', y') \delta(x' - x_m) \delta(y' - y_m) dx' dy' = H_x^i(x_m, y_m) \quad (3.32)$$

which is the incident field evaluated at the center of moment method cell m . Similar results hold for H_y^i , and E_z^i for the TM polarization case and E_x^i , E_y^i , and H_z^i in the TE polarization case.

3.5 Far Zone Scattering and 2-D Echo Width

As we stated earlier, we use the external Green's function to determine the fields in the free space region resulting from the currents within the gap region. To determine the 2-D echo width of the scattering from the gap, we will need to evaluate Equation (2.61) an infinite distance away from the gap region.

From Equations (2.22) and (2.52), we see that the \hat{z} -directed fields are given by the third row of each matrix. The scattered fields needed to compute the echo width of the gap will then be, for TM polarization,

$$E_z^s = - \left(\langle G_{zx}^{ext}, M_x \rangle + \langle G_{zy}^{ext}, M_y \rangle + j\omega\mu_r \langle G_{zz}^{ext}, J_z \rangle \right) \quad (3.33)$$

and for TE polarization,

$$H_z^s = \langle G_{zx}^{ext}, J_x \rangle + \langle G_{zy}^{ext}, J_y \rangle - j\omega\epsilon_r \langle G_{zz}^{ext}, M_z \rangle \quad (3.34)$$

where the J s and M s are the volumetric equivalent unknown currents computed via the moment method of Section 3.2, and G_{zx}^{ext} , G_{zy}^{ext} and G_{zz}^{ext} are the external Green's functions necessary to radiate the fields of these currents into the medium outside the slab. These expressions are given by Equations (2.66), (2.67) and (2.61) respectively.

With the array spacing chosen to be $D_x = \lambda_1/2$, we are assured that only the $n = 0$ plane wave mode will survive into the far field as all evanescent plane wave modes will decay exponentially with distance away from the interface. This enables us to simplify Equations (2.61), (2.66) and (2.67) to give

$$G_{zx}^{ext} = -\frac{k_o}{4\pi} \int_{-1}^1 e^{-jk_1[(d-y')r_{y1}-x'r_{x1}]} T_r^{ext} e^{-jk_o[(y-d)r_{y0}+xr_{x0}]} ds_{x_o} \quad (3.35)$$

$$G_{zy}^{ext} = \frac{k_o}{4\pi} \int_{-1}^1 \frac{r_{x1}}{r_{y1}} e^{-jk_1[(d-y')r_{y1}-x'r_{x1}]} T^{ext} e^{-jk_o[(y-d)r_{y0}+xr_{x0}]} ds_{x_o} \quad (3.36)$$

$$G_{zz}^{ext} = -\frac{jk_o}{4\pi k_1} \int_{-1}^1 \frac{e^{-jk_1[(d-y')r_{y1}-x'r_{x1}]} T^{ext} e^{-jk_o[(y-d)r_{y0}+xr_{x0}]} ds_{x_o}}{r_{y1}} \quad (3.37)$$

as our external Green's function expressions, where in each r_{x1} , r_{y1} , r_{x0} , and r_{y0} , $n = 0$. We also recall that T^{ext} and T_r^{ext} have slightly different forms for TM and TE polarization cases.

With these expressions now available to us, we can compute the far zone scattered fields from the gap. It is interesting to observe the behavior of the integrand of the canonical external Green's function as the field (receiver) location moves increasingly away from the source location. In Figure 3.13, we examine the behavior of this integrand function for the three receiver locations shown. We note that as the receiver location recedes away from the source location (in the gap re-

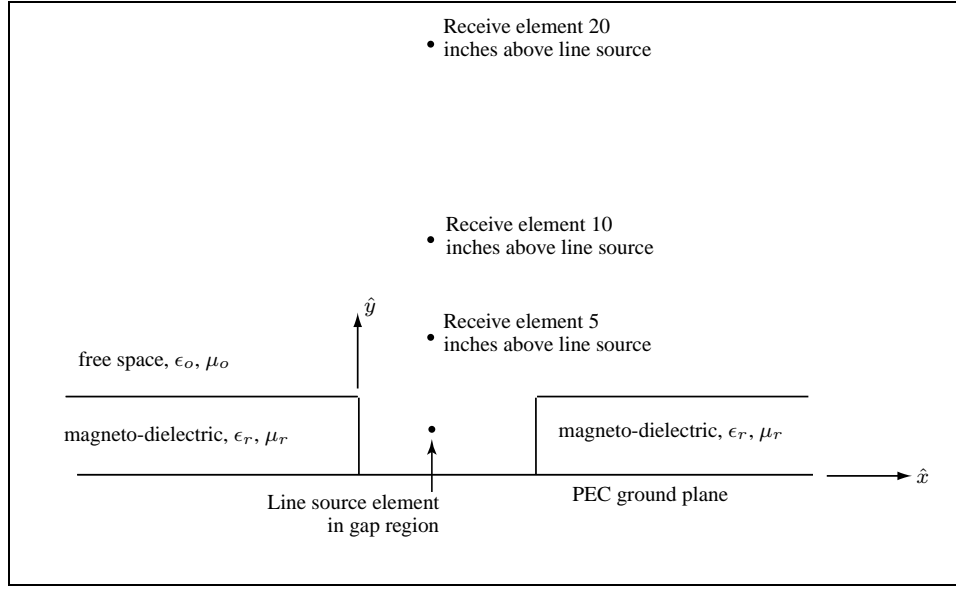


Figure 3.14 Examine external Green's function integrand at receive element locations shown

gion), the integrands become increasingly oscillatory as demonstrated by the progression shown in Figures 3.15 through 3.17. The shape of the integrands in Figures 3.15 - 3.17 become increasingly reminiscent of the classical examples leading to the development of the stationary phase method.

In order to apply stationary phase to the integrals in Equations (3.35) - (3.37), we recall (referring to Figure 2.2) that the parameter $s_{x_1} = \sin \phi_1$ where ϕ_1 is the scan angle of the hypothetical ASM array inside the slab coating material. The factor r_{x_1} , for the central plane wave mode term $n = 0$, is equivalent to s_{x_1} (apart from the complex constant $\frac{Re(k)}{k}$). Then, since $r_{y_1} = \sqrt{1 - r_{x_1}^2}$, r_{y_1} can be likened to the cosine of the array scan angle and we substitute $r_{y_1} = \cos \phi_1$. Traversing the interface from the slab coating material to free space, the factors r_{x_o} and r_{y_o} give the corresponding array scan angle direction in the free space exterior region. Thus we can write $r_{x_o} = \sin \phi_o$ and $r_{y_o} = \cos \phi_o$, where ϕ_o is the 'refracted' array scan angle exterior to the slab. Making these substitutions in Equations (3.35) - (3.37), valid only for the plane wave mode term $n = 0$, and with $d \sin \phi_o = \cos \phi_o d\phi_o$, we have

$$G_{zx}^{ext} = -\frac{k_o}{4\pi} \int_{-\pi/2}^{\pi/2} \cos \phi_o e^{-jk_1[(d-y') \cos \phi_1 - x' \sin \phi_1]} T_r^{ext} e^{-jk_o[(y-d) \cos \phi_o + x \sin \phi_o]} d\phi_o$$

$$G_{zy}^{ext} = \frac{k_o}{4\pi} \int_{-\pi/2}^{\pi/2} \frac{\sin \phi_1 \cos \phi_o}{\cos \phi_1} e^{-jk_1[(d-y') \cos \phi_1 - x' \sin \phi_1]} T_r^{ext} e^{-jk_o[(y-d) \cos \phi_o + x \sin \phi_o]} d\phi_o$$

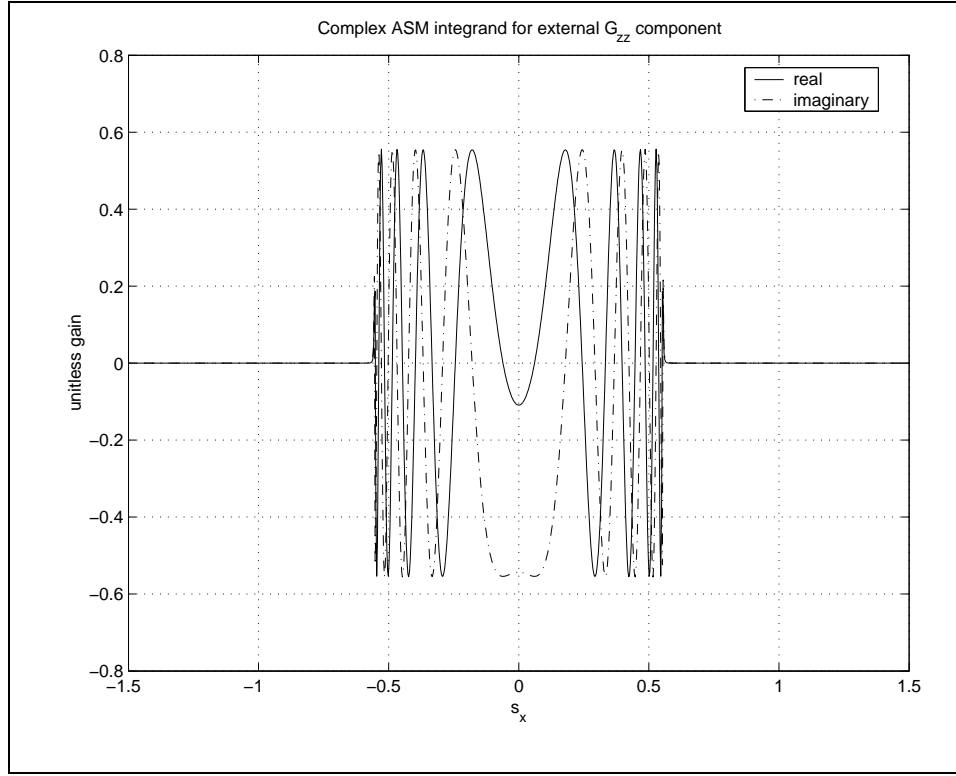


Figure 3.15 External Green's function integrand for field point in free space 5 inches directly above source point in slab. Slab coating material $\epsilon_r = 3.25$, $\mu_r = 1.0$. TM polarization, $f = 8$ GHz

$$G_{zz}^{ext} = -\frac{jk_o}{4\pi k_1} \int_{-\pi/2}^{\pi/2} \frac{\cos \phi_o}{\cos \phi_1} e^{-jk_1[(d-y') \cos \phi_1 - x' \sin \phi_1]} T^{ext} e^{-jk_o[(y-d) \cos \phi_o + x \sin \phi_o]} d\phi_o$$

To apply the stationary phase method to these integral expressions we look at the common exponential term $e^{-jk_o[(y-d) \cos \phi_o + x \sin \phi_o]}$ and rewrite it as $e^{-jk_o \rho \cos(\phi_o - \phi_b)}$ after converting to a cylindrical coordinate system where

$$\rho = \sqrt{(y-d)^2 + x^2}$$

and

$$\phi_b = \tan^{-1} \left(\frac{x}{y-d} \right)$$

The geometry and various substitutions made in converting the integrals to a form appropriate for applying the stationary phase procedure are depicted in Figure 3.18. Proceeding, we rewrite the

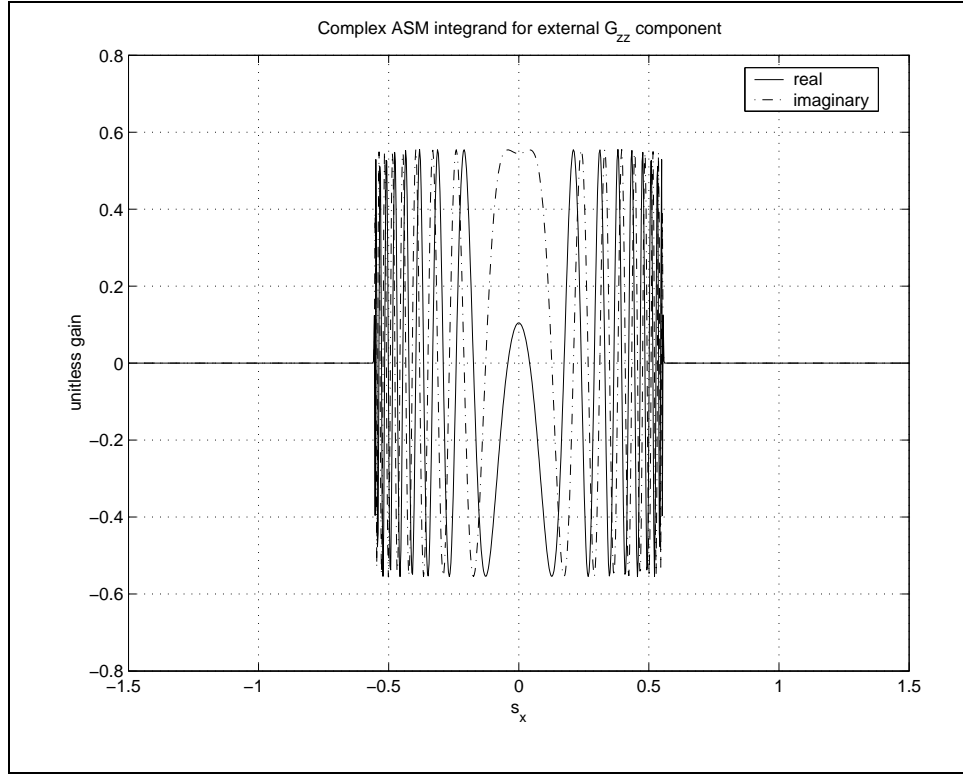


Figure 3.16 Field point in free space 10 inches directly above source point in slab. Slab coating material $\epsilon_r = 3.25$, $\mu_r = 1.0$. TM polarization, $f = 8$ GHz

Green's function expressions as

$$G_{zx}^{ext} = \int_{-\pi/2}^{\pi/2} F_{zx}(\phi_o) e^{-jk_o \rho \cos(\phi_o - \phi_b)} d\phi_o$$

$$G_{zy}^{ext} = \int_{-\pi/2}^{\pi/2} F_{zy}(\phi_o) e^{-jk_o \rho \cos(\phi_o - \phi_b)} d\phi_o$$

$$G_{zz}^{ext} = \int_{-\pi/2}^{\pi/2} F_{zz}(\phi_o) e^{-jk_o \rho \cos(\phi_o - \phi_b)} d\phi_o$$

where

$$F_{zx}(\phi_o) = -\frac{k_o}{4\pi} \cos \phi_o e^{-jk_1[(d-y') \cos \phi_1 - x' \sin \phi_1]} T_r^{ext}$$

$$F_{zy}(\phi_o) = \frac{k_o}{4\pi} \frac{\sin \phi_1 \cos \phi_o}{\cos \phi_1} e^{-jk_1[(d-y') \cos \phi_1 - x' \sin \phi_1]} T_r^{ext}$$

and

$$F_{zz}(\phi_o) = -\frac{jk_o}{4\pi k_1} \frac{\cos \phi_o}{\cos \phi_1} e^{-jk_1[(d-y') \cos \phi_1 - x' \sin \phi_1]} T_r^{ext}$$

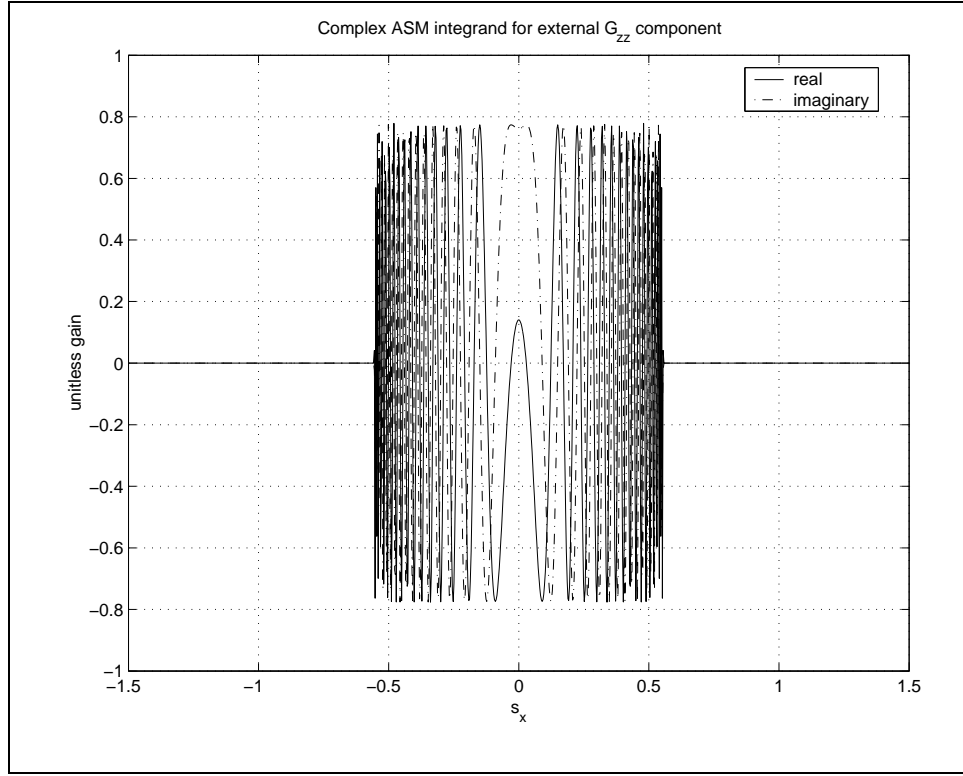


Figure 3.17 Field point in free space 20 inches directly above source point in slab. Slab coating material $\epsilon_r = 3.25$, $\mu_r = 1.0$. TM polarization, $f = 8$ GHz

With $\rho \rightarrow \infty$, we identify the large parameter in each integrand as $k_o\rho$.

Applying the stationary phase procedure [28: Section 4.2c], we identify the stationary phase point as that which satisfies the condition

$$\frac{\partial}{\partial \phi_o} \cos(\phi_o - \phi_b) = 0$$

This occurs at $\phi_o = \phi_b$ and we approximate the far zone integral expressions as

$$G_{zx}^{ext} \approx \frac{-k_o \cos \phi_b}{4\pi} e^{-jk_1[(d-y') \cos \phi_1 - x' \sin \phi_1]} T_r^{ext}(\phi_b) \sqrt{\frac{2\pi}{k_o\rho}} e^{-j(k_o\rho - \frac{\pi}{4})} \quad (3.38)$$

$$G_{zy}^{ext} \approx \frac{k_o \sin \phi_1 \cos \phi_b}{4\pi \cos \phi_1} e^{-jk_1[(d-y') \cos \phi_1 - x' \sin \phi_1]} T_r^{ext}(\phi_b) \sqrt{\frac{2\pi}{k_o\rho}} e^{-j(k_o\rho - \frac{\pi}{4})} \quad (3.39)$$

$$G_{zz}^{ext} \approx \frac{-jk_o \cos \phi_b}{4\pi k_1 \cos \phi_1} e^{-jk_1[(d-y') \cos \phi_1 - x' \sin \phi_1]} T_r^{ext}(\phi_b) \sqrt{\frac{2\pi}{k_o\rho}} e^{-j(k_o\rho - \frac{\pi}{4})} \quad (3.40)$$

where we see that the integral for each n in the summation has evaluated to just the area of the cell, A_n .

We can repeat this process for each of the other five components comprising the far zone electric and magnetic field for each polarization. Along with Equation (3.41), we have for the far zone electric field in TM polarization:

$$- < G_{zy}^{ext}, M_y > = - \sum_{n=1}^N d_{yn} G_{zy}^{ext}(x_n, y_n) \quad (3.42)$$

$$-j\omega\mu_r < G_{zz}^{ext}, J_z > = -j\omega\mu_r \sum_{n=1}^N c_n G_{zz}^{ext}(x_n, y_n) \quad (3.43)$$

For TE polarization, we have by dual analogy the expressions for the far zone \hat{z} -direct magnetic field, Equation (3.34):

$$< G_{zx}^{ext}, J_x > = \sum_{n=1}^N d_{xn} G_{zx}^{ext}(x_n, y_n) \quad (3.44)$$

$$< G_{zy}^{ext}, J_y > = \sum_{n=1}^N d_{yn} G_{zy}^{ext}(x_n, y_n) \quad (3.45)$$

$$-j\omega\epsilon_r < G_{zz}^{ext}, M_z > = -j\omega\epsilon_r \sum_{n=1}^N c_n G_{zz}^{ext}(x_n, y_n) \quad (3.46)$$

This completes our numerical implementation of the theory developed in Chapter 2. We next look at the results of this implementation and compare these results to other computer codes and measurements obtained using actual absorber and gap filler materials.

IV. Results

The quantity we use to measure the scattering due to the gap is the radar cross section (RCS), and we could discuss the RCS of the gap and the contribution it makes to the total RCS of, say, a larger body upon or within which the gap exists (see Figure 1.1). In this work we have restricted ourselves to the two dimensional case in which the metallic surface is represented by an infinite, PEC ground plane. The two dimensional version of the RCS is known as the echo width and our results will be presented in terms of this quantity. The idealization of a 2D structure is not uncommon in observables work and valuable insight into more complex 3D scattering phenomena and potential treatment solutions can be gained in this manner [32].

We begin the discussion by recalling the gap geometry shown in Figure 3.1. The computer model developed in this work allows the slab coating material to possess both dielectric and magnetic properties, i.e., within the slab coating, we allow for both $\epsilon_r \neq 1$ and $\mu_r \neq 1$. Thus the term ‘magneto-dielectric’ implies that the coating material is of this more general nature rather than, say, a pure dielectric material. We have also restricted the slab coating material to be homogeneous, isotropic, and linear.

The gap region may be filled with either air or perhaps another magneto-dielectric material different from that of the slab coating material. At this time, the computer code developed in this dissertation is restricted to dealing with gap filler materials that are homogeneous, isotropic, and linear. These restrictions could be removed by directly assigning, via table lookup or some other method, inhomogeneous and/or anisotropic properties to individual moment method cells in the gap region. The filler material must also be of the same thickness as the slab coating. To overcome this restriction would require development of a T-factor appropriate for that geometry.

We are also limited to cases where the slab coating material is the same height and has the same material properties on both sides of the gap. This is an example of a restriction that could not be removed through use of a different T-factor, but rather where an altogether different procedure would be required. Finally, while the gap shown in Figure 3.1 is representative in terms of its shape and dimensions, wider or narrower, and non-rectangular gaps are possible, as well as are gaps in thicker coatings.

In this chapter, we will compare the results and output of the computer code developed in this dissertation to several different reference methods. These reference methods consist of two computer codes and data from RCS range measurements. The measurements were performed at the Air Force Research Laboratory (AFRL) Multi-Spectral Measurement Facility (MMF) at Wright-Patterson AFB. The measurement procedures and how the measurement data was processed is described in Appendix D.

The first computer code, another hybrid Green's function / Moment Method computer code, was developed by former AFIT faculty member, Dr. J. Paul Skinner. The development of this code, which is described in further detail in Appendix F, is essentially the starting point for the work in this dissertation. The operation of Skinner's code is basically the same as the hybrid code developed in this dissertation, but is implemented in FORTRAN and runs on a 450 MHz UltraSparc II workstation. The second computer code is the industry standard Ram2d code developed by the Northrop-Grumman Corporation. This FORTRAN code has been under development for many years and is well optimized for operation on workstation-class computers. For the comparisons presented in this chapter, Ram2d is run on the same 450 MHz UltraSparc II workstation as is the Skinner code. Before proceeding, we describe how Ram2d was used as a reference comparison.

4.1 The Ram2d Numerical Test Body

In nearly every result to be presented in this Chapter, the hybrid code developed in this work will be compared to the Ram2d code. This code, as described in [33], is a 2D surface integral equation (SIE) Moment Method code that also uses pulse basis functions with delta function testing (point matching). While Ram2d is designed to compute the scattering from bodies infinite along an axis of translation (hence the 2D designation), the transverse dimensions of the body must be finite. The Green's function employed in the Ram2d SIE formulation is the 2D free space Green's function Equation (2.1) but in which the value of the propagation constant k is that of free space as opposed to that of the slab coating material. Since scattering objects in Ram2d are modelled as bodies with finite transverse dimensions, the infinite slab-coated ground plane geometry cannot be modelled with Ram2d.¹ So, in order to compare the echo width results from

¹Ram2d has an infinite ground plane option but the Green's function for that case cannot account for an infinite slab coating on the ground plane.

Ram2d to that generated by the hybrid code, it is necessary to employ a numerical test body. The Ram2d numerical test body constructed for generation of this comparison data is depicted in Figure 4.1.

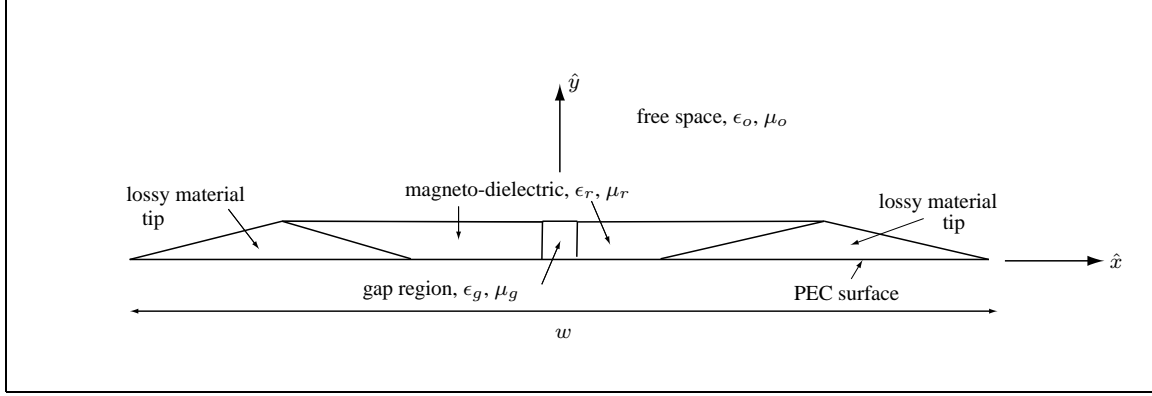


Figure 4.1 Ram2d numerical test body of width w . Lossy material tips have properties similar to slab coating but with added magnetic loss. Drawing not to scale.

With this test body, two separate runs of Ram2d are necessary to determine the scattering due to the presence of the gap: one with the gap present in the numerical test body and one without the gap (this we refer to as a ‘background’ run). The results of these separate runs are then coherently subtracted with the resulting difference being the scattered signal response due to the gap. The coherent subtraction process used to produce the Ram2d results is quite similar to the coherent subtraction process used in the compact range to measure the scattering from the gaps. This procedure is described further in Appendix D.

The gap region in the test body is given the dimensions of the gap being modelled. For the background run of Ram2d, the gap is given the same properties as the slab coating material. For the second run, the gap region properties are changed to correspond to the properties of the gap filler material, which can be air or some other magneto-dielectric material. The thickness of the gap region and the slab coating material are set to represent the geometry modelled by the hybrid code. The width of the test body, w , can be varied but, as discussed below, must be set wide enough so that surface waves supported by the slab coating material do not dominate the scattering response due to the gap.

A thin finite-width body such as this will support surface wave modes inside the slab coating material, which are altered by the presence of the gap to such an extent that they may not

completely cancel in the coherent subtraction. This is the case for both TM and TE polarization. Lossy material tips are therefore added to each end of the numerical test body to minimize these surface wave contributions. The amount of loss incorporated into these tips is small, usually set to $\epsilon_r'' = 1$ or 1.5 , depending on the properties of the slab material (for denser coatings the higher values are used). If the values of the lossy tips are too drastically different from the slab coating material, additional scattering contributions may arise.

As is evident in the Ram2d results shown in this Chapter, the lossy tips are effective for TM polarization although some residual may persist. The lossy tips are not as effective for TE polarization and significant travelling wave residual is seen in many cases. It was found that the best way to mitigate the effects of residual travelling waves in the Ram2d calculations was to make w as long as possible although this increases the size of the resulting impedance matrix that must be inverted by Ram2d. Failure to add these lossy tips to the numerical test body leads to poor results for Ram2d TE polarization calculations. Bodies for which w is too narrow leads to poor results in both polarizations. Values of w used to generate the results presented in this chapter were 10 or 11 inches, the shorter for cases where sufficient loss was present in the slab coating material.

4.2 Gap in Pure Dielectric Slab Coating, TM Polarization

The first results we present are for the monostatic echo width of a gap in slab coatings that are pure, lossless dielectrics ($\mu_r = 1$) illuminated by a TM polarized wave (the electric field is purely \hat{z} -directed, parallel to the axis of the gap). To compute results for a pure dielectric slab material the only Green's function component needed is the G_{zz} , or canonical, Green's function term of Equation (2.51). We compare the results of our hybrid code (indicated as 'Simpson' in the following plots) to results obtained with the Skinner code ('Skinner'), and to Ram2d ('Ram2d'). Comparisons using Skinner's code are presented in echo width in decibels relative to the wavelength, denoted as dB/λ .

In our first comparison, plotted in Figure 4.2, we have the results for the echo width of a 100 mil (0.1 inch) wide air gap, 40 mils thick, at 8 GHz for a slab coating with $\epsilon_r = 3.25$. We see the 'Simpson' and 'Skinner' codes produce graphically equivalent results and are both in very good agreement with the Ram2d result.

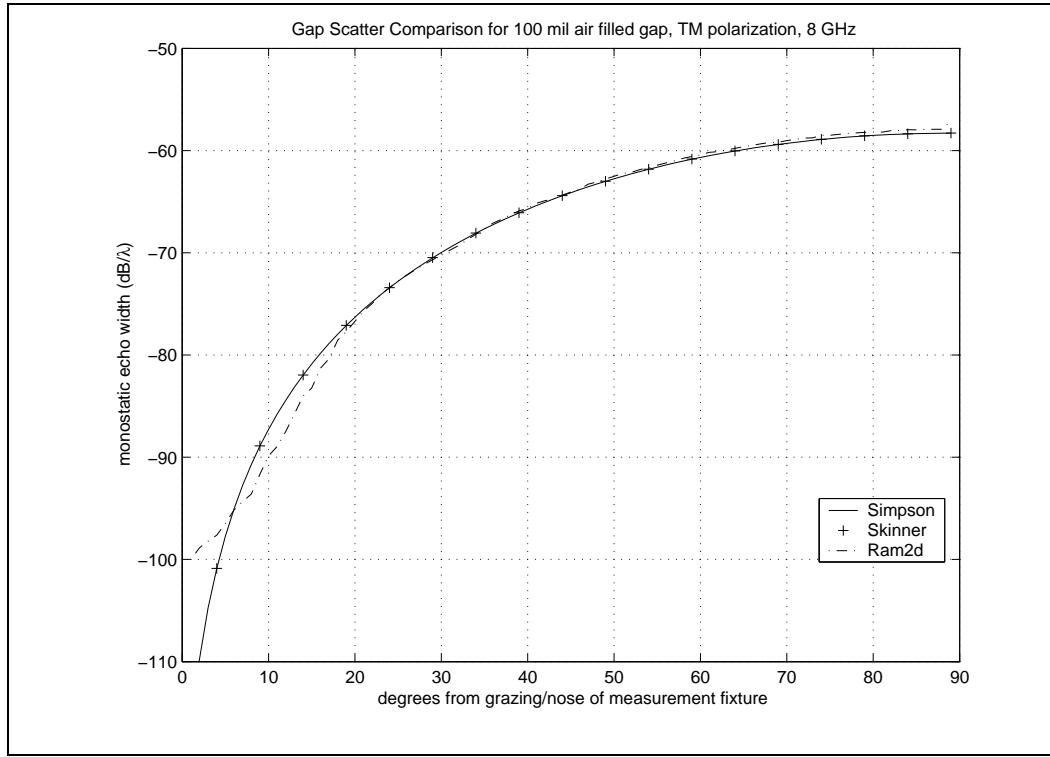


Figure 4.2 Comparison for rectangular air gap 100 mils wide. Slab coating material thickness = 40 mils, $\epsilon_r = 3.25$, $\mu_r = 1.0$, frequency = 8.0 GHz.

The gap region was gridded into five volumetric moment method cells across the width of the gap by two along the depth (or height) of the gap for the Simpson and Skinner codes (hereafter referred to using the shorthand ‘5 x 2’). For this gap geometry this produces moment method cells 20 mils square (square cells are desirable to minimize error in the various quadrature approximations described in Chapter 3). For the dielectric constant of 3.25 at 8 GHz, the wavelength in the slab coating material is approximately 0.82 inches. 20 mil square cells are just under $\lambda/40$ (λ the wavelength in the slab coating material) per side. For Ram2d, which is a ‘surface’ integral equation code, five line segment elements across the width of the gap (top and bottom) and two along the walls of the gap (left and right sides) were used (we will again call this ‘5 x 2’ even though it actually represents 14 individual line segment elements). This produces as closely as possible a similar grid representation of the gap region in each of the computer codes. But, since for the hybrid codes the number of unknowns come only from the gap region, each had only to fill and solve a 10 x 10 matrix, a process that takes less than thirty seconds for the ‘Simpson’ code implemented in Matlab®, and even less for the ‘Skinner’ code running in FORTRAN.

In the Ram2d result, some residual travelling wave effect is still evident, especially for the low grazing angles from zero to about 20° . To reduce this effect, the numerical test body width was set to $w = 11$ inches. With the gap region gridding as stated above, this produced a total of 1177 unknowns (1177 x 1177 matrix) for the entire test body, with Ram2d automatically generating the remainder of the test body discretization using the default setting of 20 segments per wavelength. Ram2d solved this system in just over two minutes CPU time per run. Setting the test body width to a value greater than 11 inches would reduce the surface wave effects but at the cost of having to invert a larger impedance matrix and consequently longer run times.

The vast majority of the Ram2d run time is spent solving (inverting) the matrix. Very little time is expended in actually filling the matrix, in this first example, only about 4 seconds were needed. In contrast to this, the hybrid codes spend the majority of their time filling their matrices, and the matrix solve time for both the Simpson and Skinner codes is almost insignificant compared to the fill time.

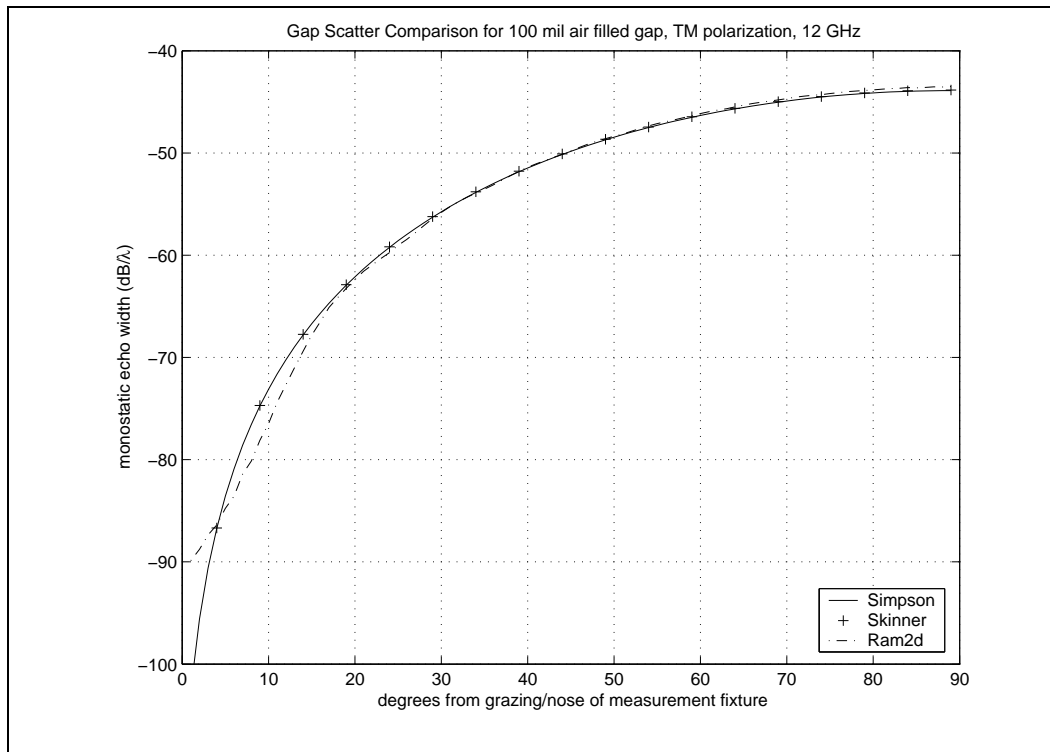


Figure 4.3 Comparison for rectangular air gap 100 mils wide. Slab coating material thickness = 40 mils, $\epsilon_r = 3.25$, $\mu_r = 1.0$, frequency = 12.0 GHz.

Next, in Figure 4.3, we show results for the same geometry and material parameters, but at a frequency of 12 GHz. Again, the agreement is very good with the ‘Simpson’ and ‘Skinner’ codes overlaying. In this case, the gridding of the gap region again was 5 x 2. This corresponds to square cells less than $\lambda/25$ on a side. The hybrid codes took less than 30 seconds to compute this result.

The Ram2d test body was again set to 11 inches to minimize the effect of travelling waves on the result. This resulted in 1735 unknowns in Ram2d and the code took over 18 minutes to complete it’s solution. Generation of the coherently subtracted result through the post processing procedure described earlier is quite fast and does not impact the stated Ram2d run times.

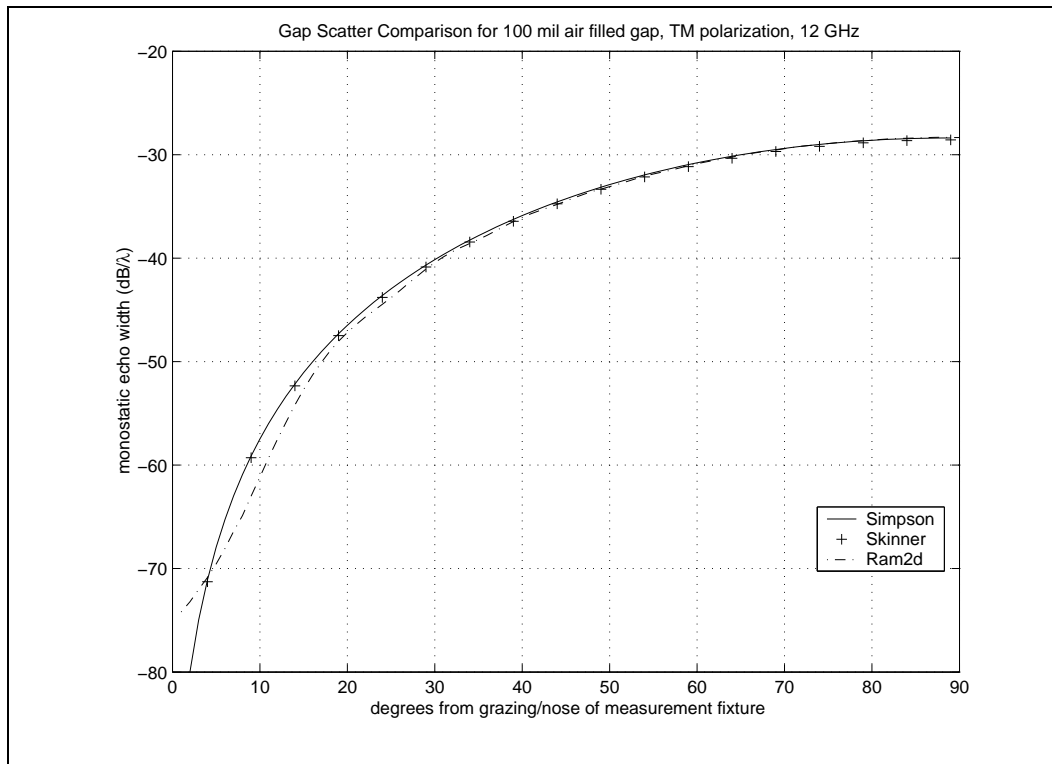


Figure 4.4 Comparison for rectangular air gap 100 mils wide. Slab coating material thickness = 40 mils, $\epsilon_r = 10.6$, $\mu_r = 1.0$, frequency = 12.0 GHz.

In Figure 4.4, we increase the dielectric constant of the slab coating to $\epsilon_r = 10.6$ while maintaining the frequency at 12 GHz. As one would expect, we observe an increase in the scattering level. All three codes are in good agreement that the increase is about 16 dB. Again the ‘Simpson’ and ‘Skinner’ codes virtually overlay.

The gridding used for this case is 10×4 , which corresponds to square cells less than $\lambda/30$ per side. The 40×40 matrix was filled and solved in the hybrid codes in less than three minutes.

The Ram2d test body was again set to $w = 11$ inches which produced 1758 unknowns. This 1758×1758 matrix for each run was solved in just under 20 minutes. In cases like this, the hybrid approach compares quite favorably, as obtaining a result in less than three minutes is clearly superior to obtaining the same result in 40 minutes.

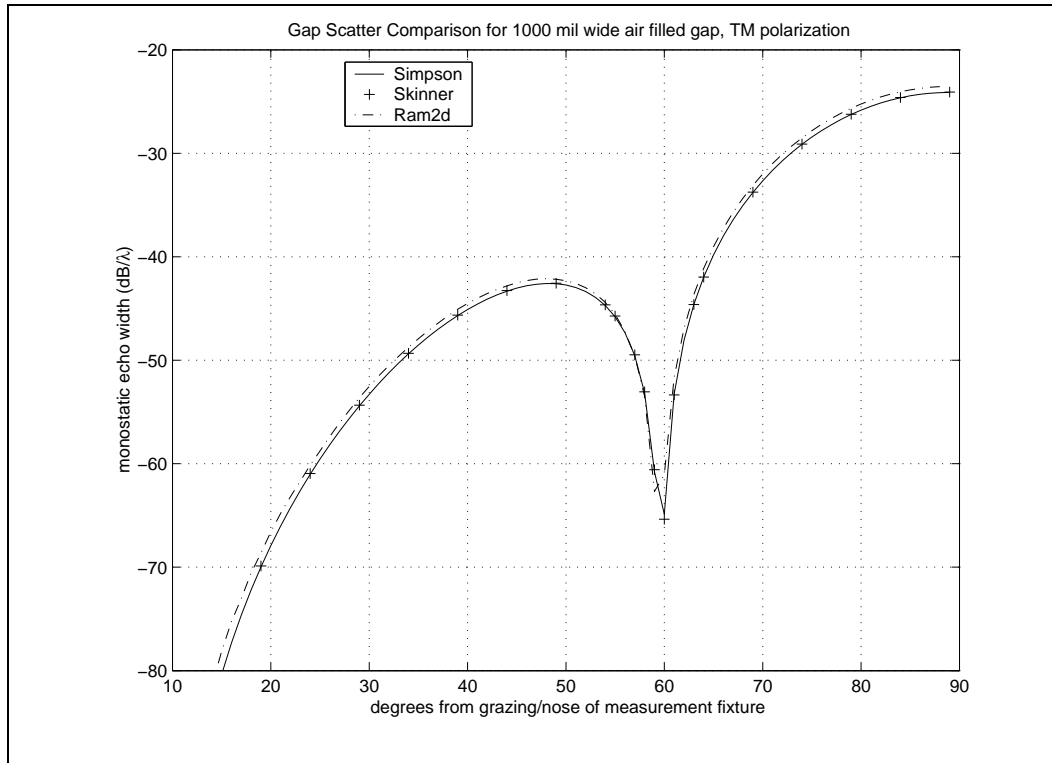


Figure 4.5 Comparison for rectangular air gap 1000 mils wide. Slab coating material thickness = 40 mils, $\epsilon_r = 3.25$, $\mu_r = 1.0$, frequency = 12.0 GHz.

In Figure 4.5, we return the dielectric constant of the slab material to $\epsilon_r = 3.25$ but extended the rectangular gap to a width of 1 inch, which is slightly greater than the free space wavelength at 12 GHz. This produces more structure in the echo width pattern. The agreement between the hybrid codes and Ram2d is again seen to be quite good both in terms of the levels and the location of the null.

The gridding used for the case plotted in the Figure 4.5 is 50×2 . This is the same cell size as was used in producing the results presented in Figure 4.3. The 'Simpson' code, running in Matlab®

on a 450 MHz Pentium II PC, took over 12 minutes to compute this result. The ‘Skinner’ code, running in FORTRAN on a 450 MHz UltraSparc II workstation, required just over 90 seconds.

The Ram2d test body was set to 11 inches with the gap region occupying the one inch in the center. This produced 1816 unknowns. The matrix inversions and coherent subtraction required 40 minutes.

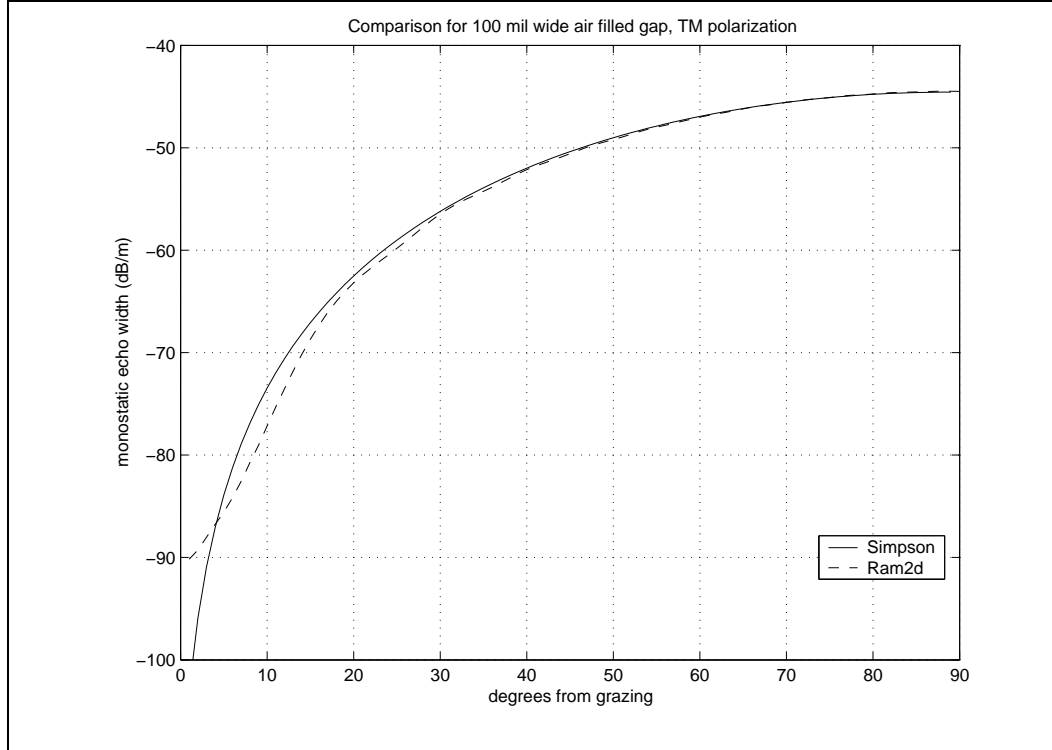


Figure 4.6 Comparison for rectangular air gap 100 mils wide. Slab coating material thickness = 40 mils, $\epsilon_r = 10.6 - j1.5$, $\mu_r = 1.0$, frequency = 12.0 GHz.

Next we look at results for cases where the slab coating has a loss component. Figure 4.6 shows the results for a case where the slab coating has a permittivity $\epsilon_r = 10.6 - j1.5$. A 10 x 4 grid was used. In this case, the two codes agree fairly well out to a little less than 10° from grazing, at which point the residual travelling wave effects cause the Ram2d echo width pattern to diverge. So, even with the loss in the slab coating material, an 11 inch Ram2d test body was used to try to minimize the surface wave effect. This produced 1758 unknowns in the Ram2d computation which required nearly 42 minutes to obtain the coherently subtracted results shown here. The hybrid code required approximately 90 seconds to compute its result, the increased speed due

to the lossy material properties enabling more rapid convergence in the bounce correction term integrations during the matrix fill operation.

For this case we cannot compare to the Skinner code because that code does not allow for complex (lossy) dielectric permittivities. We also plot the results in this figure and those to follow on the scale of decibels relative to a meter, dB/m .

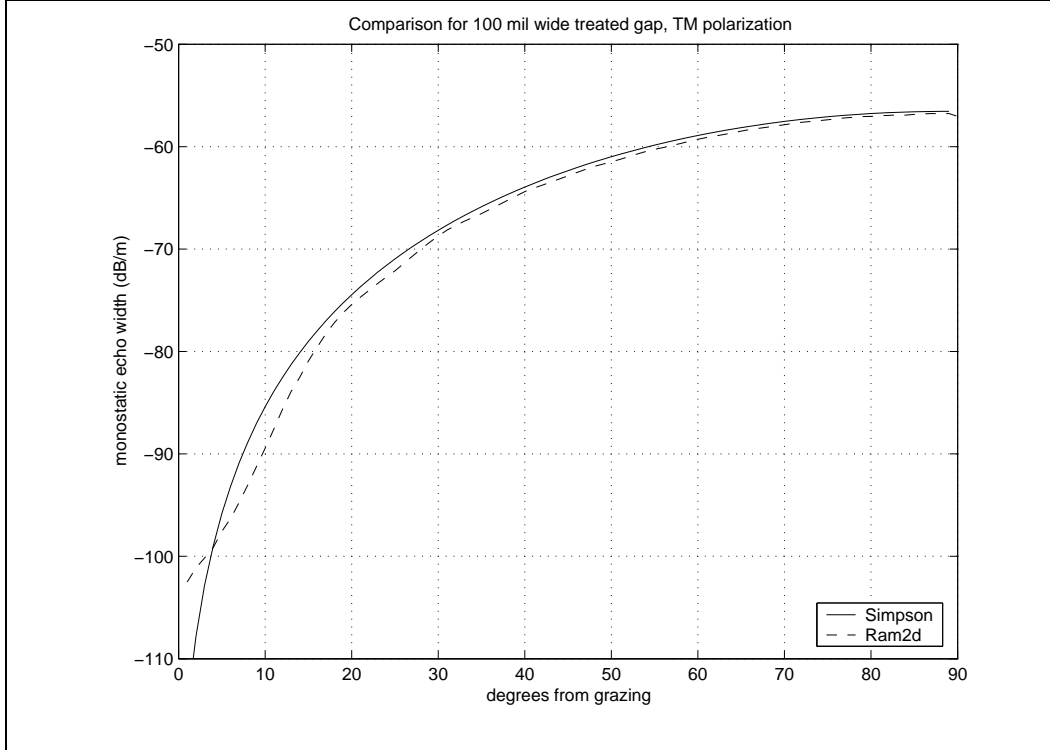


Figure 4.7 Comparison for treated rectangular gap 100 mils wide. Slab coating material thickness = 40 mils, $\epsilon_r = 10.6 - j1.5$, $\mu_r = 1.0$, filler material $\epsilon_g = 12.5 - j1.8$, $\mu_g = 1.0$, frequency = 12.0 GHz.

Next in Figure 4.7, we show results for a case where the gap is filled with a lossy dielectric filler material having permittivity $\epsilon_g = 12.5 - j1.8$. The slab coating material retains the same dielectric properties as the case shown in Figure 4.6. With the lower contrast between the gap filler and slab coating materials, we could readily anticipate the lower level of scattering indicated in the figure.

Gridding of the gap region is again set to 10 x 4 here to produce square moment method cells. However, we notice the agreement between the hybrid code and Ram2d is not quite as good

in this case as it was in the previous case, the only difference between them being that the gap filler is no longer air but rather a dielectric with the properties given above.

It was shown in Section 3.2.1, in our volumetric basis - point matching solution, that the constitutive properties of the gap filler material enter into the matrix only through the diagonal elements (the ‘self’ entries) of the matrix. Therefore a change in contrast between the slab coating and gap filler materials is manifested only in entries on the diagonal of the matrix. Off diagonal matrix entries make the same contribution to the matrix solution as in the previous (air-filled gap) case. With Ram2d, on the other hand, where there are 1758 diagonal entries in its impedance matrix for this case, we see that only 28 are altered by the change in gap filler materials. So in the hybrid code, all of the matrix diagonal elements are altered by the change in gap filler materials, but in Ram2d, fewer than 1.6% of the diagonal elements change. One might well suspect that Ram2d produces a result closer to the true solution. Moment method techniques more sophisticated than point matching are available but have not been implemented in this dissertation. More is said about this in Chapter 5 where we summarize the dissertation and discuss recommendations for future work.

In Figure 4.8, we present results for scattering from a non-rectangular gap. This gap is of trapezoidal shape, 140 mils wide at the top of the gap and 100 mils wide at the bottom as shown in Figure 4.9. The gap is air filled so we can compare and contrast the results of this result to those seen in Figure 4.6. The discretization of the gap region is 12×4 but with the trapezoidal shape of the gap region, the resultant cells are not square and, from the discussion in Chapter 3 regarding errors associated with cells of higher aspect ratio, we can expect some increase in error for this computation. With the 12×4 gridding, the cells do not exceed an aspect ratio greater than 1.2:1 and it is evident that the results between the two codes are still in rather good agreement, both in terms of pattern shape and scattering level, out to a monostatic angle less than 10° from grazing where we again see residual travelling wave effects in the Ram2d echo width pattern.

Upon close examination of Figure 4.8 and comparing it to the result in Figure 4.6, we notice a slight increase in the level of scattering produced by this trapezoidal gap as compared to the rectangular gap. Both codes are in agreement as to the amount of increase in the level of scattering of approximately 2 dB.

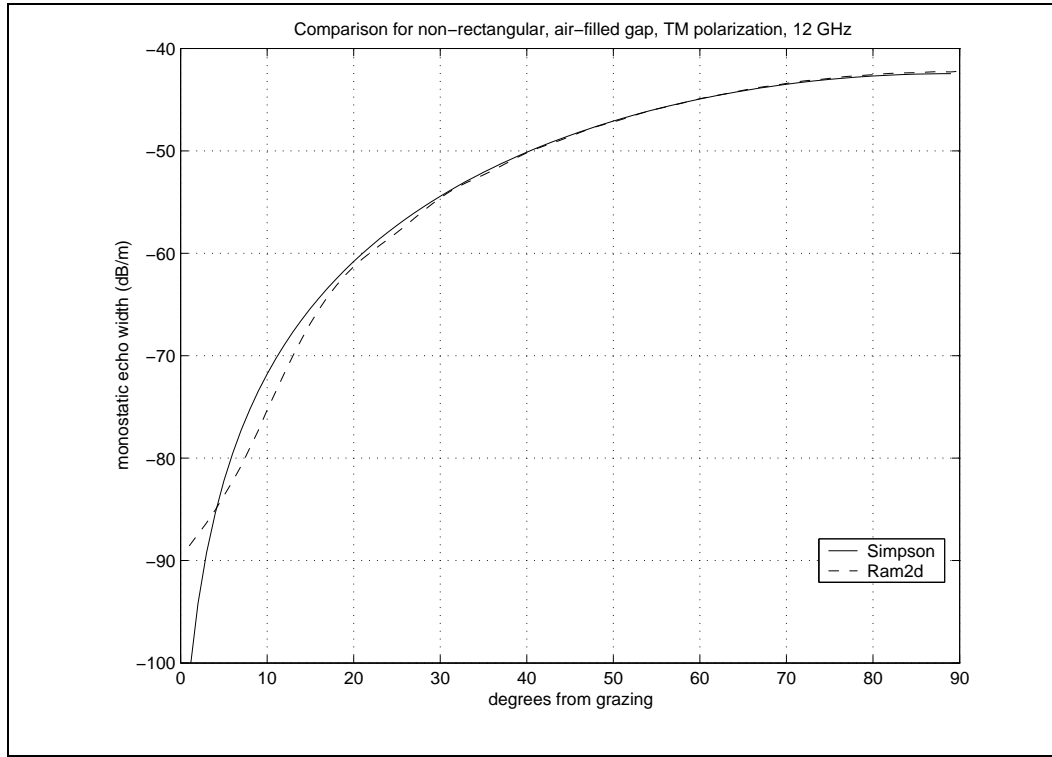


Figure 4.8 Comparison for air filled non-rectangular gap. Slab coating material thickness = 40 mils, $\epsilon_r = 10.6 - j1.5$, $\mu_r = 1.0$, frequency = 12.0 GHz.

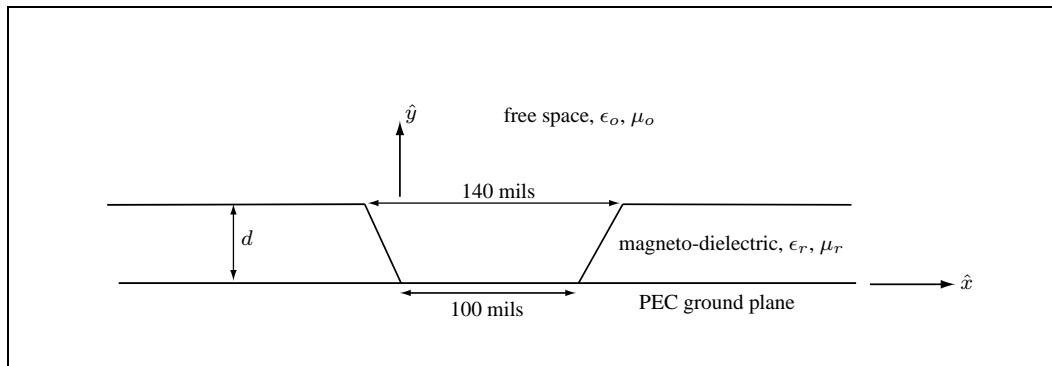


Figure 4.9 Gap Geometry for Results Plotted in Figure 4.8. (Drawing not to scale.)

In Figure 4.10 we present results for another non-rectangular gap, this time in a slab coating material with $d = 200$ mils and in which the gap is thin and canted as shown in Figure 4.11. For this computation the width of the gap is set to $t = 50$ mils. For a gap canted to one side like this, one would expect an asymmetric scattering pattern. But the asymmetry in the scattering levels as the monostatic incidence angle scans from one side to the other is subtle for these material properties,

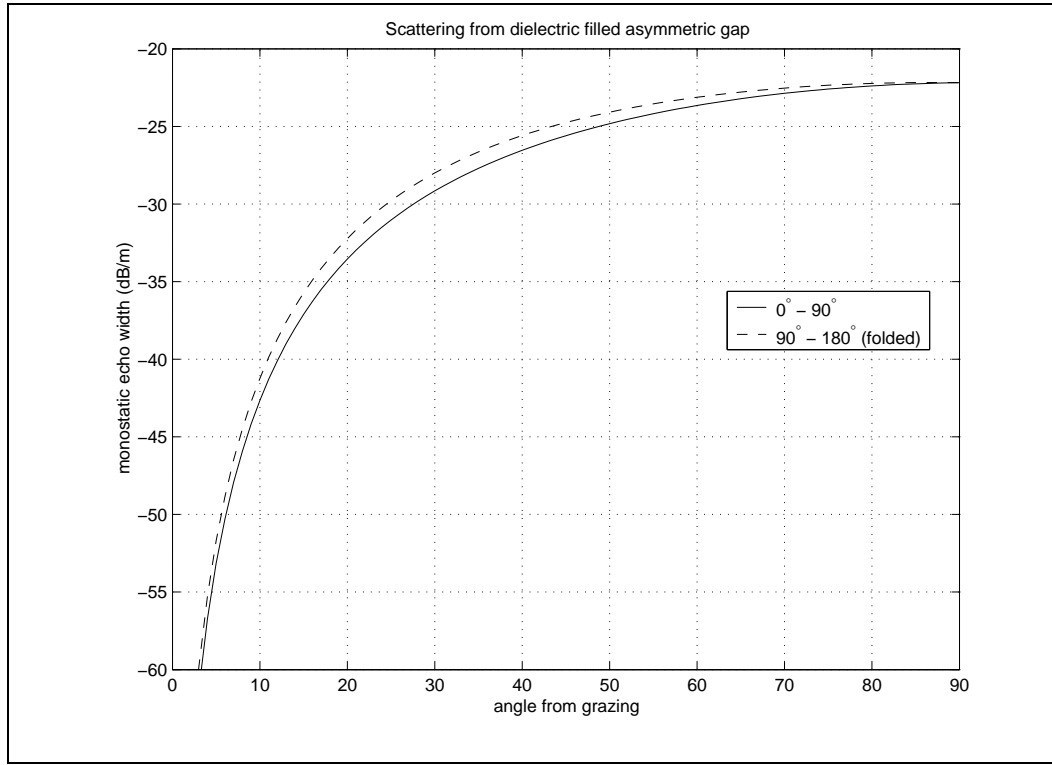


Figure 4.10 Results for dielectric filled, 50 mil wide, canted gap. Slab coating material thickness = 200 mils, $\epsilon_r = 3.25 - j1$, $\mu_r = 1.0$. Dielectric filler $\epsilon_g = 15.5$. Frequency = 12.0 GHz.

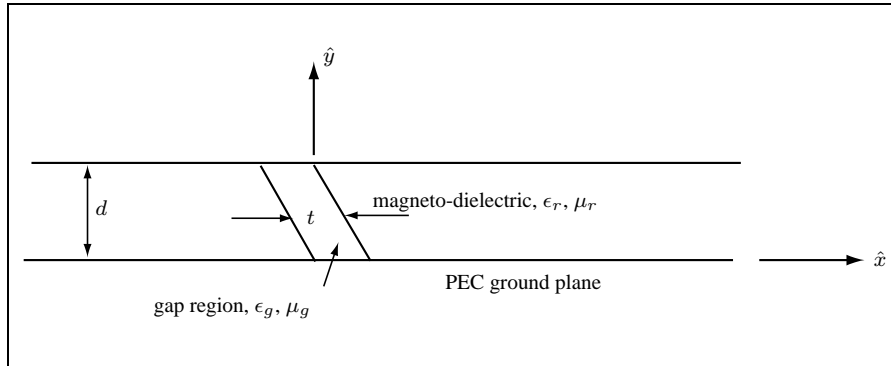


Figure 4.11 Gap Geometry for Results Plotted in Figure 4.10. (Drawing not to scale.)

and in order to achieve a noticeable effect, the gap is filled with a lossless dielectric having $\epsilon_r = 15.5$, and the thickness of the slab increased to 200 mils. No Ram2d result is displayed here because, even with the lossy slab coating material, residual surface wave effects were significant. The result plotted in Figure 4.10 is folded back onto itself to emphasize the asymmetry in the resultant scattering pattern.

A gap region gridding of 5×20 was used for this case and the resultant gap region cells were parallelograms, 10 mils in width and 10 mils in height (the canted sides having length ~ 10.3 mils). The increased error we can expect for this cell geometry should be less than that incurred by a cell having aspect ratio 1.25:1 (the x distance between the acute angle vertices of these parallelogram cells is 12.5 mils). According to the algorithm used in Chapter 3 to estimate the error for increased aspect ratio cells, the error in the direct self terms is less than 1% for this case.

Summarizing the results presented in this section, the hybrid code is seen to agree quite well with the Ram2d code, which is based on an entirely different analytical formulation. The hybrid code, not surprisingly, produces results graphically equivalent to those produced by the Skinner code (in the cases for which the Skinner code is applicable). For gaps in a pure dielectric slab coating material, these results provide some validation of both the theory developed in Chapter 2 and the numerical implementation of that theory described in Chapter 3.

4.3 *Gap in Magneto-dielectric Material and Comparison to Measurements, TM Polarization*

In this section we move on to present results comparing the output of the hybrid Green's function/moment method computer code developed in this work (indicated by 'Simpson' in the plots to follow) to output of Ram2d ('Ram2d') and to measurements obtained in the AFRL Multispectral Measurement Facility (MMF) compact radar cross section measurement range ('Measured'). Descriptions of the MMF compact range, the test fixture employed in the gap scattering measurements, and the procedures used to acquire and process the measured data are contained in Appendix D.

The range measurement results are included to provide a sort of 'reality check' for the computed results for both the hybrid and Ram2d codes. We cannot expect these simulated² 2D measured results to match well the predicted results because of the nature of the physical test body and the somewhat non-standard procedures required to obtain the RCS of the gaps alone (see Appendix D). Nevertheless, the measured results agree remarkably well with the predictions from both codes. In the results to be presented in this section, both the shapes and levels of the measured echo width patterns are in fair agreement with those obtained from the codes.

²'simulated' in that the results are a 2D conversion approximation of measurement data obtained from a 3D test fixture

In generating comparative measurement data for this dissertation, it was decided to limit the measurement frequencies to the range 8 to 12 GHz, so as not to unduly impact the schedule of the MMF compact range. Beginning at the low end of this range, we show in Figure 4.12 the TM polarization result for the echo width of a 100 mil wide, rectangular air-filled gap at 8 GHz. In

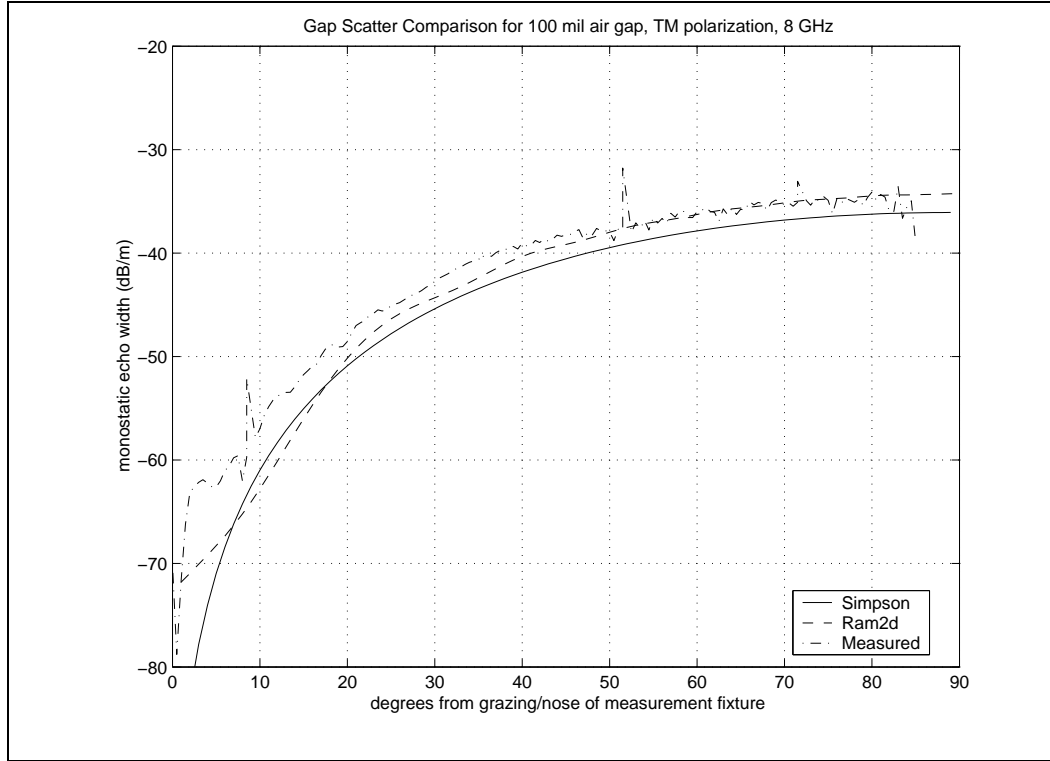


Figure 4.12 Comparison for 100 mil wide, air filled rectangular gap. At 8 GHz, the slab coating material $\epsilon_r = 10.6$, $\mu_r = 1.7 - j1.3$. Slab thickness is 40 mils.

Figures 4.13 and 4.14, we show echo width results for the same gap geometry at 10 and 12 GHz. Each of these results are plotted on 60 dB scales ranging from -80 dB/m to -20 dB/m so that changes in scattering level for various cases are more apparent.

Note that the magnetic permeability of the slab coating material exhibits a frequency dependence. The properties of the slab coating materials were determined in the Materials Measurements Laboratory (MML), another laboratory within the MMF. Measurement of the material properties are described in Appendix E. Input data to both the Simpson and Ram2d codes reflects this frequency dependence in the permeability of the slab coating material.

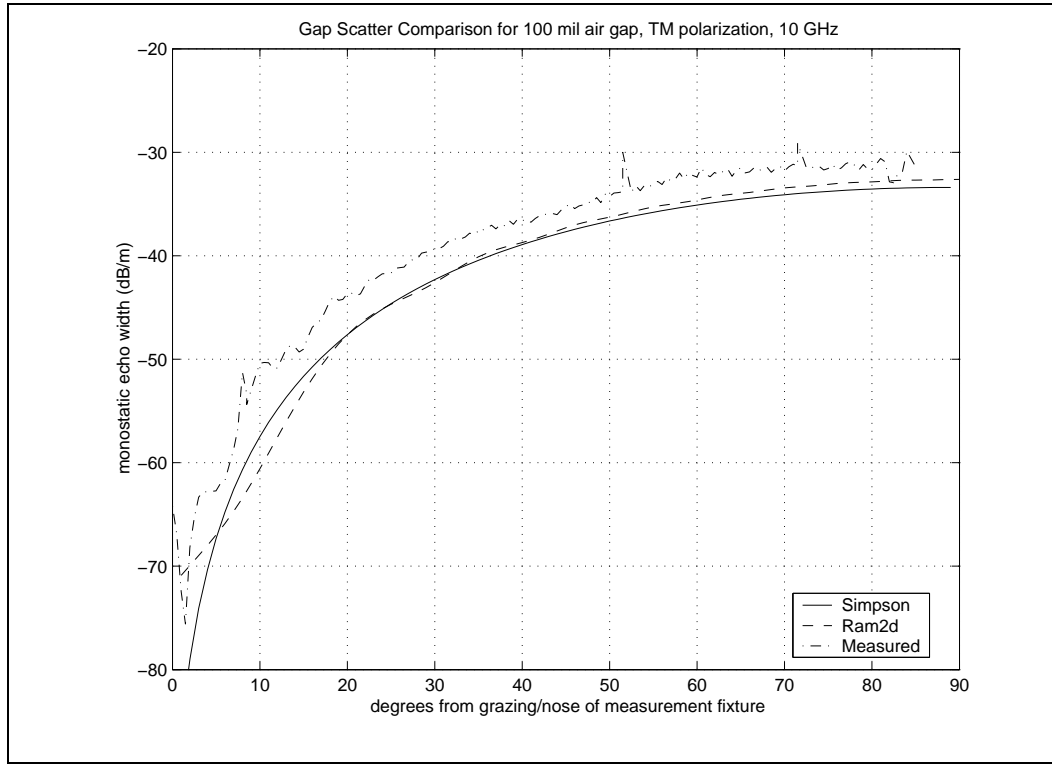


Figure 4.13 Comparison for 100 mil wide, air filled rectangular gap. At 10 GHz, the slab coating material $\epsilon_r = 10.6$, $\mu_r = 1.45 - j1.3$. Slab thickness is 40 mils.

For Figures 4.12 through 4.14, the discretization of the gap region was kept to 10×4 so as to obtain square moment method cells. Since the slab coating material now has a magnetic permeability in addition to a dielectric permittivity, the full dyadic Green's function matrix is needed to compute the coupling in the gap region. From the theoretical development presented in Chapter 2, we know that with these material properties, each pulse basis cell results in 3 unknown volume equivalent currents. Thus the 10×4 grid of the gap region now results in a 120×120 matrix. The hybrid code running in Matlab[®] required between 10 and 15 minutes to produce the results shown in these figures. The unknown count in Ram2d ranged from 1088 at 8 GHz to 1608 at 12 GHz (using a 10 inch test body for each). At 8 GHz, this required 20 minutes to produce the displayed coherent subtraction results, increasing to just under one hour for the results at 12 GHz.

Comparing Figures 4.12, 4.13, and 4.14, we observe that agreement varies between the Simpson and Ram2d codes even though the gap region gridding remains constant (the results are converged as discussed in Section 4.5). According to Wang [26] and Peterson [34], the volumet-

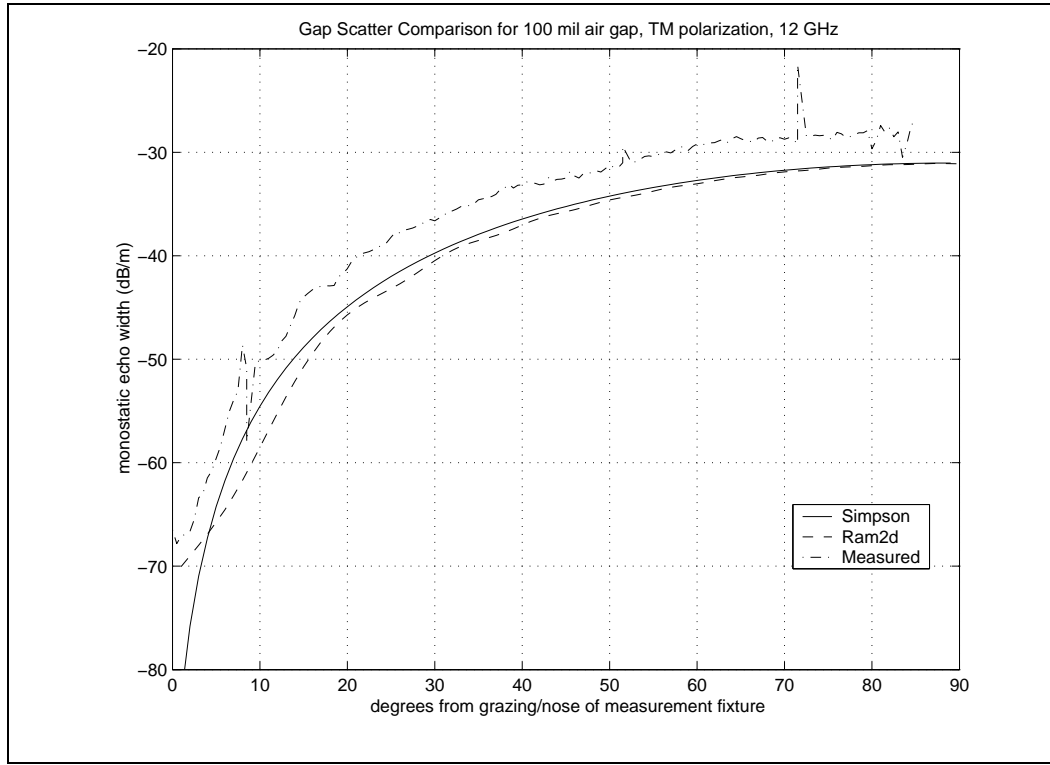


Figure 4.14 Comparison for 100 mil wide, air filled rectangular gap. At 12 GHz, the slab coating material $\epsilon_r = 10.6$, $\mu_r = 1.3 - j1.3$. Slab thickness is 40 mils.

ric moment method approach suffers greater numerical instabilities when the operator involves derivatives of the Green's function, which are now needed in these cases to compute the magnetic equivalent currents. Ram2d, which is a surface integral equation code (where surfaces are modelled as 2D line segments), does not suffer as strongly from these effects. While the agreement seems to worsen as the contrast increases between the slab coating and gap filler materials' magnetic properties, the figures indicate that the techniques are still in rough agreement (certainly there is no change in the trends indicated in plots). In fact, as noted by Harrington [38], usable results can still be obtained with point matching even if the pulse basis functions, strictly speaking, are not in the domain of the operator. However, as discussed in [26] and [34], basis and testing functions smoother than pulse basis and delta testing functions may help reduce this disagreement.

For a filled or 'treated' gap, we show in Figures 4.15 through 4.17 the results at frequencies 8, 10, and 12 GHz respectively. The agreement between the Simpson and Ram2d code is good. The better agreement in these cases is likely the result of the reduced contrast in the permeability

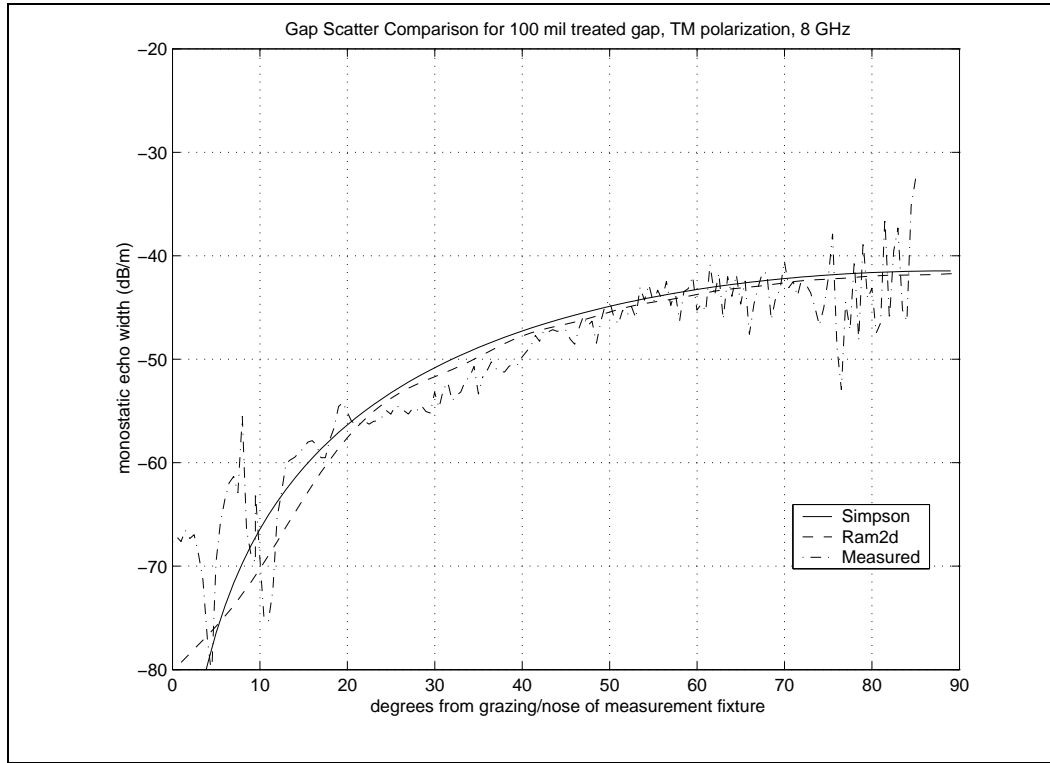


Figure 4.15 Comparison for 100 mil wide, treated rectangular gap. At 8 GHz, the slab coating material $\epsilon_r = 10.6$, $\mu_r = 1.7 - j1.3$ and the gap filler material $\epsilon_g = 15.5$, $\mu_g = 1.95 - j2.0$. The slab thickness is 40 mils.

between the gap filler and slab coating materials, this time lessening the impact of the pulse basis functions on the operators which produce the magnetic equivalent currents. Discretization of the gap region is 10×4 in Figures 4.15 and 4.16 (leading to 120×120 matrices), and 12×5 in Figure 4.17 (resulting in a 180×180 matrix). The unknown count for Ram2d again ranged from 1088 at 8 GHz to 1608 at 12 GHz (1338 at 10 GHz) and the results displayed in Figure 4.17 required just over one hour of computation time.

Finally, in Figures 4.18 and 4.19, we show results for a 60 mil wide gap, air-filled and treated respectively, at a frequency of 10 GHz. The better agreement for the treated gap is likely due to the decreased contrast between the slab coating and gap filler materials as mentioned above. Discretization of the gap region is 6×4 both in figures, requiring just over 10 minutes for the hybrid code to compute it's result in each case. Ram2d, with a 10 inch test body, produced 1326 unknowns and required nearly an hour of computation time to produce the results plotted in both Figures 4.18 and 4.19.

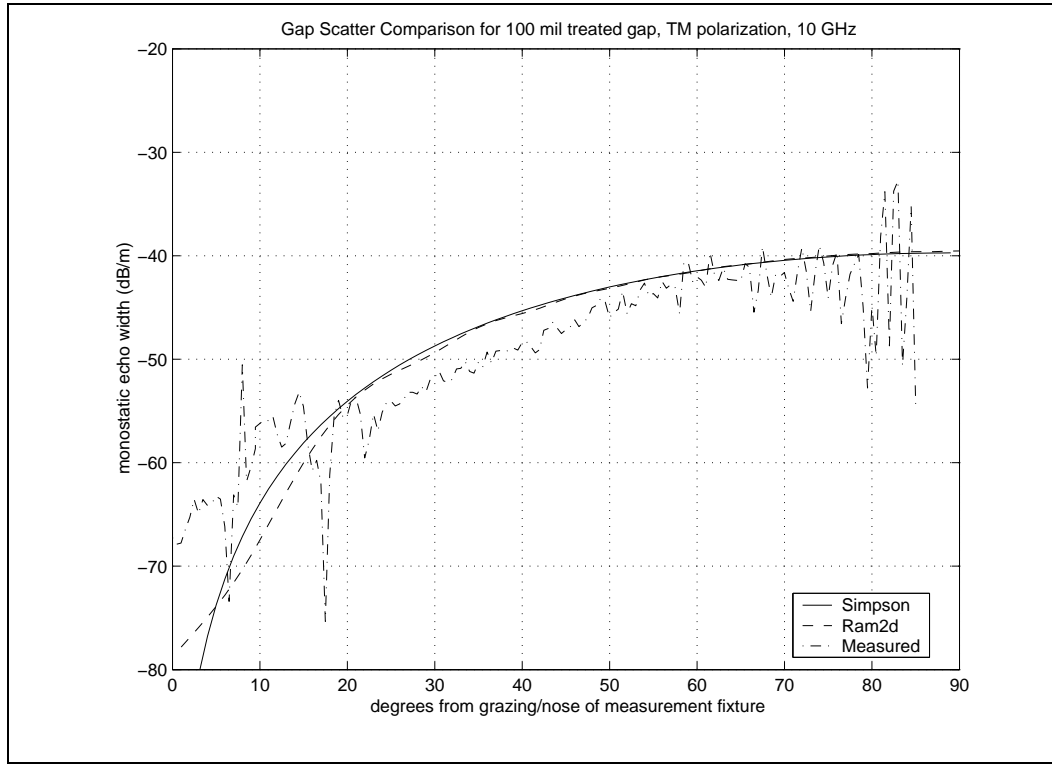


Figure 4.16 Comparison for 100 mil wide, treated rectangular gap. At 10 GHz, the slab coating material $\epsilon_r = 10.6$, $\mu_r = 1.45 - j1.3$ and the gap filler material $\epsilon_g = 15.5$, $\mu_g = 1.7 - j1.9$. The slab thickness is 40 mils.

To summarize the results presented in this section, we see that the hybrid code agrees well with the results obtained with Ram2d but that the results can be obtained much more rapidly with the hybrid code. In the present implementation of the hybrid code, numerical errors in the moment method solution, due to the choice of the point matching method approach, are seen to arise for these cases where magnetic equivalent currents must be incorporated into the solution. However, for gaps in lossy magneto-dielectric slab coating materials, these results would still tend to validate the theory developed in Chapter 2. The problems indicated in these results simply tell us that the point matching moment method solution approach is not as robust for these cases.

4.4 Gap in Magneto-dielectric Material and Comparison to Measurements, TE Polarization

We now look at results obtained for the case of TE polarization. Due to the stronger singularities present in the ASM Green's function integrands for TE polarization, the TE polarization hybrid code is even less robust than the hybrid code for TM polarization. In order to insure conver-

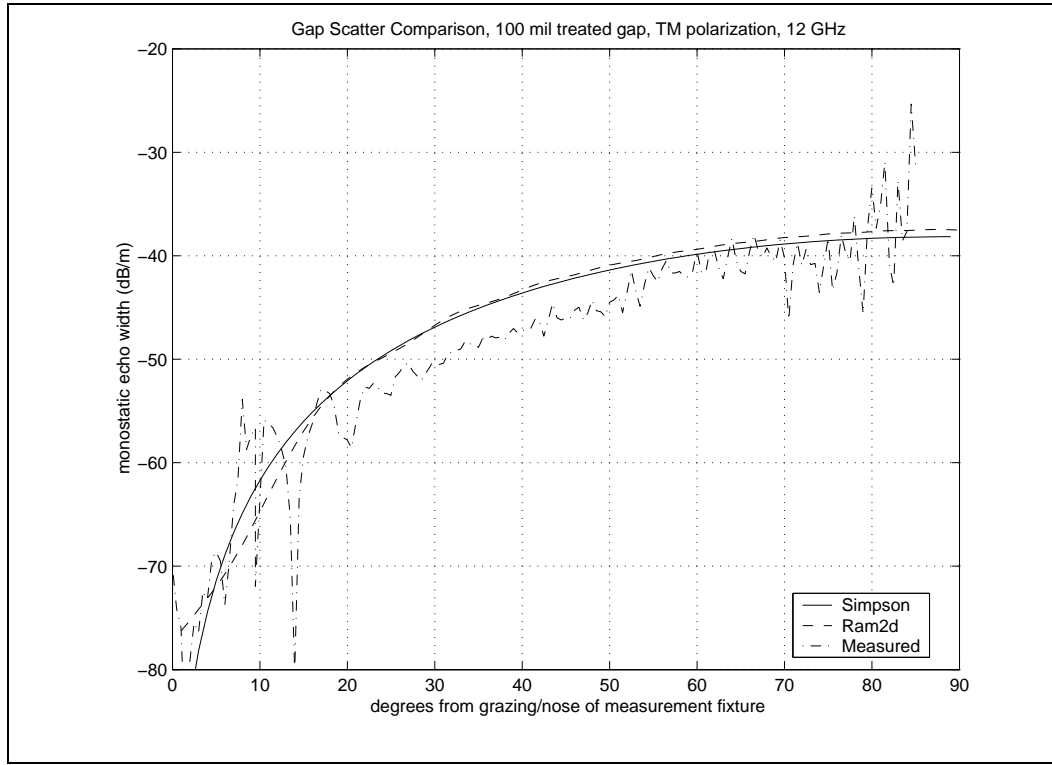


Figure 4.17 Comparison for 100 mil wide, treated rectangular gap. At 12 GHz, the slab coating material $\epsilon_r = 10.6$, $\mu_r = 1.3 - j1.3$ and the gap filler material $\epsilon_g = 15.5$, $\mu_g = 1.5 - j1.9$. The slab thickness is 40 mils.

gence of the numerical integration routine used in the hybrid code, some amount of loss is required in the magneto-dielectric slab coating. Fortunately, all practical magneto-dielectric materials exhibit loss, so the utility of the technique is still valid. For the TE polarization case, the quadrature methods for the Green's function bounce correction terms do not converge for lossless slab coating materials.

We will again include comparisons to simulated 2D measurements obtained at the MMF compact range. For TE polarization, we notice the measured results suffer a from a problem similar to the residual travelling wave seen in most of our Ram2d results. For the test fixture shape, the TE polarized field orientation induces stronger finite body effects such that they do not subtract as well, resulting in an echo width pattern of slightly different shape. Nevertheless, we see that the scattering levels are generally in agreement.

The first case presented for TE polarization in Figure 4.20 is for a gap in a low density magneto-dielectric slab coating. The material has $\epsilon_r = 3.25 - j1.0$, $\mu_r = 2.0$, and is 40 mils thick.

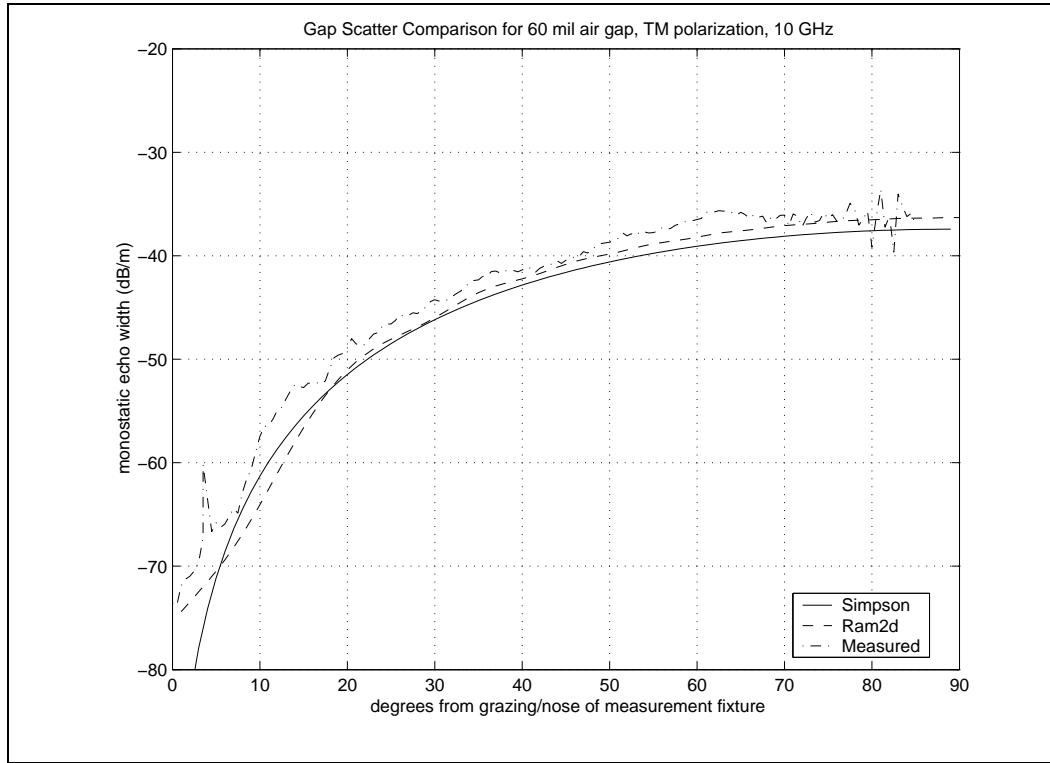


Figure 4.18 Comparison for 60 mil wide, air filled rectangular gap. At 10 GHz, the slab coating material $\epsilon_r = 10.6$, $\mu_r = 1.45 - j1.3$. The slab thickness is 40 mils.

Comparisons can be obtained with the Ram2d code but, as mentioned earlier, not the ‘Skinner’ code since that code does not address the TE polarization case. Discretization of the gap region for Figure 4.20 is 7×3 , producing a 63×63 matrix in the hybrid code. Due to slower convergence of the numerical integrations of the bounce correction terms in the various Green’s function components for TE polarization, the hybrid code required in excess of 8 minutes to produce the result shown here.

Significant residual surface wave effects are evident for the Ram2d result. With a like degree of discretization in the gap region, Ram2d produced 1585 unknowns with a 10 inch test body (requiring just over 13 minutes) and 1745 unknowns with an 11 inch test body (requiring over 25 minutes). Lengthening the test body did not significantly reduce the surface wave residual.

We next present results of the hybrid code and compare them to results from both the Ram2d code and to measurements obtained in the AFRL compact RCS range. These results correspond to the results for TM polarization presented in the previous section. We see in Figures 4.21 through

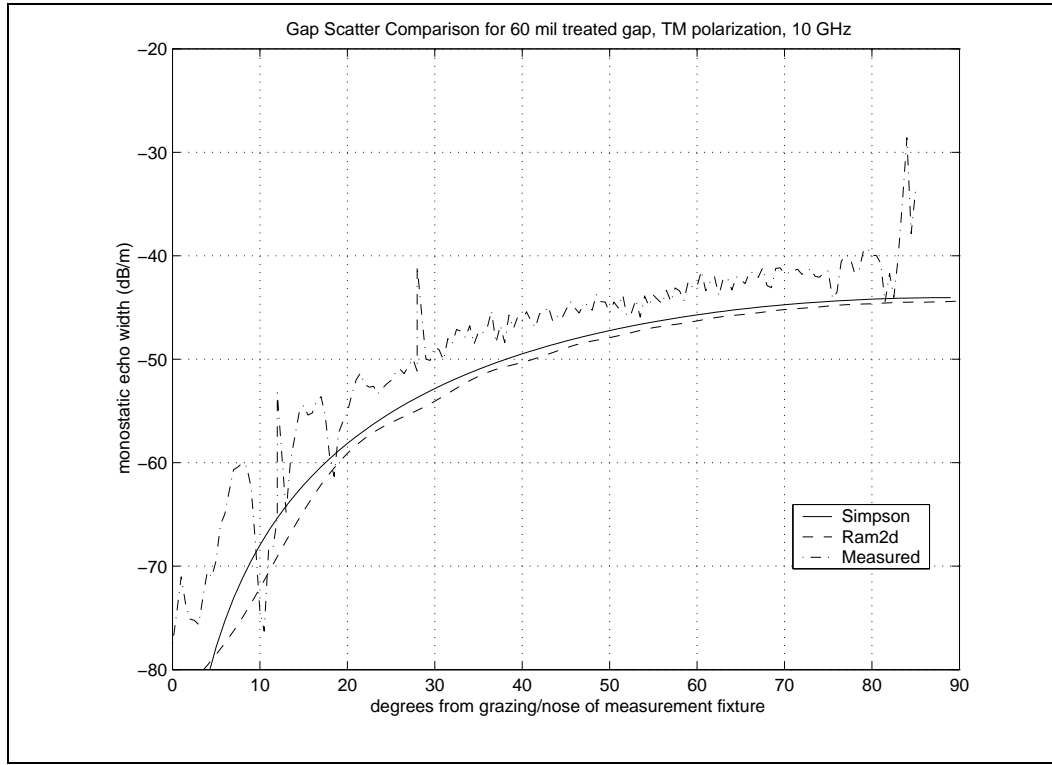


Figure 4.19 Comparison for 60 mil treated gap. Slab coating material $\epsilon_r = 10.6$, $\mu_r = 1.45 - j1.3$ and the gap filler material $\epsilon_g = 15.5$, $\mu_g = 1.7 - j1.9$. Slab thickness is 40 mils.

4.23 that the hybrid code achieves very good agreement with Ram2d for cases with untreated 100 mil wide gaps. The discretization of the gap region for the TE polarization cases is the same as was used for TM polarization and we have used Ram2d test bodies of the same length. Significant travelling wave residual is evident in all of the Ram2d results but the basic pattern shape and level is in fair agreement with that obtained with the hybrid code. One interesting observation is that for the result in Figure 4.21, the Ram2d result was obtained more quickly than the hybrid code result. This again is due to the fact that the TE code runs more slowly than for a comparable TM case because of the slower convergence of the bounce correction terms in the Green's function components. A gap region gridding of 10×4 (120×120 matrices) was used for all three figures and the Ram2d unknown count was 1088, 1338, and 1608 respectively. The hybrid code then required 16 minutes on average to compute the results plotted in these three figures. Ram2d required just over 10 minutes for the result plotted in Figure 4.21, over 20 minutes for Figure 4.22, and 34 minutes for Figure 4.23.

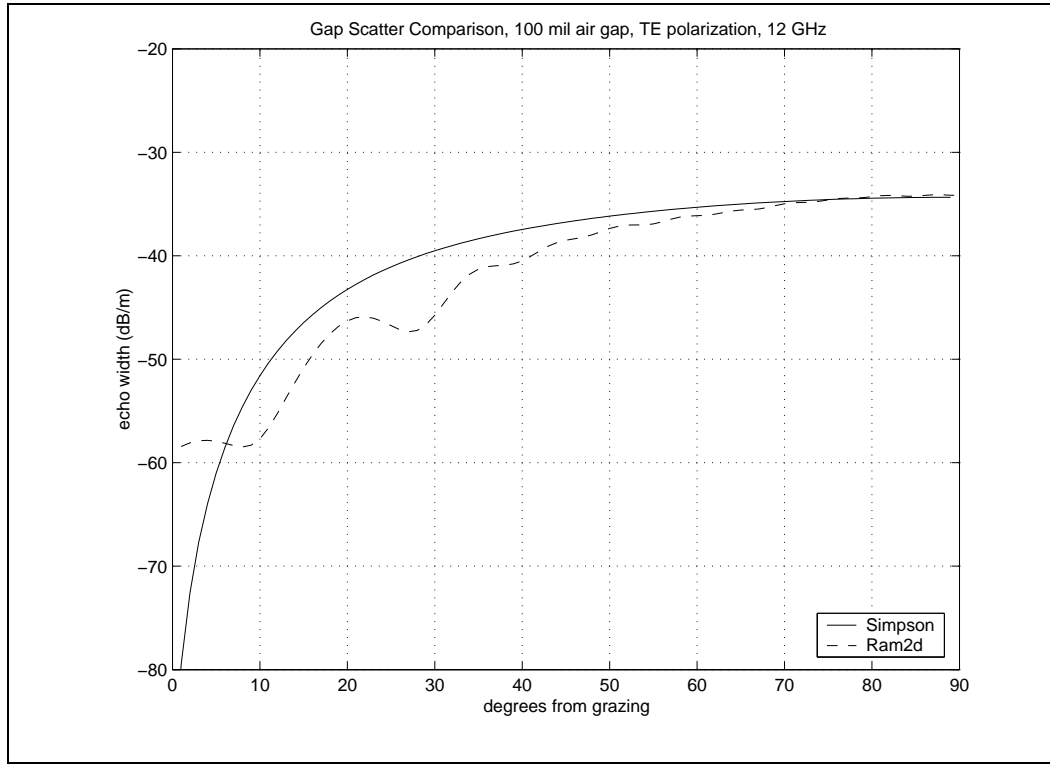


Figure 4.20 100 mil wide, air filled rectangular gap at 12 GHz. Slab coating material $\epsilon_r = 3.25 - j1.0$, $\mu_r = 2.0$. Slab thickness is 40 mils.

We present in Figures 4.24 through 4.26, monostatic echo width results for treated gaps for the TE polarization case. Results are plotted for the 100 mil wide treated gap at 8, 10, and 12 GHz respectively. Agreement between the Simpson and Ram2d codes is within a couple *dB* at 12 GHz but is seen to worsen for the lower frequency cases. In fact, the agreement for the case at 8 GHz is no better than 5 *dB*. In all three cases the contrast between the permittivities of the slab coating material and the gap filler materials is the same. As we go lower in frequency, there is a slight increase in the contrast of the permeabilities of the two materials, and we observe that it has the dual effect to that which was observed for the TM polarization case. Gap region gridding is the same in these cases as it was in Figures 4.15 through 4.17 for the corresponding TM polarization cases; 10 x 4 for Figures 4.24 and 4.25, and 12 x 5 for Figure 4.26. Run times were similar to those achieved in the air-filled TE polarization gap cases except for the 12 GHz result (a 180 x 180 matrix) which required nearly 30 minutes to complete compared to nearly 45 minutes for the Ram2d result.

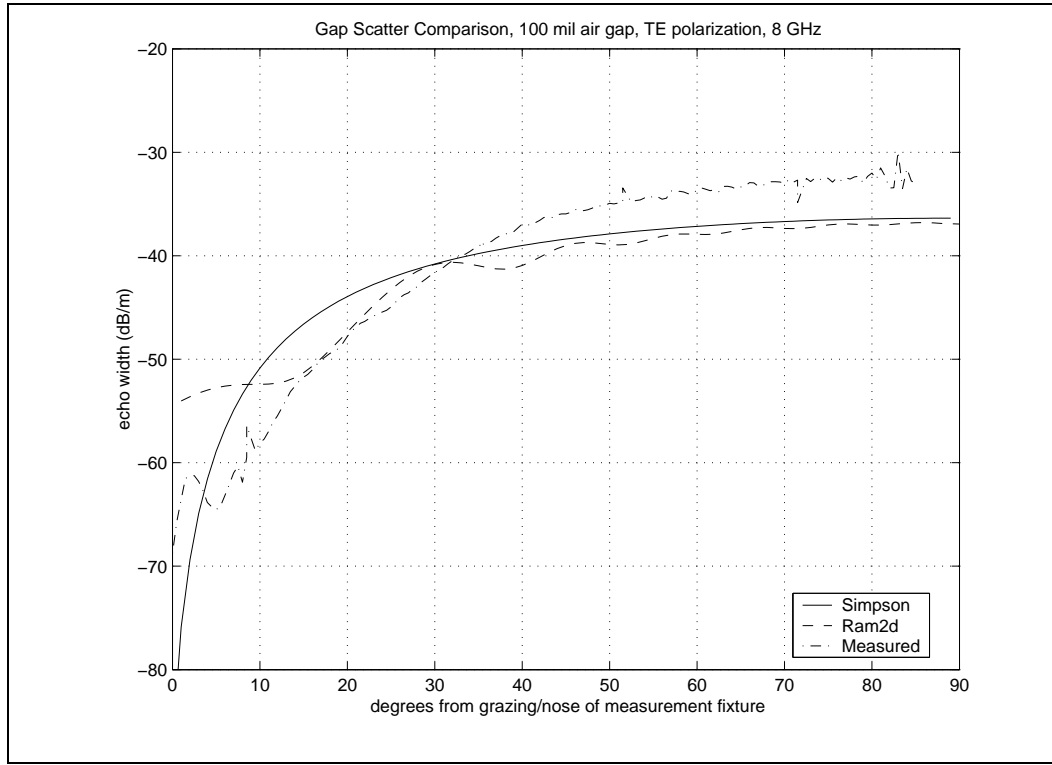


Figure 4.21 Comparison for 100 mil wide, air filled rectangular gap. At 8 GHz, the slab coating material $\epsilon_r = 10.6$, $\mu_r = 1.7 - j1.3$. The slab thickness is 40 mils.

Finally in Figures 4.27 and 4.28, we present results for the 60 mil gap for TE polarization, analogous to the TM polarization cases shown in Figures 4.18 and 4.19. In Figure 4.27 is shown the TE polarization echo width of the 60 mil wide air gap at 10 GHz. The agreement here is very good between the hybrid and Ram2d codes. For the case of the treated 60 mil gap plotted in Figure 4.28, the agreement is less impressive due to the same effect that was observed for the wider gap results. Again, the difference arises due to the change in contrast between the slab coating and gap filler materials.

In summary of this section, we see that the hybrid code struggles more to compute results in agreement with Ram2d. Nevertheless, the results are supportive of the notion that the theory developed in Chapter 2 holds and that the differences between the hybrid and Ram2d code results are not due to any problems with the theory but rather with the particular numerical implementation methods. In the next section, we address the issue of convergence of the hybrid code and show that

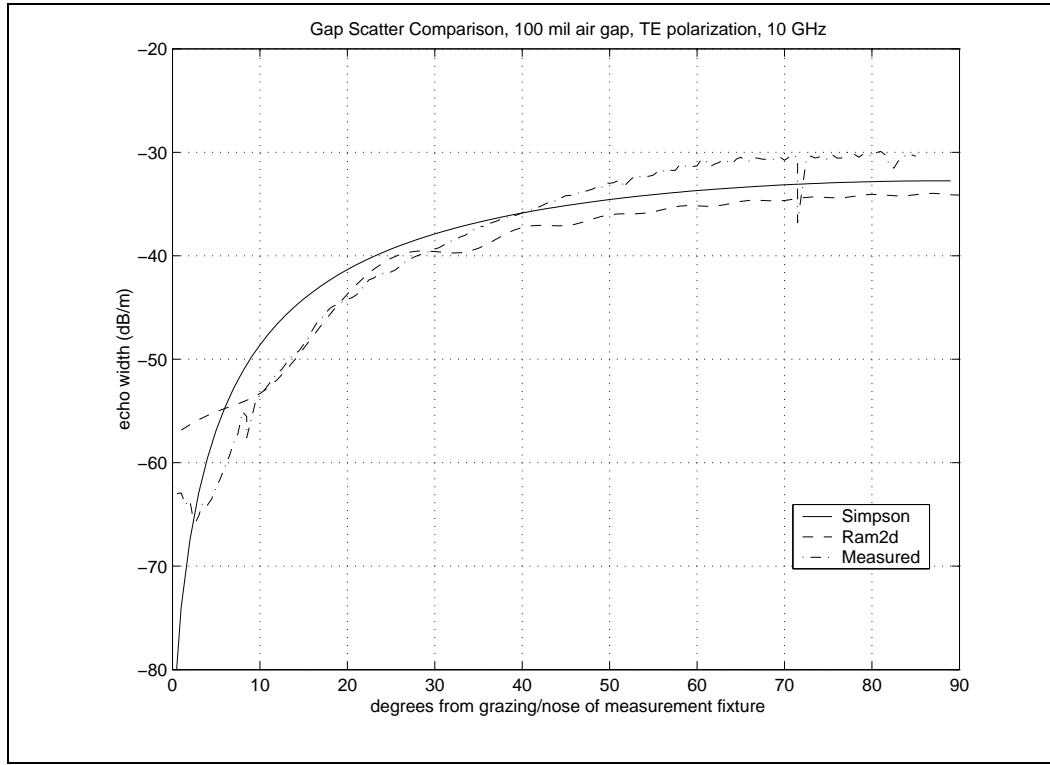


Figure 4.22 Comparison for 100 mil wide, air filled rectangular gap. At 10 GHz, the slab coating material $\epsilon_r = 10.6$, $\mu_r = 1.45 - j1.3$. The slab thickness is 40 mils.

the results presented here are at least numerically converged, which tends to confirm the suspicion that modelling errors are responsible for the differences between the hybrid code and Ram2d.

4.5 Convergence of the Hybrid Code

In any computational modelling effort one must be concerned with convergence of the numerical approximations employed. Here we look at two cases presented earlier and repeat them, varying the degree of discretization to observe the effect on the end results. The degree of discretization of the gap region is dictated by the properties of either the slab coating material or the gap filler material, with preference given to whichever is greater (denser, in an electromagnetic sense). The ratio of the real part of the propagation constant in the media (whichever is greater, slab or gap filler) to the propagation constant in free space is multiplied by a ‘discretization parameter’ to establish the ‘number of cells per wavelength’ into which the gap region is divided. We

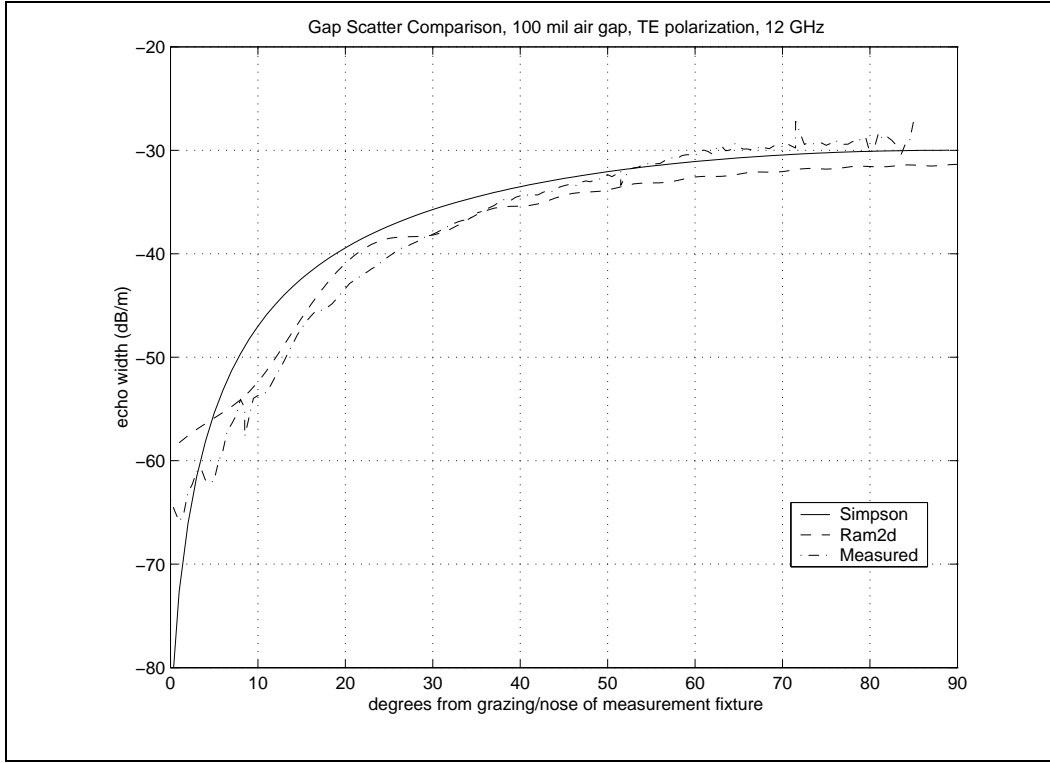


Figure 4.23 Comparison for 100 mil wide, air filled rectangular gap. At 12 GHz, the slab coating material $\epsilon_r = 10.6$, $\mu_r = 1.3 - j1.3$. The slab thickness is 40 mils.

express this numerically as

$$\text{discretization} \approx dp \cdot Re(\sqrt{\epsilon_r \mu_r})$$

where ϵ_r, μ_r are the relative constitutive properties in the slab coating material and ‘dp’ is the discretization parameter, an integer normally set to a value $dp = 20$, and where we have assumed that the slab coating material properties are greater than those of the gap region (i.e., $\epsilon_r \mu_r > \epsilon_g \mu_g$). It is the integer dp that is altered to increase or decrease the degree of discretization of the gap region in the hybrid code.

For our convergence study, the cases we choose to examine are those in which the agreement between the hybrid code and Ram2d was poorest. We make this choice intentionally because we are interested in seeing if a convergence issue might help explain the poor agreement. For TM polarization we look at the results obtained at 8 GHz. For the case plotted originally in Figure 4.12, the value of dp was set to produce a gap region discretization of 10×4 , which produced the desirable square moment method cells. Varying the value of dp in the hybrid code from a

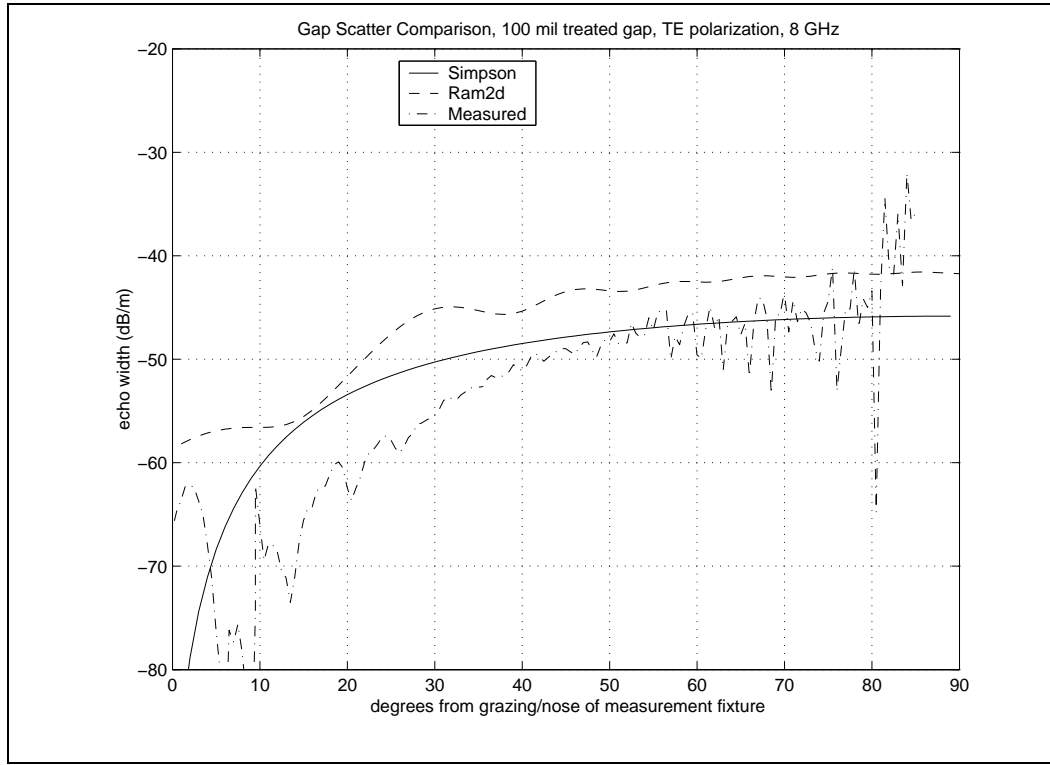


Figure 4.24 Comparison for 100 mil wide, treated rectangular gap. At 8 GHz, the slab coating material $\epsilon_r = 10.6$, $\mu_r = 1.7 - j1.3$ and the gap filler material $\epsilon_g = 15.5$, $\mu_g = 1.95 - j2.0$. The slab thickness is 40 mils.

low of 8 to a high of 30 results in discretizations ranging from 3 x 1 to the 10 x 4 used. These results are plotted in Figure 4.29 in the normal scale used earlier and in Figure 4.30 in an expanded scale to more clearly show the progression towards convergence. With the exception of the 3 x 1 discretization, which we would say is not converged, we see that the rest produce results that, essentially, are graphically equivalent on the scale of the original plot. The figure displays a clear progression to convergence and we see that even at a value of $dp = 20$ (resulting in a discretization of 7 x 3) the result is converged (the 7 x 3 curve and the 10 x 4 curve overlay in Figure 4.30).

The next case presented in Figure 4.31 is the treated gap configuration for TE polarization at 8 GHz, plotted originally in Figure 4.24. In this case, the degree of discretization is dictated by the gap filler material since it has higher relative permeability and permittivity compared to the slab coating material. Here, dp is varied from a low of 5 to a high of 25 resulting in gap region discretizations ranging from 3 x 1 to 11 x 5. Again, except for the 3 x 1 case, which could not be

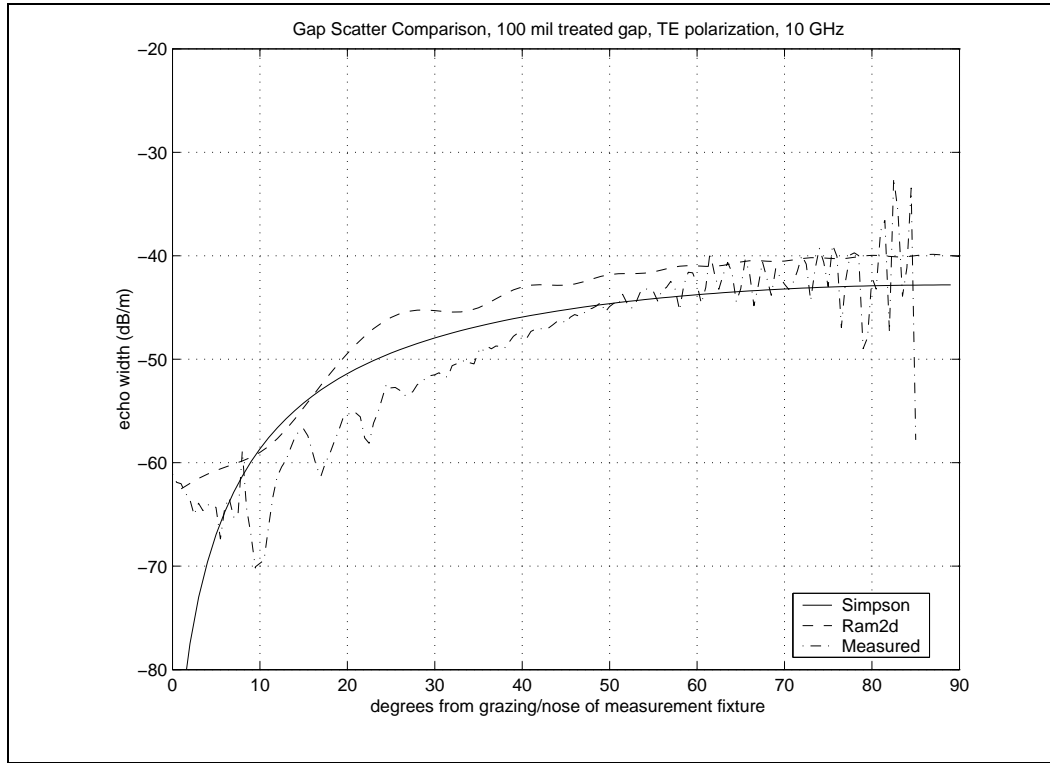


Figure 4.25 Comparison for 100 mil wide, treated rectangular gap. At 10 GHz, the slab coating material $\epsilon_r = 10.6$, $\mu_r = 1.45 - j1.3$ and the gap filler material $\epsilon_g = 15.5$, $\mu_g = 1.7 - j1.9$. The slab thickness is 40 mils.

considered converged, all others produce graphical equivalence on the original scale. Figure 4.32 then shows an expanded scale to more clearly display the convergence progress.

The Ram2d users manual [33] recommends a minimum discretization level for obtaining accurate results with Ram2d. This value, which is set as a default discretization value, was used in the Ram2d data presented in this Chapter for areas of the test body away from the gap region. Near the gap region, the discretization level can be increased above the default value. As has been mentioned earlier, in the gap region itself, Ram2d is manually set to produce a like degree of discretization as that used for the hybrid code. Ram2d was run for various cases with both finer and coarser discretizations of the numerical test body. Through this process, it was determined that the Ram2d results are converged and that the default setting for discretization of the entire test body is sufficient. The gap region itself, however, is always gridded to the same level as used by the hybrid code for each case.

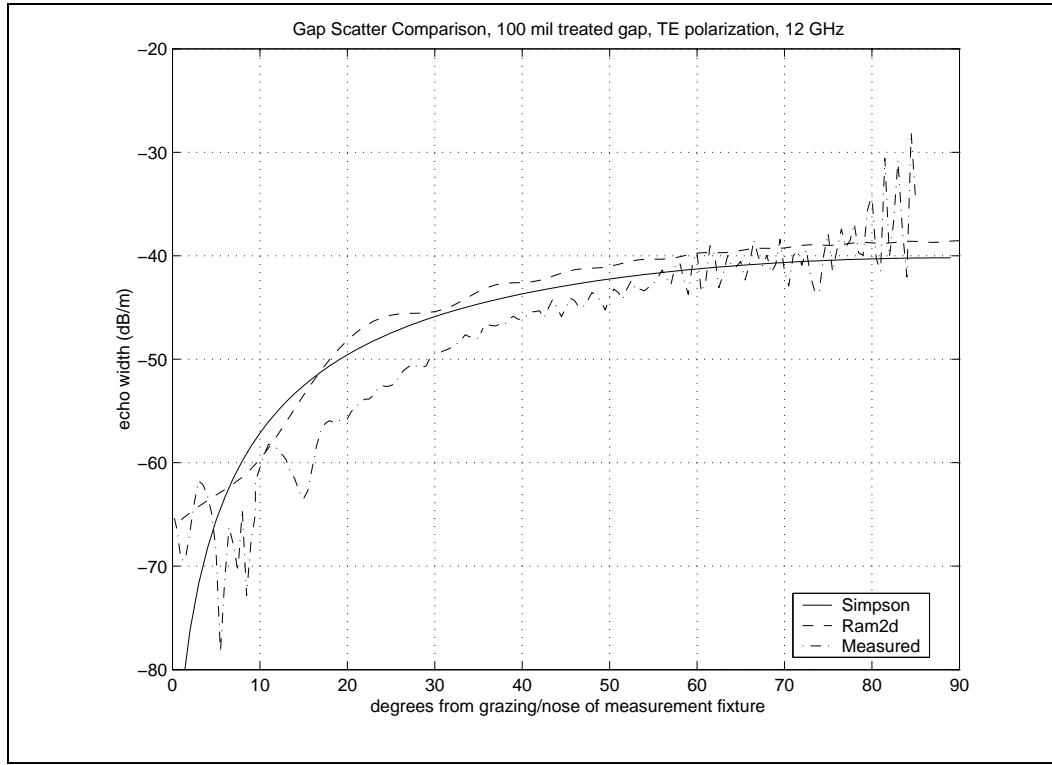


Figure 4.26 Comparison for 100 mil wide, treated rectangular gap. At 12 GHz, the slab coating material $\epsilon_r = 10.6$, $\mu_r = 1.3 - j1.3$ and the gap filler material $\epsilon_g = 15.5$, $\mu_g = 1.5 - j1.9$. The slab thickness is 40 mils.

The results in this section clearly imply that the hybrid code was at least approaching numerical convergence in the results displayed in Sections 4.3 and 4.4. Thus, the differences in agreement between the hybrid code and Ram2d are the result of other numerical factors, the most significant of which have already been mentioned.

4.6 Summary of Results

The hybrid and Ram2d codes are seen to be in good general agreement for both TM and TE polarization. Problems are evident in the hybrid code for the case of a lossy magneto-dielectric slab coating and gap filler materials in that contrast between the gap filler and the slab produces an error effect that is dual for the two polarizations: lower magnetic permeability contrast improves the TM polarization result but worsens the TE polarization result. However, it has already been noted that this effect is due to the chosen numerical implementation methods of the theory developed in Chapter 2 as opposed to a weakness in the theory itself.

For a given gap geometry at a particular frequency, the hybrid code solves a much smaller matrix than Ram2d. Because of this, the hybrid codes implemented in Matlab® (which has not been optimized in any fashion) compute the scattering result much more rapidly than Ram2d for nearly every case examined. This is really not surprising however, as Ram2d is a general purpose code and is capable of computing the scattering from a much wider variety of structures than the special purpose hybrid code.

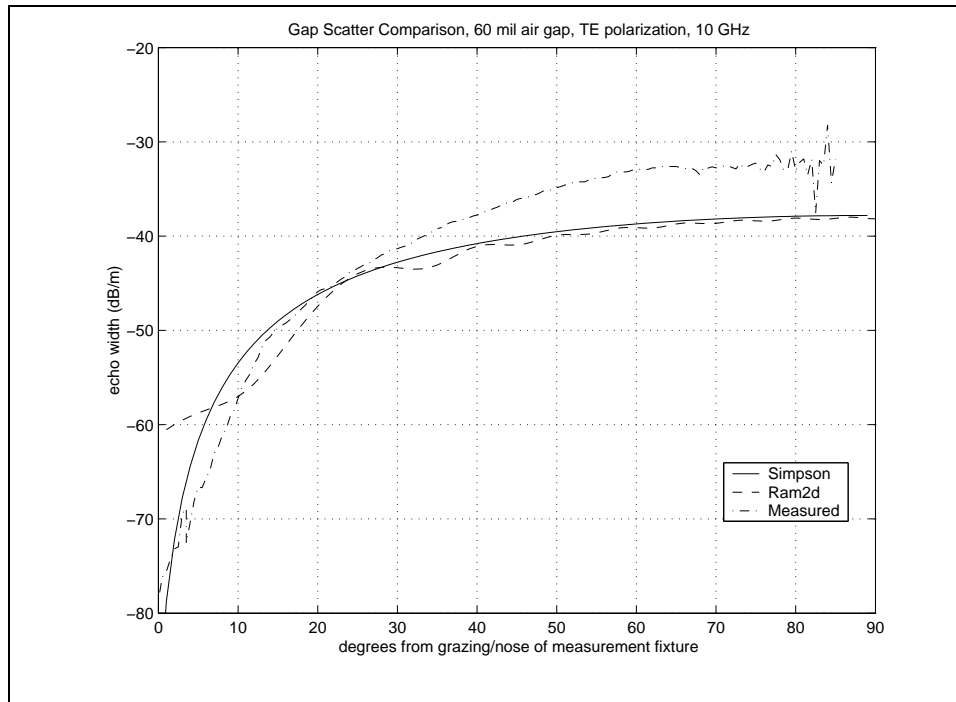


Figure 4.27 Comparison for 60 mil wide, air filled rectangular gap. At 10 GHz, the slab coating material $\epsilon_r = 10.6$, $\mu_r = 1.45 - j1.3$. The slab thickness is 40 mils.

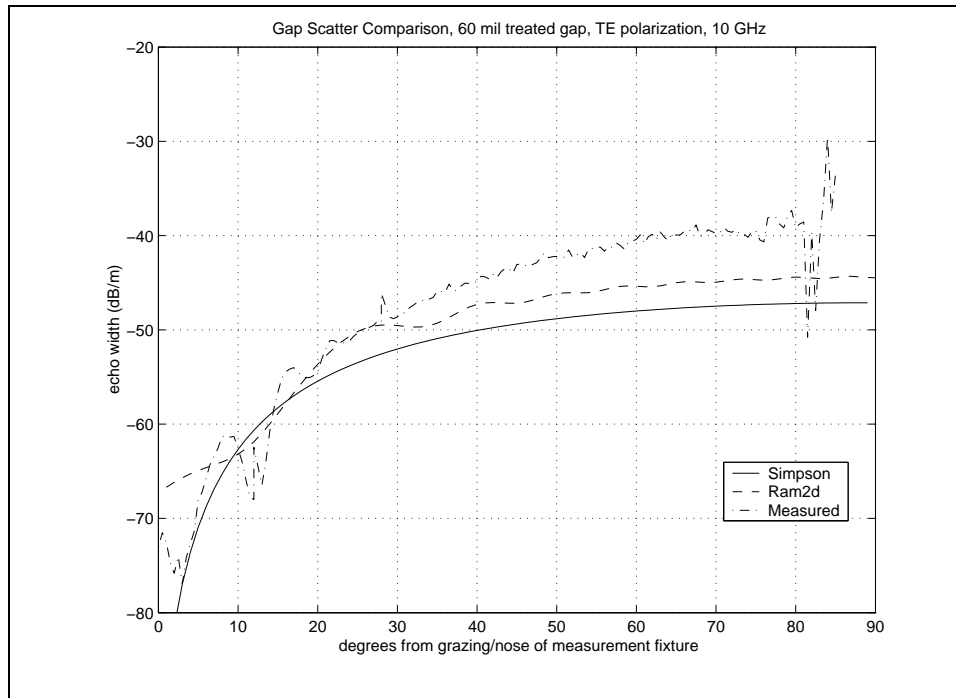


Figure 4.28 Comparison for 60 mil wide, treated rectangular gap. At 10 GHz, the slab coating material $\epsilon_r = 10.6$, $\mu_r = 1.7 - j1.3$ and the gap filler material $\epsilon_g = 15.5$, $\mu_g = 1.7 - j1.9$. The slab thickness is 40 mils.

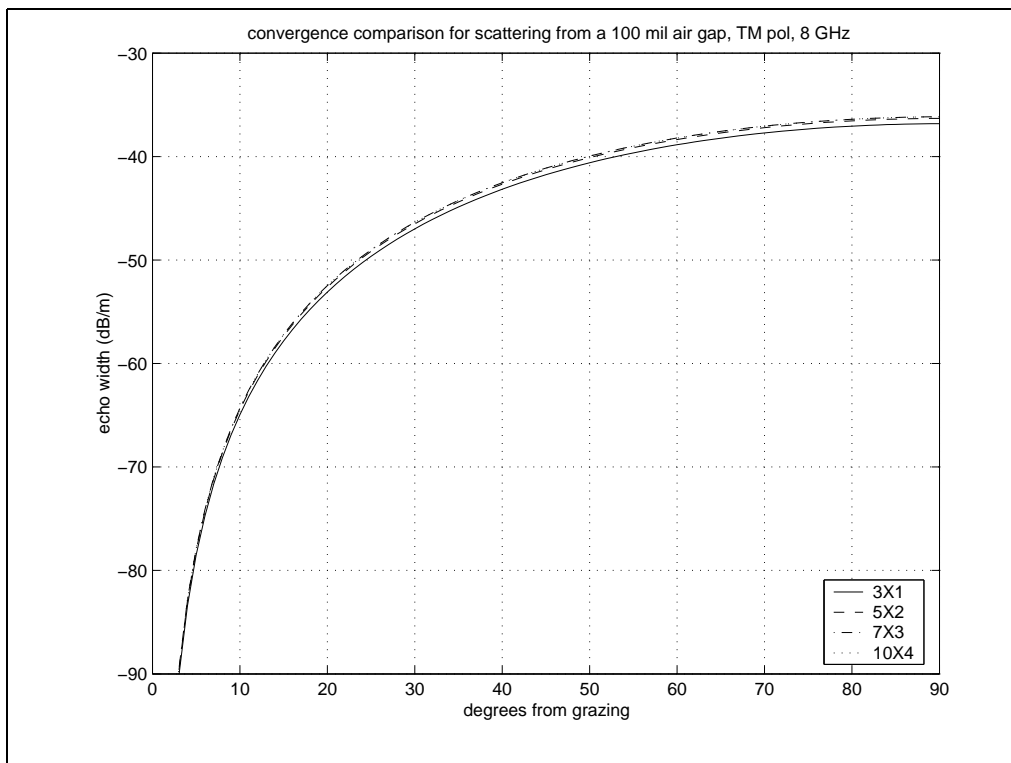


Figure 4.29 Slab coating material $\epsilon_r = 10.6$, $\mu_r = 1.7 - j1.3$. Slab thickness is 40 mils.

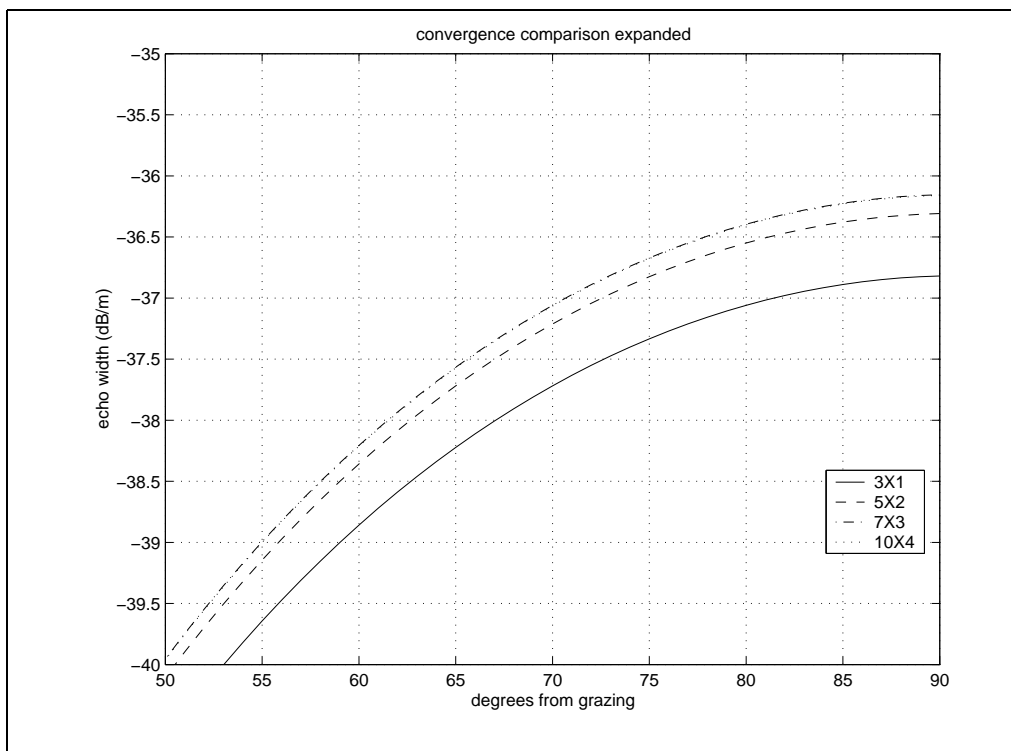


Figure 4.30 Expanded y-axis scale detailing progression toward convergence.

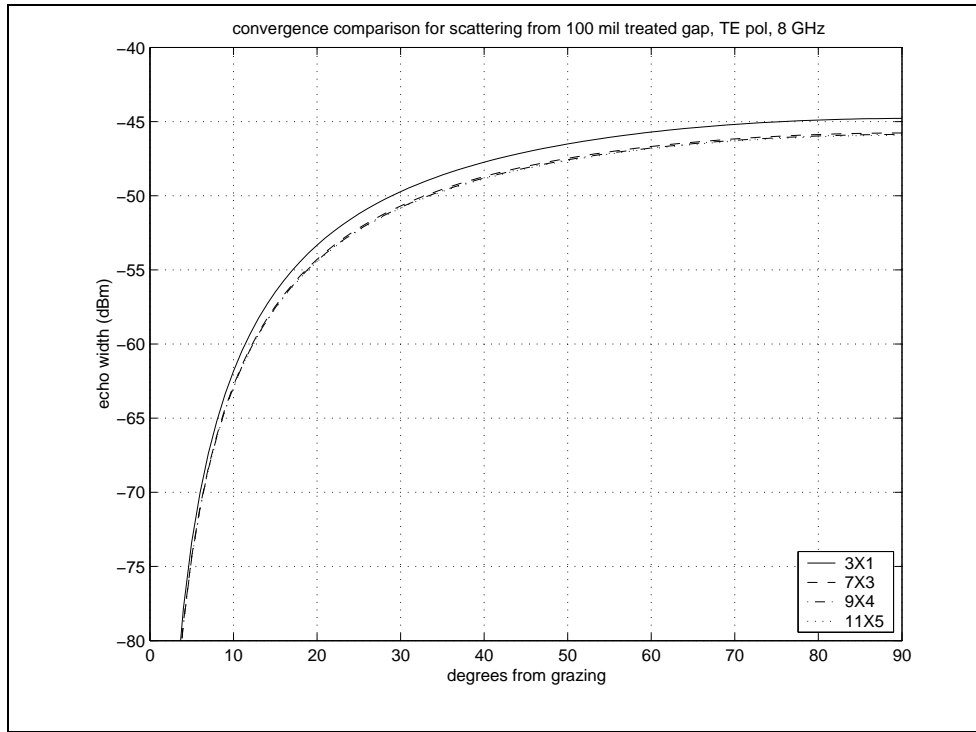


Figure 4.31 Slab coating material $\epsilon_r = 10.6$, $\mu_r = 1.7 - j1.3$; gap filler material $\epsilon_g = 15.5$, $\mu_g = 1.95 - j2.0$. Slab thickness is 40 mils.

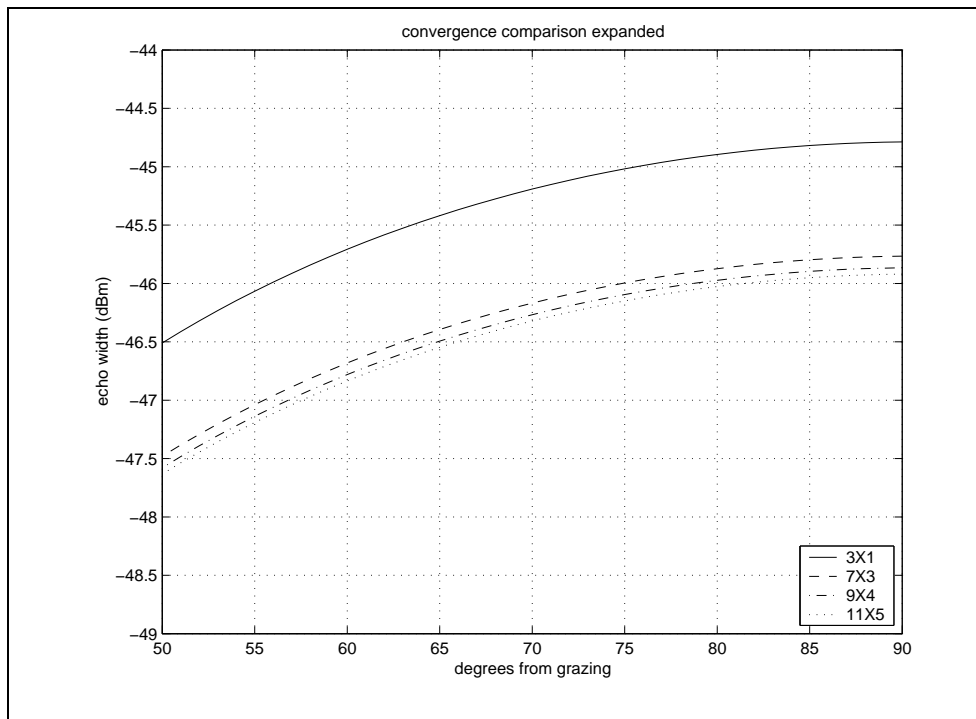


Figure 4.32 Expanded y-axis scale detailing convergence progress.

V. Summary

5.1 Conclusion

In this dissertation, the hybrid Green's function / Method of Moments (MoM) technique has been demonstrated for the problem of electromagnetic scattering from a gap in a magneto-dielectric coating on an infinite PEC ground plane. A 2D version of this hybrid technique implemented in Matlab® was compared to an industry-standard 2D FORTRAN MoM code (Ram2d), to measurements obtained in the AFRL Multispectral Measurement Facility's compact radar cross section range, and, for some cases, to a 'proof of concept' code developed by former AFIT faculty member Major J.P. Skinner (described in Appendix F). From the results presented in Chapter 4, the technique is seen to work well for the case of TM polarization. The technique also works for the TE polarization case but is less robust compared to the TM polarization case due to the more severe singularities encountered in the Green's functions and T-factors for TE polarization.

Compared to 'standard' MoM computer codes the hybrid Green's function / MoM technique trades off impedance matrix solve time for matrix fill time. Additionally, it also trades off two runs of the standard MoM code (since runs with and without the gap present in the numerical test body are required) to determine the scattering due specifically to the presence of the gap to a single run of the hybrid code. While the Ram2d code is a well-optimized FORTRAN code compiled and run on a single UltraSPARC-II processor workstation running at 450 MHz, for many cases the hybrid code, written and run in the Matlab® programming environment, is much faster on a 450 MHz Pentium II PC running multiple applications. However, for some cases the TE polarization code can be very slow since the numerical integration routines in Matlab® take longer to converge in the TE case. In fact, for a lossless slab coating, Matlab® numerical integration routines in the current implementation of the TE polarization code do not converge.

Thus, we conclude this dissertation by stating that the hybrid technique is a qualified success. More work is needed, however, to bring it to the point where it could be employed in an actual engineering environment, and many questions remain concerning the scope of applicability of the hybrid code. For instance, for slab coating materials with higher constitutive property values (higher index of refraction), the singularities (in the bounce correction integrands) occurring at the

critical angles will move closer together. At some point, the currently implemented integration routine will require modification to be able to adequately address that case.

In the following section, we recommend and discuss several additional areas of improvement in both the theory and the computer codes developed in this dissertation.

5.2 *Recommendations for Further Development*

One of the original premises of this work was that by developing the bounce correction term of the Green's function through use of the Array Scanning Method we could avoid the requirement to evaluate Sommerfeld integrals. We show in Appendix B that the two approaches are in fact very closely related, the major difference being the evaluation of the ASM integrals based on the concept of a spectrum of distinct plane wave modes. The ASM is formulated so that the integration of the bounce correction term is performed along the real axis of the scan angle parameter variable of integration. In our numerical implementation, this integration is performed allowing for finite jumps at the location of potential singularities. This is seen to work well enough for the case of TM polarization. However, the stronger singularities encountered in the TE polarization case argue that a more sophisticated singularity extraction procedure is needed, and this is the first recommendation. Successful application of an improved singularity extraction algorithm (e.g., Methods II or III of Section 6.2 of [39]) would undoubtedly broaden the applicability of the TE polarization code.

Another original premise of this work was that the pulse basis / delta function testing procedure—also known as point matching—would be adequate in the MoM solution. This produced disagreement in the results of the codes compared for cases where, say, in the TM polarization case, the slab coating possessed $|\mu_r| > 1$ because that solution requires the presence of magnetic volume equivalent currents. For the TM polarization case, magnetic volume equivalent currents introduce derivatives of the scalar (or canonical) Green's function term into the solution vector, and with the pulse basis set approximation, produces numerical artifacts that do not approximate well the equivalent currents in the gap region. To avoid this difficulty, it is recommended that smoother basis and testing functions be employed in the MoM procedure. This recommendation is also made by Peterson [34] and the interested reader is directed there for more details. The price one pays, however, in using smoother basis and testing functions in the hybrid formulation is that more

function evaluations of the ASM-derived bounce correction integrals are required, which will add to the overall amount of computation time.

Some improvements can also be implemented in terms of the shape of the gaps analyzed by the code. Currently, the code is restricted to analyzing gaps that are trapezoidal in shape. This limitation could be overcome by using a different algorithm for gridding the gap region. Nothing in the theory developed in Chapter 2 restricts application to a gap, say, of triangular shape, where the sides of the gap come to a vertex at the bottom of the gap. Only the gridding algorithm used in the current implementation prevents us from analyzing that case. Another limitation of the current code (but, again, not in the theory) is that the gap region must be of the same depth as the slab coating material. To remove this restriction would require that a T-factor for such a case be developed. Also, the current gap region gridding algorithm restricts the gap to be filled with a homogeneous material. As material property inputs to the code are currently structured, gap filler material properties are assigned equally to all cells within the gap region. This could easily be altered to assign properties to either specific cells or specific rows of cells, thus allowing for inhomogeneous gap fillers, with no changes to the theoretical formulation presented in Chapter 2.

The final recommendation is for the obvious extensions of the theory and codes to the 2D oblique incidence case and, eventually, to the full 3D case. While analysis of 2D gaps provides insight into the scattering levels resulting from a gap, the ultimate question would be of their contribution to the RCS of some platform of interest. 3D gaps will be much more complicated in their geometry so much of the effort here would be in techniques for gridding of the 3D gaps. The spectral domain Green's functions and T-factors for the 3D case are readily available in the literature [19].

Appendix A. Spatial Domain to Spectral Domain Transformation via the Poisson Sum Formula

Consider the Green's function of a single radiating 2-D wire element in a magneto-dielectric medium as in Equation (2.1). The Green's function for such an element is known to be [15, 17, 18]

$$G_{wire}(\bar{\rho}, \bar{\rho}') = -\frac{j}{4} H_o^{(2)}(k | \bar{\rho} - \bar{\rho}' |) \quad (\text{A.1})$$

where again, k is the propagation constant in the magneto-dielectric medium and is in general a complex number, $k = k' - jk''$.

Now imagine creating an infinite array of wires around this wire, parallel to the x -axis, with inner-element spacing D_x as was done in Section 2.1 (see Figure (2.2)). Each element has a current of like amplitude but is shifted in phase by an amount proportional to the spacing between the elements in accordance with the Floquet Theorem [1, 26]. The Green's function for this array will then be

$$G_{array, spatial}(\bar{\rho}, \bar{\rho}') = -\frac{j}{4} \sum_{m=-\infty}^{\infty} H_o^{(2)} \left(k \sqrt{(mD_x - (x - x'))^2 + (y - y')^2} \right) e^{jk' s_x m D_x} \quad (\text{A.2})$$

which is identical to Equation (2.2). Note that the phase progression on each of the array elements is dictated by k' , the real part of k , as the loss component of the propagation constant plays no role in the phase progression between the elements.

In Section 2.1, we stated that the Poisson Sum formula was used to convert this spatial domain sum into a spectral domain sum which was likely to converge much more quickly than the original spatial domain sum. In this appendix, we briefly outline the procedure used to arrive at Equation (2.3).

The Poisson Sum formula is stated as [19, 21]

$$\sum_{m=-\infty}^{\infty} \mathcal{F}(m\omega_o) e^{jm\omega_o t} = T \sum_{n=-\infty}^{\infty} f(t + nT) \quad (\text{A.3})$$

in which $\mathcal{F}(\omega)$ and $f(t)$ represent a Fourier transform pair defined as

$$\int_{-\infty}^{\infty} f(t) e^{-j\omega t} dt = \mathcal{F}(\omega) \leftrightarrow f(t) = \frac{1}{2\pi} \int_{-\infty}^{\infty} \mathcal{F}(\omega) e^{j\omega t} d\omega$$

To convert the sum of Hankel functions into it's spectral domain equivalent, we utilize transform pair 917 from [29]. In our notation, and employing the equality $K_o(jz) = \frac{\pi}{2j} H_o^{(2)}(z)$ [15: Appendix IV], this transform pair can be expressed as

$$H_o^{(2)}\left(k\sqrt{\omega^2 + y^2}\right) \leftrightarrow \frac{e^{-jy\sqrt{k^2 - t^2}}}{\pi\sqrt{k^2 - t^2}} \quad (\text{A.4})$$

To proceed with the Poisson Sum formula, we identify $\mathcal{F}(m\omega_o) = H_o^{(2)}(\cdot)$ and make the following variable associations: $m\omega_o = mD_x$, $t = k's_x$, $T = \frac{2\pi}{\omega_o} = \frac{2\pi}{D_x}$, $t + nT = k's_x + \frac{2\pi n}{D_x}$. We now insert these variables into their respective places to arrive at the following spatial domain - spectral domain identity,

$$\frac{-j}{4} \sum_{m=-\infty}^{\infty} H_o^{(2)}\left(k\sqrt{(mD_x)^2 + y^2}\right) e^{jk'mD_x s_x} = \frac{-j}{4} \frac{2\pi}{D_x} \sum_{n=-\infty}^{\infty} \frac{e^{-jy\sqrt{k^2 - (k's_x + \frac{2\pi n}{D_x})^2}}}{\pi\sqrt{k^2 - (k's_x + \frac{2\pi n}{D_x})^2}}$$

Next, through the Fourier Transform shifting property, we shift the spatial side by x , observe the consequent spectral shift, and make some obvious simplifications to arrive at

$$\frac{-j}{4} \sum_{m=-\infty}^{\infty} H_o^{(2)}\left(k\sqrt{(mD_x - x)^2 + y^2}\right) e^{jk'mD_x s_x} = \frac{-j}{2D_x} \sum_{n=-\infty}^{\infty} e^{-jx(k's_x + \frac{2\pi n}{D_x})} \frac{e^{-jy\sqrt{k^2 - (k's_x + \frac{2\pi n}{D_x})^2}}}{\sqrt{k^2 - (k's_x + \frac{2\pi n}{D_x})^2}}$$

As a final step, we shift the field point (x, y) away from the source point (x', y') to give us the slightly more general result

$$\begin{aligned} G_{array}(\bar{\rho}, \bar{\rho}') &= \frac{-j}{4} \sum_{m=-\infty}^{\infty} H_o^{(2)}\left(k\sqrt{(mD_x - (x - x'))^2 + (y - y')^2}\right) e^{jk'mD_x s_x} \\ &= \frac{-j}{2D_x} \sum_{n=-\infty}^{\infty} e^{-j(x-x')(k's_x + \frac{2\pi n}{D_x})} \frac{e^{-j(y-y')\sqrt{k^2 - (k's_x + \frac{2\pi n}{D_x})^2}}}{\sqrt{k^2 - (k's_x + \frac{2\pi n}{D_x})^2}} \end{aligned} \quad (\text{A.5})$$

At this point, application of the Poisson Sum formula is complete and Equation (A.5) displays the spatial domain - spectral domain equivalent representations of the Green's function of the 2-D infinite array of wire element radiators. We can now set the array spacing parameter D_x to give us our final result. For this, we choose to set $D_x = \frac{\lambda}{2}$ where λ is the wavelength in the medium in which the array resides. In the geometry of this dissertation, that will be the wavelength within the magneto-dielectric slab medium. With D_x set to $\frac{\lambda}{2}$, we note that $\frac{2\pi n}{D_x} = \frac{4\pi n}{\lambda} = 2k'n$. Placing this into (A.5), we now have our final form for the spectral domain Green's function.

$$G_{array, spectral}(\bar{\rho}, \bar{\rho}') = \frac{-j}{2kD_x} \sum_{n=-\infty}^{\infty} e^{-jk(x-x')\frac{k'}{k}(s_x+2n)} \frac{e^{-jk(y-y')\sqrt{1-(\frac{k'}{k}(s_x+2n))^2}}}{\sqrt{1-(\frac{k'}{k}(s_x+2n))^2}} \quad (A.6)$$

The factor D_x in the denominator is left unchanged at this time because it will be utilized later as will be seen in Appendix B on the application of the array scanning method to this Green's function expression.

We see that factors introduced in Chapter 2 can now be readily identified from this spectral domain expression. We have $r_x = \frac{k'}{k}(s_x + 2n) = \frac{Re(k)}{k}(s_x + 2n)$ and $r_y = \sqrt{1 - r_x^2}$. How these factors are employed is explained in greater detail in Chapter 2, especially those factors entering into the choice of the root of r_y . By using these definitions, we can further compact the spectral domain expression into the form given in Equation (2.3), repeated here for convenience.

$$G_{array} = -\frac{j}{2kD_x} \sum_{n=-\infty}^{\infty} \frac{e^{-jk(\bar{\rho}-\bar{\rho}') \cdot \hat{r}_{1\pm}}}{r_{y1}} \quad (A.7)$$

Appendix B. The Array Scanning Method

We saw in Appendix A how the Poisson Sum formula is used to derive our spectral domain Green's function formula, Equation (2.3). If we look again at the spatial domain expression, Equation (2.2),

$$\begin{aligned} G_{array}(\bar{\rho}, \bar{\rho}') &= -\frac{j}{4} \sum_{m=-\infty}^{\infty} H_o^{(2)} \left(k \sqrt{(mD_x - (x - x'))^2 + (y - y')^2} \right) e^{jk' s_x m D_x} \\ &= \sum_{m=-\infty}^{\infty} G_m e^{jk' s_x m D_x} \end{aligned} \quad (\text{B.1})$$

we see that Equation (B.1) is a Fourier series and note that the zeroth order ($m = 0$) coefficient of the series, $G_o = G_{wire}(\bar{\rho}, \bar{\rho}')$, Equation (A.1).

The motivation for our use of the Array Scanning Method is to obtain a spectral domain Green's function expression for a single wire element radiator analogous to Equation (A.1). To do this, we step back and consider the Fourier series of a periodic function. From [20], we designate $f(t)$ an arbitrary but periodic function with period T such that $f(t + T) = f(t)$. The usual relationships associated with a Fourier series can be written for this function, such as expressing it as a sum of exponentials,

$$f(t) = \sum_{n=-\infty}^{\infty} c_n e^{jn\omega_o t}, \quad \omega_o = \frac{2\pi}{T}$$

where

$$c_n = \frac{1}{T} \int_{-T/2}^{T/2} f(t) e^{-jn\omega_o t} dt$$

We can also form the function

$$f_o(t) = \begin{cases} f(t) & |t| < \frac{T}{2} \\ 0 & |t| > \frac{T}{2} \end{cases}$$

and express $f(t)$ as the sum

$$f(t) = \sum_{n=-\infty}^{\infty} f_o(t + nT)$$

We next define the transform of $f_o(t)$

$$\mathcal{F}_o(\omega) = \int_{-\infty}^{\infty} f_o(t) e^{-j\omega t} dt = \int_{-T/2}^{T/2} f(t) e^{-j\omega t} dt \quad (\text{B.2})$$

and, by implication, the additional relationship

$$c_n = \frac{1}{T} \int_{-T/2}^{T/2} f(t) e^{-jn\omega_o t} dt = \frac{\mathcal{F}_o(n\omega_o)}{T} \quad (\text{B.3})$$

equating the coefficients c_n of the Fourier series of $f(t)$ to the Fourier transform $\mathcal{F}_o(\omega)$ of the function $f_o(t)$.

From Appendix A, we write the shifted Poisson Sum formula

$$\sum_{m=-\infty}^{\infty} \mathcal{F}(m\omega_o + W) e^{jm\omega t} = T \sum_{n=-\infty}^{\infty} e^{-jW(t+nT)} f(t + nT)$$

and apply Equations (B.2) and (B.3), with $m = 0$, to get

$$\mathcal{F}_o(W) = \int_{-T/2}^{T/2} \sum_{n=-\infty}^{\infty} e^{-jW(t+nT)} f(t + nT) dt = T c_o$$

or

$$c_o = \frac{1}{T} \int_{-T/2}^{T/2} \sum_{n=-\infty}^{\infty} e^{-jW(t+nT)} f(t + nT) dt \quad (\text{B.4})$$

If we relate this result back to our discussion of the spatial and spectral domain forms of the Green's function for the single wire element radiator, and the comments immediately following Equation (B.1), we see we have arrived at an equivalence of G_o , the spatial domain Green's function for the single wire element radiator (Equation (A.1)), to the spectral domain expression on the right hand side.

Recognizing the form of the right hand side of Equation (B.4), we insert Equation (A.6) and utilize the same variable substitutions and simplifications defined for application of the Poisson Sum formula in Appendix A. This results in the relation

$$-\frac{j}{4} H_o^{(2)}(k | \bar{\rho} - \bar{\rho}' |) = \frac{-j}{4\pi k} \int_{-k'}^{k'} \sum_{n=-\infty}^{\infty} e^{-jk(x-x') \frac{k'}{k}(s_x+2n)} \frac{e^{-jk(y-y') \sqrt{1-(\frac{k'}{k}(s_x+2n))^2}}}{\sqrt{1-(\frac{k'}{k}(s_x+2n))^2}} d(k' s_x)$$

As a last step, we relocate the constant k' and simplify the corresponding limits of integration to arrive at our final form

$$G_{wire}(\bar{\rho}, \bar{\rho}') = \frac{-jk'}{4\pi k} \int_{-1}^1 \sum_{n=-\infty}^{\infty} e^{-jk(x-x')\frac{k'}{k}(s_x+2n)} \frac{e^{-jk(y-y')\sqrt{1-(\frac{k'}{k}(s_x+2n))^2}}}{\sqrt{1-(\frac{k'}{k}(s_x+2n))^2}} ds_x \quad (\text{B.5})$$

which relates the integrated sum of plane waves emanating from the artificial array of wire element radiators to the Green's function for the single wire element radiator. The spectral domain integral has the physical interpretation of scanning the artificial array phasing through an angle range restricted to real space, $-1 \leq s_x \leq 1$, thereby summing the contribution from each real plane wave mode. And so, as alluded to a number of times before, the technique is referred to as the 'Array Scanning Method' (ASM).

It is fair to ask what has been gained through this sequence of manipulations. As stated in several sources [27, 28], the spatial domain Green's functions do not lend themselves to problems containing stratified-layer geometries.¹ The need to incorporate Fresnel reflection and transmission coefficients dictates that a spectral domain expression be used since the integrand of our ASM integral is an expansion in which each 'mode' is a plane wave term. The Fresnel reflection and transmission coefficients then modify each plane wave term accordingly. It remains only to introduce the T-factor concept [19, 21] to incorporate a stratified layer geometry (in our case, a magneto-dielectric slab) into the problem. The T-factor will not alter the phase relationship between the array elements and therefore, does not alter the scan integration. Thus, one is left with an expression for the field from a single wire in terms of the field from an infinite array of wires.

Another way to arrive at the same formal expression as the ASM integral result is by comparison to the perhaps more familiar Sommerfeld integral expressions found in the literature. From [28: (33), pg 487], for instance, the spectral domain free space Green's function is given as (in our coordinate geometry),

$$\bar{G}_f(\hat{\rho}, \hat{\rho}') = \frac{-j}{4\pi} \int_{-\infty}^{\infty} \frac{\exp \left[-j\eta(x-x') - j\sqrt{k^2 - \eta^2}|y-y'| \right]}{\sqrt{k^2 - \eta^2}} d\eta \quad (\text{B.6})$$

¹these comments are equally valid for the three-dimensional case

We make the variable substitution $\eta = kr_x \rightarrow d\eta = kdr_x$ and pull the factor k out of the square root terms. This results in the expression

$$\bar{G}_f(\hat{\rho}, \hat{\rho}') = \frac{-j}{4\pi} \int_{-\infty}^{\infty} \frac{\exp \left[-jk(x-x')r_x - jk\sqrt{1-r_x^2}|y-y'| \right]}{\sqrt{1-r_x^2}} dr_x$$

and we see that we can again make the assignment $r_y = \sqrt{1-r_x^2}$. Inserting this into the expression above and collecting like terms enables us to write,

$$\bar{G}_f(\hat{\rho}, \hat{\rho}') = \frac{-j}{4\pi} \int_{-\infty}^{\infty} \frac{e^{-jk[(x-x')r_x + |y-y'|r_y]}}{r_y} dr_x \quad (\text{B.7})$$

In our ASM integral, the variable r_x was split into two parts, a continuous variable part s_x plus an additive discrete variable part $2n$. Taken together, these two components of r_x , weighted by the complex constant $\frac{Re(k)}{k}$, constituted a continuous variable over an infinite range. We see that is exactly what we've obtained starting from the Sommerfeld integral expression. To complete the comparison, we introduce modifications to Equation (B.7) that will put it in precisely the same form as Equation (B.5), most of these arguments being based on physical reasoning.

First, we introduce a notation to emphasize the functional dependence of r_x on both s_x and n . We do this by setting $r_x \rightarrow C(s_x, n)$, where C is the complex constant $\frac{Re(k)}{k}$. Next, we break up the infinite integration range and create an infinite series of finite integrals over s_x . We write this as

$$\begin{aligned} \bar{G}_f(\hat{\rho}, \hat{\rho}') = & \dots - \frac{j}{4\pi} \int_{-\ell}^{\ell} \frac{e^{-jk[(x-x')C(s_x, n) + |y-y'|r_y]}}{r_y} d(C(s_x, n)) \Big|_{n_{-1}} \\ & - \frac{j}{4\pi} \int_{-\ell}^{\ell} \frac{e^{-jk[(x-x')C(s_x, n) + |y-y'|r_y]}}{r_y} d(C(s_x, n)) \Big|_{n_0} \\ & - \frac{j}{4\pi} \int_{-\ell}^{\ell} \frac{e^{-jk[(x-x')C(s_x, n) + |y-y'|r_y]}}{r_y} d(C(s_x, n)) \Big|_{n_1} \dots \quad (\text{B.8}) \end{aligned}$$

where l is some finite range of integration on the variable s_x and we have not yet specified the functional form for n . We have, however, implicitly specified our desire that n be such that the integration is symmetric over s_x , i.e., that the range of integration be symmetric from $-l$ to $+l$. We

also admit that we will force n into the role of a discrete variable such that $dr_x = Cds_x$ in each integral in the series.

At this point, we desire to maintain the physical interpretation of scanning the phase of the artificial array and that s_x be interpreted as a scan angle parameter (direction cosine). Looking normally into the array, we equate s_x to the sine of the angle from normal and scan from -90° to $+90^\circ$. This will enable us to set $l = 1$. With this range established, it is then a simple argument that the functional form for n be simply $+2n$ in order to maintain the continuity of the original integration variable. Thus we establish $(s_x, n) = (s_x + 2n)$ and the infinite sum of integrals is expressed as

$$\bar{G}_f(\hat{\rho}, \hat{\rho}') = \frac{-j Re(k)}{4\pi k} \sum_{n=-\infty}^{\infty} \int_{-1}^1 \frac{e^{-jk \left[(x-x') \frac{Re(k)}{k} (s_x+2n) + |y-y'| r_y \right]}}{r_y} ds_x \quad (B.9)$$

where C has been replaced by the value $\frac{Re(k)}{k}$ and the functional form of r_x is implicit in each occurrence of the variable r_y . Arguments regarding the order of integration and summation are given elsewhere in this dissertation and it should suffice to say that convergence of the integrals demonstrated in Chapters 2 and 3 (including those containing the T-factors) validate the interchange of the operations. This expression is therefore identical to Equation (B.4) and is our desired result.

This completes our look at the Array Scanning Method and demonstrates that it is both completely rigorous and is a special case of the Sommerfeld integral representation seen frequently in the literature.

Appendix C. Additional Plots of the ASM Integrand

In Section 3.1, a number of plots of various ASM-derived Green's function bounce correction term integrands were presented to provide insight into the challenges faced by the numerical integration routine needed to evaluate these terms. In this appendix, a number of additional cases are presented in an effort to complete the discussion. We present these additional cases in this appendix to minimize disruption of flow of the text in Chapter 3. We reiterate, however, that we intentionally present only a small set of plots as it would be impossible to present plots representative of every conceivable case. Our goal in this appendix is to present cases that collectively exhibit all the features of these integrand functions that directly impact the numerical integration process. Integrand function behavior for cases of different slab coating material properties is similar to the behavior exhibited in the plots displayed here and in Section 3.1. We also refer the reader to Figure 3.1 for we will again assume this geometry of the gap region for the figures presented in this appendix.

C.1 Additional Integrand Functions for Dyadic Green's Function Components

In Section 3.1.2, plots of various components of the dyadic Green's function matrix were presented for a case where the slab coating material had the lossless constitutive properties $\epsilon_r = 3.25$, $\mu_r = 2$, for both TM and TE polarization. We also noted that the TE polarization case produces more strongly singular integrand function behavior. Simply stated, the TE polarization case is the more difficult to handle from the point of view of a numerical integration routine and most of the plots presented in this appendix will be for that polarization.

In this section, we present additional plots of these matrix Green's function components but for the case where the slab coating material has the lossy constitutive properties $\epsilon_r = 3.25$, $\mu_r = 2 - j1$ to complement the plots presented in Section 3.1.2 for lossless material properties. We will restrict the plots presented to the case of TE polarization since adding the loss component renders the TM polarization integrand functions comparatively easy to integrate (though still requiring numerical integration). The frequency will again be set to 11.8 GHz, the slab coating material thickness is taken to be 40 mils, and the source point (x', y') and field point (x, y) are placed at $(0, 0)$, $(100, 40)$ respectively, as was done for all the cases plotted in Chapter 3.

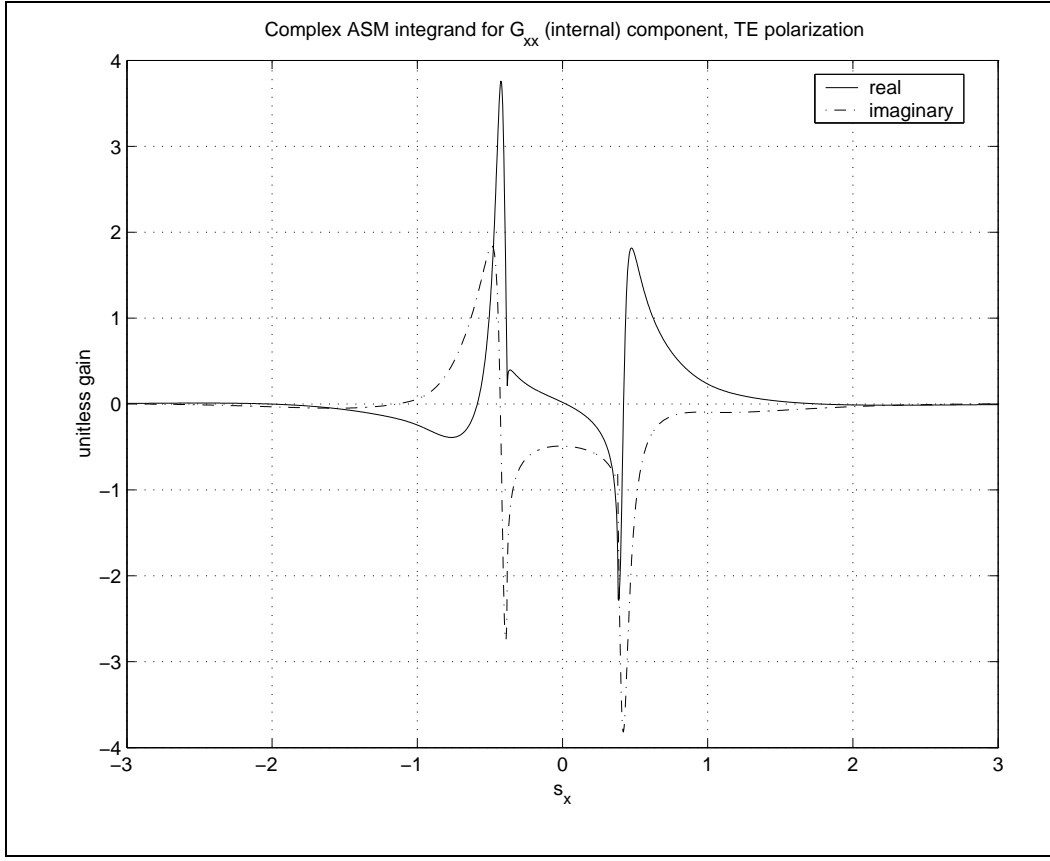


Figure C.1 Source point at $(x', y')=(0, 0)$, field point at $(x, y)=(100, 40)$. Slab coating material $\epsilon_r = 3.25$, $\mu_r = 2.0 - j1$.

In Figure C.1, we display the G_{xx} integrand function for the case where the slab coating material has the indicated lossy constitutive properties. For convenience, we display the equation here again,

$$G_{bounce, xx} = \frac{jRe(k_1)}{4\pi k_1} \int_{-1}^1 \sum_{n=-\infty}^{\infty} T r_{y1} e^{-jk_1[(x-x')r_{x1} + |y-y'|r_{y1}]} ds_{x1} \quad (C.1)$$

and note that T is the T-factor for TE polarization given in Equation (2.56). We see the function exhibits singular behavior at the critical angles (which occur, for this choice of slab coating material properties, at $|s_x| \simeq 0.3811$) but not at $s_x = \pm 1$. The function decays to zero fairly rapidly beyond $|s_x| > 1$ and there is no evidence of symmetry in the function.

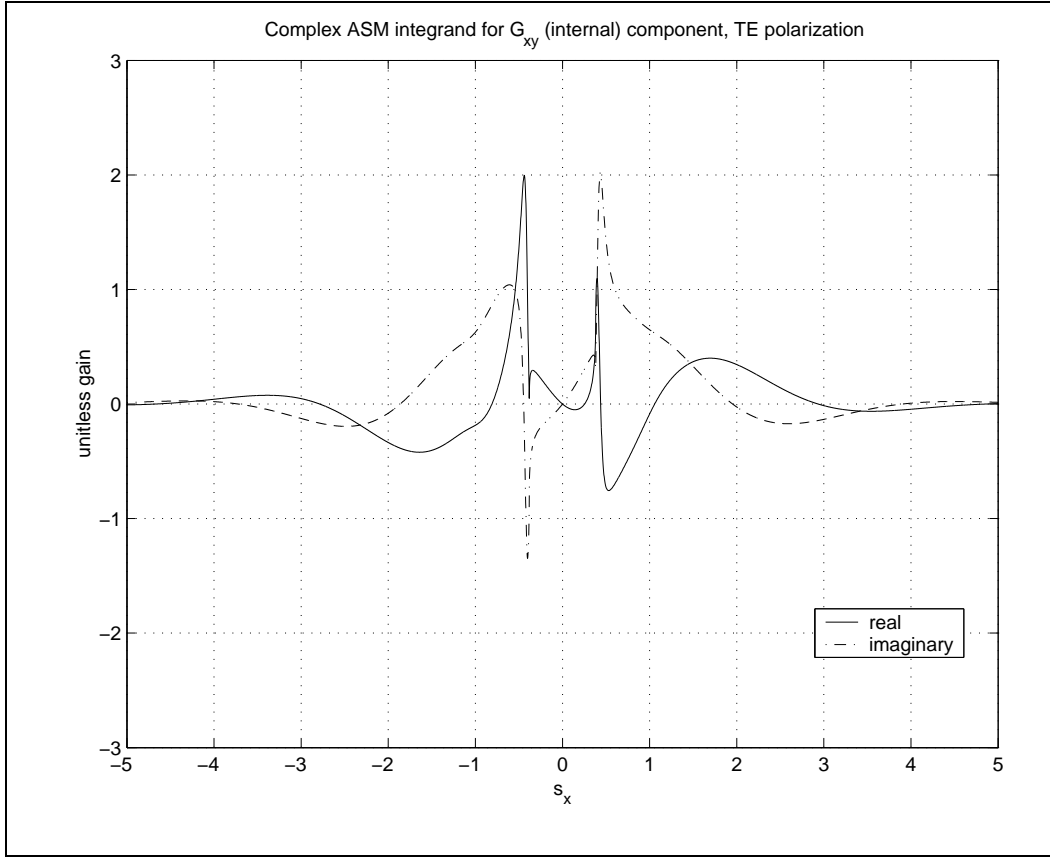


Figure C.2 Source point at $(x', y')=(0, 0)$, field point at $(x, y)=(100, 40)$. Slab coating material $\epsilon_r = 3.25$, $\mu_r = 2 - j1$.

Figure C.2 shows the G_{xy} component integrand function. The equation for this component of the Green's function is

$$G_{bounce, xy} = -\frac{jRe(k_1)}{4\pi k_1} \int_{-1}^1 \sum_{n=-\infty}^{\infty} T^r r_{x1} e^{-jk_1[(x-x')r_{x1} + |y-y'|r_{y1}]} ds_{x1} \quad (C.2)$$

where T^r is the reduced T-factor for TE polarization given by Equation (2.58). As we saw in Figure C.1, this function also exhibits the singularity at the critical angles but not at $s_x = \pm 1$. And while again there is no evidence of symmetry, this function decays to zero more slowly than did the G_{xx} component.

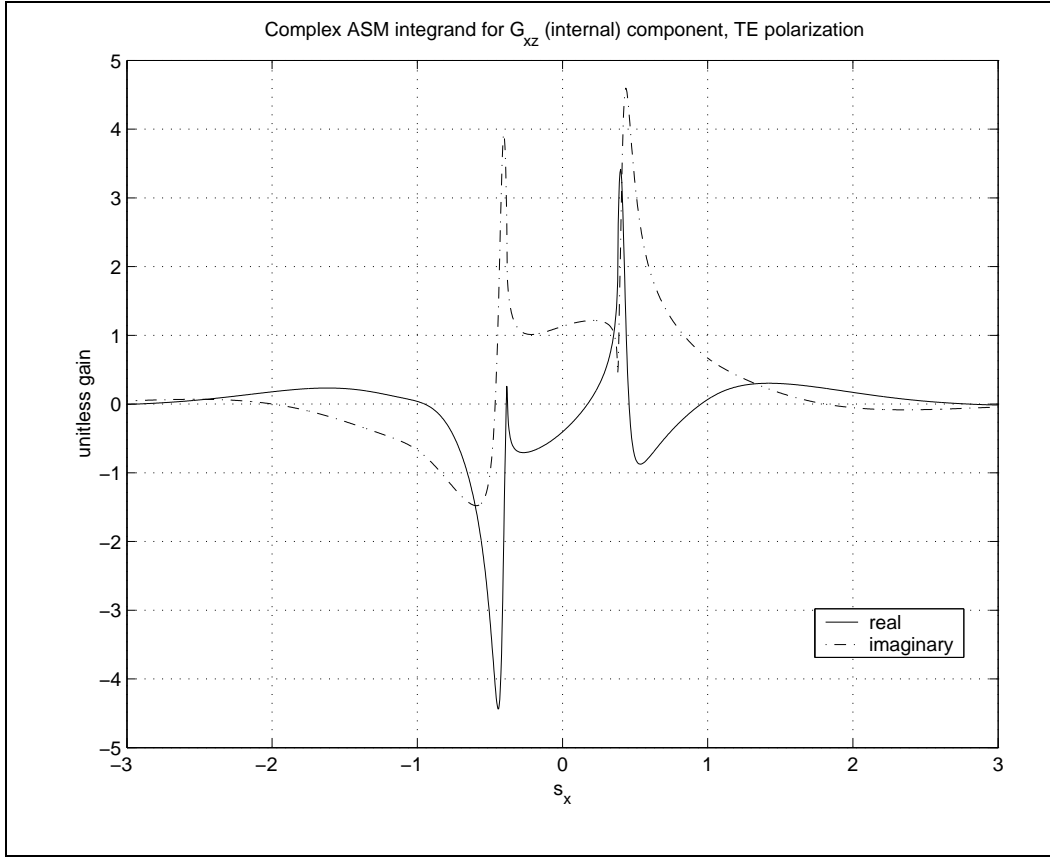


Figure C.3 Source point at $(x', y')=(0, 0)$, field point at $(x, y)=(100, 40)$. Slab coating material $\epsilon_r = 3.25$, $\mu_r = 2 - j1$.

The G_{xz} component is plotted in Figure C.3. The equation for this function is given by

$$G_{bounce, xz} = \frac{Re(k_1)}{4\pi} \int_{-1}^1 \sum_{n=-\infty}^{\infty} T^r e^{-jk_1[(x-x')r_{x1} + |y-y'|r_{y1}]} ds_{x1} \quad (C.3)$$

Again, we see the singularities at only the critical angles. We truncate the plot to $|s_x| = 3$ as the function has nearly decayed to zero at this point. No symmetry is evident in this function.

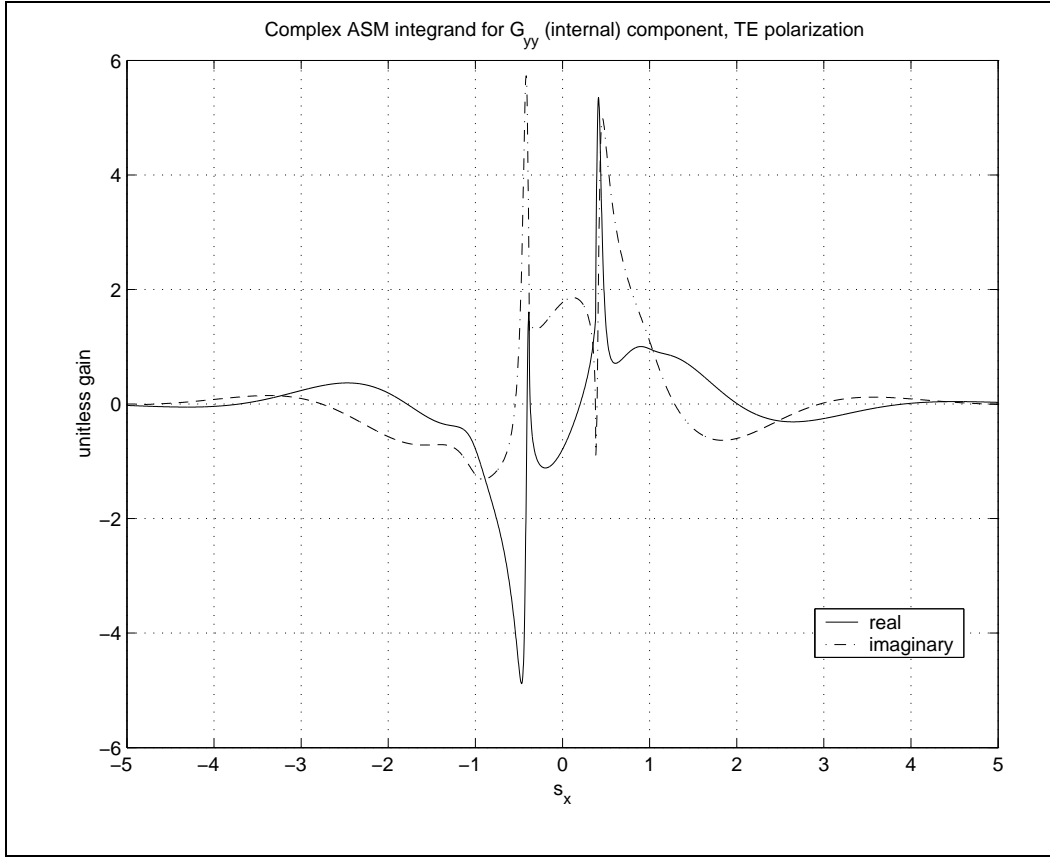


Figure C.4 Source point at $(x', y')=(0, 0)$, field point at $(x, y)=(100, 40)$. Slab coating material $\epsilon_r = 3.25$, $\mu_r = 2 - j1$.

As we have seen before, the G_{yy} component is arguably the most complicated integrand function as supported by the plot in Figure C.4. The equation is given by

$$G_{bounce, yy} = -\frac{jRe(k_1)}{4\pi k_1} \int_{-1}^1 \sum_{n=-\infty}^{\infty} \left[\frac{T}{r_{y1}} + 2r_{y1}T^r \right] e^{-jk_1[(x-x')r_{x1} + |y-y'|r_{y1}]} ds_{x1} \quad (C.4)$$

and while there are no singularities at $s_x = \pm 1$, there are traces of complicated behavior. Again we see no evidence of symmetry and the function decays to zero more slowly than in some of the others cases presented.

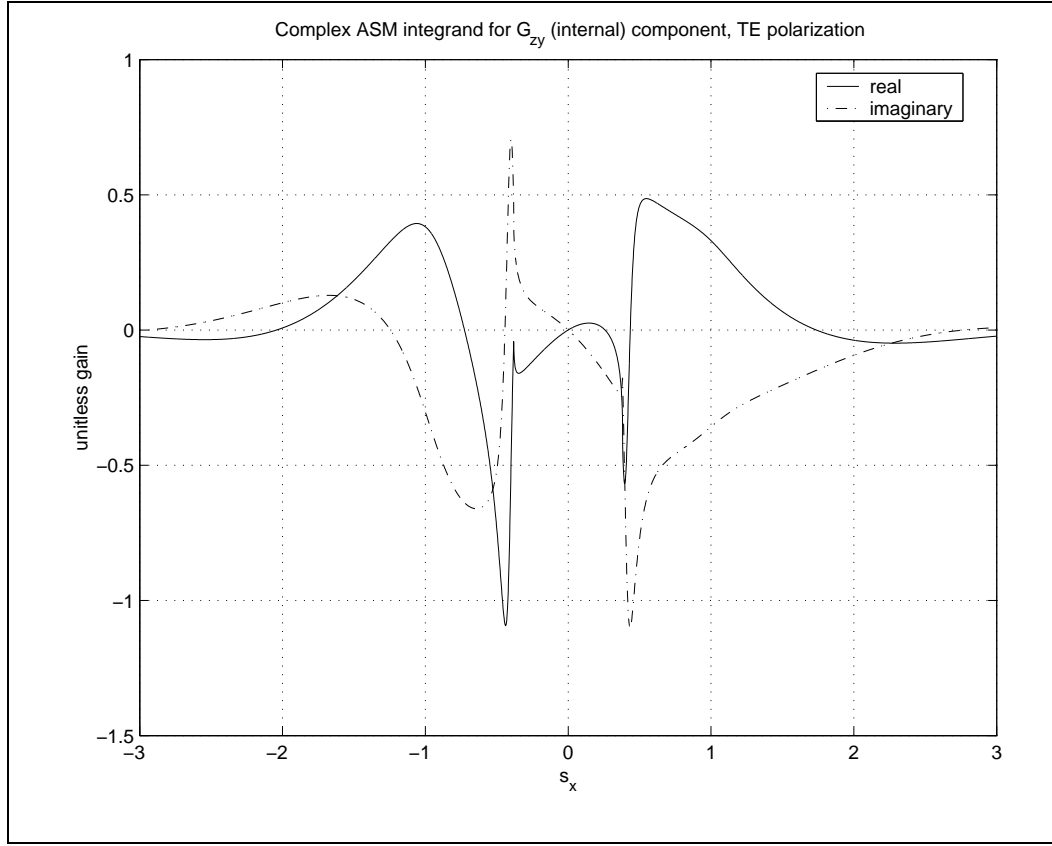


Figure C.5 Source point at $(x', y')=(0, 0)$, field point at $(x, y)=(100, 40)$. Slab coating material $\epsilon_r = 3.25$, $\mu_r = 2.0$.

The G_{zy} component integrand function is displayed in Figure C.5. This function is given by the equation

$$G_{bounce, zy} = -\frac{Re(k_1)}{4\pi} \int_{-1}^1 \sum_{n=-\infty}^{\infty} T \frac{r_{x1}}{r_{y1}} e^{-jk_1[(x-x')r_{x1} + |y-y'|r_{y1}]} ds_{x1} \quad (C.5)$$

and is similar to the previous four figures in that singular behavior is observed only at the critical angle locations. No symmetry is evident for this case and the function decays to zero beyond $|s_x| > 3$, so the plot is truncated at that point to emphasize the behavior of the function in the central region.

The integrand functions plotted in Figures C.1 through C.5 are similar in that all exhibit singularities at the critical angle points, are non-symmetric, and have decayed to zero for $|s_x| > 5$.

The quadrature routine must necessarily avoid the singular points and range over plane wave mode terms from $n = -2$ to $n = 2$, which corresponds to s_x ranging from -5 to 5 .

C.2 Integrand Functions for the Case of Self Coupling

At this point, we move the locations of the source and field elements such that they are collocated in the center of the gap region. The resulting integrand functions will need to be integrated to determine the self-coupling contribution of each Green's function term. We look at several cases to see what might change in the behavior of these integrands.

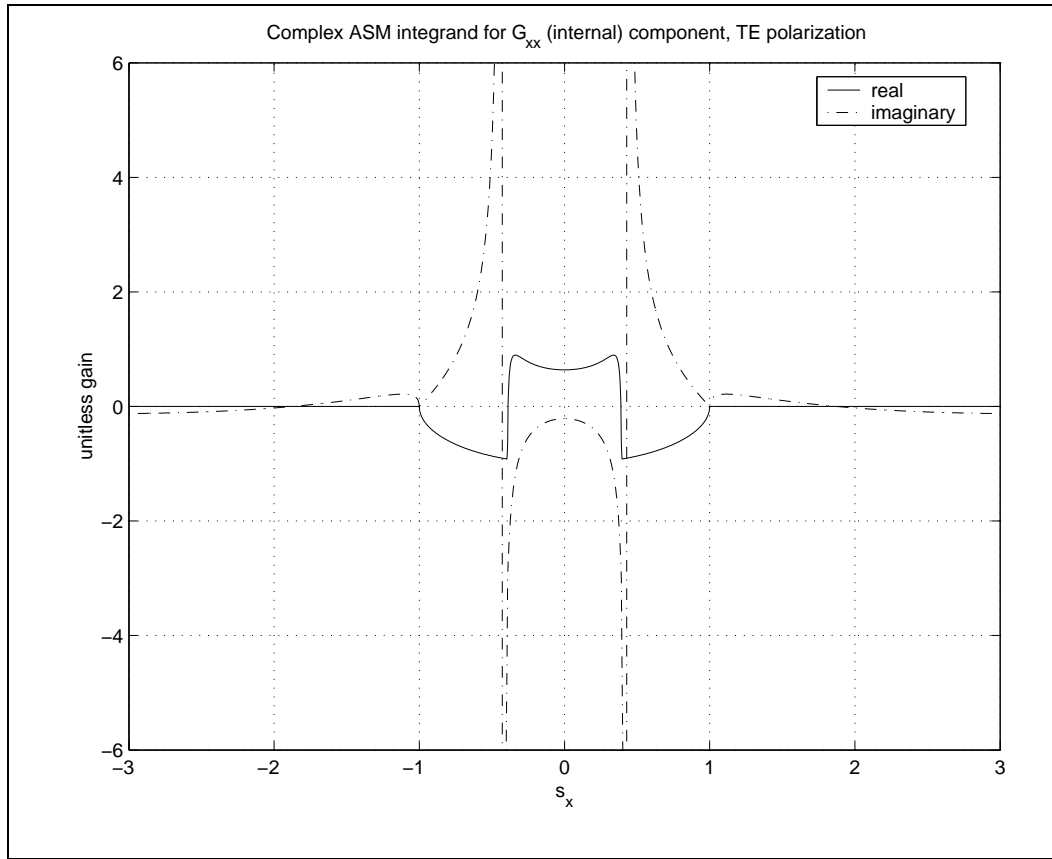


Figure C.6 Source point at $(x', y') = (50, 20)$, field point at $(x, y) = (50, 20)$. Slab coating material $\epsilon_r = 3.25$, $\mu_r = 2.0$.

We look first again at the G_{xx} component, given by Equation (C.1), and see that fairly strong singularities occur at the critical angle locations (TE polarization) and that singularities occur at $s_x = \pm 1$ for this case with a lossless slab coating material. The function is even-symmetric about $s_x = 0$, even in the central region, so folding the range of integration about $s_x = 0$ is possible.

Even though the source and field points are collocated ($y = y'$), the function decays to zero beyond $|s_x| > 3$.

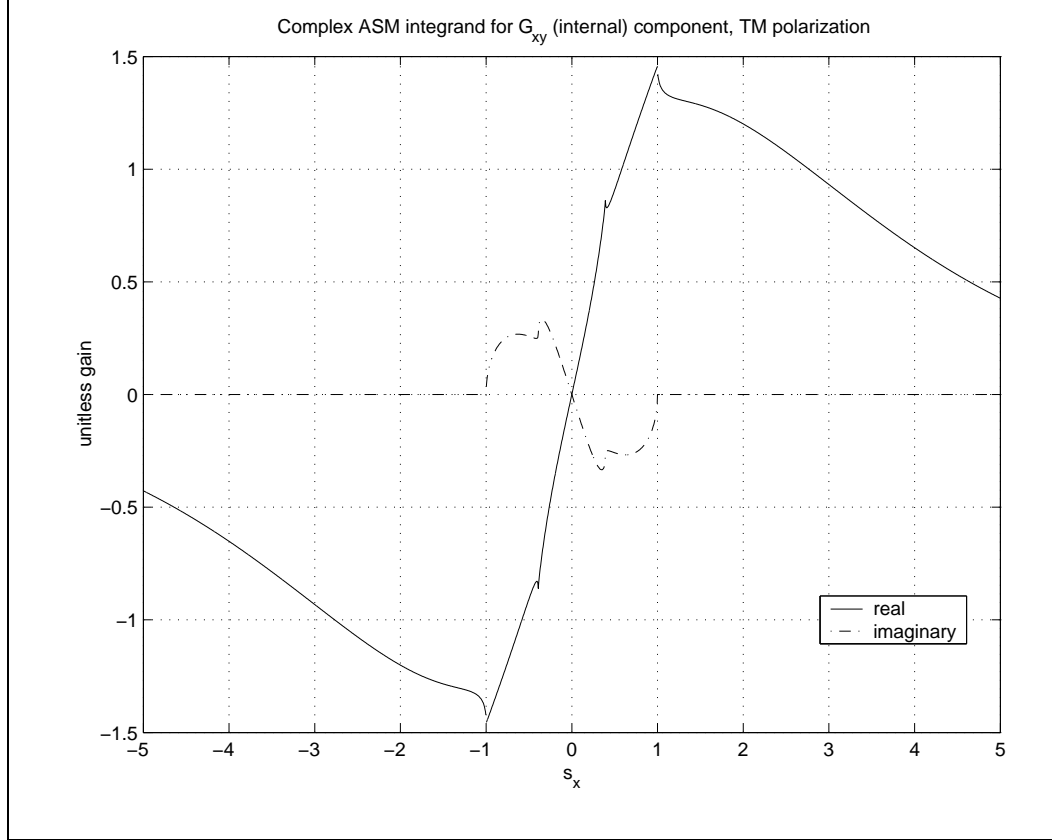


Figure C.7 Source point at $(x', y')=(50, 20)$, field point at $(x, y)=(50, 20)$. Slab coating material $\epsilon_r = 3.25$, $\mu_r = 2.0$.

Figure C.7 displays the integrand function of Equation (C.2) for the G_{xy} component for TM polarization. Even with the singularities at the critical angles and $|s_x| = 1$, the most striking feature of this plot is the odd-symmetry about $s_x = 0$. Evidently this function will integrate to zero, which is good given the slow rate of decay of the function seen at $|s_x| \geq 5$. Recalling from the theoretical development in Chapter 2 that $G_{xy} = G_{yx}$, so Green's function components G_{yx} will also display the odd symmetry and consequently integrate to zero.

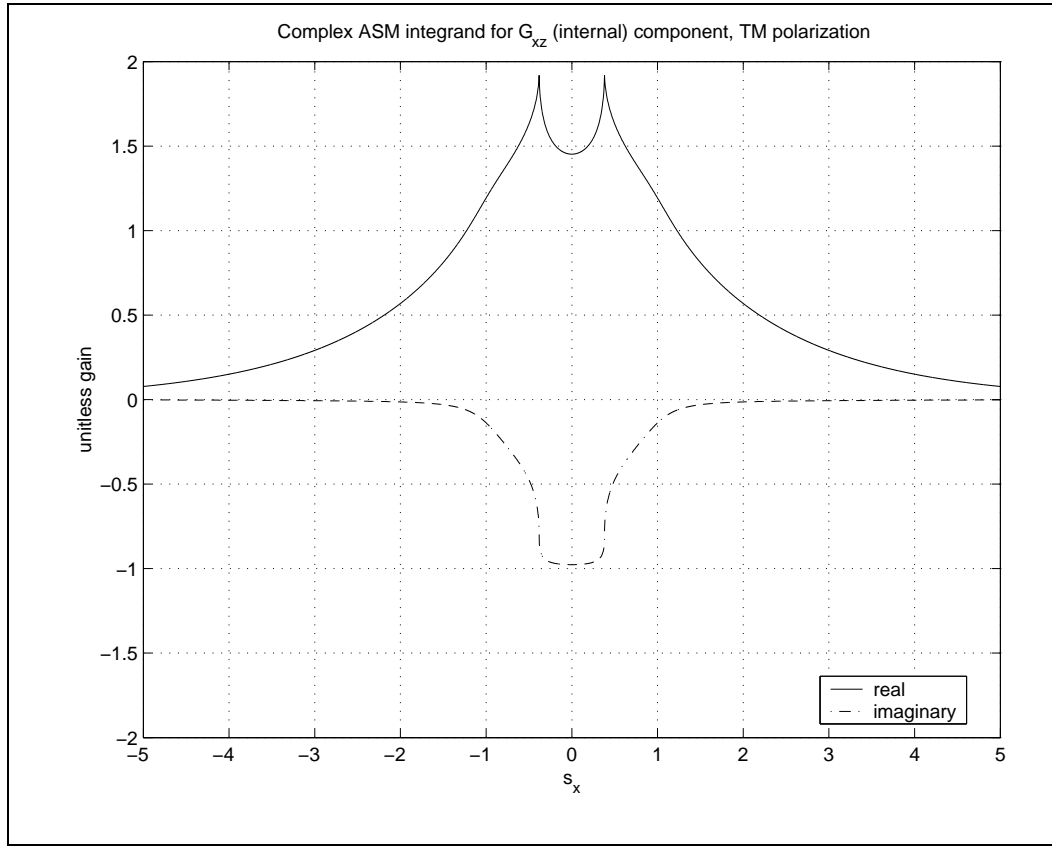


Figure C.8 Source point at $(x', y')=(50, 20)$, field point at $(x, y)=(50, 20)$. Slab coating material $\epsilon_r = 3.25$, $\mu_r = 2 - j1$.

For the G_{xz} component, again for TM polarization, we use lossy slab coating material properties and see that the singularities at $|s_x| = 1$ are no longer present. And while the function decays to zero fairly slowly it is even-symmetric about $s_x = 0$ allowing for the range of integration to be folded.

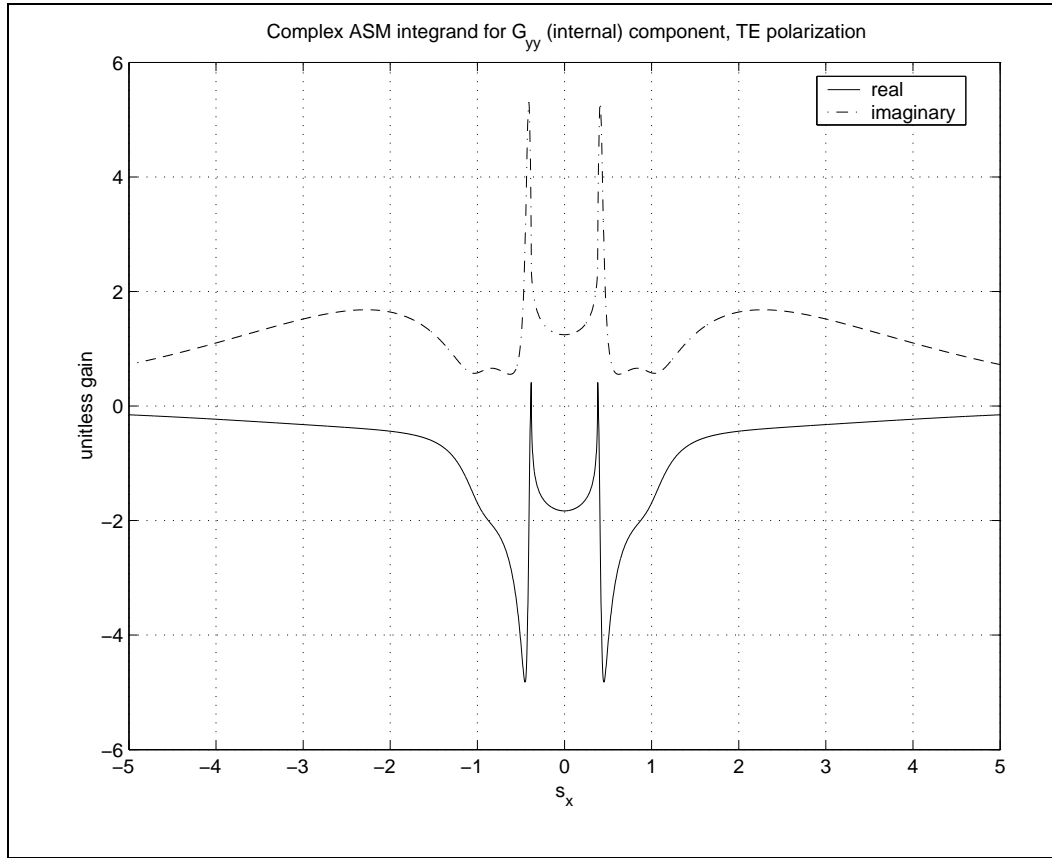


Figure C.9 Source point at $(x', y')=(50, 20)$, field point at $(x, y)=(50, 20)$. Slab coating material $\epsilon_r = 3.25$, $\mu_r = 2 - j1$.

For the G_{yy} component integrand function, Equation (C.4), plotted in Figure C.9 for TE polarization, we have again used lossy properties for the slab coating material with full expectation that lossless material properties would result in a much more complicated function plot. For this ‘self’ term, we see a slowly decaying, even-symmetric plot with singularities at the critical angle locations.

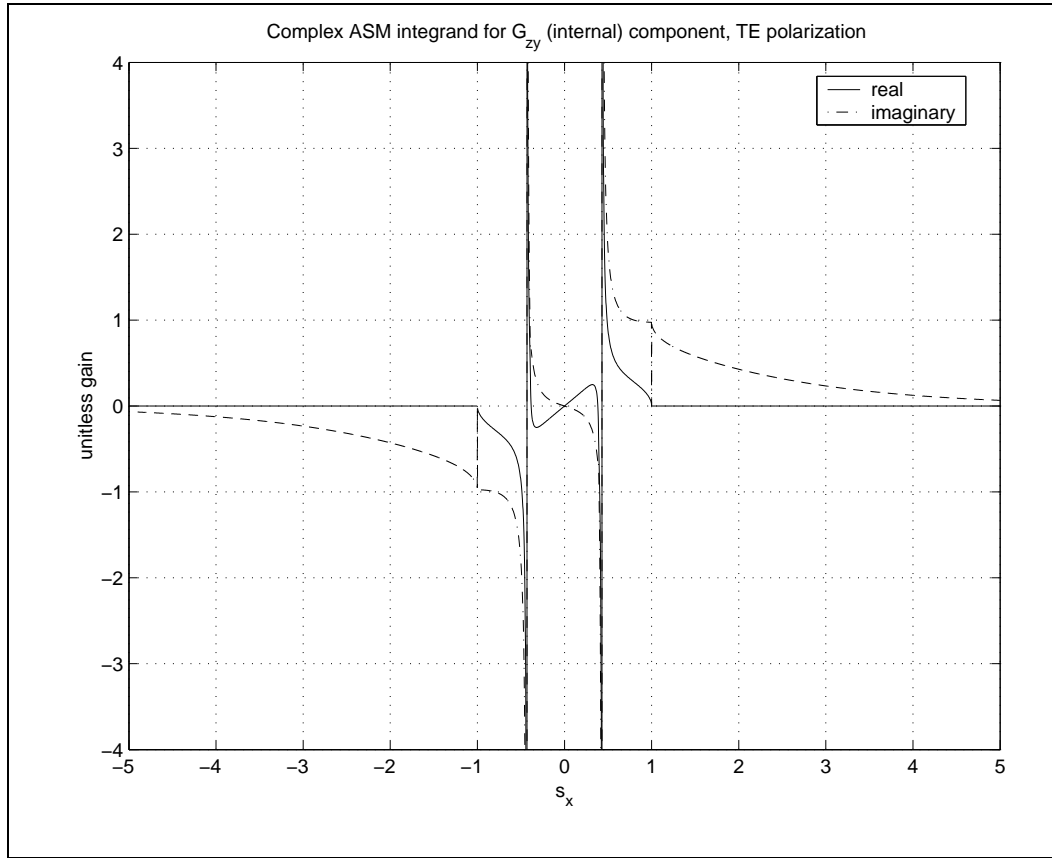


Figure C.10 Source point at $(x', y')=(50, 20)$, field point at $(x, y)=(50, 20)$. Slab coating material thickness = 40 mils, $\epsilon_r = 3.25$, $\mu_r = 2$.

In Figure C.10 we show the integrand function plot for the G_{zy} component of Equation (C.5) for a lossless slab coating material. The expected singularities are present but the interesting feature of this plot is the odd-symmetric behavior of the function, implying that it will integrate to zero. This additionally implies that the corresponding G_{yz} term would also evaluate to zero for this case since $G_{yz} = -G_{zy}$.

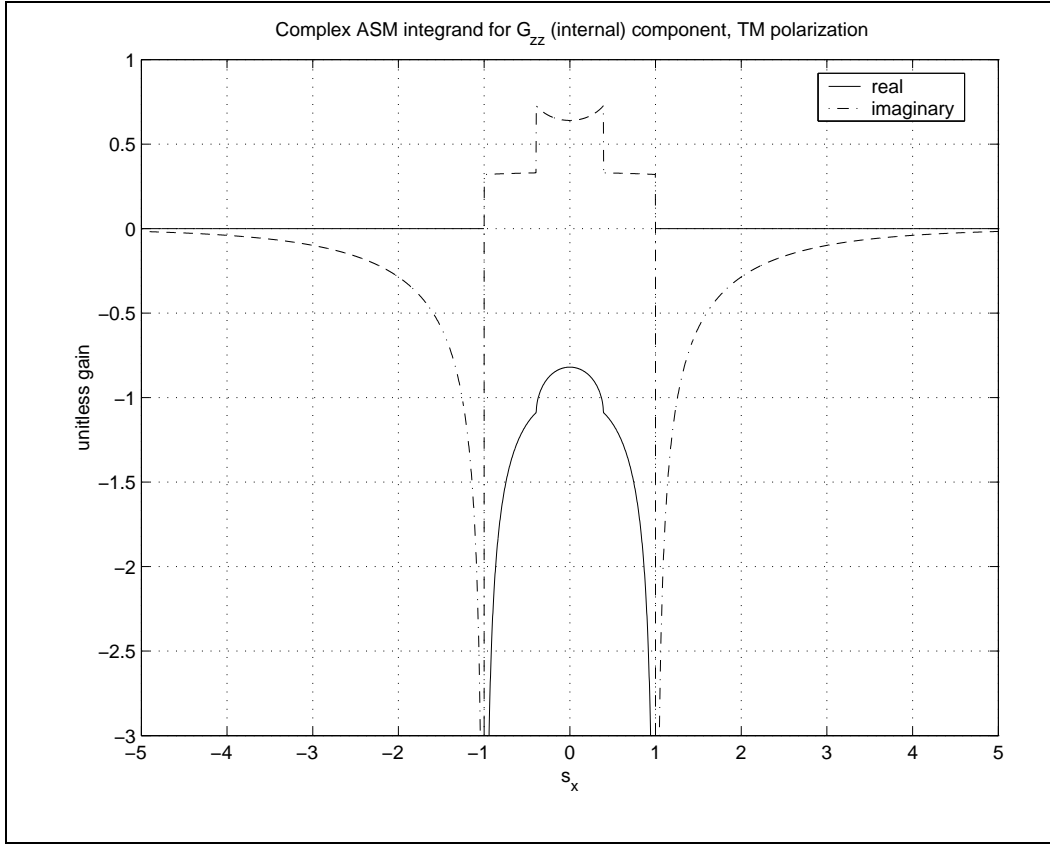


Figure C.11 Source point at $(x', y')=(50, 20)$, field point at $(x, y)=(50, 20)$. Slab coating material $\epsilon_r = 3.25$, $\mu_r = 2.0$.

We return now to the G_{zz} component term, the canonical Green's function expression, plotted for the self term case for TM polarization. We see the symmetric behavior typical for the self term cases for all the Green's function components but also, singular behavior at $|s_x| = 1$ and at the critical angle locations. This last example of singular behavior (at the critical angles for G_{zz}) was not observed in the canonical Green's function terms shown in Chapter 3 for TM polarization.

The self term integrand function behavior plotted in Figures C.6 through C.11 indicate that some computational efficiency may be gained by folding the range of integration around $s_x = 0$. Additionally, for two of the Green's function components (G_{xy} and G_{zy}), no integration of the self term is needed since these functions are odd-symmetric about $s_x = 0$. The integration algorithm must still avoid singularities at the critical angle points and, for lossless material cases, singularities at $s_x = \pm 1$.

C.3 Green's Function Integrands for Cases With Vertical Separation of Source and Receiver

In each example presented for the self coupling case the integrand functions displayed some type of symmetry. For cases where the gap region is rectangular, there will occur cases where the source and receiver are vertically separated ($y \neq y'$) but will retain the same x location value ($x = x'$). We will look next at three examples for such a case.

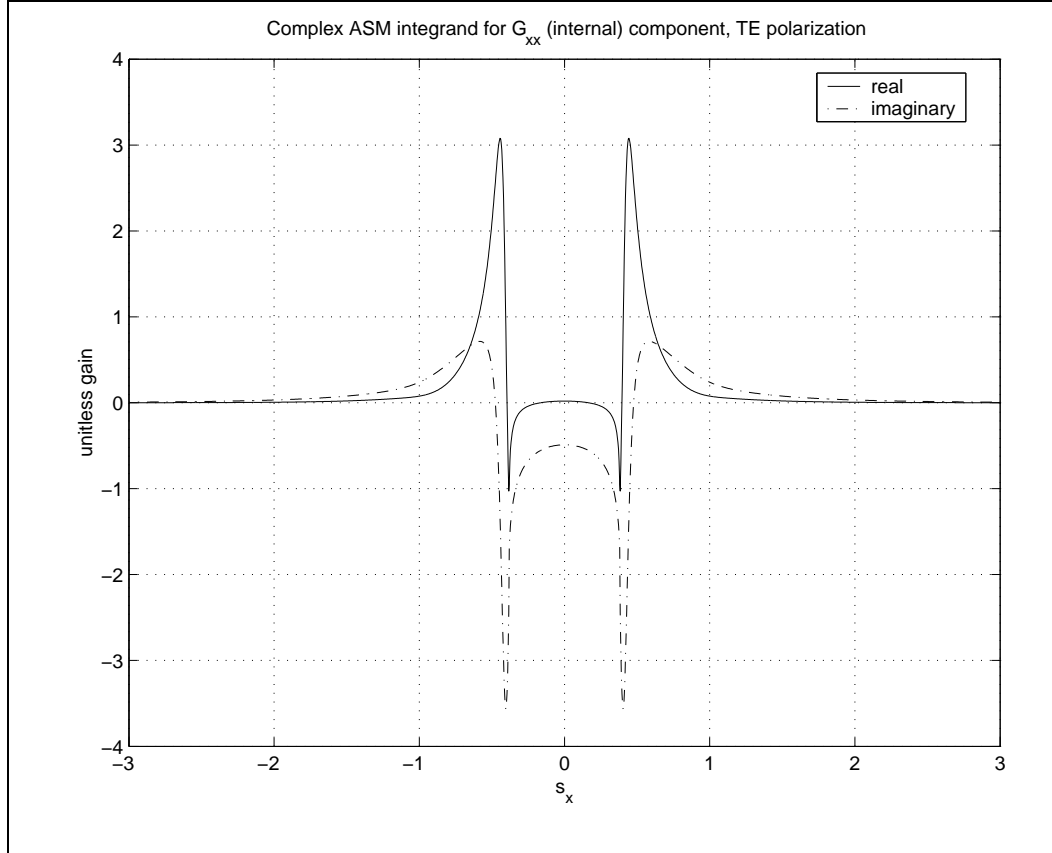


Figure C.12 Source point at $(x', y') = (80, 0)$, field point at $(x, y) = (80, 40)$. Slab coating material $\epsilon_r = 3.25$, $\mu_r = 2 - j1$.

In Figure C.12 is plotted the integrand function for the G_{xx} term for a lossy slab coating material for TE polarization. The function is even-symmetric with singularities at the critical angle points. The vertical separation of the source and receiver locations produces a rapid decay of the function for higher order plane wave modes, i.e., where $|s_x| > 1$.

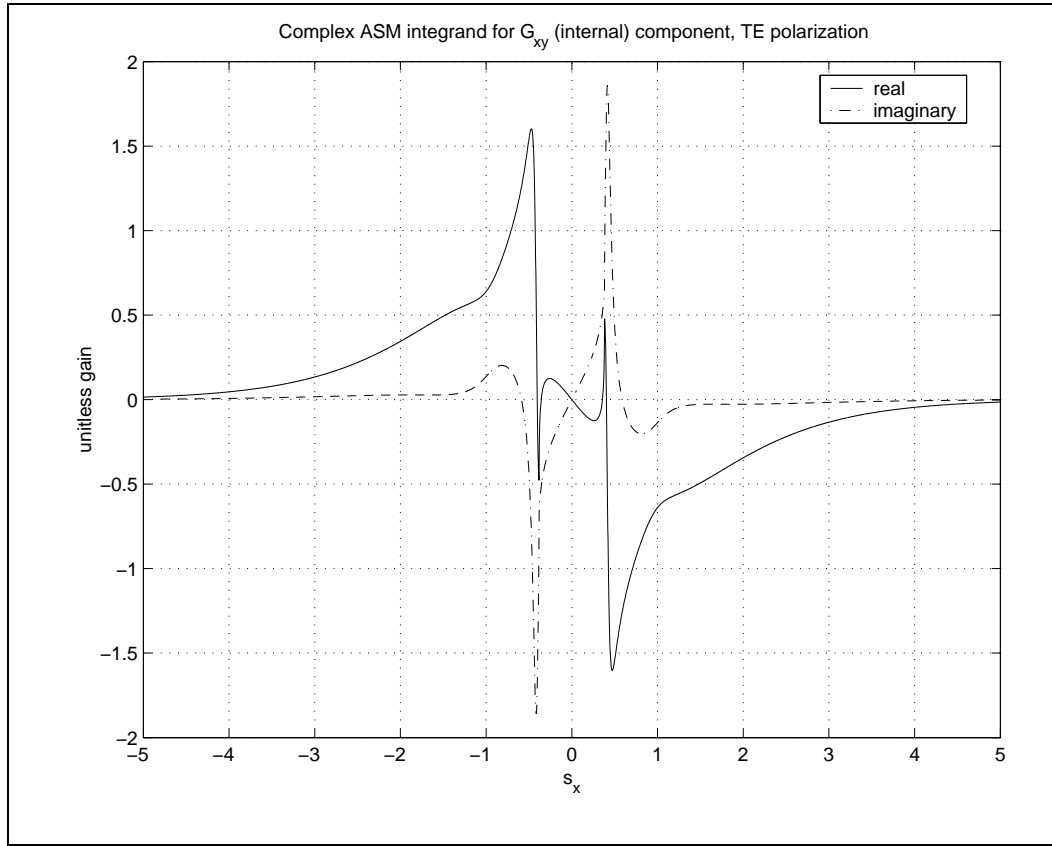


Figure C.13 Source point at $(x', y')=(80, 0)$, field point at $(x, y)=(80, 40)$. Slab coating material $\epsilon_r = 3.25$, $\mu_r = 2 - j1$.

The G_{xy} component is plotted in Figure C.13, again for a case where the slab coating material is lossy. Once again, we see this component is odd-symmetric and will integrate to zero. This also implies that the G_{yx} component will vanish for this case. Evidently, whenever $x = x'$ for these components, the bounce correction term will vanish.

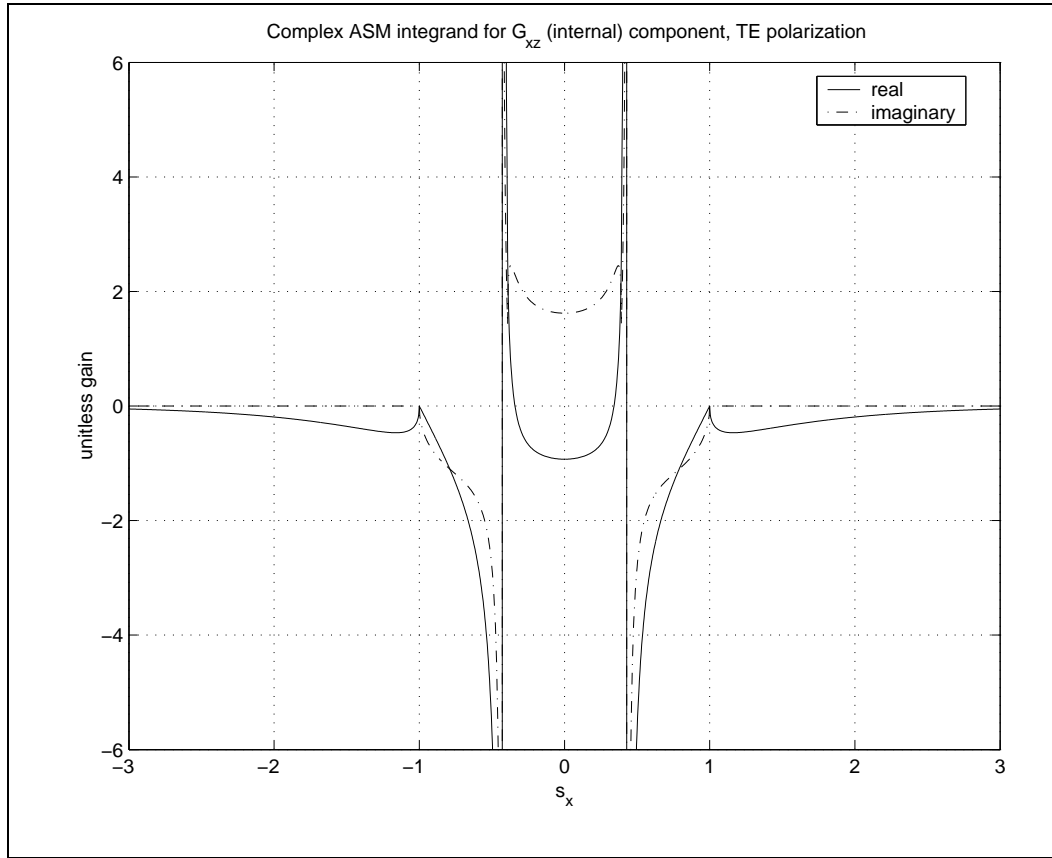


Figure C.14 Source point at $(x', y')=(80, 0)$, field point at $(x, y)=(80, 40)$. Slab coating material $\epsilon_r = 3.25$, $\mu_r = 2$.

In Figure C.14 we have plotted the G_{xz} component for a lossless slab coating material. We see the strong singularities at the critical angles and even symmetry about $s_x = 0$. This integrand function can thus be folded to help expedite the numerical integration process.

Figures C.12 through C.14, in combination with the previous section, tell us that for any case where the source and field point have the same x coordinate value, the integrand functions possess symmetry that can be utilized to speed the numerical integration process. This can be realized, for some cases, by folding the range of integration (and avoiding the singularities at the critical angle points and $|s_x| = 1$ for lossless materials), or skipping the integration altogether for those components which produce an odd-symmetric integrand function.

C.4 Green's Function Integrands for Cases With Horizontal Separation of Source and Receiver

It has become evident that for any case where the source and receiver x -coordinate locations are equivalent (i.e., $x = x'$), the resulting integrand functions will display either even or odd symmetry. The vertical separation between the source and receiver works to our advantage, forcing a more rapid decay of the functions to zero for higher order plane wave modes. We look next at what happens for the case when the source and receiver locations have the same y -coordinate value but are horizontally separated, i.e., $y = y', x \neq x'$.

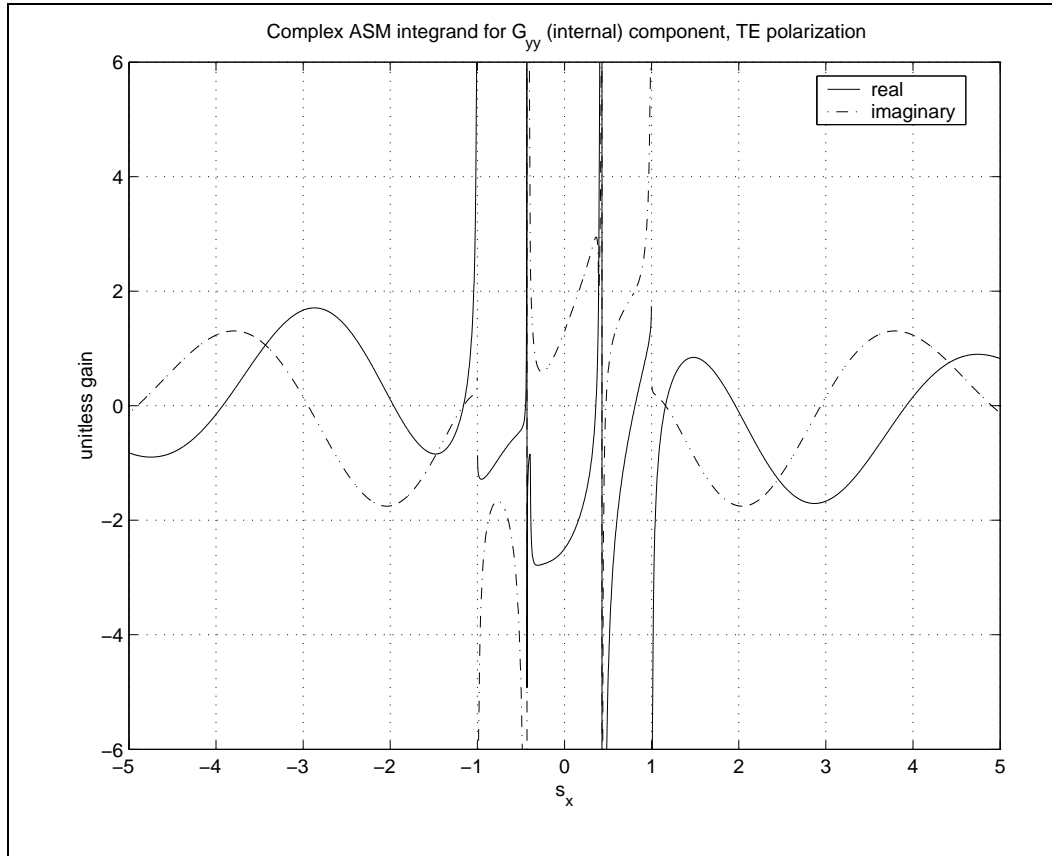


Figure C.15 Source point at $(x', y') = (0, 20)$, field point at $(x, y) = (100, 20)$. Slab coating material $\epsilon_r = 3.25$, $\mu_r = 2.0$.

The G_{yy} Green's function component integrand function for this case is plotted in Figure C.15. Clearly the function decays very slowly to zero and a number of higher order plane wave mode terms will contribute to the integral. The symmetry of this function also dictates that no folding of the integration range is possible. The singularities at the critical angles and at $|s_x| = 1$ are consistent with what has been observed earlier for this Green's function component.

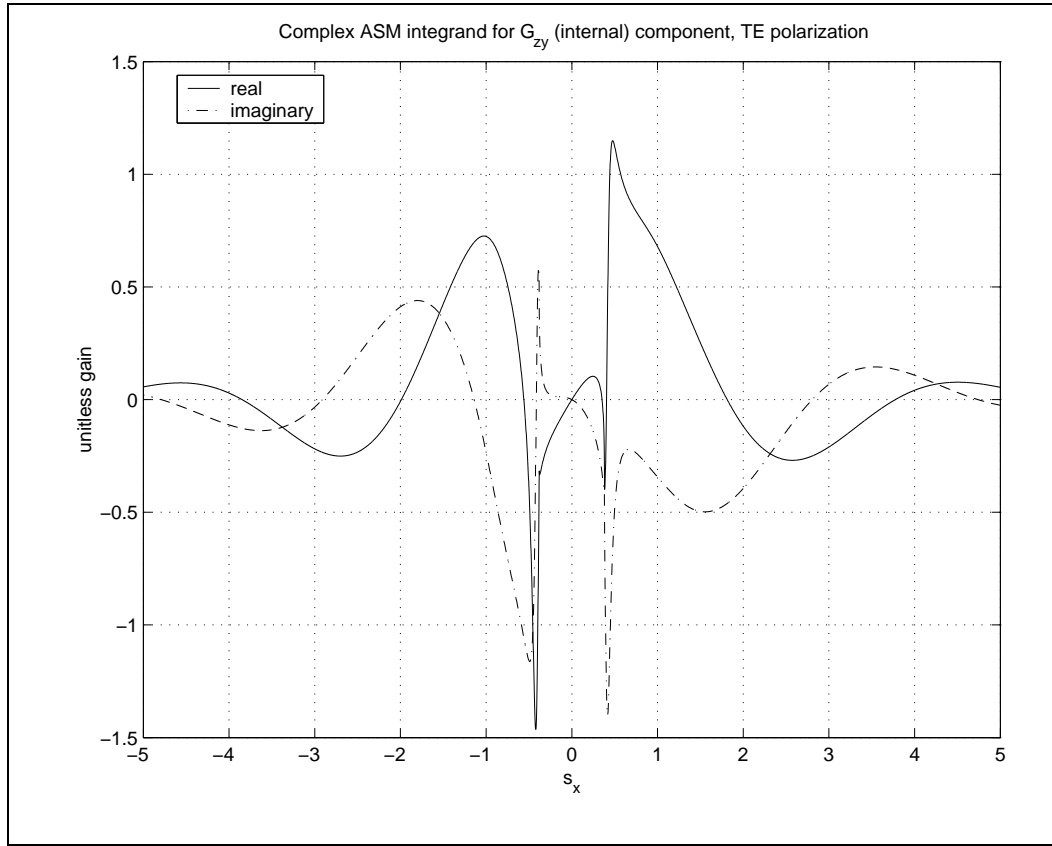


Figure C.16 Source point at $(x', y')=(0, 20)$, field point at $(x, y)=(100, 20)$. Slab coating material $\epsilon_r = 3.25$, $\mu_r = 2 - j1$.

Plotted in Figure C.16 is the G_{zy} component for a lossy slab coating material case. As in the previous case, there is no evidence of symmetry and the function decays to zero slowly for higher order plane wave modes.

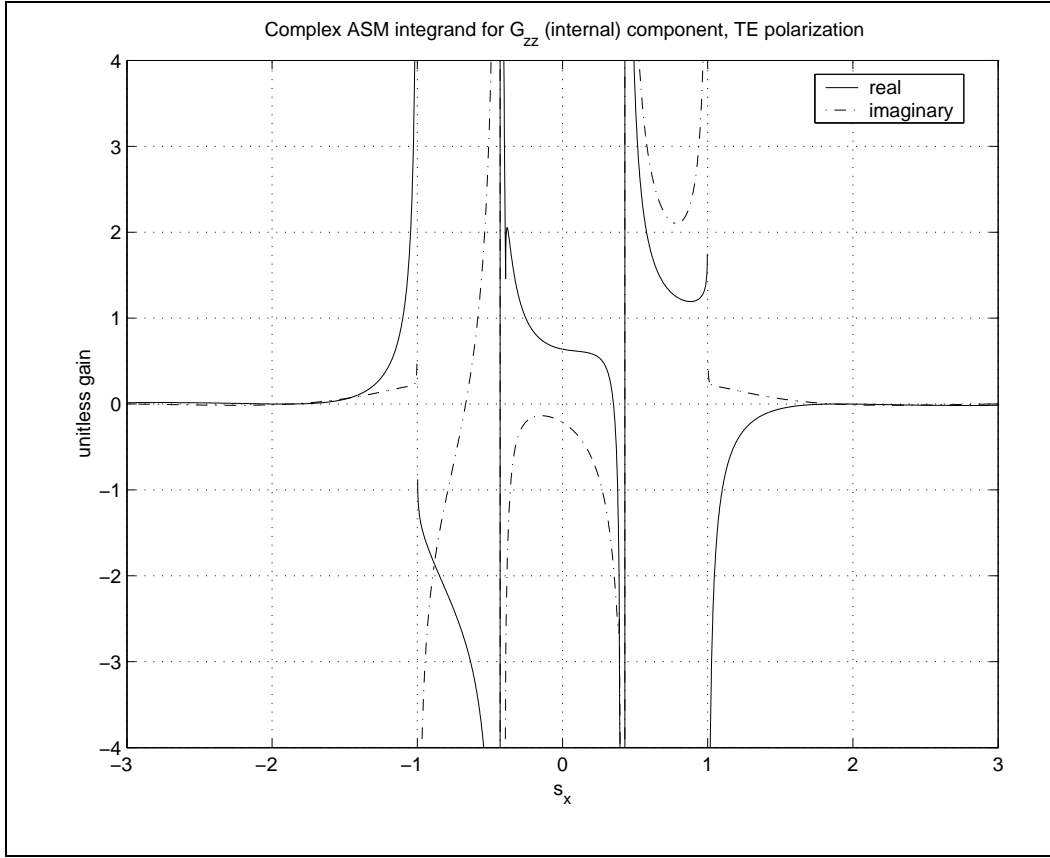


Figure C.17 Source point at $(x', y')=(0, 20)$, field point at $(x, y)=(100, 20)$. Slab coating material $\epsilon_r = 3.25$, $\mu_r = 2$.

Finally, we present the G_{zz} component in Figure C.17 for a lossless slab coating material. We see, in contrast to the previous two figures, this function still decays to zero quite rapidly for $|s_x| > 1$ implying that only a few plane wave mode terms need to be included in the integration.

Figures C.15 through C.17 convey the bad news that for cases with only horizontal coupling between the source and field points, the range of integration must be extended to incorporate a larger number of plane wave mode terms than is needed for cases with vertical separation. This is due to the fact that the integrand functions do not exponentially decay for cases where $y = y'$. This situation will occur quite frequently in our gap regions as they conform to the horizontally parallel boundaries of the ground plane and the slab material - free space interface. This will more seriously impact gap regions that might be considered ‘wide.’ ‘Narrower’ gaps will be affected to a lesser extent.

C.5 Appendix C Summary

To summarize what has been observed both in this appendix and in the integrand function plots displayed in Section 3.1, we see that, in general, the numerical integration routine will have to integrate over several plane wave mode terms beyond the central ($n = 0$) region. Some cases, such as whenever $x = x'$ (source and receiver locations vertically aligned), will allow either a folding of the range of integration or an outright avoidance of the need to evaluate the integral due to odd-symmetry in the integrand function. In general, the quadrature routine will need to avoid the singularities that occur at the critical angle points. In order to be able to handle lossless materials, the quadrature routine must also avoid the singularities at $|s_x| = 1$.

The integrand function plots demonstrate that the integration routine must be both adaptive and recursive due to the wide variety of function shapes and variations in smoothness within each particular ‘range’ of the s_x variable (e.g., the range $s_c \leq s_x \leq 1$). The integration routine used in evaluating the bounce correction term integrals is described in more detail at the end of Section 3.1.

Appendix D. Echo Width Measurements and the AFRL Compact Range

We presented data in Chapter 4 that was obtained using the advanced compact Radar Cross Section (RCS) measurement range located within the AFRL Multispectral Measurement Facility. A cross section drawing of the compact range is shown in Figure D.1. As shown in the drawing, the compact range illuminates the target with a plane wave produced by the optical configuration of the range. Because the transmitter and receiver utilize the same feed antenna, the range measures only a monostatic signal from the target. The optical configuration of the compact range, an offset-fed Gregorian geometry, is optimized to produce a minimum amount of cross polarization energy contamination in the measurements and a ‘quiet zone’ nearly the size of a full scale fighter aircraft. This quiet zone is the volume surrounding the target location in which a very close approximation to an ideal plane wave (uniform amplitude with no phase variation) exists.

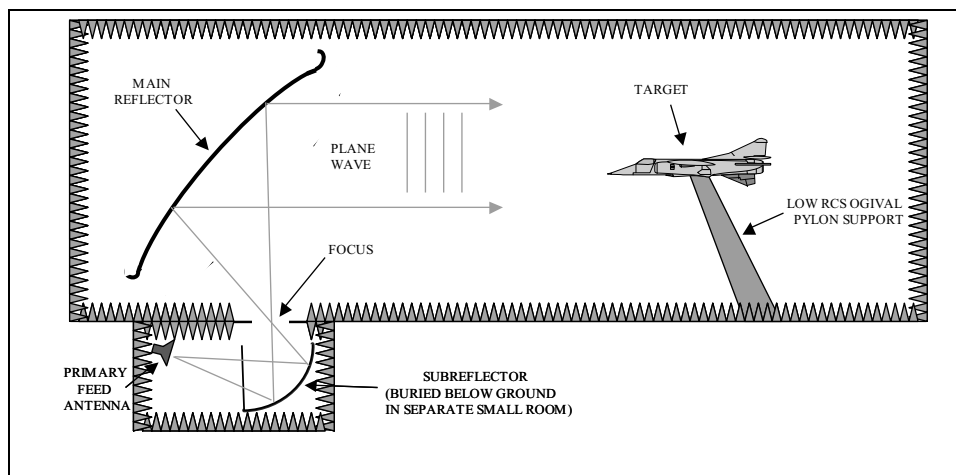


Figure D.1 A side-view drawing of the AFRL compact range. The optical configuration of the range creates a plane wave illumination of the target fixture.

The test fixture used in acquiring the data is referred to as the ‘boat’ fixture and is typically used to measure the performance of antennas or other devices or features that may need to be recessed into a shallow cavity. The fixture is shown in the drawings in Figures D.2 and D.3 and in the series of photos shown in Figures D.4 through D.6. The boat, as a low-RCS test fixture, is principally designed to enable measurement of these antennas or features when the boat fixture is illuminated near nose-on and for a limited range of incidence angles from nose-on up towards the normal to the fixture (coming up out of the plane of the paper in Figure D.2). The boat is not designed as a fixture for illumination near broadside, as broadside illumination results in a strong

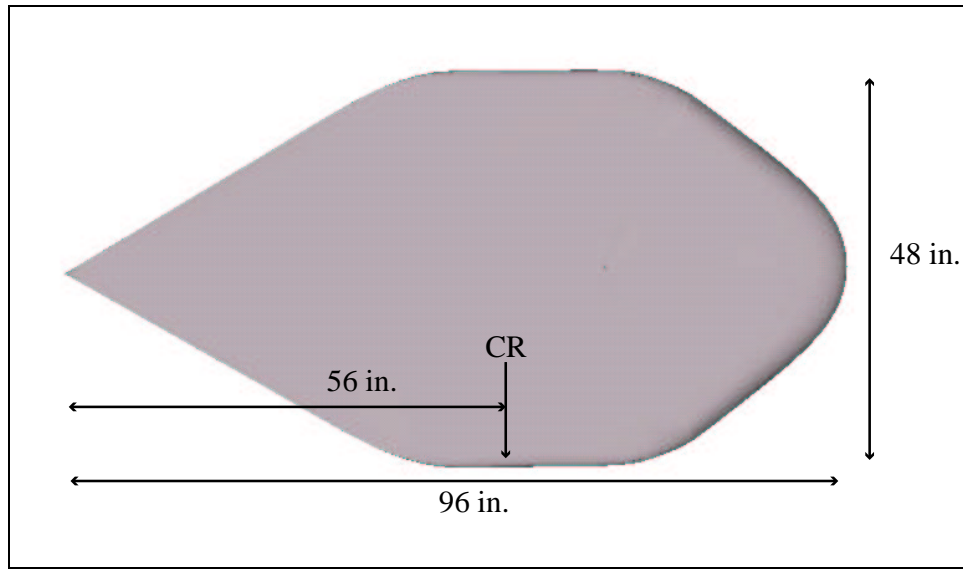


Figure D.2 Top-down view of the 'boat' test fixture. The fixture is 8 feet long, 4 feet wide, and 8 inches thick. 'CR' is center of rotation.

reflected signal from the large planar area of the fixture seen in Figure D.2, which would overwhelm the scattered signal from any object under test, including small 18" gaps cut into absorber panels located near the nose of the fixture. This is why the measurement data plots presented in Chapter 4 are all terminated at 85° from the nose of the fixture (5° from broadside). Additionally, with the extra target handling required to fill the gaps with the RAM 'butter' gap filler material, plus the time required to allow the gap filler material to cure, sufficient phase error crept into the measurement to produce the noisy signals for the treated gap measurement results.

When illuminated along the sharp tip (nose) of the fixture, the monostatic scattered signal is very low. With the boat considered part of the range background in the measurements, phase error becomes highly sensitive to any perturbations in the range such as fixture positioning changes or drift in the electronic equipment. For the lowest signal levels measured on the boat test fixture, significant variation in the results are seen below about 15° in the data plots in Chapter 4. With the extra time and physical handling needed to acquire the treated gap data, this noise is seen to worsen, sometimes over the entire range of sweep angles.

As seen in the photos in Figures D.4 through D.6, commercially available sheet MagRAM was placed on the top of the fixture from the tip extending back 48" on the fixture. With the base of MagRAM applied to the boat fixture, an initial set of RCS measurements was taken forming the

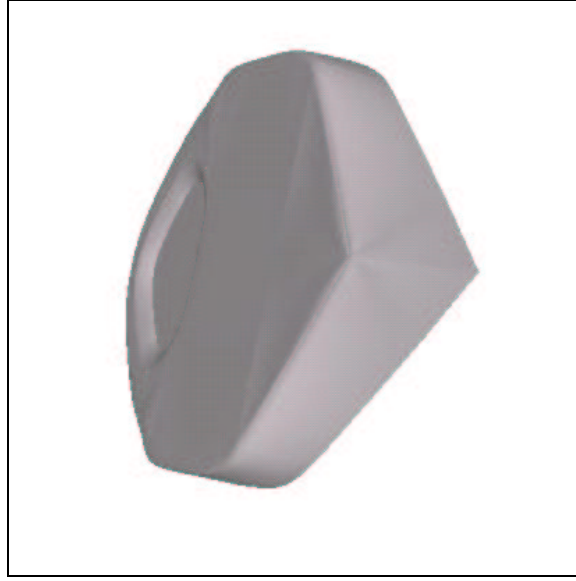


Figure D.3 A view of the ‘boat’ test fixture looking down the tip (nose) of the fixture from below waterline to show how the sharp tip is flared on the bottom side of the fixture.

baseline or ‘background’ for the measurements to follow. Afterwards, at a point 22” back from the tip, 18” long gaps were cut into the MagRAM to produce the ‘2D gaps’ (two different gap widths were cut, 100 mils wide and 60 mils wide, each requiring a new base absorber layer to be affixed to the boat fixture). After the empty (or air) gaps were measured, the gaps were filled (or treated) with the butter material. After a curing period, the fixture containing the treated gaps was then remeasured. Once these data sets were obtained, the background was coherently subtracted from the ‘gap’ measurements to obtain the scattering due to the gaps alone.

The data acquired from the compact range is calibrated three dimensional RCS data. For the comparison data shown in Chapter 4, this data is converted to 2-D using the approximation [15]

$$\sigma_{2-D} \simeq \sigma_{3-D} \frac{\lambda}{2l^2}$$

where l is the length of the gap and λ is the illumination wavelength. As is evident from some of the plots included in Chapter 4, no smoothing of the raw RCS data was performed.

The typical procedure used in the compact range to produce calibrated RCS data is referred to as a coherent or ‘vector’ subtraction process. A measurement is made first of the ‘empty’ range with only the pylon, floors, and walls contributing to the empty range signal. This is known as

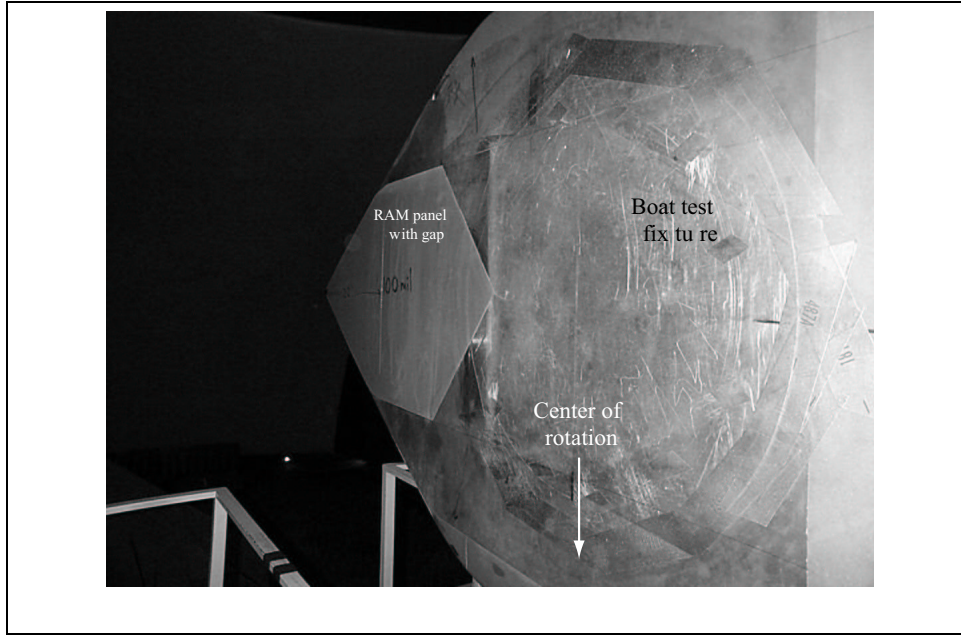


Figure D.4 A view of the ‘boat’ test fixture showing the relative locations of the center of rotation, the base absorber panel, and the gap.

the range background response signal. This background signal is carefully stored in the form of amplitude and phase. The target is then carefully placed atop the pylon and measured, the target scatter signal also being stored in the form of amplitude and phase data. Finally, a calibration target of known RCS level is measured and the calibration signal stored as amplitude and phase data. The RCS of the target is finally determined through the expression

$$\sigma_{target,calibrated} = \frac{\sigma_{target} - \sigma_{background}}{\sigma_{calibration} - \sigma_{background}}$$

where the subtractions take into account the complex vector nature of each of the stored signals. When carefully performed by experienced range technicians, this vector subtraction process is quite sensitive and highly accurate.

For this dissertation project, the process of gathering data using the boat fixture employed the atypical procedure of leaving the boat fixture affixed to the top of the pylon during acquisition of the background measurement. By doing this, the boat fixture is essentially considered as part of the range. For the purpose of measuring the scattering due solely to the presence of the gap in the base absorber material, this approach is required. This calls for extreme care on the part of the



Figure D.5 The gap is located 22 inches back from the tip and 34 inches from the center of rotation of the boat fixture.

range technicians since movement of the boat fixture between various measurements must to be kept to an absolute minimum. Any movement of the fixture between target data and background measurements would create an error source in the final data that could not be removed through any data post-processing technique.

The photos in Figure D.4 through D.6 show several views of part of the boat fixture, the base absorber layer (or the ‘slab coating material’), and the 18 inch gap cut into the base absorber material made during the course of taking the measurements. Unfortunately, no presentable photos of the gap with the gap filler material applied were obtained. It is evident that some experimentation took place during the course of the measurements regarding how far back onto the fixture the absorber panel was extended. Although the gaps were cut with the use of a metal template, they were cut by hand by the range technicians. Thus the actual length, width, squareness of the gap over it’s length, and other error factors could contribute to ambiguities in the measured data shown in Chapter 4.

In the opening paragraphs of Section 4.3 it was stated that we could not expect the simulated 2D measurements to match well with the predicted results from the computer codes due to the nature of the test body and the non-standard procedures used to acquire the data. As a way of sum-

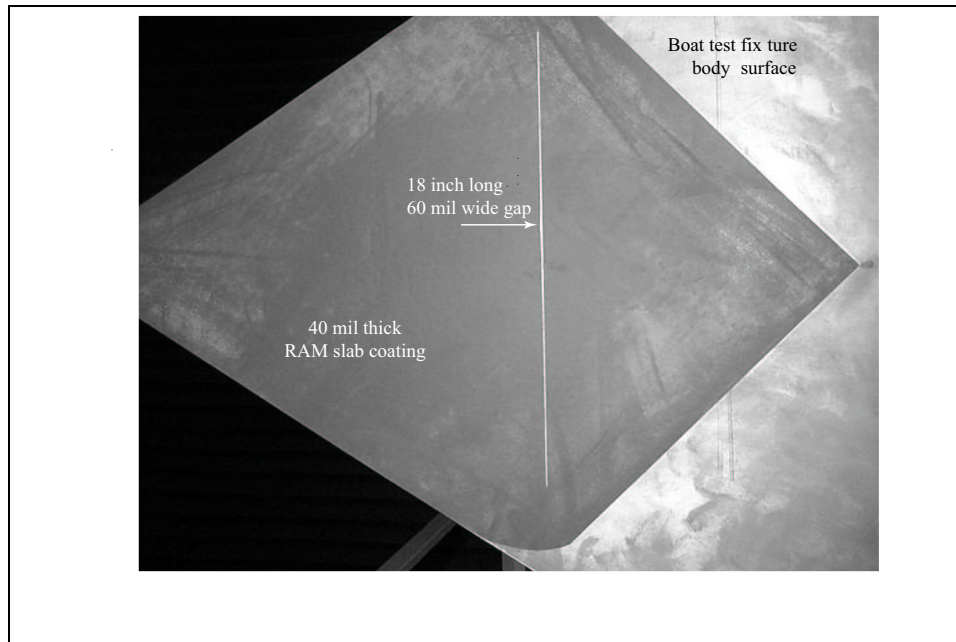


Figure D.6 A view of the 60 mil wide gap cut into the absorber panel.

marizing this appendix, we would now like to complete this thought although we do not provide a complete analysis of the scattering from the boat test fixture as that would take us too far afield.

Like the Ram2d numerical test body described in Chapter 4, the boat test fixture is a finite body but, unlike the Ram2d test body, is not infinite in any of its dimensions. While difficult to see in Figures D.2 and D.3, the boat is terminated in a sharp tip at its nose and has sharp edges along the top of the fixture leading away from the nose. These features could be expected to produce surface waves inside the absorber panels into which the gaps were cut. As with the Ram2d test body, these surface waves would be more pronounced for the polarization corresponding to TE polarization with respect to the gap (this would be horizontal polarization in the range). Additionally, with the geometry of the boat test fixture evident in the drawings, the scattering characteristics (RCS patterns) of the fixture for the two polarizations are very different. The combined effect is that various residuals (the combined interaction of these other scattering sources with the gaps) are evident in some of the plots presented in Chapter 4, primarily for the TE polarization case in which the shape of the echo width pattern is slightly different. Suffice it to say that these residuals result from the much more complicated 3D features of the boat test fixture as compared to the Ram2d numerical test body.

As seen in the photo in Figure D.4, the gaps are offset nearly three feet from the center of rotation of the boat test fixture. This gap offset was done intentionally to separate the scatter signal of the gap from that of the pylon. This is necessary since the anticipated scattering from these sources was expected to be near the same level. With this offset, the locus of the gap transcribes an arc in the range as the test fixture is rotated. For the frequencies at which the gaps are measured, one might well expect changes in amplitude and phase that could lead to erroneous results. In fact, from the data shown in Chapter 4, some variation in amplitude may be evident. However, the characteristics of the data plotted in Chapter 4 suggest that only random noise artifacts and, perhaps, drift due to material cure time and target handling, contributed to the data presented.

As a whole, the conditions under which the measurement of the scattering from the gaps was obtained were notably different from the assumptions used in the predictions. That the results between the measurements and the computer codes agreed as well as they did is quite remarkable. Overall, this is a testament to the quality of the compact range and the skill of the personnel who accomplished these measurements.

Appendix E. Measurement of Material Properties

In Chapter 4, numerous data plots are shown in exhibiting the performance of the hybrid Green's function MoM code developed in this dissertation. Some of the more interesting plots compare the performance of the hybrid code to an industry-standard (well documented, validated, and widely used) 2-D RCS computer code, Ram2d, and to actual measurement data taken in the AFRL Multi-spectral Measurement Facility (MMF) advanced compact range facility as described in Appendix D. In this Appendix, we more thoroughly describe the materials used in these measurements, the slab coating and gap filler materials, and discuss how their properties were determined.

Another of the laboratories located within the AFRL Multispectral Measurement Facility (MMF) is the Materials Measurements Laboratory (MML). The purpose of this laboratory is to measure the electromagnetic properties of materials, which include a materials' electric permittivity and magnetic permeability. The MML provided electromagnetic property values for the slab coating and gap filler materials used in the measurements for this dissertation.

Material electromagnetic property measurements in the MML are obtained using a number of different test fixtures. The slab coating and gap filler materials properties used in this dissertation were measured with an apparatus known as the focused arch. This device is shown in the photo in Figure E.1 and in the cross section drawing in Figure E.2. The focused arch was developed by

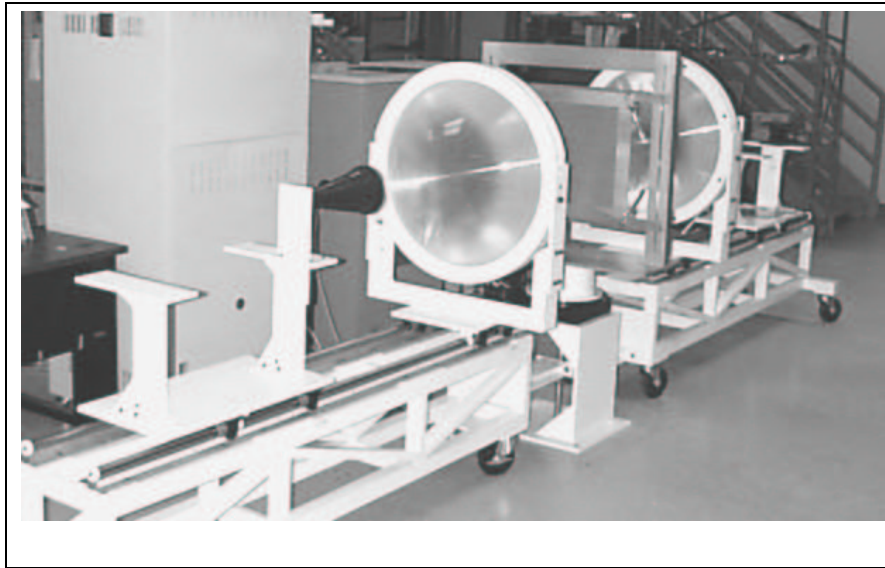


Figure E.1 Photo of the GTRI Focused Arch Apparatus

researchers at the Georgia Tech Research Institute and uses dielectric lenses to focus microwave energy onto a ‘spot’ on the sample. This spot exhibits a Gaussian roll-off amplitude profile and, in the central portion of the beam, a minimal phase taper. This simulates, in a fairly compact arrangement, a plane wave illumination of the sample under test.

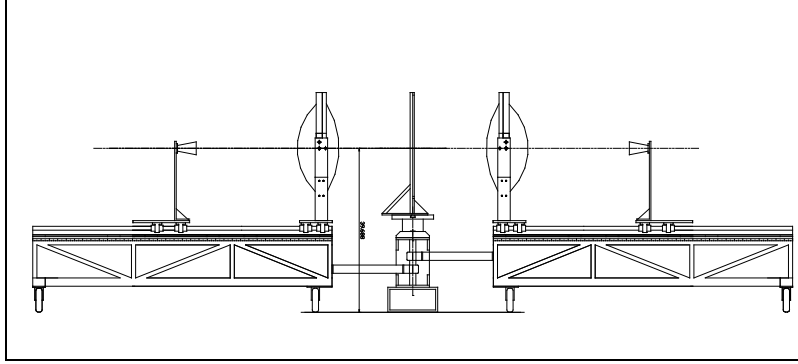


Figure E.2 Cross Section Drawing of the GTRI Focused Arch System

The focused arch measurement system is driven by a Hewlett-Packard 8510C vector network analyzer. Since the constitutive properties, ϵ and μ , of the material samples cannot be measured directly, inversion algorithms are used to extract the complex permittivity and permeability of a material sample (from measurement of the material’s reflection (S_{11}) and transmission (S_{21}) coefficients). Several inversion algorithms are available and the two used in the MML are based on the Nicolson-Ross-Weir (NRW) [40] [41] inversion algorithm and the Baker-Jarvis iterative method [42].

Errors occurring in the process of converting focused arch Gaussian beam measurements to plane wave quantities (reflection and transmission coefficients) is addressed in a recent article by Petersson and Smith [35]. These conversion factors and errors associated with them, known network analyzer error sources, material sample thickness and material sample placement uncertainties (distance from the horn or lens to the sample) are all factored into the inversion algorithms and are used to produce measurement error estimates in conjunction with extraction of the sample’s constitutive property values. Although written for measurements performed in waveguides, many of these potential error sources have been analyzed and published by the researchers at the National Institute of Standards and Technology [43], and have been incorporated into the inversion algorithms used in the MML.

The materials used in the compact range measurements were commercial, off the shelf products commonly employed in the antenna and electromagnetic scattering communities. The material used as the slab coating material was manufactured by R & F Products, RFSW-N-.038-GP, part number 2026. Measurement results on this sample produced the permittivity and permeability data shown in Figures E.3 and E.4.

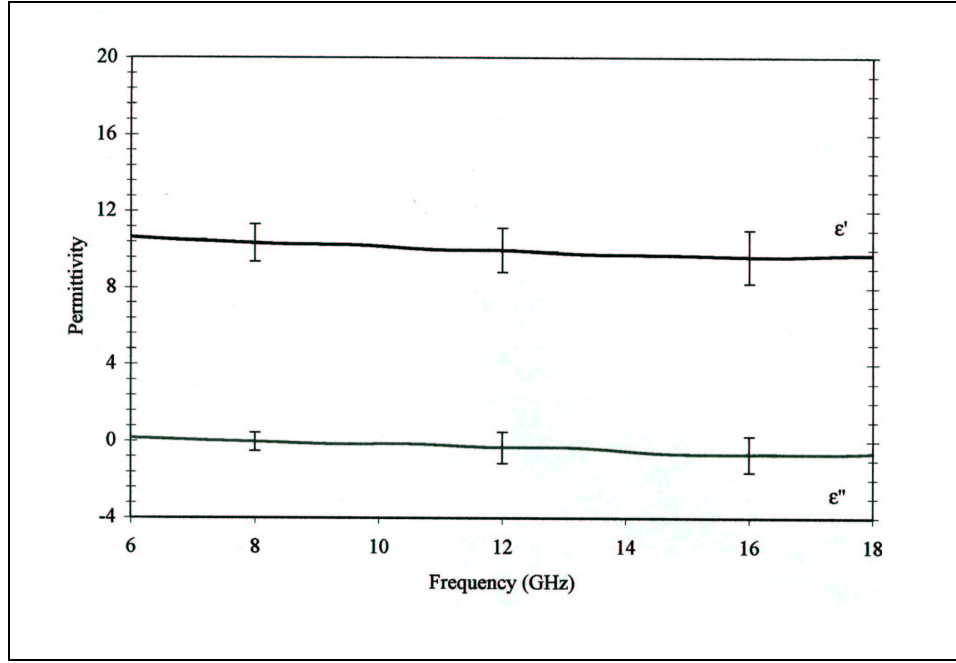


Figure E.3 Slab coating material permittivity.

Examining the measured permittivity data from the slab coating material, we notice that the curve for ϵ'' appears to dip slightly below zero at the upper end of the frequency range. This is a mathematical artifact of the inversion algorithm used to compute the errors associated with the permittivity from the measured S_{11} , S_{21} data. The algorithm computes (and plots) the permittivity value based on the error statistics analysis described above. For low loss material samples, computation of the error bars can easily result in negative ϵ'' values, to the extent that the algorithm computes a negative error-averaged value. This is seen even in data published in the original paper of Nicolson and Ross [40] (the sample holder pictured in Figure 7 of [40] is still in use today in the MML, but was not used to obtain the data shown in this appendix). This is a fairly common occurrence in material measurements and the usual (and correct) action is to disregard the small negative ϵ'' values and substitute $\epsilon'' = 0$. This is not to say that a negative value of ϵ'' cannot

exist. A negative value for ϵ'' can occur if the material exhibits a dielectric resonance of some type. However, since no such resonance behavior is observed (or expected) for the materials used in the measurements, the negative error bar values are mathematical artifacts, and we can safely presume that the lower extremes of the error bars for ϵ'' are actually zero.

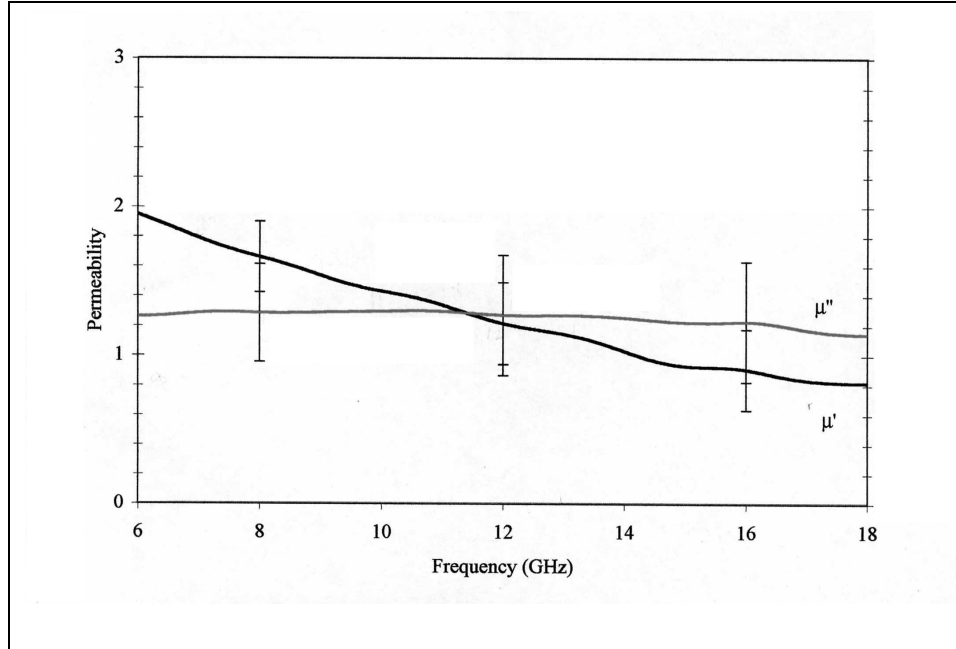


Figure E.4 Slab coating material permeability

The material used as the gap filler was a curable RAM butter, C-RAM KRS-124, batch B982474, manufactured by the Cuming Microwave Corporation. Several samples were cast, including both X-band waveguide and focused arch samples. These samples were not degassed so they contained a number of small air bubbles, which contribute to the ambiguities in determination of the gap filler constitutive properties. The X-band waveguide results were inconsistent, exhibited large error bars, and were not reported by the MML. The focused arch sample was cast as a ~ 1.2 mm thick sheet ~ 15 cm by 15 cm. Measurement results on this cured sample produced the permittivity and permeability data shown in Figures E.5 and E.6. The RAM butter gap filler material has a limited shelf life and was discarded upon completion of the testing.

As is seen in the materials properties data plots, a significant amount of uncertainty exists in the determination of both sets of material constitutive properties. It is reasonable to ask what effect these uncertainties might have on the determination of echo width of the gaps studied in this

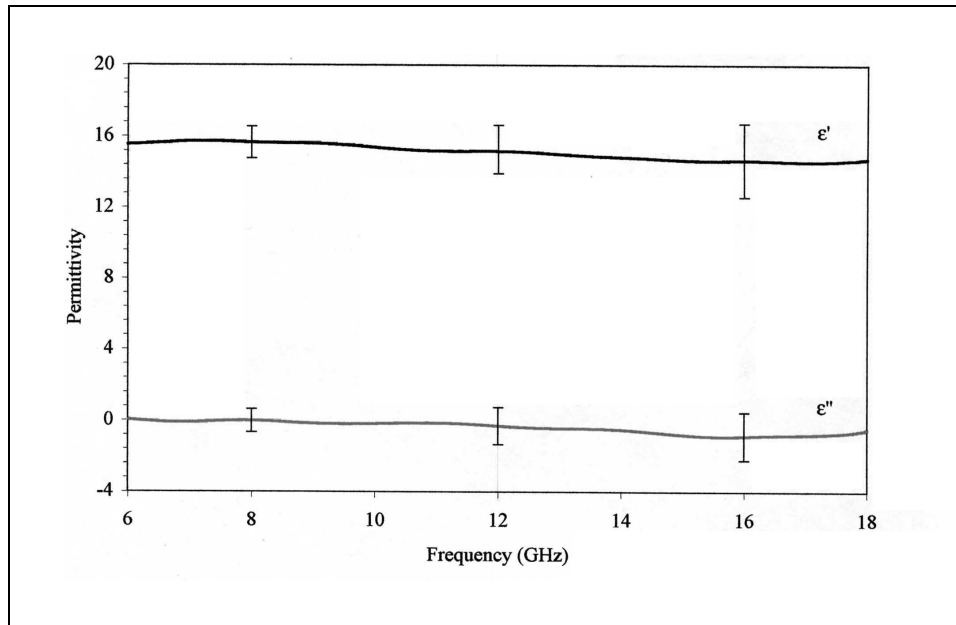


Figure E.5 Gap filler material permittivity

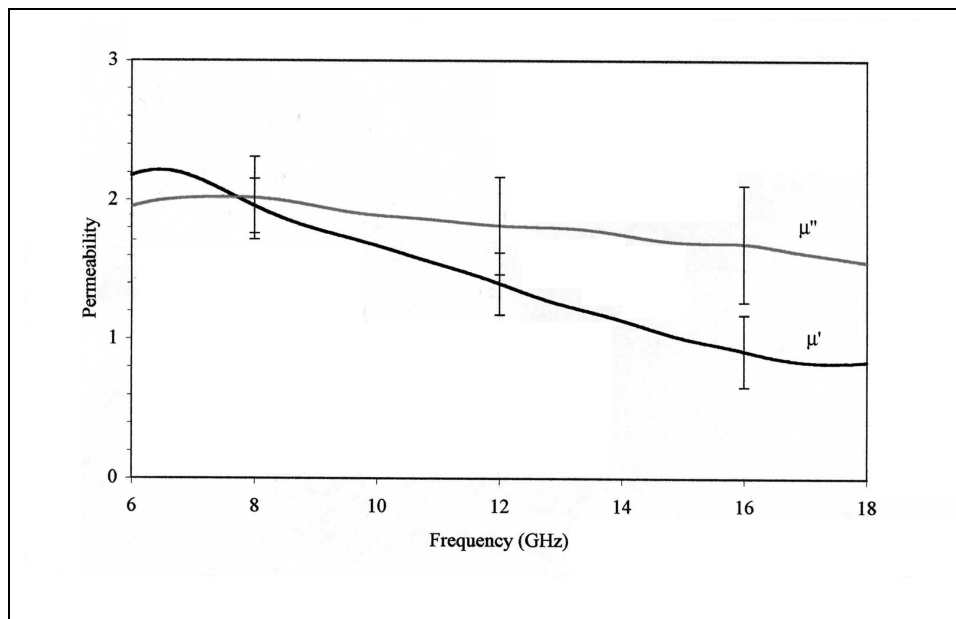


Figure E.6 Gap filler material permeability

dissertation. To address this issue, several runs were made using material property values indicated by the extremes of the error bars in Figures E.3 - E.6. These results are plotted in Figures E.7 and E.8 for an untreated and treated (filled) rectangular gap 100 mils wide. These results are computed at 8 GHz, which upon examination of data presented thus far, are certainly representative of a 'best

case' since, as we go higher in frequency, scattering levels (echo widths) due to the gap become higher and the error bars on our materials property measurements increase with frequency.

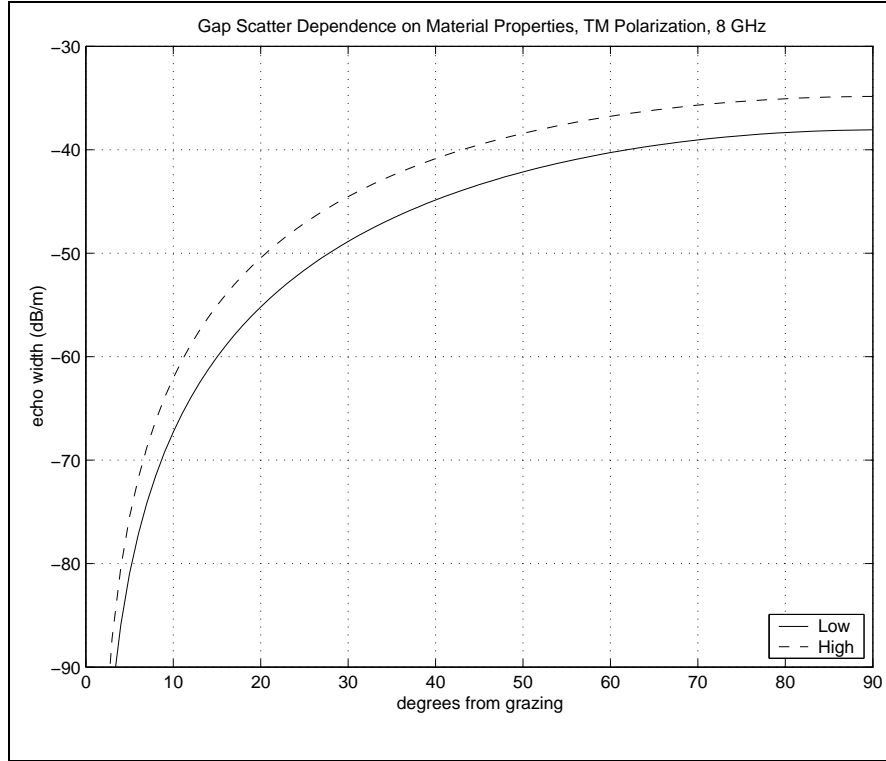


Figure E.7 Comparison for 100 mil wide, air filled rectangular gap with material property values taken from the extremes of the error bars shown in Figures E.3 and E.4. The slab thickness is 40 mils.

The material properties used in producing Figures E.7 and E.8, taken from Figures E.3 through E.6, are shown in the following table, where 'LOW' refers to the lower extremes of the error bars and 'HIGH' refers to the upper extremes of the error bars, in Figures E.3 through E.6 at 8 GHz.

	LOW	HIGH
slab	$\epsilon_r = 9.6$ $\mu_r = 1.5 - j1.0$	$\epsilon_r = 11.2 - j0.4$ $\mu_r = 1.9 - j1.6$
filler	$\epsilon_g = 14.8$ $\mu_g = 1.8 - j1.8$	$\epsilon_g = 16.6 - j0.6$ $\mu_g = 2.1 - j2.3$

One may note from Figures E.3 and E.5 that the values used in the computations for ϵ_r and ϵ_g in the 'LOW' cases do not include the negative imaginary values for the permittivities as shown in the figures. As discussed above, the value of ϵ'' used in both cases was $\epsilon'' = 0$.

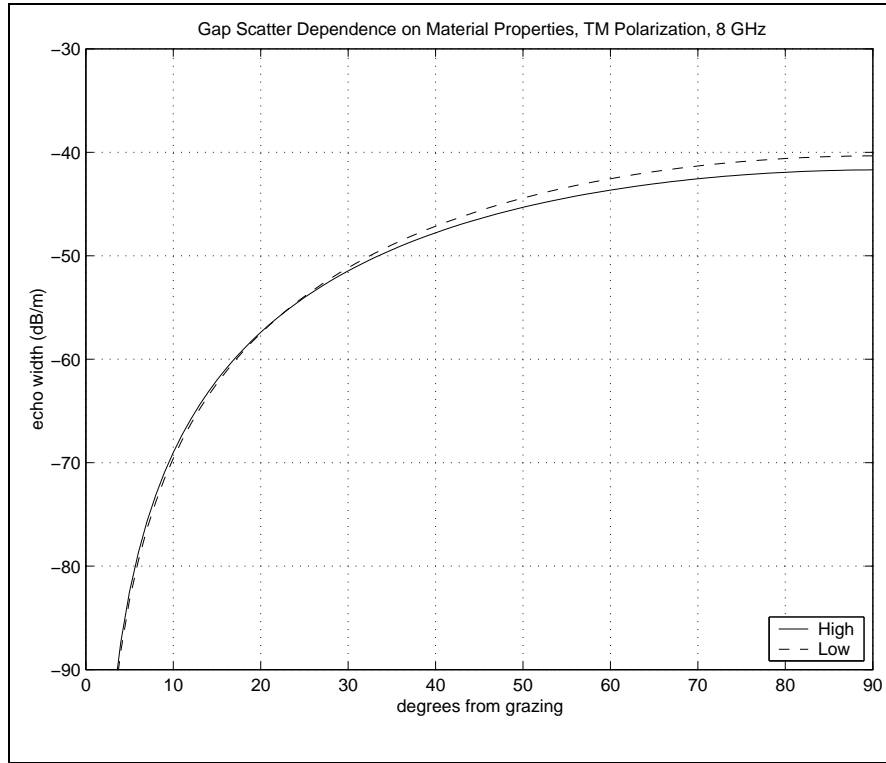


Figure E.8 Comparison for 100 mil wide, treated rectangular gap with material property values taken from the extremes of the error bars shown in Figures E.3 through E.6.

For the data shown in Figure E.7, the gridding of the gap region for the ‘LOW’ case was 6x3 elements while that for the ‘HIGH’ case was 7x3. For Figure E.8, the gridding was 8x4 for the ‘LOW’ case and 9x4 for ‘HIGH.’

An interesting effect is observed in comparing the data presented in these two figures. In Figure E.7, the echo width of the gap for the ‘HIGH’ material property values is $-34.8\text{dB}/m$ compared to $-38.1\text{dB}/m$ for the ‘LOW’ material property values. This difference of more than 3dB is significant and is indicative of the importance of obtaining accurate materials property measurements in low observables work. For the treated gap in Figure E.8, we see the difference is less drastic, but, interestingly, it is also inverted from the previous figure: the normal incidence echo width is $-41.7\text{dB}/m$ for the ‘HIGH’ material property values compared to $-40.3\text{dB}/m$ for the ‘LOW’ material property values, a difference of less than 1.5dB . If we contrast the respective material property values for each case (subtract the slab coating material property values from those of the gap filler) we see the contrast is less for the case of the ‘HIGH’ values. Comparing

the results of Figure E.7 to Figure E.8, we see greater echo width reduction for the ‘HIGH’ values case, $\sim 6.9dB$ compared to $\sim 2.2dB$ for the ‘LOW’ case. This is exactly what is expected from a gap filler material: closely match the properties of the base coating to reduce the RCS impact of the gap.

Appendix F. A Synopsis of the Skinner Theory and Code

In 1995, then AFIT/ENG faculty member Dr. J. Paul Skinner authored a paper entitled “*TM Scattering from a Gap in a Dielectric Coating on an Infinite Ground Plane*” which became the starting point for the work presented in this dissertation. Since this paper was never published in the literature it is synopsized in this Appendix.¹ What follows is a synopsis of the theory of the hybrid Moment Method / Green’s function technique as developed by Dr. Skinner. We make no attempt to replicate any of the comparative data included in Skinner’s paper as the computer code written by Skinner is well validated against Ram2d in the first several data plots in Chapter 4. So, while the theoretical development here is almost verbatim, this appendix is not a complete replication of his original paper. The synopsis will conclude with a comparison of what Skinner’s original work was intended to accomplish and how his work was extended and expanded in this dissertation.

F.1 Introduction

This paper examines the problem of scattering by a rectangular gap in a dielectric coated ground plane, as shown in Figure F.1. A plane wave illuminates the gap (with infinite length in

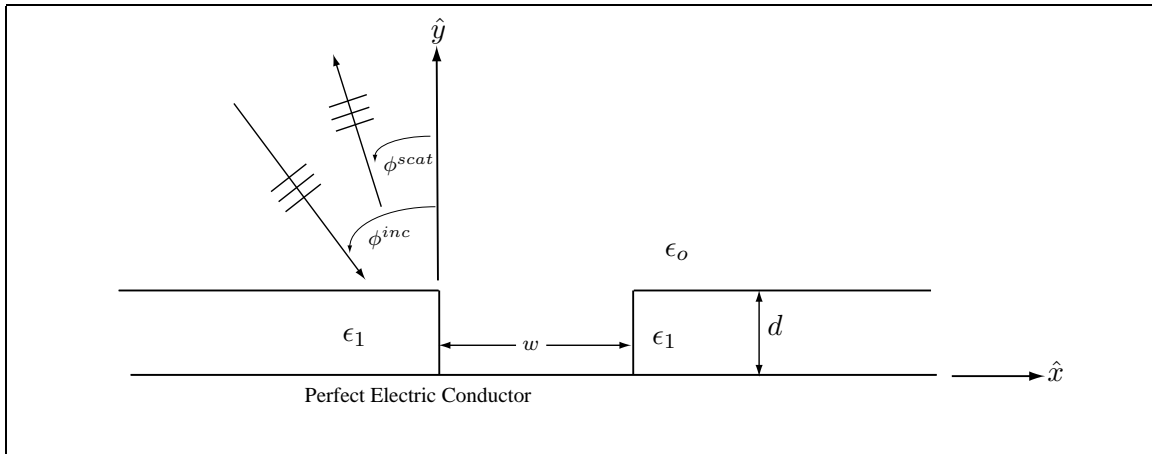


Figure F.1 Rectangular Gap in a Dielectric Coated Ground Plane

z) from the angle ϕ^{inc} off normal. We wish to examine the far zone scattering in the direction ϕ^{scat} . This angle takes on a positive value for the backscatter quadrant and a negative value for the forward scattering quadrant in the expressions to come (assuming $\phi^{inc} > 0$). The dielectric

¹With permission of Lt. Col. J. Paul Skinner

constant of each semi-infinite slab is $\epsilon_1 = \epsilon_r \epsilon_o$. The permeability of the slab material is the same as that of free space. The thickness of the slab is d and the gap width is w . In this paper, the TM_z polarization is considered, such that the electric field is \hat{z} directed.

The technique used in this paper to analyze the gap scattering is the hybrid moment method/Green's function method [3]. The article [3] gives references to dozens of previous journal articles documenting the use of the hybrid moment method/Green's function technique for a variety of scattering problems.

The expression of the Green's function for a dielectric coated ground plane is traditionally put in the form of a Sommerfeld integral. In this paper, however, several techniques are used to separate the Green's function into terms which can be handled efficiently. The remainder of the paper is broken into sections describing the integral equation formulation and moment method solution, the Green's function, and the computation of far zone scattered fields.

F.2 Integral Equation and Moment Method Solution

Again, consider the geometry depicted in Figure F.1. Let us begin by defining the nominal permittivity function, as if the gap were not present, i.e.,

$$\epsilon_{nom}(x, y) = \begin{cases} \epsilon_1, & 0 < y < d \\ \epsilon_o, & d < y \end{cases} \quad (F.1)$$

We will also refer to $\epsilon(x, y)$ as the true dielectric function of position with the gap present, which differs from ϵ_{nom} only within the gap region. In the spirit of the volume equivalence principle [15], one may define equivalent scattering currents caused by the dielectric change when the gap is created. This current is

$$\overline{J}_{eq} = j\omega(\epsilon_o - \epsilon_1)\overline{E} \quad (F.2)$$

throughout the gap region, and zero elsewhere. With this current and using the $e^{j\omega t}$ time convention, we may express Ampere's Law as

$$\nabla \times \overline{H} = j\omega\epsilon_{nom}\overline{E} + \overline{J}_{eq} \quad (F.3)$$

and with the substitution of Faraday's Law, form the vector wave equation

$$\nabla \times \nabla \times \bar{E} - \beta_{nom}^2 \bar{E} = -j\omega\mu_o \bar{J}_{eq} \quad (F.4)$$

where β_{nom} is the wavenumber associated with the nominal permittivity (i.e., $\beta_{nom} = \omega\sqrt{\mu_o\epsilon_1}$ for $0 < y < d$, and $\beta_{nom} = \omega\sqrt{\mu_o\epsilon_o}$ for $d < y$). From Equation (F.4), we can think of \bar{J}_{eq} as a source of scattered fields in the presence of the nominal (no gap) geometry, such that

$$\bar{E} = \bar{E}^{ginc} + \bar{E}^{scat} \quad (F.5)$$

We refer to the “generalized” incident fields, \bar{E}^{ginc} , as those existing due to an incident plane wave onto the nominal (no gap) geometry.

In the *TM* case, the electric field is purely \hat{z} directed and the vector wave equation reduces to the simpler scalar equation,

$$(\nabla_t^2 + \beta_{nom}^2)\bar{E}_z = j\omega\mu_o J_{eqz} \quad (F.6)$$

where $\nabla_t^2 = \nabla^2 - \partial^2/\partial z^2$. We use the forcing function on the right hand side of F.6 to generate the scattered fields, leaving the generalized incident fields as a solution to the corresponding homogeneous equation. With a free space based incident field of

$$E_z^{inc}(x, y, \phi^{inc}) = e^{j\beta_o d \cos \phi^{inc}} e^{-j\beta_o x \sin \phi^{inc}} \tau_{0,1} \left[\frac{e^{-j\beta_1(d-y) \cos \phi_1} (1 - e^{-j2\beta_1 y \cos \phi_1})}{1 + \Gamma e^{-j2\beta_1 d \cos \phi_1}} \right] \quad (F.7)$$

In Equation (F.7), we make use of the refracted angle ϕ_1 within the slab, which is found by Snell's Law,

$$\beta_1 \sin \phi_1 = \beta_o \sin \phi^{inc} \quad (F.8)$$

The symbols $\tau_{0,1}$ and Γ represent Fresnel transmission (from free space into the dielectric) and reflection (inside dielectric onto dielectric-free space interface) coefficients. They are

$$\tau_{0,1} = \frac{2\eta_1 \cos \phi^{inc}}{\eta_1 \cos \phi^{inc} + \eta_0 \cos \phi_1} \quad (F.9)$$

and

$$\Gamma = \frac{\eta_1 \cos \phi^{inc} - \eta_0 \cos \phi_1}{\eta_1 \cos \phi^{inc} + \eta_0 \cos \phi_1} \quad (\text{F.10})$$

where η refers to the intrinsic impedance of the appropriate medium.

Consider a Green's function which obeys

$$(\nabla_t^2 + \beta_{nom}^2)G(\vec{\rho}, \vec{\rho}') = -\delta(\vec{\rho} - \vec{\rho}') \quad (\text{F.11})$$

with the spatially dependent β_{nom} , along with the Sommerfeld radiation condition and the PEC boundary condition,

$$G(x, 0; x', y') = 0 \quad (\text{F.12})$$

This Green's function will take on the forms of an “internal” Green's function (G^{int}) for $0 < y < d$, and an “external” Green's function (G^{ext}) for $d < y$. In either case, the source will always be within the “former” gap region ($0 < x' < w, 0 < y' < d$) for the applications to follow.

Once the Green's function is determined, the scattered fields are found as

$$E_z^{scat}(\vec{\rho}) = -j\omega\mu_o \int \int_{Gap} J_{eqz}(\vec{\rho}') G(\vec{\rho}, \vec{\rho}') d\vec{\rho}' \quad (\text{F.13})$$

The equivalent scattering current are found by solving the volumetric EFIE which arises from Equation (F.5), i.e.,

$$E_z^{scat}(\vec{\rho}) = \frac{J_{eqz}(\vec{\rho})}{j\omega(\epsilon_o - \epsilon_1)} + j\omega\mu_o \int \int_{Gap} J_{eqz}(\vec{\rho}') G(\vec{\rho}, \vec{\rho}') d\vec{\rho}' \quad (\text{F.14})$$

This equation can be solved in an approximate sense by a moment method procedure with rectangular volume pulse basis functions ($P_n = 1$ within the n th cell, and zero elsewhere) with point matching in the centers of the rectangular cells (designated by locations $\vec{\rho}_m$, where m runs from 1 to N). Assuming discretization into N uniformly generated rectangular cells with the gap, the matrix equation follows:

$$[V] = [Z + \Delta Z] [I] \quad (\text{F.15})$$

where

$$V_m = E_z^{ginc}(\bar{\rho}_m) \quad (\text{F.16})$$

$$Z_{mn} = j\omega\mu_o \int \int_{nthcell} G^{int}(\bar{\rho}_m, \bar{\rho}') d\bar{\rho}' \quad (\text{F.17})$$

$$\Delta Z_{mn} = \frac{\delta_{mn}}{j\omega(\epsilon_0 - \epsilon_1)} \quad (\text{F.18})$$

The next section discusses methods to handle the internal Green's function in the evaluation of Z_{mn} .

F.3 Internal Green's Function

The Green's function for radiation of a filament of current within a grounded dielectric slab to points also within the slab is split into a free space type Green's function and an additional term which accounts for the bounces that waves take along the planar boundaries. That is, we choose to express the internal Green's function as

$$G^{int}(\bar{\rho}, \bar{\rho}') = -\frac{j}{4} H_o^2(\beta_1 |\bar{\rho} - \bar{\rho}'|) + G_{bounces}(\bar{\rho}, \bar{\rho}') \quad (\text{F.19})$$

In forming this split, we recognize only the free space Green's function term to possess a singularity associated with co-location of a source and observation point. For the integrations to be performed, the free space singularity can be handled with a circle extraction method, as is often used when performing 2-D moment method solutions for volume equivalent currents [30].

The bounce term in the internal Green's function may be formulated by using the Array Scanning Method (ASM), in an application similar to that found in [37]. This approach avoids the formation of a Sommerfeld integral, and retains a fair amount of computational efficiency. To form the ASM derived solution, we envision not just one radiating filament of current, but an entire infinite array of periodic filaments within the dielectric slab, as depicted in Figure F.2. The currents on the filaments are identical in amplitude, but vary in phase with a linear phase progression to steer the radiation in some direction. Using a directional cosine phase steering parameter s_{x_1} , the

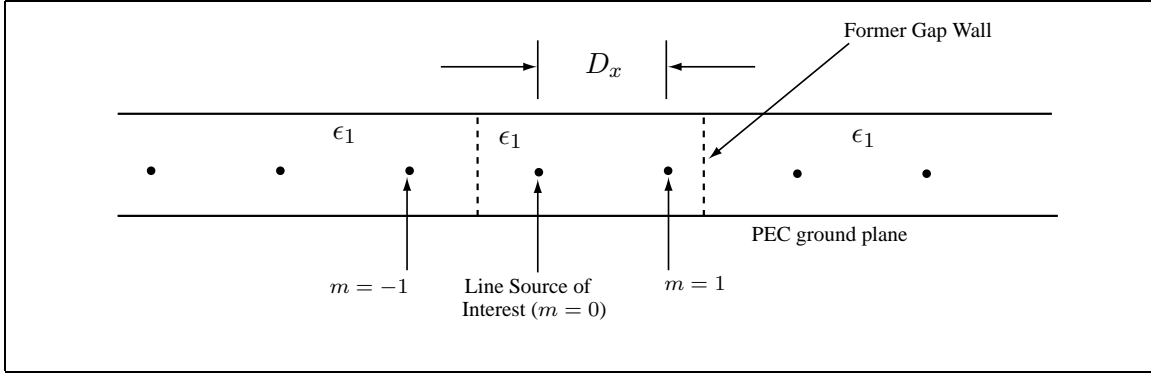


Figure F.2 Infinite Array of Radiating Current Filaments for use in the Integrand in the Array Scanning Method

radiation from the entire array in a homogeneous space may be formed in the spatial sum,

$$G_{array, homo} = -\frac{j}{4} \sum_{m=-\infty}^{\infty} H_o^{(2)} \left(\beta_1 \sqrt{(x - mD_x)^2 + y^2} \right) e^{j\beta_1 m D_x s_{x_1}} \quad (F.20)$$

By using Poisson's sum formula [20], one can transform this into a spectral sum of plane waves,

$$G_{array, homo} = -\frac{j}{2\beta_1 D_x} \sum_{n=-\infty}^{\infty} \frac{e^{-j\beta_1 (\bar{R} - \bar{R}') \cdot \hat{r}_1}}{r_{y_1}} \quad (F.21)$$

where $\hat{r}_1 = \hat{x}r_{x_1} + \hat{y}r_{y_1}$,

$$r_{x_1} = s_{x_1} + \frac{n\lambda_1}{D_x} \quad (F.22)$$

and

$$r_{y_1} = \sqrt{1 - r_{x_1}^2} \quad (F.23)$$

The positive root is chosen for the finite number of propagating plane waves, and the “-j” root is chosen for the evanescent plane waves, to maintain the radiation condition.

Using the methods of Munk [23], the radiation of an array within a stratified media can be written from the radiation in free space with an additional factor dubbed the T-factor. This T-factor accounts for the infinite geometric series of bounces each plane wave (propagating or evanescent) takes along the planar boundaries. Mathematically, we have

$$G_{array, slab} = G_{array, homo} \cdot T \quad (F.24)$$

For the present application, the T-factor is

$$T = \frac{\Gamma e^{-j2\beta_1 dr_{y1}} \left(e^{j\beta_1(y+y')r_{y1}} - 2 \cos[\beta_1(y-y')r_{y1}] \right) - e^{-j\beta_1(y+y')r_{y1}}}{1 + \Gamma e^{-j2\beta_1 dr_{y1}}} \quad (\text{F.25})$$

where

$$\Gamma = \frac{\eta_o r_{y1} - \eta_1 r_{y_o}}{\eta_o r_{y1} + \eta_1 r_{y_o}} \quad (\text{F.26})$$

and

$$r_{y_o} = \sqrt{1 - r_{x_o}^2} \quad (\text{F.27})$$

with

$$r_{x_o} = \frac{\beta_1}{\beta_o} r_{x1} \quad (\text{F.28})$$

Note that $\hat{r}_0 = \hat{x}r_{x_o} + \hat{y}r_{y_o}$ is the propagation unit vector for the plane wave in free space (beyond the slab). Also note that the above T-factor does not include a direct plane wave propagation (only bounce terms), since we chose to separate this out into the single Hankel function in Equation (F.19).

Using the Array Scanning Method (ASM) with an inter-element spacing of $D_x = \lambda_1/2$, the “bounced” radiation from a single filament at (x', y') is

$$G_{bounces} = \frac{1}{2} \int_{-1}^1 G_{array,slab} ds_{x1} \quad (\text{F.29})$$

$$= -\frac{j}{4\beta_1 D_x} \int_{-1}^1 \sum_{n=-\infty}^{\infty} \frac{e^{-j\beta_1(\bar{R}-\bar{R}')\cdot\hat{r}_1}}{r_{y1}} \cdot T ds_{x1} \quad (\text{F.30})$$

where T is defined in Equation (F.25). This may appear to be an intimidating expression since an infinite sum of plane waves with complicated T-factors is embedded in the integrand, but from our choice of D_x , we force only the $n = 0$ plane wave to be propagating, and the evanescent plane waves decay extremely fast with the bounce paths. In practice, only the $n = 0$ and ± 1 terms need to be included for sufficient numerical convergence in most situations. The ASM does require numerical integration, however, though the domain is bounded. The integrand will become singular for the $n = 0$ term due to the denominator of the T-factor going to zero at the resonant excitation of surface waves. These surface wave poles are guaranteed to occur only if $|s_{x1}| > \sqrt{\epsilon_o/\epsilon_1}$, i.e.,

beyond the critical angle. Their location may be found with a Newton-Raphson search, and their contribution to the integral may be extracted in closed form, as described in [37]. If one doesn't wish to locate and extract the surface wave contributions in closed form, a practical solution is to add a little loss to β_1 , for use in the denominator of the T-factor. This keeps the integrand bounded with little distortion in the resulting integral evaluation.

F.4 Far Zone Scattered Fields

The calculation of external scattered fields uses Equation (F.13) with the external Green's function. To form G^{ext} , we may again make use of the Array Scanning Method, with the concept of extracting the radiation of a single filament of current from an infinite array of filaments. The approach is similar to that presented in the previous section, except a different T-factor is now necessary to give the net transmission from the slab into free space. The result of the ASM procedure is

$$G^{ext} = -\frac{j}{4\pi} \int_{-1}^1 \sum_{n=-\infty}^{\infty} \frac{e^{-j\beta_1(\bar{R}-\bar{R}')\cdot\hat{r}_1}}{r_{y1}} T^{ext} ds_{x1} \quad (F.31)$$

where

$$T^{ext} = \tau e^{-j\beta_o(y-d)r_{yo}} e^{-j\beta_1(d-y')r_{y1}} \frac{1 - e^{-j2\beta_1 y' r_{y1}}}{1 + \Gamma e^{-j2\beta_1 d r_{y1}}} \quad (F.32)$$

and

$$\tau = \frac{2\eta_o r_{y1}}{\eta_o r_{y1} + \eta_1 r_{yo}} \quad (F.33)$$

The Γ in Equation (F.32) is defined in Equation (F.26).

For far zone scattering, the evanescent plane waves in Equation (F.31) may be dropped, leaving only the $n = 0$ term. The limits of the ASM integral may also be truncated to where s_{x1} corresponds to a critical angle (thus, the T-factor will never be singular). The integrand is highly oscillatory, with increasing frequency of oscillations as the field observation radius ρ increases. Thus, numerical evaluation of Equation (F.31) is difficult, but as noted for a similar far zone ASM application in [37], the integral may be evaluated in closed form by the stationary phase method. Performing this evaluation and making use of the algebraic expression in Equation (F.7), the far

zone external Green's function is

$$G_{fz}^{ext} = -\frac{j}{4} \sqrt{\frac{2}{\pi\beta_o\rho}} e^{j\pi/4} e^{-j\beta_o\rho} E_z^{ginc}(x', y', \phi^{scat}) \quad (F.34)$$

This result can also be derived by use of reciprocity.

With this far zone external Green's function, the far zone scattered field is

$$\begin{aligned} E_{fz,z}^{scat}(\phi^{scat}) &= -\frac{\omega\mu_o}{4} \sqrt{\frac{2}{\pi\beta_o\rho}} e^{j\pi/4} e^{-j\beta_o\rho} \sum_{n=1}^N I_n \\ &\cdot \int \int_{nthcell} E_z^{ginc}(x', y', \phi^{scat}) dx' dy' \end{aligned} \quad (F.35)$$

At this point in his original paper, Dr. Skinner continued with an effort to validate the theory just presented. We will not reproduce this portion of his paper but go on to provide a short description of his resulting computer code.

F.5 Skinner's *gaptm* Computer Code

Based on the theory developed in the preceding sections, a FORTRAN computer code was developed by Skinner to generate comparative data for validation purposes. It is this computer code, called *gaptm*, that was used in this dissertation to generate the 'Skinner' data plotted in Figures 4.2 through 4.5. In this section, we briefly summarize the *gaptm* code and compare and contrast it to the code developed as part of this dissertation research.

The *gaptm* code is highly streamlined and requests user keyboard inputs of the variables for the width of the gap, dielectric slab thickness, slab dielectric constant (real), the illumination frequency, and finally a discretization parameter that is used to determine the gridding of the rectangular gap. Upon completion of these inputs, *gaptm* then computes the location of the centers of the gap region cells and indexes them.

In contrast to the procedure used in *gaptm*, the codes developed in this dissertation read complex material property data (for both the slab coating and gap filler materials), frequency, and gap vertices (capable of producing non-rectangular gap geometries) from input files. The

discretization parameter is hard wired into the code but could easily be read in as part of the input file.

The impedance matrix generated by the *gaptm* code is the same as that generated by the TM polarization code developed in this dissertation for a pure dielectric case, where the Green's function is the canonical G_{zz} term, Equation (2.51). The primary difference lies in the manner in which the bounce correction terms are integrated. In *gaptm*, Skinner used two fixed Simpson's rule quadrature routines, one for the propagating plane wave mode term (the central region) and one for a single evanescent plane wave mode term ($n = 1$). In these routines, the integrand function is folded, assuming symmetry about $s_x = 0$. While seemingly crude, the results presented in Chapter 4 indicate that the assumption works well for lossless slab coating materials.

To compute his direct coupling term, Skinner used a routine he had written to compute the Hankel function with a real-valued argument. To invert his impedance matrix Skinner used a routine based on the Crout reduction procedure (see Section 2.2 of [39]). By contrast, the 'Simpson' code uses the 'Amos' routines implemented in Matlab[®] version 6 to compute the direct terms because they allow for complex-valued arguments, and the Matlab[®] built-in function 'INV' to invert the resulting impedance matrix. As was mentioned earlier, the matrix inversion process in these hybrid codes is very rapid compared to matrix fill time.

With these differences the two hybrid codes produce results that are almost graphically equivalent in the figures shown in Chapter 4. Added flexibility was needed in the codes developed in this dissertation to be able to handle lossy materials, gaps filled with material other than air, non-rectangular gap geometries, and TE polarization.

F.6 Comparison of Skinner Theory to Dissertation

Some of the limitations in the theory as developed by Dr. Skinner² are immediately obvious. The most obvious one is that he limited his development to the TM polarization case using an Electric Field Integral Equation (EFIE). Secondly, he restricted his development to lossless dielectric

²We point out that Skinner's purpose was to initiate a research topic suitable for a Ph.D. student - namely, the author of this dissertation. This dissertation is a direct result of Skinner's motivating work.

slab coating materials as well as gaps that were filled only with air. He then also limited his gap geometries to being rectangular in shape.

Expansion of the theory to the TE polarization case required either development of a dyadic Green's function version of the scalar Green's function developed by Skinner (as was done in this dissertation) or use of a Magnetic Field Integral Equation (MFIE) formulation. Expansion of the theory to account for magnetic materials also would require development of either a dyadic Green's function approach or an MFIE-form for TM polarization to handle the volume magnetic equivalent currents. Taking the dyadic Green's function and coupled integral equations approach in this dissertation simultaneously took care of both of these expansions in the theory.

The expansion of the theory to handle lossy materials required subtle extensions to many of the equations and constants presented by Skinner, but can be traced to the expression for r_{x_1} and the propagation constant of the medium. In this dissertation, in Equation (2.5), $r_{x_1} = \frac{Re(k)}{k}(s_{x_1} + \frac{n\lambda_1}{D_x})$. One immediately recognizes that for the lossless material case, this is equivalent to the form used by Skinner in Equation (F.22). It may be argued that a more straightforward extension of the propagation constant in this dissertation may have been to use the definition $\gamma = \alpha + j\beta$ where α is the attenuation constant. Had this approach been adopted here, the factor $Re(k)/k$ would be replaced by $\gamma/j\beta$, but the end results would not be affected by this change.

Finally, we point out that a more robust gap region gridding scheme was adopted in this dissertation to be able to handle non-rectangular gap geometries. Since most of the slab coating materials are fairly thin, and the gaps fairly narrow, this extension may be of minimal impact as the non-rectangular gaps perturb the echo width patterns only slightly. However, these differences can be detected, so this extension is a valid one.

In summary, the theory as developed by Skinner and presented in this appendix, combined with the results from his computer code shown in Chapter 4, show that his initial work is a special case of the theory and computer code capability developed in this dissertation. For lossless slab coating material, air-filled gaps, and TM polarization, both codes can be used and should produce the same result. The results presented in Chapter 4 indicate that this is so.

Bibliography

1. Collin, R.E., *Field Theory of Guided Waves*, Second Edition, IEEE Press, The Institute of Electrical and Electronic Engineers, Inc., New York, 1991.
2. Newman, E.H., "TM and TE Scattering by a Dielectric/Ferrite Cylinder in the Presence of a Half-Plane," *IEEE Trans. on Antennas Propagat.*, Vol. AP-34, No. 6, pp.804-813, June 1986.
3. Newman, E.H., "An Overview of the Hybrid MM/Green's Function Method in Electromagnetics," *Proc. IEEE*, Vol. 76, No. 3, pp. 270-282, March 1988.
4. Final Report, "Scattering from Generic Surface Discontinuities," Volumes I, II, V, and VI, WRDC-TR-90-9001, Northrop Corporation Aircraft Division, Hawthorne, CA, June 1990.
5. Senior, T.B.A. and J.L. Volakis, "Scattering by Cracks and Gaps," *IEEE Trans. on Antennas Propagat.*, Vol.AP-37, No.6, pp.744-750, June 1989.
6. Senior, T.B.A., K. Sarabandi and J.R. Natzke, "Scattering by a Narrow Gap," *IEEE Trans. on Antennas Propagat.*, Vol. AP-38, No.7, pp.1102-1110, July 1990.
7. Dominek, A.K., H.T. Shamansky and N. Wang "Scattering from Three-Dimensional Cracks," *IEEE Trans. on Antennas Propagat.*, Vol. AP-37, No.5, pp.586-591, May 1989.
8. Asvestas, J.S. and R.E. Kleinman, "Electromagnetic Scattering by Indented Screens," *IEEE Trans. on Antennas Proagat.*, Vol. AP-42, No. 1, pp. 22-30, January 1994.
9. Bindiganavale, S.S. and J.L. Volakis, "Scattering by a Narrow Groove in an Impedance Plane," *Radio Science*, Vol. 31, No. 2, pp. 401-408, March-April 1996.
10. Moore, J. and H. Ling, "Scattering by Gaps in Coated Structures," *Journal of Electromagnetic Waves and Applications*, Vol. 7, No. 3, pp. 325-344, 1993.
11. Aberle, J.T. "Hybrid Finite Element/Moment Method Solution of Two-Dimensional Scattering Problems," *IEEE APS Int. Symposium Digest*, Vol. 3, pp. 1398-1399, 1994.
12. Ling, H., J. Moore, D. Bouche and V. Saavedra, "Time-Frequency Analysis of Backscattered Data from a Coated Strip with a Gap," *IEEE Trans. on Antennas Propagat.*, Vol. AP-41, No. 8, pp. 1147-1150, August 1993.
13. Newman, E.H., "TM Scattering by a Dielectric Cylinder in the Presence of a Half-Plane," *IEEE Trans. on Antennas Propagat.*, Vol. AP-33, No. 7, pp. 773-782, July 1985.
14. Michalski, K.A., R.D. Nevels and D. Zheng, "Comparison of Lorentz and Coulomb Gauge Formulations for TE Wave Scattering by 2-D Surfaces of Arbitrary Shape in the Presence of a Circular Cylinder," *IEEE Trans. on Antennas Propagat.*, Vol. AP-38, No. 5, pp. 732-739, May 1990.
15. Balanis, C.A., *Advanced Engineering Electromagnetics*, John Wiley & Sons, Inc., New York, 1989.
16. Tai, C.T., *Dyadic Green Functions in Electromagnetic Theory*, Second Edition, IEEE Press, The Institute of Electrical and Electronic Engineers, Inc., New York, 1994.

17. Harrington, R.F., *Time Harmonic Electromagnetic Fields*, McGraw Hill Book Co. Inc., New York, 1961.
18. Van Bladel, J., *Electromagnetic Field Theory*, Revised Printing, Hemisphere Publishing Co., New York, 1985.
19. Munk, B.A., *Frequency Selective Surfaces: Theory and Design*, John Wiley & Sons, Inc., New York, NY, 2000.
20. Papoulis, A., *The Fourier Integral and Its Application*, Chapter 3, McGraw Hill Book Co. Inc, New York, 1962.
21. Munk, B.A. and G.A. Burrell, "Plane-Wave Expansion for Arrays of Arbitrarily Oriented Piecewise Linear Elements and Its Application in Determining the Impedance of a Single Linear Antenna in a Lossy Half-Space" *IEEE Trans. on Antennas Propagat.* Vol. AP-27, No.3, pp 331-343, May 1979.
22. Skinner, J.P. and Munk, B.A. "Mutual Coupling Between Parallel Columns of Periodic Slots in a Ground Plane Surrounded by Dielectric Slabs," *IEEE Trans. on Antennas Propagat.* Vol. AP-40, No.11, pp 1324-1335, Nov 1992.
23. Munk, B.A., G.A. Burrell and T.W. Kornbau, "A General Theory of Periodic Surfaces in a Stratified Dielectric Medium," Technical Report AFAL-TR-77-219, The Ohio State University, Columbus, Ohio, November 1977.
24. Dudley, D.G, *Mathematical Foundations for Electromagnetic Theory*, IEEE Press, The Institute of Electrical and Electronic Engineers, New York, 1994.
25. Amos, D.E., "A Portable Package for Bessel Functions of a Complex Argument and Nonnegative Order," *Trans. Math. Software*, 1986.
26. Wang, J.J.H. *Generalized Moment Methods in Electromagnetics, Formulation and Computer Solution of Integral Equations*, John Wiley & Sons, New York, 1991.
27. Tyras, G., *Radiation and Propagation of Electromagnetic Waves*, Academic Press, New York, 1969.
28. Felsen, L.B. and N. Marcuvitz *Radiation and Scattering of Waves*, IEEE Press, The Institute of Electrical and Electronic Engineers, New York, 1994.
29. Campbell, G.A. and R.M. Foster *Fourier Integrals for Practical Applications*, D. Van Nostrand Company, Inc., New York, 1948.
30. Richmond, J.H., "Scattering by a Cylinder of Arbitrary Cross Section," *IEEE Trans. on Antennas Propagat.* Vol. AP-13, No. 5, pp. 334-341, May 1965.
31. Abramowitz, M. and I.A. Stegun (Ed.), *Handbook of Mathematical Functions*, Dover Publications, Inc., New York, 1970.
32. Schultz, J.W., Simpson, G., Reinhardt, G. and Bashore, S., *Methods for Measuring the Effectiveness of Conductive Caulks Used in the Treatment of Gaps and Cracks*, Have Forum 1999 Conference, San Antonio, TX, June 1999.

33. McClary, R.L., "Ram2d, 2D Integral Equation Computer Code," User's Manual, Northrop Grumman Corporation, Pico Rivera, CA, Feb 1995.
34. Peterson, A.F., S.L. Ray and R. Mittra, *Computational Methods for Electromagnetics*, IEEE Press, The Institute of Electrical and Electronic Engineers, New York 1998.
35. Petersson, L.E.R. and G.S. Smith, "An Estimate of the Error Caused by the Plane-Wave Approximation in Free-Space Dielectric Measurement Systems," *IEEE Trans. on Antennas Propagat*, Vol. AP-50, No. 6, pp 878-887, June 2002.
36. Knott, E.F., J.F. Shaeffer and M.T. Tuley, *Radar Cross Section*, Second Edition, Artech House, Boston, 1993.
37. Skinner, J.P., "Scattering from a Finite Collection of Transverse Dipoles and Axial Slot Arrays with Edge Effects," Ph.D. Dissertation, The Ohio State University, Columbus, Ohio, 1991.
38. Harrington, R.F., *Field Computation by Moment Methods*, R.E. Krieger Publishing Co. Inc., Malabar, Florida, 1968.
39. Isaacson, E. and H.B. Keller, *Analysis of Numerical Methods*, Dover Publications, Inc., New York, 1994.
40. Nicolson, A.M. and G.F. Ross, "Measurement of the Intrinsic Properties of Materials by Time-Domain Techniques," *IEEE Trans. Instrum. Meas.*, Vol. IM-19, pp. 377-382, Nov 1970.
41. Weir, W.B., "Automatic Measurement of Complex Dielectric Constant and Permeability at Microwave Frequencies," *Proc. IEEE*, Vol. 62, pp. 33-36, January 1974.
42. Baker-Jarvis, J., M.D. Janezic, J.H. Grosvenor, Jr. and R.G. Geyer, *Transmission/Reflection and Short-Circuit Line Methods for Measuring Permittivity and Permeability*, NIST Technical Note 1355-R, National Institute of Standards and Technology, United States Department of Commerce, December 1993.
43. Baker-Jarvis, J., *Transmission/Reflection and Short-Circuit Line Permittivity Measurements*, NIST Technical Note 1341, National Institute of Standards and Technology, United States Department of Commerce, July 1990.

Vita

George R. Simpson graduated from Western Brown Senior High School in Mt. Orab, Ohio, in May 1977. He graduated from The University of Kentucky in Lexington, Kentucky, with a Bachelor of Science degree in Electrical Engineering in December 1981. He is a distinguished graduate of the Air Force Institute of Technology, graduating with a Master of Science degree in Electrical Engineering in December 1985.

From 1981 to 1989, he was a commissioned officer in the United States Air Force, serving in duty assignments in San Antonio, Texas and Los Angeles, California. In October 1989, he became a civil servant, joining the Air Force Research Laboratory Signature Technology Office at Wright Patterson Air Force Base, Ohio. He returns to the Signature Technology Office upon graduation.

REPORT DOCUMENTATION PAGE				<i>Form Approved OMB No. 0704-0188</i>					
<small>The public reporting burden for this collection of information is estimated to average 1 hour per response, including the time for reviewing instructions, searching existing data sources, gathering and maintaining the data needed, and completing and reviewing the collection of information. Send comments regarding this burden estimate or any other aspect of this collection of information, including suggestions for reducing the burden, to Department of Defense, Washington Headquarters Services, Directorate for Information Operations and Reports (0704-0188), 1215 Jefferson Davis Highway, Suite 1204, Arlington, VA 22202-4302. Respondents should be aware that notwithstanding any other provision of law, no person shall be subject to any penalty for failing to comply with a collection of information if it does not display a currently valid OMB control number.</small> PLEASE DO NOT RETURN YOUR FORM TO THE ABOVE ADDRESS.									
1. REPORT DATE (DD-MM-YYYY) 08-10-2002		2. REPORT TYPE PhD Dissertation		3. DATES COVERED (From - To) Dec 1997 - Sep 2002					
4. TITLE AND SUBTITLE Electromagnetic Scattering From a Gap in a Magneto-Dielectric Coating on an Infinite Ground Plane				5a. CONTRACT NUMBER					
				5b. GRANT NUMBER					
				5c. PROGRAM ELEMENT NUMBER					
6. AUTHOR(S) George R. Simpson				5d. PROJECT NUMBER					
				5e. TASK NUMBER					
				5f. WORK UNIT NUMBER					
7. PERFORMING ORGANIZATION NAME(S) AND ADDRESS(ES) Air Force Institute of Technology Graduate School of Engineering and Management (AFIT/EN) 2950 P Street, Bldg 640 WPAFB OH 45433-7765				8. PERFORMING ORGANIZATION REPORT NUMBER AFIT/DS/ENG/02-03					
9. SPONSORING/MONITORING AGENCY NAME(S) AND ADDRESS(ES) AFRL/SNS Attn: Dr. Kueichien C. Hill 2519 K Street, Bldg 254 WPAFB OH 45433-7602				10. SPONSOR/MONITOR'S ACRONYM(S)					
				11. SPONSOR/MONITOR'S REPORT NUMBER(S)					
12. DISTRIBUTION/AVAILABILITY STATEMENT APPROVED FOR PUBLIC RELEASE; DISTRIBUTION UNLIMITED									
13. SUPPLEMENTARY NOTES									
14. ABSTRACT The electromagnetic scattering from a gap in a magneto-dielectric coating on an infinite ground plane is analyzed. In this context, the gap forms a break only in the magneto-dielectric coating while the ground plane is continuous and unbroken. Volume equivalence is used to convert the gap region to one containing unknown volumetric equivalent electric and magnetic currents. The equivalent problem then is one of these currents radiating in the presence of an unbroken, grounded magneto-dielectric slab. A Green's function for this geometry is developed consisting of two terms: a direct coupling term and a correction term to account for the multiple reflected wave series resulting from the grounded-slab geometry. This correction term is formulated using periodic array theory and is derived using the Array Scanning Method. A set of coupled integral equations based on the equivalent currents is then solved via the Method of Moments using pulse basis and delta testing functions. The model can represent a gap that is of a general 2D shape (the gap is assumed to be infinite in it's translational direction) and can be filled with an inhomogeneous material possessing isotropic magnetic and dielectric constitutive properties different from those of the slab coating. Scattering from the gap is evaluated for plane wave illumination in both TM and TE polarization with respect to the gap.									
15. SUBJECT TERMS Electromagnetic Scattering, Method of Moments, Green's Functions, Array Scanning Method									
16. SECURITY CLASSIFICATION OF: <table border="1" style="width: 100%; border-collapse: collapse;"> <tr> <td style="width: 33%; padding: 2px;">a. REPORT U</td> <td style="width: 33%; padding: 2px;">b. ABSTRACT U</td> <td style="width: 33%; padding: 2px;">c. THIS PAGE U</td> </tr> </table>			a. REPORT U	b. ABSTRACT U	c. THIS PAGE U	17. LIMITATION OF ABSTRACT UL		18. NUMBER OF PAGES 193	
a. REPORT U	b. ABSTRACT U	c. THIS PAGE U							
					19a. NAME OF RESPONSIBLE PERSON William D. Wood, Maj, USAF (ENG)				
					19b. TELEPHONE NUMBER				